The biophysical processes controlling the South-East Madagascar Bloom



University of Cape Town

Ahmad Fehmi Dilmahamod

Department of Oceanography

University of Cape Town

This dissertation is submitted for the degree of

Doctor of Philosophy

University of Cape Town August 2018

The copyright of this thesis vests in the author. No quotation from it or information derived from it is to be published without full acknowledgement of the source. The thesis is to be used for private study or non-commercial research purposes only.

Published by the University of Cape Town (UCT) in terms of the non-exclusive license granted to UCT by the author.

University of Cape Town

Supervisors:

- Prof. Chris Reason

Department of Oceanography, University of Cape Town.

- Dr Pierrick Penven

Univ. Brest, CNRS, IRD, Ifremer.

Laboratoire d'Oceanographie Physique et Spatial.

- Assoc. Prof. Juliet Hermes

South African Environmental Observation Network, Egagasini node.

Department of Oceanography, University of Cape Town.

Nelson Mandela Metropolitan University.

- Dr Borja Aguiar-González

School of Marine Science and Policy. College of Earth, Ocean and Environment, University of Delaware.

South African Environmental Observation Network, Egagasini node.

Publication published on the present work:

• Citation: Dilmahamod, A. F., Aguiar-González, B., Penven, P., Reason, C. J. C., De Ruijter, W. P. M., Malan, N., & Hermes, J. C. (2018). SIDDIES corridor: A major east-west pathway of long-lived surface and subsurface eddies crossing the subtropical South Indian Ocean. *Journal of Geophysical Research: Oceans*, 123. https://doi.org/10.1029/2018JC013828

Declaration

I hereby declare that except where specific reference is made to the work of others, the contents of this dissertation are original and have not been submitted in whole or in part for consideration for any other degree or qualification in this, or any other University. This dissertation is the result of my own work and includes nothing which is the outcome of work done in collaboration, except where specifically indicated in the text. This dissertation contains less than 75,000 words including appendices, bibliography, footnotes, tables and equations and has less than 150 figures.

Ahmad Fehmi Dilmahamod

August 2018

Acknowledgements

Coming to the end of a long and fascinating journey, will not make me forget all those who have supported, helped, encouraged, and collaborated in the accomplishment of this thesis. First of all, this work would have not been possible without the guidance and expertise of my four supervisors: Prof. Chris Reason, Dr. Pierrick Penven, Assoc. Prof. Juliet Hermes and Dr. Borja Aguiar-Gonzalez. Chris, your critical eye and exceptional scope of knowledge have largely improved this thesis. Pierrick, thank you for hosting me in Brest and for providing some constructive and honest feedbacks which have been invaluable to the shaping and writing of this manuscript. Your imagination and enthusiasm have been extremely inspiring. Additionally, a special thanks to you for my newly found interest in boat racing, that you have passed onto me during our long conversations. Juliet, your extraordinary support and expert advice throughout this thesis process have been incredible. You always had the right words of encouragement and I will be forever grateful for all the opportunities you gave me. Borja, working with you has been great. I highly admire your eye for each and every detail, and for your dedication. Your assistance and genuine feedbacks have enormously been helpful in this thesis.

I would also like to thank Prof. Will de Ruijter, for his ambition and vision which have been indispensable in broadening the scope of this research. Within the department of Oceanography at UCT, the scientific discussions with Assoc. Prof. Marcello Vichi, Dr. Neil Malan, Dr. Charine Collins and Dr. Issufo Halo, have undoubtedly enhanced the quality of this work. Their scientific support and enthusiastic way of transmitting their knowledge have been inspirational. My special thanks to Dr. Serena Illig for tolerating my enormous amount of questions and never-ending scientific discussions, which proved to be useful in widening my research.

I gratefully acknowledge the National Research Foundation Innovation Doctoral Schol-

arship (Grant UID: 90270) for funding this research. In addition, I acknowledge the funding received from the South African Environmental Observation Network (SAEON), the International Centre for Education, the Marine and Atmospheric Sciences over Africa (ICEMASA) and l'Institut de Recherche pour le Développement (IRD). In particular, I would like to thank Assoc. Prof. Juliet Hermes and Dr. Francis Marsac for all the efforts made to secure funds on my behalf. Additionally, all simulations were performed on the high-performance computers (Caparmor and UCT HPC Cluster).

More importantly, words fail to express my gratitude towards my parents who have provided me with the strength and unconditional support. Their prayers have strengthened me throughout these years. Their immense belief in me have only kept me motivated. My earnest gratitude to my brother Zehree, my sister Rushda and her little angel Aareez, who are the pillars that hold my life. I would also like to thank Daneeja, Katherine, Neil, Laura, Jerome, Vincent, Pauline, the Mauritian and French crews, who all deserve a special mention for their amazing company during these last few years. Lastly, I would like to express my appreciation to some special people for putting up throughout the various stages of this adventure, and for their unconditional support and inexhaustible patience. Thank you all for preserving my sanity.

Abstract

Phytoplankton blooms are ecological hotspots in the ocean, and are fundamental to the biogeochemical cycling of elements, the storage of carbon and the ability to regulate the atmospheric carbon dioxide; and the life in the ocean. The South-East Madagascar Bloom, one of the largest blooms in the global ocean, coexists with the poleward flowing South-East Madagascar Current (SEMC), the eastward flowing South Indian Ocean Countercurrent (SICC) as well as westward-propagating surface and subsurface-intensified eddies. This austral summer bloom extends largely towards the open ocean, from the Madagascan coasts up to ∼65°E and it exhibits an intriguing interannual variability. A variety of observational datasets as well as a high resolution coupled physical-biogeochemical model, based on CROCO-PISCES, are used to explore the biophysical processes associated with the bloom and these westward-propagating eddies.

Based on historical observational data, the bloom is shown to occur in a region of shallow mixed layer, with the surface layer exhibiting lower salinity, a possible signature of the coastal poleward flowing SEMC waters. The testing of various hypotheses revealed a dampening of the coastal current-driven upwelling south-east of Madagascar during bloom months. A dipole mesoscale feature is also prevalent close to the Madagascan coast during the bloom, from which a new hypothesis emerges. This new hypothesis states that the region south/south-east of Madagascar, influenced by local mesoscale turbulence, acts as a gate for the SEMC to flow either towards the African continent, or into the bloom region through an early retroflection, hence fertilizing the bloom.

The model produces a sporadic enhancement of chlorophyll-a in the subsurface levels, associated with a low-salinity surface signature. The mean local circulation associated with the simulated bloom also reveals a dipole structure, as in observed datasets.

Nitrate from subsurface levels (upwelling) as well as from the Madagascan coast (advection) is shown to influence the simulated bloom. A Lagrangian experiment shows dispersion of higher percentages of particles in the bloom region during bloom years and south of Madagascar during non-bloom years.

Mesoscale eddies, originating close to Australia and which propagate westward towards southern Africa, can potentially impact the South-East Madagascar Bloom. In this study, a vast majority of these features have been shown to be subsurface-intensified eddies. A co-located eddy tracking dataset with Argo profiling floats are used to devise a subsurface-eddy identification method, which is based on the steric dynamic height anomaly of a specific eddy. Adding to the 'eddy-zoo', these eddies are termed 'SIDDIES' (South Indian ocean eDDIES), occurring as surface (surfSIDDIES) and subsurface (subSIDDIES) features. They travel along the latitudinal band range of 15°S to 35°S which we name the 'SIDDIES corridor'. Advecting warm and fresh water during their propagation, cyclonic (anticyclonic) subSIDDIES contribute about 58% (32%) of the total eddy-heat flux in the South Indian Ocean. Anticyclonic subSIDDIES have also been found to be the sole, high-saline water eddy-conveyor towards the western South Indian Ocean. These eddies could also possibly transport nutrients throughout their journey, impacting the biogeochemistry of the ocean near Madagascar.

Table of contents

List of figures **xi**

List of tables **xxiv**

Nomenclature **xxiv**

1 Introduction **1**

1.1 Background Information 1

1.2 Motivation 3

2 Literature Review **5**

2.1 The Indian Ocean: General Overview 5

2.1.1 Large-scale wind variability 6

2.1.2 Mean Oceanic Circulation 7

2.1.3 Mesoscale Variability 16

2.2 The South-East Madagascar Bloom 23

2.2.1 General Description 24

2.2.2 Hypothesis 27

2.3 Summary 34

3 Materials and Methods **36**

3.1 Observed Datasets 37

3.2 Regional Ocean Modelling System - ROMS 41

3.2.1 Motivation 41

3.2.2 Model Description 42

3.3 Pelagic Interaction Scheme for Carbon and Ecosystem Studies - PISCES 50

3.3.1 Motivation 50

3.3.2 Model Description 51

3.4 South-West Indian Ocean (SWIO) CROCO-PISCES configuration . . . 56
3.4.1 Regional Simulation . . . 56
3.4.2 Surface forcing . . . 57
3.4.3 Lateral boundaries and initial conditions . . . 58
3.4.4 Initialization . . . 59
3.5 Assessing the South-West Indian Ocean (SWIO) configuration . . . 61
3.5.1 Physical Properties . . . 61
3.5.2 Biogeochemical Properties . . . 77
3.6 Conclusion . . . 84

4 A revisit of the South-East Madagascar Bloom 86
4.1 Introduction . . . 86
4.2 Bloom Description . . . 91
4.2.1 Temporal Variability . . . 91
4.2.2 Mean spatial structure and variability of the bloom . . . 96
4.2.3 Vertical Structure . . . 102
4.2.4 Summary . . . 109
4.3 Hypothesis Testing . . . 109
4.3.1 Mixed Layer Depth . . . 110
4.3.2 Plankton wave . . . 112
4.3.3 Iron Runoff . . . 114
4.3.4 Ekman Pumping . . . 116
4.3.5 Upwelling South of Madagascar . . . 118
4.4 Influence of large-scale climate modes . . . 120
4.5 Local currents: SEMC and SICC . . . 122
4.6 Discussion and Summary . . . 126

5 Local Influences of the South-East Madagascar Current on the South-East Madagascar Bloom 132
5.1 Introduction . . . 132

5.2 Results . . . 135
5.2.1 Simulated South-East Madagascar Bloom . . . 135
5.2.2 Mean circulation associated with the bloom . . . 148
5.3 Discussion . . . 160
5.4 Summary . . . 165

6 Subsurface intensified eddies in the South Indian Ocean 166
6.1 Introduction . . . 166
6.2 Data and Methods . . . 170
6.2.1 Eddy Available Potential Energy (EAPE) . . . 170
6.2.2 Eddy Tracking Algorithm . . . 172
6.2.3 Argo Float Data . . . 172
6.2.4 Subsurface Eddies Identification Method . . . 174
6.2.5 Eddy Composition . . . 176
6.3 Results . . . 177
6.3.1 Eddy Statistics and Vertical Structure . . . 177
6.3.2 SubSIDDIES vertical characteristics and propagation . . . 185
6.3.3 Heat and Freshwater Fluxes . . . 190
6.4 Discussion and Summary . . . 197

7 Summary and future research 204
7.1 Perspectives . . . 211

Bibliography 214

List of Acronyms A - 238

List of figures

2.1 Monsoon wind stress fields from the 1990-1998 National Center for Environmental Prediction (NCEP) climatology (vectors) [*Kalnay et al.*, 1996] and depths of 20°C isotherm (Z20) from Simple Ocean Data Assimilation (SODA, mean for 1992-2001, color shaded) for (a) January, (b) June, (c) August and (d) November. [After *Schott et al.* [2009] . . . 7

2.2 Schematic representation of the large-scale surface circulation of the Indian Ocean in (a) summer monsoon and (b) winter monsoon. The acronyms indicate the main currents. [After *Schott et al.* [2009]] 8

2.3 Schematic diagrams of the upper circulation of the south-east Indian Ocean near Australia associated with the source regions of the Leeuwin Current (top panel). These diagrams are proposed based on the links identified through the POP1 IB model particle trajectories shown in the study of *Domingues et al.* [2007]. [After *Domingues et al.* [2007]] 9

2.4 Schematic representation describing the modes of the EMC extension. The shading indicates isobaths with 1000 m separation where greater depths correspond to darker shading. [After *Siedler et al.* [2009]] 12

2.5 Schematic representation of the upper layer circulation of the South Indian Ocean. Currents indicated are the three branches of the South Indian Countercurrent (northern [nSICC], central [cSICC], and southern [sSICC]). The Question marks (?) indicate regions where the circulations are still a matter of debate: the retroflection of the EMC and its connection to the SICC, and the connection between the SICC and the tropical EGC. Spirals indicate the southward-propagating Mozambique Channel eddies. Yellow shadings show the Indonesian Throughflow Water (ITW) and the subtropical Water (STW) regions. Water depths are blue shadings from the Smith-Sandwell 2 min bathymetry. [After *Menezes et al.* [2014]] 15

2.6 Seasonal distributions of eddy kinetic energy ($cm^2\ s^{-2}$) in the southeast Indian Ocean in (a) spring (August–October), (b) summer (November-January), (c) autumn (February - April) and, (d) winter (May-July). [Adapted from [*Jia et al.*, 2011a]] 18

2.7 Hydrographic properties along sections T8 and T9 transects (a, b) Salinity along sections T8 and T9, respectively. (c) Potential temperature (in °C) along section T8. (d) Temperature (in °C) along section T9. [After *Nauw et al.* [2006]] 21

2.8 Monthly maps of chlorophyll (mg m^{-3}) for January–April off Madagascar, 20°S–35°S, between 1998 and 2007. [After *Wilson and Qiu* [2008]] . . . 25

2.9 (a) Time series of mean [Chl] from SeaWiFS and MODIS sensors, between 24°S–33°S and 48°E–66°E (solid line) and between 24°S–33°S and 70°E–88°E (dotted line). (b) Time series of the bloom index defined by normalizing mean Chl in the bloom area (solid line in Figure 2.9a to the area farther east (dotted line). (c) The index for the four bloom years plotted together for comparison. [After *Uz* [2007]] 26

2.10 Tracks of cyclones for the first 3 months of years 1997–2005. Symbol size is proportional to maximum sustained wind speed. The year is marked in the upper left of each panel, in bold characters if a strong bloom was observed that year. (bottom) Storms for all of the bloom years (1997, 1999, 2000, 2002, and 2004) and nonbloom years (1998, 2001, 2003, and 2005), respectively. [After *Uz* [2007]] 30

3.1 Horizontal distribution of variable points on a staggered Arakawa C-grid [From *Hedstrom* [1997]] 47

3.2 Vertical distribution of variable points on a staggered Arakawa C-grid (From www.myroms.org) 48

3.3 Vertical σ-coordinate system approach in ROMS. [From www.myroms.org] 49

3.4 Architecture of PISCES model. C represents carbon, Chl is for chlorophyll, DOM is Dissolved Organic Matter, POM indicates Particulate Organic Matter in big and small forms. From *Aumont and Bopp* [2006]. 52

3.5 The extension of SWIO child domain (red box), embedded into the parent domain. The bathymetry (m) of the parent and child domains are shown in color. The average resolution over the South-East Madagascar Bloom (child domain) is ∼9 km. 57

3.6 Integrated volume properties, over the parent domain, of physical variables for the 24 years (1990-2013) of model run. The red line shows the mean over the 24 years. 60

3.7 Surface properties of biogeochemical variables, over the parent domain, for the 24 years (1990-2013) of model run. The red line shows the mean over the 24 years. 60

3.8 Panels on the left (a, b, c) represent sea surface temperature values (°C), and those on the right sea surface salinities (psu) (d, e, f) for an annual climatology of the last 21 years of the analyzed run (1993-2013). Top panels portray SWIO outputs (a, e), mid panels GLORYS outputs (b, e), and bottom panels are from AVHRR (c) and CARS09 (f). 62

3.9 The left column represents the difference in sea surface temperature (°C) between GLORYS and AVHHRR (a, top panel), and between SWIO and AVHRR (b, bottom panel). The right column displays the difference in sea surface salinity (psu) between GLORYS and CARS09 (c, top panel), and between SWIO and CARS09 (d, bottom panel). 63

3.10 Part of the model's domain indicating the locations of the two main transects: a zonal transect A and a meridional transect B. 64

3.11 Vertical distribution of temperature (°C) (a, b, c; first row) and salinity (psu) (d, e, f; second row) through the top 1000 m of transect A at 25°S. The first, second and third columns represent the tracers from SWIO, GLORYS and CARS09 respectively. 65

3.12 Vertical distribution of density (Kg m^{-3}) along transect A (25°S)from (a) SWIO, (b) GLORYS, and (c) CARS09, respectively. 66

3.13 Temperature-Salinity showing water mass properties along the horizontal transect A, spanning from 47.8°E to 80°E for (a) CARS09, (b) WOA13, and (c) SWIO. 66

3.14 Vertical distribution of temperature (°C) (a, b, c; first row) and salinity (psu) (d, e, f; second row) through the top 1000 m of transect B at 52°E. The first, second and third columns represent the tracers from SWIO, GLORYS and CARS09 respectively. 68

3.15 Vertical distribution of density (Kg m^{-3}) along transect B (52°E) from (a) SWIO, (b) GLORYS, and (c) CARS09, respectively. 69

3.16 Temperature-Salinity showing water mass properties along the vertical transect B, spanning from 6°S-40°S for (a) CARS09, (b) WOA13, and (c) SWIO. 69

3.17 Monthly climatology of mixed layer depth in (a) box A, representative of the bloom region, and (b) box B, representative of the Mozambique Channel region. (c) shows the location of boxes A and B. 70

3.18 Mean surface geostrophic eddy kinetic energy (EKE; $cm^2\ s^{-2}$) for the 1993-2013 period, derived from (a) AVISO, (b) SWIO without nesting effects and, (c) SWIO with nesting effects. Black contours show the analogous mean sea-surface height fields, with contours indicating 5 cm delineations of SSH. 71

3.19 Part of the model's domain indicating the locations of transects through which the volume transport of the main flows of the South-West Indian Ocean is calculated. 73

3.20 Time series of volume transport calculated across the main South-West Indian Ocean's currents indicated in Figure 3.18 from 1993 to 2013. The mean transport and its standard deviation is given for each flow structure, as well as the depth of the water volume through which the transport is calculated. 75

3.21 Interannual variability of SST (°C) from AVHRR (black line) and SWIO (red line) in the South-East Madagascar Bloom region (50°E-55°E; 24°S-28°S) 76

3.22 Subtropical Indian Ocean Dipole (SIOD) indices, extracted from remotely-sensed AVHRR (Black line), HadISST (Blue) and the model SWIO (Red). The correlation was performed at a 99% significance level. 77

3.23 Mean austral summer Chl-a concentration (mg m^{-3}) from ESA OC-CCI averaged over 1998 to 2013. The transect (white line) indicates the location (47°E-70°E; 25°S;) along which the vertical structure of biogeochemical variables are investigated. 78

3.24 (a) and (d) displays mean seasonal Chl-a concentration (mg m^{-3}) in austral summer and winter from ocean colour dataset (ESA OC-CCI), respectively. (b) and (e) shows mean modelled Chl-a concentration in the surface (0-20 m) layers in austral summer and winter, respectively. The difference between modelled Chl-a and satellite data for (c) austral summer and (f) austral winter, are shown in the last row. 79

3.25 Vertical structure of mean Chl-a concentration (mg m^{-3}) along Transect A, from December to April. 80

3.26 Mean (December-April) surface nitrate concentration (μmol L^{-1}) from (a) CARS09, (b) SWIO and (c) the difference between SWIO and CARS09. 81

3.27 Mean (December-April) nitracline depth (m) from (a) CARS09, (b) SWIO and (c) the difference between SWIO and CARS09. 81

3.28 Vertical structure of mean December-April nitrate concentration (μmol L^{-1}) along transect A, from (a) CARS09 and (b) SWIO. 82

3.29 Mean (December-April) surface oxygen concentration (μmol L^{-1}) from (a) CARS09, (b) SWIO and (c) the difference between SWIO and CARS09. 83

3.30 Vertical structure of mean (December-April) oxygen concentration (μmol L^{-1}) along transect A, from (a) CARS09 and (b) SWIO. 83

4.1 Monthly climatology from 1998-2016 of ESA OC-CCI Chl-a concentration (mg m^{-3}) in a box south-east of Madagascar, defined as the bloom box by *Uz* [2007]. 92

4.2 (a) Mean ESA OC-CCI Chl-a concentration in January 1999, overlaid with boxes W and E. (b) displays an extended time series (1998-2016) of the bloom index as defined in *Uz* [2007]. The shading designates the bloom years identified by *Uz* [2007] in their shorter time series (1997-2005). *Uz* [2007] used a composite of SeaWiFS and MODIS Aqua images. 93

4.3 Histogram of maximum difference between 'bloom box' and box E. The vertical dotted black line at 0.07 mg m^{-3} indicates the threshold used to separate bloom from non-bloom years. The line at 0.16 mg m^{-3} separates the normal bloom from major bloom years. 94

4.4 (a) Time series of mean ESA OC-CCI Chl-a concentration in the bloom box. (b) Bloom index computed by subtracting Chl-a of box E from Box W. In (b), the red dotted line indicates the threshold of 0.07 mg m^{-3} (identified in Figure 4.3), which distinguish the bloom years and non-bloom years. Peaks above the blue line (0.16 mg m^{-3}) indicate major blooms. In both (a) and (b) and corresponding later figures, the grey shading indicates the bloom years identified from the red dotted line (0.07 mg m^{-3} of chlorophyll-a difference between boxes W and E). 95

4.5 (a) Spatial maps of mean ESA OC-CCI Chl-a concentration (mg m^{-3}) during months of maximum austral summer bloom identified in Figure 4.4b. (b) Same as (a) but during months of minimum Chl-a concentration during austral summer. 97

4.6 Spatial maps of the months of maximum ESA OC-CCI Chl-a concentration (mg m^{-3}) observed in 'bloom box', from 1998 to 2016. The asterisk* denotes years identified as bloom years from Figure 4.4b. . . 99

4.7 Spatial maps of the difference between months of maximum ESA OC-CCI Chl-a concentration (mg m^{-3}) observed in 'bloom box' and the mean composite bloom, from 1998 to 2016. The asterisk* denotes years identified as bloom years from Figure 4.4b. 100

4.8 Time-latitude hovmöller of (a) AVISO eddy kinetic energy (cm^2 s^{-2}) along the meridional transect (24°S-28°S; 50°E) which captures the position of SICC, and (b) ESA OC-CCI Chl-a concentration (mg m^{-3}) along the same transect which caputures both the austral summer and winter blooms. 101

4.9 (a) Composite of Chl-a concentration during identified bloom years, overlaid with box West (26°-29°S and 40°-43°E) and East ((26°-29°S and 48°-51°E). (b) and (c) display the Chl-a anomalies in box west and box east respectively, with respect to the 1998-2016 mean Chl-a concentration. 102

4.10 (a) The positions of bloom profiles (red) and non-bloom profiles (black) in the bloom box, separated by the 35.4 psu isohaline (green line). (b) and (c) displays the number of bloom profiles (red) and non-bloom profiles (black) surveyed in each austral summer months (January - April) from 2002 to 2015. 103

4.11 The mean vertical thermohaline structure of the water column associated with bloom (red line) and non-bloom (black line) years on the fresher side (upper panels) and saltier side (lower panels) of the salinity front. The red (black) dotted lines show the mixed layer depth of bloom (non-bloom) era, from a temperature threshold (a,d) and density threshold (c,f). 105

4.12 Annual Climatology of sea surface salinity derived from (a) CARS09 and from the (b) SWIO model averaged over the 1993-2013 period. . . 106

4.13 A snapshot of ESA OC-CCI Chl-a data on 25th January 2008, with the positions of 4 floats. Floats 1 and 2 are located in an enhanced Chl-a region (bloom) whereas Floats 3 and 4 are located in a non-bloom region. The bottom pannels give the vertical structure at these 4 floats's location. The assigned blue lines display the mixed layer depth from each profile based on (b) temperature and (d) density threshold. 107

4.14 Same as (Figure 4.13) but using a snapshot of ESA OC-CCI Chl-a data on 5th March 2012. 108

4.15 Time series of mixed layer depth anomalies (m) from *de Boyer Montégut* [2004] (black line) and *Li et al.* [2017b] (red line) in the bloom box. The blue dotted line indicates an optimized threshold with the blue dots indicating months when the threshold works. 111

4.16 (a) Daily and (b) detrended monthly time series of eddy diffusivity(A_H; $m^2\ s^{-1}$) in the bloom box. 113

4.17 Time series of CMAP (a) pentad precipitation anomalies (mm day^{-1}) and (b) monthly precipitation anomalies averaged over 47.5°E-52.5°E and 12.5°S-25°S, as in *Uz* [2007]. 115

4.18 Time series of (a) 2-weeks running mean of daily W_{ek} (m s^{-1}) and (b) monthly anomaly of W_{ek}, computed from QSCAT data (black line) and ERA-Interim data (red line) in the bloom region 117

4.19 (a) Upwelling index computed from sea surface temperature as in *Ramanantsoa et al.* [2018a]. (b) Chl-a anomalies (mg m^{-3}) around the southern tip of Madagascar, on the continental shelves. 119

4.20 Time series of (a) Nino 3.4 Index (b) Dipole Mode Index and (c) SIOD Index, against years of bloom occurrence (gray) shading. 121

4.21 Mean AVISO geostrophic velocities (m s^{-1}) during the bloom period. The red lines indicate the location of the different transects; the EMC (as per *Ponsoni et al.* [2015, 2016]), South EMC and SICC. 123

4.22 Hovmöller of (a) alongshore geostrophic velocities (m s^{-1}) of the EMC at around 22°S; (b) zonal component of the South EMC with the mean velocity (black line) overlaid; and (c) zonal component of the SICC with its mean velocity (black line) overlaid. The mean velocities are calculated over the specific latitude ranges for each transect. The arrows indicate the bloom years. 124

4.23 Mean sea level anomaly (SLA; m) overlaid with surface geostrophic velocities from AVISO, (a) one month before and during peak month of major bloom years identified by our threshold; and (b) January-February of non-bloom years. 130

5.1 Averaged surface geostrophic velocities on a 1993-2013 time frame in (a) AVISO and (b) SWIO model. SICC illustrates the latitudinal band of the South Indian Ocean Countercurrent. 136

5.2 Time series of simulated Chl-a concentration (mg m^{-3}) in the bloom box proposed by *Uz* [2007], from 1993 to 2013. 137

5.3 Mean (upper row, a and b) surface (0-20 m) and (lower row, c and d) subsurface (20-40 m) Chl-a concentration (mg m^{-3}) from 23/02/2004 to 13/03/2004 (first column) and 13/12/2009 to 28/12/2009 (second column). The two delineated overlaid boxes define the regions where the modelled bloom occurs (bloow W). A box further east (box E) captures the winter bloom. 137

5.4 Monthly climatology of Chl-a concentration (mg m^{-3}) averaged along the 0-20 m (black line) and 20-40 m (red line) depth ranges, in (a) box W and (b) box E. 139

5.5 Histogram of occurrences (months) of monthly maximum Chl-a differences (mg m^{-3}) between box W and box E, in the surface (black line) and subsurface (red line) levels. The vertical dotted blue line at 0.07 mg m^{-3} indicates the threshold used to separate bloom from non-bloom years. 139

5.6 (a) Mean Chl-a concentration (mg m^{-3}) in box W, and (b) time series of the difference of Chl-a concentration between box W and box E. The gray shadings indicate austral summer months (December-April). The blue dotted line indicates a threshold value of 0.07 mg m^{-3} from which bloom years can be separated from non-bloom years. 141

5.7 Spatial maps of mean Chl-a concentration (mg m^{-3}) during months of maximum bloom occurrence (left column), identified in Figure 5.6, and months of non-bloom occurrence (right column). The first row shows Chl-a from remotely-sensed ESA OC-CCI data and the second row shows Chl-a data, in the subsurface levels, from SWIO. 143

5.8 Spatial maps of the months of maximum simulated Chl-a concentration (mg m^{-3}) observed in box W during bloom years. The white box shows the location of the 'model bloom box'. 145

5.9 Mean (December-April) modelled salinity (psu), averaged over the first 40 m, from 1993 to 2013. The red lines denote the isohalines crossing the bloom box namely the 35.4, 35.5, 35.6 and 35.7 psu isohalines. The black box shows the position of the 'model bloom box'. 146

5.10 The model mean water column structure associated with bloom (red line) and non-bloom (black line) years on the fresher side (upper panels) and saltier side (lower panels) of the 35.6 psu salinity front. The red (black) dotted line shows the mixed layer depth during bloom (non-bloom) months (a and d). 147

5.11 Comparisons between the remotely sensed sea level anomalies (m) from AVISO (first row) and the simulated sea surface height anomalies by SWIO (second row), during (a and c) bloom and (b and d) non-bloom periods. The surface geostrophic velocities were overlaid. S1, S2 and S3 denote structures of the mean circulation. 149

5.12 Time series of averaged simulated Chl-a and NO_3 concentration observed in the bloom box, in the upper 40 meters (a and d) for the 1994 (first column) and the 1995 (second column) events; simulated NO_3 fluxes per unit area, over the first 40 m (b and e), with the red and blue lines indicating flux from the subsurface (Vadv) and from the Madagascan coast (Eadv). The Total flux (horizontal + vertical) is shown by the black line. Hovmöller of the mean vertical structure of salinity in the 'model bloom box' for the (c) 1994 and (f) 1995 events are displayed. . 152

5.13 Same as Figure 5.12 but for the 1996 (first column) and 2004 (second column) events. 153

5.14 Time series of wind stress curl computed from (a) QSCAT and (b) SWIO; and associated Chl-a concentration from (c) ESA OC-CCI and (d) SWIO, from January 2004 till May 2004. 154

5.15 Same as Figure 5.12 but for the 2005 (first column) and 2006 (second column) events. 155

5.16 Same as Figure 5.12 but for the 2008 (first column) and 2009 (second column) events. 155

5.17 The release area of langrangian particles in the SEMC, as represented in SWIO. The two delineated boxes indicate the region through which the langragian particles are tracked 157

5.18 Time series of the percentage of lagrangian particles arriving in the (a) 'model bloom box' and (b) south of Madagascar region. 158

5.19 Location of particles during (a) bloom event of December 2004, and (b) non-bloom event of 2001. 159

6.1 **(a)** Mean surface geostrophic eddy kinetic energy (EKE; $cm^2\ s^{-2}$) calculated from 12 years (2002-2013) AVISO data. **(b)** Mean EAPE ($J\ m^{-3}$) at 150 m depth with two black boxes delineating regions of interest. **(c)** shows a mean latitudinal (24°S-28°S) vertical section of EAPE across the South Indian Ocean (40°E to 120°E). 171

6.2 Steric Dynamic Height anomaly, h', (m) for surface (small dots) and subsurface (large dots) intensified cyclonic (blue) and anticyclonic (red) eddies 175

6.3 Vertical sections of potential temperature (°C; 1^{st} and 2^{nd} columns; a,b,e,f) and salinity anomalies (psu; 3^{rd} and 4^{th} columns; c,d,g,h) across composite cyclonic (top) and anticyclonic (bottom) surface and subsurface eddies, at ΔY=0, in the eastern South Indian Ocean, over the box shown in Figure 6.1a. 179

6.4 Vertical sections of the rotational speed anomaly ($cm\ s^{-1}$) of the composite surface CEs (a) and AEs (c) and subsurface CEs (b) and AEs (d) in the eastern Indian Ocean. 181

6.5 Vertical sections of potential temperature (°C; 1^{st} and 2^{nd} columns) and salinity anomalies (psu; 3^{rd} and 4^{th} columns) across composite cyclonic (top) and anticyclonic (bottom) surface and subsurface eddies in the western Indian Ocean. 183

6.6 Vertical sections of the rotational speed anomaly (cm s^{-1}) of the composite surface CEs (a) and AEs (c) and subsurface CEs (b) and AEs (d) in the western Indian Ocean. 184

6.7 Mean θ/S diagrams of (a) anticyclonic subSIDDIES and (b) cyclonic subSIDDIES, in the western and eastern regions of interest. Subtropical Underwater is indicated as 'STUW, South Indian Central Water as 'SICW' and for Antarctic Intermediate Water as 'AAIW'. 186

6.8 Histogram distribution of maximum positive salinity depths and their corresponding potential density of subSIDDES in the eastern Indian Ocean (a, b) and western Indian Ocean (c, d). 187

6.9 Depth of isopycnal layers corresponding to favoured water mass properties of (a) cyclonic and (b) anticyclonic subSIDDIES. 188

6.10 Tracks of subSIDDIES studied in the (c,d) eastern and (d,f) western South Indian Ocean, with blue (red) indication CE (AE). The black dots show their formation location. 189

6.11 Mean vertical profiles of the nonlinearity parameter of the four eddy-types (surface and subsurface CEs and AEs) for the western (a) and eastern (b) South Indian Ocean. 191

6.12 Mean available heat anomaly (J m^{-1}; left column) and available salt anomaly (Kg m^{-1}; right column) associated with the four eddy-types in the eastern South Indian Ocean. 192

6.13 Same as Fig. 6.12 but for the western South Indian Ocean. 194

6.14 Resultant vectors associated to the mass (a), heat (b) and freshwater flux(c) of each eddy-types (see legend), in the eastern and western South Indian Ocean region. The background displays (a) streamlines of sea surface height representing geostrophic mean circulation, (b) salinity and (c) temperature, both salinity and temperature averaged between 50 and 150m depth. 196

List of tables

4.1 Events of bloom and non-bloom years, with bloom years being defined as normal and major blooms. The month at which the bloom is maximum is stated in the fourth column. Bloom years are listed in bold. The '?' indicates the ambiguous classification of 2011. 96

4.2 A summary of the different hypotheses linked to the South-East Madagascar Bloom, with the bloom intensity denoted by + (Normal Bloom) and ++ (Major Bloom). Hypotheses which hold true, according to the optimized threshold in the hypothesis-testing model, during bloom and non-bloom occurrence are denoted as ✓. The lag at which the hypothesis holds and their specific success rate are also stated. Bloom years in the first column are listed in bold and absence of data for some years are denoted as 'N/A' 125

5.1 Events of bloom and non-bloom years, with bloom years listed in 'bold'. The month at which the bloom is maximum is stated in the third column. 142

5.2 Summary of which bloom event is dominated by incoming eastward fluxes or vertical fluxes of NO_3. 156

6.1 Statistical characteristics of surface and subsurface eddies in the Eastern South Indian Ocean. ± refers to the standard deviation from the mean. 178

6.2 Statistical characteristics of surface and subsurface eddies in the Western South Indian Ocean. ± refers to the standard deviation from the mean. 183

6.3 Vertical extent, volume, thermohaline contents and associated heat/freshwater flux of 4 distinct eddy-types in the western and eastern Indian Ocean regions. 195

Chapter 1

Introduction

1.1 Background Information

The South Indian Ocean (SIO) is exceptionally diverse, exhibiting large variability in terms of physical and biogeochemical processes. Spanning from Australia/south-east Asia, where warm and fresh Pacific waters enter the basin through the Indonesian Throughflow (ITF), to the African continent where the Agulhas Current (AC) sheds rings into the southern Atlantic Ocean, SIO is one of the most interesting regions of study. Unlike the southern Atlantic and Pacific Oceans, the South Indian Ocean remains an under-sampled area in time and space.

Due to the northern part of the Indian Ocean being bounded by the Asian continent, a strong meridional land-sea contrast exists [*Schott*, 1983], inducing one of the strongest monsoon system on Earth. The dominant wind-variability of the monsoon system influences the wind-driven circulation including the South Equatorial Current (SEC), the North-East and South-East Madagascar Currents (NEMC and SEMC). South of the Equator, the stable Southeast Trade Winds and the Southern Hemisphere Westerlies preside over 10°S-32°S and 32°S-60°S, respectively. The seasonal variability associated to the Southeast Trade Winds, maximum in austral winter [*Schott et al.*, 2009], modulates the meridional extent of the subtropical gyre [*Ffield et al.*, 1997]. The SEC, fed by water through the ITF, flows westward between 7°S and 15°S and bifurcates at the east coast of Madagascar into the NEMC and SEMC [*Chapman et al.*, 2003; *DiMarco et al.*, 2002; *Schott et al.*, 1988]. The SEMC proceeds poleward until it rounds the southern tip of Madagascar. This region of the south-west Indian Ocean is

complex, both in terms of physical and biogeochemical processes. After rounding the southernmost tip of Madagascar, the SEMC exhibits three different routes, each of which may only exist periodically. It can either flow west/south-westward [*Gründlingh*, 1987, 1993; *Grundlingh 1985*, 1985], sheds dipoles which propagate south-westward towards the AC [*De Ruijter et al.*, 2004; *Ridderinkhof et al.*, 2013], or undergoes a non-persistent retroflection to feed in the Madagascar Basin [*Halo et al.*, 2014a; *Siedler et al.*, 2009]. In the same region, a shallow current is present, namely the South Indian Ocean Countercurrent (SICC) [*Menezes et al.*, 2014; *Palastanga et al.*, 2007; *Siedler et al.*, 2006]). It has an eastward component, against the established theories of wind-driven circulation. Concurrently, mesoscale eddies, with a genesis area west of Australia, propagate westward towards Madagascar, against the mean flow, at a preferential latitudinal band (20°S-32°S) [*Jia et al.*, 2011a; *Zheng et al.*, 2015]. These eddies can either occur as surface-intensified or sub-surface intensified features [*Nauw et al.*, 2006], and can act as a vector of transport for warm and fresh water as well as trace elements.

A unique feature present south-east of Madagascar is the occurrence of one of the largest dendroid bloom in the global oceans, namely the South-East Madagascar Bloom [*Longhurst*, 2001]. Locked to austral summer season (January-February), this bloom has one of the strongest interannual modulations in ocean biology. It varies remarkably in terms of its initiation and termination month, as well as its spatial extent [*Wilson and Qiu*, 2008]. It can exhibit a surface area greater than 1.7 million km^2 [*Uz*, 2007], with potential ramifications on the biogeochemistry of the region. Several studies have focussed on the biophysical processes responsible for driving this feature. Different hypothesis involving the mixed layer dynamics [*Longhurst*, 2001], a possible plankton wave [*Srokosz et al.*, 2004], iron runoff due to tropical cyclones[*Uz*, 2007], coastal upwelling brining nutrients [*Lévy et al.*, 2007; *Raj et al.*, 2010] or dissolved iron [*Srokosz and Quartly*, 2013; *Srokosz et al.*, 2015] to the surface waters, have been proposed but none have been, as yet, clearly substantiated. A cruise in 2005, described as

a non-bloom year by *Uz* [2007], reveals the presence of nitrogen-fixers [*Srokosz and Quartly*, 2013] namely, *Trichodesmium*, south of Madagascar and *Rhizosolenia clevei* (with symbiont *Richelia intracellularis*) further to the east [*Poulton et al.*, 2009].

1.2 Motivation

Phytoplankton, keystone microscopic algae, are fundamental players in the ocean owing to its role in primary production. Known as ecological hotspots when they occur in high concentration [*Chassot et al.*, 2010; *Hjort*, 1926; *Ryther*, 1969], the timing, location and intensity of a phytoplankton bloom can dictate life cycles and migration patters of zooplankton grazers and fish larvae [*Boyce et al.*, 2010; *Longhurst*, 2010]. Thus, any variability in bloom phenology can have extreme ramifications for upper trophic levels. levels [*Edwards and Richardson*, 2004; *Kahru and Mitchell*, 2010; *Mackas et al.*, 2007; *Platt et al.*, 2003]. In addition, phytoplankton blooms play a major role in biogeochemical cycling of elements owing to the substantial transport of organic matter from surface waters to the oceans interior [*Naik et al.*, 2015; *Takahashi et al.*, 2009]. Hence, they contribute to the net annual uptake of carbon dioxide (CO_2) by the ocean from the atmosphere [*de Baar et al.*, 1995; *Sapiano et al.*, 2012; *Watson et al.*, 1991]. Hence, a better understanding of the biophysical processes driving its production should provide insight of the health of marine ecosystems, as well as the temporal variability of oceanic carbon cycles [*Thomalla et al.*, 2011].

The South-East Madagascar Bloom occurs in the vicinity of Madagascar and the Mascarene Islands. Covering a surface area of more than 1.7 million km^2 when it is fully developed [*Uz*, 2007], it can have an important impact on the carbon cycle. Also, its spatial extent can influence the Exclusive Economic Zone (EEZ) of the surrounding islands. This is of particular importance for these nations and their marine resources, as the bloom will influence the foraging behaviour of heterotrophs in the region and the variability of the important pelagic fisheries. Thus, it is essential to understand

the biophysical drivers at play in this complex region. Such information is necessary to improve the fishing industry in the EEZ of these islands.

In trying to understand the bloom, it is necessary to also grasp a further insight of the physical processes in play in terms of the SEMC termination regime but also of the larger dynamics in the region. Mesoscale eddies, occurring as surface-intensified [*Jia et al.*, 2011b; *Zheng et al.*, 2015] and subsurface-intensified eddies [*Nauw et al.*, 2006] in the SIO can be vectors of warm and freshwater fluxes from Australia to Madagascar, influencing the SEMC. Being one of the source regions of the AC [*Biastoch and Krauss*, 1999; *Biastoch et al.*, 1999; *De Ruijter et al.*, 2004; *Quartly et al.*, 2006; *Stramma and Lutjeharms*, 1997], it is critical to understand these features and their role on the heat and salt fluxes in the SIO. Another possible implication of the subsurface-intensified eddies is the transport of nutrients, biomass or trace elements from a remote region, consequently influencing the biogeochemistry south-east of Madagascar.

A review of the general knowledge of the Indian Ocean is given in **Chapter** 2 as well as the specific research questions. **Chapter** 3 provides a detailed description of all the observational datasets used in this thesis, a coupled biophysical (ROMS-PISCES) model as well as its evaluation against observational data. **Chapter** 4 uses a 19-year ocean colour dataset to revisit the variability of the bloom and the different hypothesis put forward by previous studies. **Chapter** 5 focuses on the coupled model to study the processes which might influence the phytoplankton bloom and test a new hypothesis. **Chapter** 6 discusses the impacts of surface and subsurface eddies on the transport of warm and freshwater across the SIO, and its possible implications on the bloom. **Chapter** 7 summarises the conclusions of this work and presents avenues for future studies.

Chapter 2

Literature Review

Although the focus of a large part of this thesis is on the South-East Madagascar Bloom, it is essential to understand the physics governing the ocean in this region. Hence, this literature review will first focus on the large scale, moving in on regional circulation, and then the second part give a detailed description of the bloom.

2.1 The Indian Ocean: General Overview

The third largest ocean of the world, the Indian Ocean, has a unique geographical setting. In contrast to the Atlantic and Pacific Oceans, its northern boundary is land-locked by the Asian continent. As a result, a lack of a western boundary current in the northern Indian Ocean prevents heat from being exported to high northern latitudes. Owing to this feature, its tropical regions are a dominant part of the extensive warm pool in the global ocean. Adjacent to the Asian continent, we find several marginal seas, which consist of the Red Sea, Persian Gulf, Arabian Sea and Bay of Bengal. In the South, the basin is open to the Southern Ocean, separated by the subpolar frontal systems. On the eastern side, Australia and the south-eastern part of Asia create a semi-continuous barrier, allowing warm Pacific Water into the tropical IO through the Indonesian Throughflow (ITF). In the West, the African continent separates the Indian Ocean from the Atlantic, from the north-western Asian continent down to the Cape Agulhas at $\sim 35°$S [*Tomczak and Godfrey*, 1994]. At this point, a complex interaction exists between Indian Ocean and Atlantic Ocean waters. Owing to this northerly-closed ocean, one of the strongest monsoon system on Earth exists resulting from a strong

meridional land-sea contrast [*Schott*, 1983]. This leads to a seasonal reversal of the winds, generating large seasonal variations in the oceanic circulation.

2.1.1 Large-scale wind variability

Surface winds are fundamental for energy exchange occurring at the air sea interface, and for the large-scale circulation of the ocean [*Rao and Ram*, 2005]. They influence sea surface roughness and, in turn, are influenced by the resulting sea state. North of 15°S, the strong monsoon system generates large seasonal variability in the mean oceanic circulation. In austral summer, north-easterlies prevail in the North Indian Ocean (Figure 2.1a), which converge with the south-east trade winds of the South Indian Ocean (SIO) [*Hastenrath and Greischar*, 1991], forming the Intertropical Convergence Zone (ITCZ). In austral winter (June - September), owing to the heating up of the northern and central Indian subcontinent, a south-north pressure gradient is induced [*Tomczak and Godfrey*, 1994]. This pressure gradient causes south-westerly winds from the tropical Indian Ocean and Arabian sea, towards the Indian subcontinent (Figure 2.1a). This period, also known as the southwest monsoon, dominates the annual wind cycle over the Indian Ocean [*Yamagata et al.*, 2004]. The time-frame from April to May and October to November are the transition periods of the northeast and southwest monsoon, respectively. During this period, strong westerlies prevail over the equatorial Indian Ocean [*Yamagata et al.*, 2004]. These generate strong equatorial eastward currents known as Wyrtki jet [*Wyrtki*, 1971], which transports ward water towards the eastern Indian Ocean.

Further south, the more stable large-scale wind pattern over the SIO is dominated by the south-east trade winds between 10°S and 32°S (Figure 2.1), and by the Southern Hemisphere Westerlies (SHW) between 32°S and 60°S, with both features persisting throughout the year. The south-east trade winds reach their maximum intensity and northernmost position in austral winter [*Schott et al.*, 2009], a response to the monsoon. As a result, the subtropical gyre present between 17°S and 47°S, intensifies and moves

southward [*Ffield et al.*, 1997]. The opposite occurs during austral summer, with the subtropical gyre losing its intensity and shifting north to 38°S.

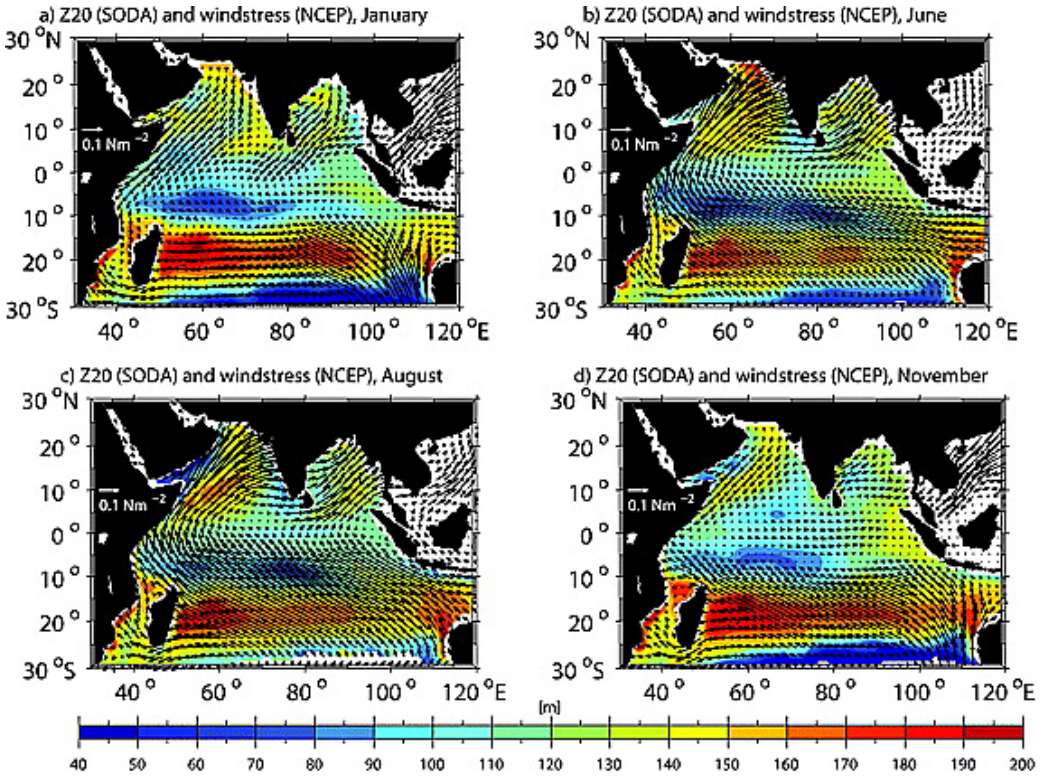


Figure. 2.1 Monsoon wind stress fields from the 1990-1998 National Center for Environmental Prediction (NCEP) climatology (vectors) [*Kalnay et al.*, 1996] and depths of 20°C isotherm (Z20) from Simple Ocean Data Assimilation (SODA, mean for 1992-2001, color shaded) for (a) January, (b) June, (c) August and (d) November. [After *Schott et al.* [2009]

2.1.2 Mean Oceanic Circulation

The wind-driven circulation of the SIO consists of two gyres: namely the subtropical anticyclonic gyre and the tropical cyclonic gyre. The latter extends from the equator to 10°S whereas the subtropical gyre extends from 17°S to 47°S, intensifying towards the southwest [*Davis*, 2005; *Reid*, 2003; *Stramma and Lutjeharms*, 1997]. The two counter-rotating gyres are separated by the westward flux of the South Equatorial Current (SEC) which is mostly fed by the ITF. Distinct differences, however, exist between the depth integrated flow and surface flow in the Indian Ocean. A summary of the mean surface oceanic circulation in the Indian Ocean is presented in Figure 2.2.

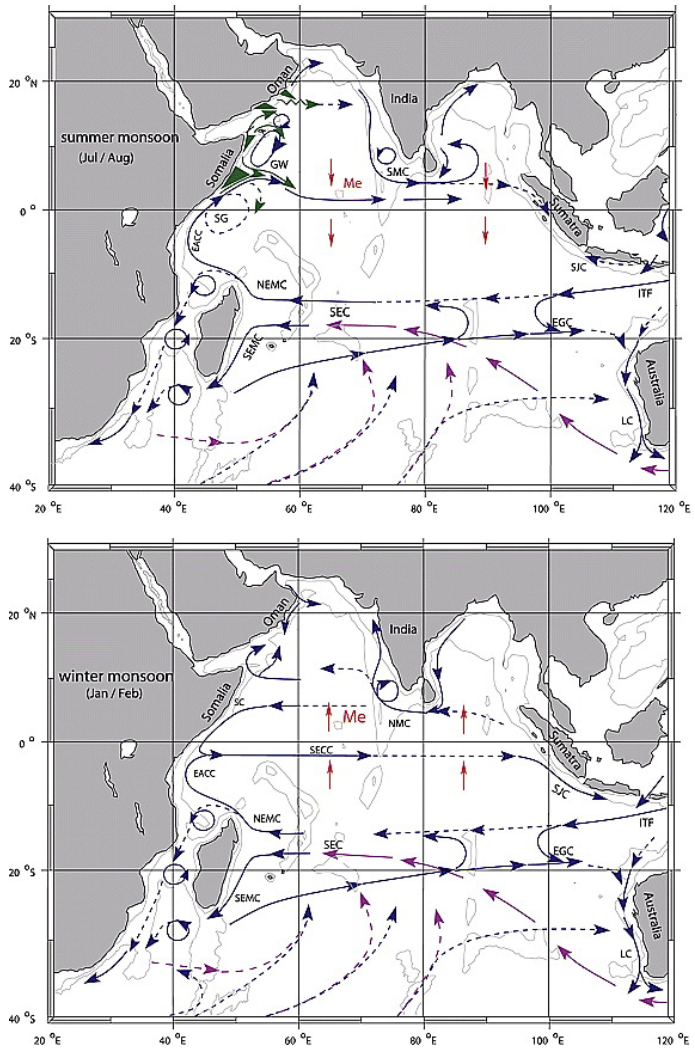


Figure. 2.2 Schematic representation of the large-scale surface circulation of the Indian Ocean in (a) summer monsoon and (b) winter monsoon. The acronyms indicate the main currents. [After *Schott et al.* [2009]]

• Indonesian Throughflow and Leeuwin Current

Water from the tropical Pacific Ocean flows into the tropical Indian Ocean through the Indonesian Seas, known as the ITF. In the global thermohaline circulation system, the ITF is the only low-latitude oceanic transfer of climate signals [*Gordon*, 1986; *Gordon and Fine*, 1996; *Talley and Sprintall*, 2005]. A hydrography study suggested an ITF flux of 10 ± 10 Sv [*Macdonald*, 1998], a transport consistent with the modelling study of *Gordon and McClean* [1999]. Local monsoon wind forcings, oceanic Rossby

waves from the Pacific Ocean and remotely forced Kelvin waves from the Indian Ocean control the ITF variability on an intraseasonal and interannual time scales [*Clarke and Liu*, 1994; *Meyers*, 1996; *Sprintall et al.*, 2000; *Wijffels and Meyers*, 2004].

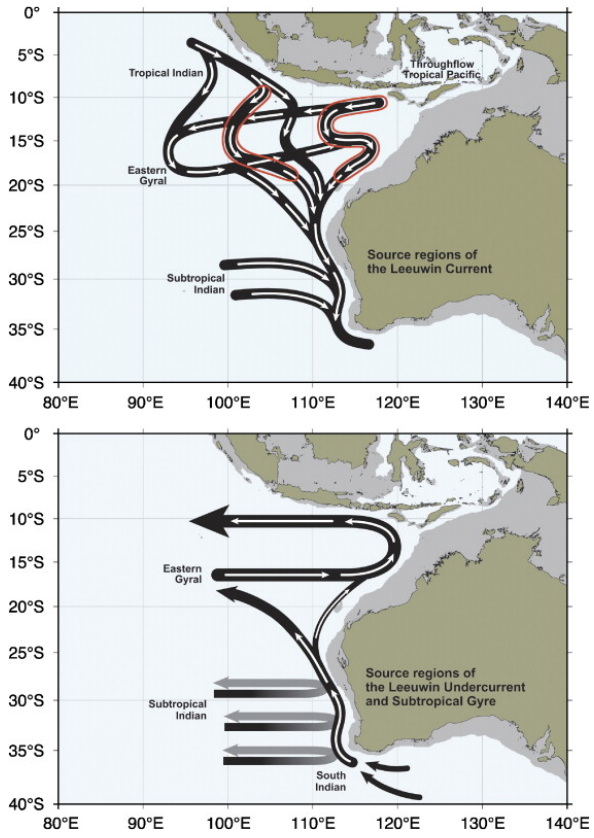


Figure. 2.3 Schematic diagrams of the upper circulation of the south-east Indian Ocean near Australia associated with the source regions of the Leeuwin Current (top panel). These diagrams are proposed based on the links identified through the POP1 IB model particle trajectories shown in the study of *Domingues et al.* [2007]. [After *Domingues et al.* [2007]]

Water masses from both the South Java Current and from the equatorial Pacific Ocean contribute extensively to the only poleward-flowing eastern boundary current in the world, the Leeuwin Current (LC) [*Domingues et al.*, 2007; *Schott et al.*, 2009]. These water masses flow westward and partly retroflect into the Eastern Gyral Current (EGC), ultimately feeding into the LC (Figure 2.3). Warmer, fresher and hence less dense, the tropical Pacific Ocean waters which enter the Indian Ocean through the ITF, induce

an anomalously large meridional pressure gradient [*Batteen and Rutherford*, 1990; *Godfrey and Ridgway*, 1985; *McCreary Jr. et al.*, 1986; *Thompson*, 1987, 1984; *Weaver and Middleton*, 1989]. An eastward, onshore geostrophic transport is induced by this pressure gradient, hence counteracting the offshore Ekman transport, contributing to the LC. Previous studies have shown that the current is weaker in summer and stronger in winter [*Smith et al.*, 1991].Two mechanisms have been put forward to explain the annual cycle in the LC. The first one is the variability in the southerly wind stress, which is stronger in austral summer [*Kundu and McCreary*, 1986; *McCreary Jr. et al.*, 1986; *Smith et al.*, 1991], and the second one being the annual variation of the meridional pressure gradient at the shelf break [*Godfrey and Ridgway*, 1985; *Morrow and Birol*, 1998].

- **South Equatorial Current**

The SEC, driven by the anticyclonic wind stress curl in the SIO [*Schott and McCreary*, 2001], is fed by the subtropical gyre and water from the Pacific Ocean, funneled through the ITF [*Gordon and McClean*, 1999; *Quadfasel et al.*, 1996; *Schott et al.*, 2009]. The flow has a mainly westward component, with its meridional extent varying between 7°S and 15°S [*Quadfasel et al.*, 1996] east of 105°E, to a band between 10°S and 20°S in the western Indian Ocean. It has been ascribed a transport of 39 Sv (1 Sv = 10^6 m^3 s^{-1}) through geostrophic estimates [*Schott and McCreary*, 2001] and through hydrographic measurements between 10°S and 16°S, an estimated transport of about 50 Sv – 55Sv [*New et al.*, 2007]. The SEC is topographically guided towards the west through a gap in the Mascarene Plateau / Wilshaw Ridge, north of Mauritius, and on reaching the Madagascar coast at around 17°S, it bifurcates to form the northern and southern extensions of the East Madagascar Current [*Chapman et al.*, 2003; *DiMarco et al.*, 2002; *Schott et al.*, 1988].

• **North-East and South-East Madagascar Current**

The northern extension, known as the North East Madagascar Current (NEMC) transports 30 Sv to the north and, after rounding the northern tip of Madagascar at Cape Amber, it flows westward towards the African continent. The current, which is about 1100 m deep, propagates at a speed of about 0.5 m s^{-1} [*Schott et al.*, 1988] and it splits into two branches on reaching the continent at 11°S. The northward branch forms the East African Coastal Current (EACC), along the Tanzanian coastal zone [*Schott et al.*, 1988], while the southward branch flows into the Mozambique Channel (MZC). From satellite and in-situ observations, it has been shown that the latter, instead of continuing as a western boundary current, breaks up into large, deep-reaching anticyclonic eddies around the narrow section of the MZC [*Collins et al.*, 2014; *De Ruijter et al.*, 2004].

The southern extension of the East Madagascar Current (EMC), known as the South-East Madagascar Current (SEMC), forms part of the western boundary current system of the subtropical gyre of the SIO [*Stramma and Lutjeharms*, 1997]. It is a narrow and intense flow, which clings to the slope, connecting the Madagascar Shelf and the deep Madagascar Basin further south [*Donohue and Toole*, 2003; *Lutjeharms et al.*, 1981] on its approach to the southern tip of Madagascar (Figure 2.4). It is considered to be one of the sources of the Agulhas Current (AC) [*Biastoch and Krauss*, 1999; *Biastoch et al.*, 1999; *De Ruijter et al.*, 2004; *Quartly et al.*, 2006; *Stramma and Lutjeharms*, 1997]. On the basis of a 2.5 year-long time-series of moored current observations, the SEMC has been shown to have a width of 60-100 km and a vertical extent up to 1000 m depth. On average, it transports 18.3 ± 8.4 Sv poleward [*Ponsoni et al.*, 2015]. Westward-propagating sea level anomalies, which are likely represented by cyclonic and anticyclonic eddies, cross the SIO at semi-annual [*Morrow and Birol*, 1998] and quarterly [*Schouten et al.*, 2002] time-scales, and interact with the SEMC inducing a bi-monthly [45-85 days] variability in its transport [*Ponsoni et al.*, 2015, 2016].

The strength of the EMC also varies on interannual time scales, mostly related to

the large-scale climate variability over the Indian Ocean. The large-scale sea surface height (SSH) signals, related to the occurrence of the Indian Ocean Dipole (IOD; *Saji et al.* [1999]), may interact with the Madagascar coast at a lag of +1 year after each IOD phase. *Palastanga et al.* [2006] showed that the local current regimes including the NEMC, SEMC and EACC exhibited a decrease in geostrophic velocities in 1995 and late 1997/1998, coinciding with positive IOD years. The IOD-induced positive SSH anomalies in the tropical and subtropical Indian Ocean induce a decrease in the intensity of the tropical gyre, and/or a northward extension of the subtropical gyre. On the other hand, during negative phases of the IOD, an intensification of the main flows was observed, pointing to a strengthening and/or southward extension of the tropical gyre, related to IOD-induced negative SSH [*Palastanga et al.*, 2006].

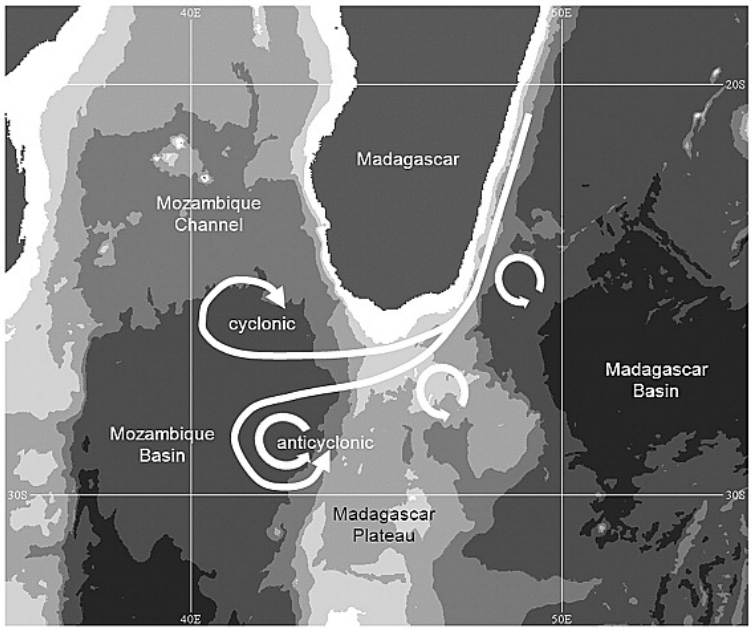


Figure. 2.4 Schematic representation describing the modes of the EMC extension. The shading indicates isobaths with 1000 m separation where greater depths correspond to darker shading. [After *Siedler et al.* [2009]]

At the southern tip of Madagascar, the SEMC separates from the continental shelf, and undergoes a very complex regime, with various routes. The first hypothesis put forward

by *Lutjeharms et al.* [1981] stated that the current retroflects and flows eastward as the East Madagascar Return Current. Evidence of such retroflection has been shown through satellite remote sensing observations, in both sea surface temperature [*DiMarco et al.*, 2000; *Lutjeharms*, 1988] and ocean colour [*Lutjeharms and Machu*, 2000], which hint at an anticyclonic motion south of Madagascar and shedding of eddies. Analysis of satellite altimetry suggests a west or south-westward drift of these eddies [*Gründlingh*, 1995]. In 2001, a study based on in-situ data from a hydrographic cruise (ACSEX II), *De Ruijter et al.* [2004] suggested that the flow of the SEMC, after rounding the southern tip, establishes an intermittent link with the AC through large pairs of counter-rotating eddies or dipoles. These dipoles are formed on a frequent and regular basis during some periods, whereas during other spells, their formation is separated by long intervals of no dipoles. The regular dipole formation is related to a strengthening of the EMC due to large scale SSH anomalies from La Niña and/or IOD negative events [*De Ruijter et al.*, 2004]. Interestingly, in late 2000, the interaction between a train of dipoles and the AC caused an anomalous eastward shift of the Agulhas Retroflection which lasted for almost half a year [*Ridderinkhof et al.*, 2013]. During this time, there was no formation of Agulhas Rings which would bring Indian Ocean waters into the South Atlantic Ocean.

However, based on satellite remotely-sensed data and a high resolution nested model, *Siedler et al.* [2009] suggested that the SEMC holds two different modes, which change from one regime to the other, depending on the intensity of the EMC. The first mode is identified as a cyclonic motion in the southern part of the MZC. This is favoured by a westward-flowing SEMC, which through friction with the inshore edge, will induce a cyclonic relative vorticity. This circulation occurs close to the newly discovered South-west MAdagascar Coastal Current (SMACC; *Ramanantsoa et al.* [2018b]). SMACC is a relatively narrow ($<$ 100 km) and shallow ($<$300 m) warm and salty poleward surface current which extends from 22°S to 26.4°S. WIth a maximum in summer and a minimum in winter, it carries on average 1.3 Sv and is forced by a strong cylonic wind stress curl, linked to a curvature of the trade winds along the southern tip of

Madagascar [*Ramanantsoa et al.*, 2018b]. The second mode of the EMC, as pointed out by *Siedler et al.* [2009], is an anticyclonic motion, owing to the south-westward flow of the SEMC and hence to the absence of frictional effects with the slope. The planetary vorticity changes result in an anticyclonic motion in order to conserve absolute vorticity. This favours a retroflection to the east and northeast (Figure 2.4). Investigating the impact of eddies on model-derived flow, *Halo et al.* [2014b] indicated that the connection between the SEMC and a retroflection could be established through the shedding of anticyclonic eddies, hence consistent with a non-persistent retroflection of the SEMC, stated by *Quartly et al.* [2006]. This partial retroflection may possibly act as a feeder to an eastward shallow current, the South Indian Ocean Countercurrent (SICC; *Palastanga et al.* [2007]; *Siedler et al.* [2006]) which flows from the Madagascar basin towards western Australia.

- **South Indian Ocean Countercurrent**

The SICC has been perceived as a well-defined and shallow countercurrent [*Palastanga et al.*, 2007; *Siedler et al.*, 2006] with an eastward component, entirely against the flow predicted by classical theories of wind-driven circulation, as seen in Figure 2.2. Although only recently acknowledged as an established trait of the SIO circulation, the eastward current between 22°S and 26°S was apparent on the Royal Netherlands Meteorological Institute's surface current maps in 1952, and the Indian Ocean Atlas's surface geopotential maps by *Wyrtki* [1971]. It was then identified as the South Indian Tropical Countercurrent and known to be associated with a thermal front [*Sharma*, 1976; *Sharma et al.*, 1978].

How and where exactly the SICC originates remains a mystery although recent studies have focussed on its dynamics [*Menezes et al.*, 2014, 2016]. Investigating the contribution of the SEMC towards the SICC using Lagrangian analysis in a Nucleus for European Modelling of the Ocean (NEMO) model, *Siedler et al.* [2006] showed

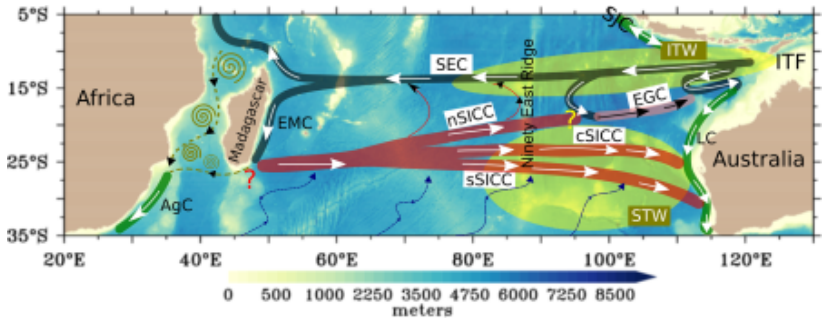


Figure. 2.5 Schematic representation of the upper layer circulation of the South Indian Ocean. Currents indicated are the three branches of the South Indian Countercurrent (northern [nSICC], central [cSICC], and southern [sSICC]). The Question marks (?) indicate regions where the circulations are still a matter of debate: the retroflection of the EMC and its connection to the SICC, and the connection between the SICC and the tropical EGC. Spirals indicate the southward-propagating Mozambique Channel eddies. Yellow shadings show the Indonesian Throughflow Water (ITW) and the subtropical Water (STW) regions. Water depths are blue shadings from the Smith-Sandwell 2 min bathymetry. [After *Menezes et al.* [2014]]

that 40% of the volume flux of the SICC arises, through a retroflection of the SEMC. The shallow stream then flows towards Australia, where it seems to connect with the tropical eastward EGC around 15°S, and ultimately the LC [*Schott et al.*, 2009]. Using an idealized eddy-resolving simulation, [*Lambert et al.*, 2016] showed that the SICC decreases if the ITF is closed, and the SICC-LC connection is eventually terminated.

On the basis of several satellite and Argo-based (CARS09 and Roemmich-Gilson Argo Climatology) data, *Menezes et al.* [2014] proposed a new spatial structure of the SICC (Figure 2.5). It emerges south of Madagascar as a well-defined and relatively strong jet, with a speed in the 9-18 cm s^{-1} range and with a width spanning a 3.8° latitude. It follows the southern limb of the northern cell of the subtropical gyre and on reaching the Central Indian Ridge [65°E-68°E at 25°S], it separates into three distinct branches (northern, central and southern). Based on three World Ocean Circulation Experiment (WOCE) cruises in 1995, zonal volume transports of 10 SV, 4 Sv and 9 Sv, at 54°E, 80°E and 95°E respectively, were assessed [*Siedler et al.*, 2006]. However, a slightly lower volume transport was observed with the new spatial extent of the

SICC. The southern branch exhibits an annual mean transport of 3-4 Sv at around 26°S, the central branch transports between 0.5 Sv at 80°E to 3-5 Sv at 110°E, and a weaker northern branch presents a transport not exceeding 1 Sv [*Menezes et al.*, 2014].

The SICC is described as weaker in austral winter and stronger in austral summer, with its zonal component varying from 6-8 cm s^{-1} in austral winter, and 8-10 cm s^{-1} in austral summer [*Jia et al.*, 2011a; *Menezes et al.*, 2014; *Palastanga et al.*, 2007]. However, the SICC branching structure has different seasonal cycles in the western, central and eastern basin. The southern SICC is stronger in December-January in the western basin, with the maximum in the central (eastern) basin occurring in August-September (October) [*Menezes et al.*, 2014]. On an interannual time-scale, periodic intensity of mesoscale eddy movement in the SIO can concurrently alter the strength of the SICC, with eddy-rich and eddy-poor time spans associated with an increased and weakened flow, respectively [*Jia et al.*, 2011b]. Investigating interannual variability of the SICC with periods less than 10 years ($T \leq 10$), *Menezes et al.* [2016] observed a quasi-biennial band (1.2 year $\leq T \leq$ 3 year), explaining more than 40% of its low-frequency variance. Another mode of variability in the ENSO (El-Niño Southern Oscillation) band (3 year $\leq T \leq$ 7 years) was also found, that explained 18% of the SICC variance. A quasi-decadal band (7 year $\leq T \leq$ 10 year) was accountable for less than 5% of the variability.

2.1.3 Mesoscale Variability

The kinetic energy associated with mesoscale variability, with scales of 10 to 100 km spatially and hundreds of days temporally, is greater by more than one order of magnitude than the mean kinetic energy of the mean flow, over almost all oceans [*Richardson*, 1983]. This variability occurs as non-linear eddies or vortices and westward propagating planetary waves known as Rossby waves. In the Indian Ocean, previous

studies have shown that the wind stress curl related to large scale climate phenomena generates westward propagating downwelling or upwelling Rossby waves, which impact the seasonal movement of the thermocline [*Rao and Behera*, 2005; *Yu and Lau*, 2005] and the surface as well as sub-surface chlorophyll-a variability [*Dilmahamod et al.*, 2016].

On the other hand, mesoscale eddies, being ubiquitous features in the ocean, have a far greater impact on the general circulation. They play a major role in the transfer of heat and salt zonally and meridionally [*Chaigneau et al.*, 2011; *Dong et al.*, 2014; *Qiu and Chen*, 2005; *Roemmich and Gilson*, 2001; *Volkov et al.*, 2008], the nutrient enrichment of oligotrophic regions [*McGillicuddy and Robinson*, 1997; *McGillicuddy et al.*, 2007; *Oschlies*, 2002], and the advection of phytoplankton cells horizontally [*Chelton et al.*, 2011a; *Lehahn et al.*, 2011; *Lévy*, 2003; *Siegel et al.*, 2011]. Previous studies inferred that changes in mesoscale activity influence the western boundary currents of the SIO namely the EMC [*Ponsoni et al.*, 2016] and the AC [*De Ruijter et al.*, 2004; *Ridderinkhof et al.*, 2013], and ultimately the inter-ocean leakage between the Indian and Atlantic Ocean [*Biastoch et al.*, 2008; *Durgadoo et al.*, 2013; *Loveday et al.*, 2014; *Penven et al.*, 2006a; *Schouten et al.*, 2002]. In the SIO, mesoscale eddies are generated along in the eastern part *Wyrtki* [1962], and then propagate westward along a latitudinal band (20°S-30°S) [*Jia et al.*, 2011a], both as surface and subsurface-intensified eddies [*Nauw et al.*, 2006], before interacting with the SEMC [*Ponsoni et al.*, 2015, 2016].

- **South-east Indian Ocean Variability**

Significant mesoscale eddy activity also occurs in the eastern SIO where eddies are pinched off from the LC west of Australia. *Wyrtki* [1962] was the first to postulate the existence of eddies in the eastern basin, with a strong semi-permanent eddy present near 32°S, 110°E. Using remotely-sensed altimetric data and hydrographic observations, *Fang and Morrow* [2003] were able to track anticyclonic eddies from

the LC, which propagate westward between 20°S-32°S. These features interacted with the bottom-topography causing a reduction in their speeds and a decay of the eddy amplitudes.

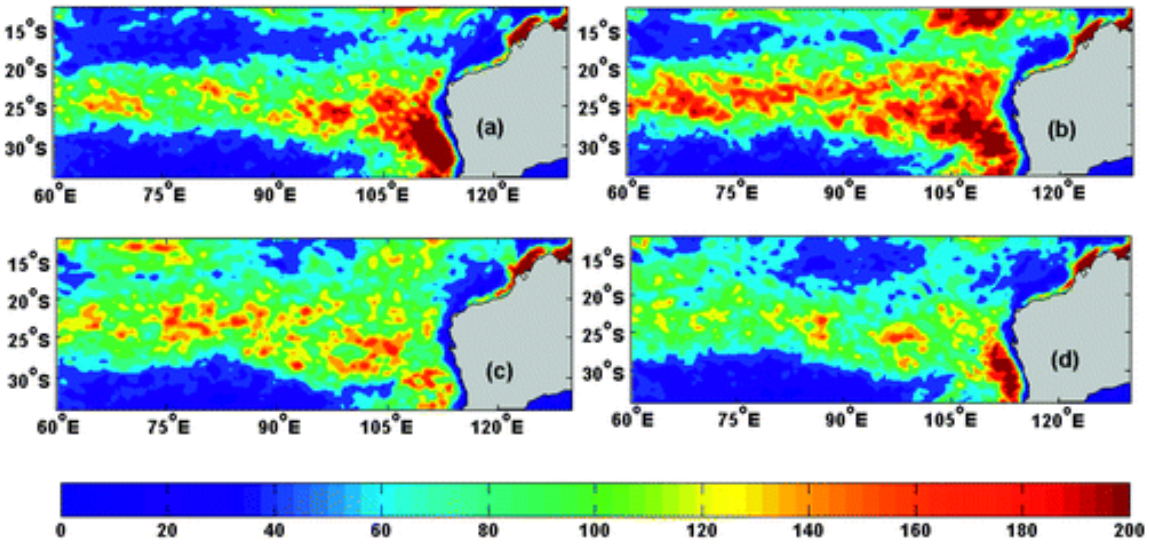


Figure. 2.6 Seasonal distributions of eddy kinetic energy (cm^2 s^{-2}) in the southeast Indian Ocean in (a) spring (August–October), (b) summer (November-January), (c) autumn (February - April) and, (d) winter (May-July). [Adapted from [*Jia et al.*, 2011a]]

The Eddy Kinetic Energy (EKE) in this region has a coherent seasonal cycle with a maximum in summer and minimum in winter [*Jia et al.*, 2011a] (Figure 2.6, with the largest number of mesoscale eddies occurring in October and the fewest in February [*Zheng et al.*, 2015]. This variability in the mesoscale energy has been attributed to the seasonal modulation of the surface intensified eastward flowing SICC and the underlying westward-flowing SEC [*Jia et al.*, 2011a]. Geostrophic convergence and meridional Ekman increase the upper-ocean meridional temperature gradient, hence strengthening the SICC front and its corresponding vertical shear. The variability of this vertical velocity shear induces an alteration of baroclinic instability, hence prevailing on the observed EKE seasonal variations [*Jia et al.*, 2011a]. Other non-local processes such as the variability of the LC and the penetration of Pacific Ocean waters in the Indian Ocean may also impact the mesoscale eddy variability in the eastern Indian ocean [*Fang and Morrow*, 2003]. The zonal band, at around 25°S, at which the

mesoscale eddies propagate eastward is shown in Figure 2.6. As noted by *Nauw et al.* [2006], this westward migration of mesoscale eddies consists also of a special type of eddies, namely subsurface-intensified eddies.

- **Subsurface-Intensified Eddies**

An important component of the variability in the ocean arises from propagation of subsurface-intensified eddies. These features are a special group of oceanic mesoscale eddies which have their cores in the subsurface layers, and they are termed subsurface eddies or subsurface vortices [*Kostianoy and Belkin*, 1989; *Mcwilliams*, 1985]. If the core is found below the thermocline, they are known as Subthermocline Eddies (STEs) and if the core is between the seasonal and permanent thermoclines, they are called Intrathermocline Eddies (ITEs) [*Barceló-Llull et al.*, 2017; *Li et al.*, 2017a; *Nauw et al.*, 2006; *Pelland et al.*, 2013; *Zhang et al.*, 2015]. Generally, their flow field is mainly horizontal and most of them have an anticyclonic motion owing to the dominance of the depression of the lower thermocline [*Filyushkin et al.*, 2011; *Gordon et al.*, 2002; *Kostianoy and Belkin*, 1989; *McGillicuddy et al.*, 2007], with a bowl and dome shape in the lower and upper thermocline, respectively. A subsurface velocity maximum is also associated with these structures. These special type of eddies display weak or no surface signatures in most cases. However, in some instances, a surface signature may be present [*Li et al.*, 2017a; *Nauw et al.*, 2006].

Subsurface eddies have been observed and studied in various regions of the ocean including the North Atlantic Ocean [*Barceló-Llull et al.*, 2017; *Bower et al.*, 1997, 2013], the North-eastern Pacific Ocean [*Garfield et al.*, 1999; *Jerónimo and Gómez-Valdés*, 2007; *Pelland et al.*, 2013; *Simpson and Lynn*, 1990], the North-western Pacific Ocean [*Li et al.*, 2017a; *Zhang et al.*, 2015], the south-eastern Pacific Ocean [*Chaigneau et al.*, 2011; *Johnson and McTaggart*, 2010], the Japan/East Sea [*Gordon et al.*, 2002] and the Indian Ocean [*Nauw et al.*, 2006; *Shapiro and Meschanov*, 1991]. Different formation

mechanisms have been attributed to these features, depending on their genesis area in the global ocean. Observational studies have shown that they are generated at upper ocean fronts [*Gordon et al.*, 2002; *Nauw et al.*, 2006; *Riser et al.*, 2016] where isopycnals from the thermocline outcrop in the winter mixed layer. In a subtropical convergence zone where wind stress curl is maximum, vertical motion set up by the large-scale wind-stress curl and convergent Ekman transport can induce a mass flux from the mixed layer to the thermocline. Another process of subduction in subsurface eddies' formation can be explained by a horizontal cross-frontal flow from a region of deep to a relatively shallow mixed layer. At upper ocean fronts, this process of subduction is mainly created by increased baroclinic instabilities, triggering regions of frontogenesis [*Spall*, 1995]. The deep, warm and salty Mediterranean water eddies (Meddies) [*Bashmachnikov et al.*, 2015; *Carton et al.*, 2010; *Hebert et al.*, 1990] and the California Undercurrent eddies (Cuddies) [*Collins et al.*, 2012; *Garfield et al.*, 1999] are formed due to baroclinic instabilities of their respective undercurrent namely, the Mediterranean Undercurrent and the California Undercurrent. In frontal regions associated with opposite-directed winds to the frontal jet, a reduced potential vorticity can generate subsurface eddies [*Thomas*, 2008]. From a numerical study of ITEs in the Japan Sea by *Hogan and Hurlburt* [2006], three other mechanisms have been inferred namely: (1) subduction of winter surface mixed layer water at frontal convergence; (2) advection of stratified water capping a pre-existing eddy and; (3) restratification of the upper layers in a pre-existing eddy due to solar heating. A study by *McGillicuddy* [2015] proposed a new mechanism which involves eddy-wind interaction driving an intense upwelling, hence inducing a doming of isopycnals in anticyclonic eddies.

In the Indian Ocean, two anticyclonic subsurface-intensified eddies, termed as Intrathermocline eddies (ITEs), were surveyed south-east of Madagascar during the Agulhas Current Sources EXperiment [ACSEX] cruise in March 2001. *Nauw et al.* [2006] gave a detailed structure of these oceanic features (Figure 2.7). The cores of the two eddies

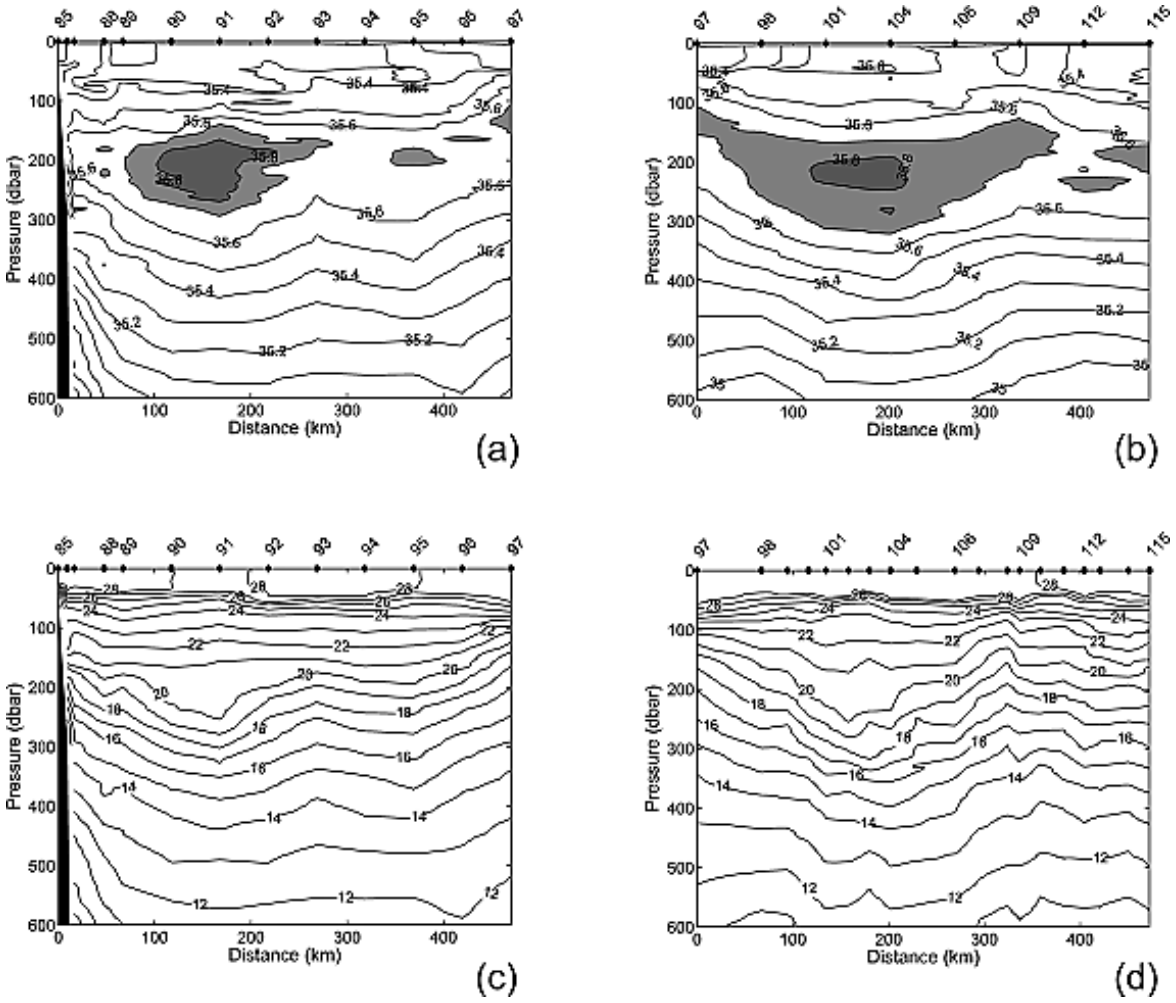


Figure. 2.7 Hydrographic properties along sections T8 and T9 transects (a, b) Salinity along sections T8 and T9, respectively. (c) Potential temperature (in °C) along section T8. (d) Temperature (in °C) along section T9. [After *Nauw et al.* [2006]]

were found at a depth of 200 m, in the thermocline, with a diameter of approximately 180 km, several times more than the local Rossby radius of deformation. A subsurface salinity maximum was present in their core (Figure 2.7) with a value exceeding 35.8 psu, higher than its surrounding waters. Both of the ITEs were anticyclonic with maximum velocities occurring at the edge of the cores. However, this anticyclonic motion could only be observed down to 1000 m depth. Conserving characteristics of their area of origin, the water mass trapped inside the core could be identified as being Subtropical Underwater (STUW). The genesis area of the anticylonic ITEs has been suggested to be in the eastern part of the subtropical gyre of the SIO, where the

saline subtropical mixed layer depth water subducts along the South Indian Tropical Front [*Nauw et al.*, 2006]. Since these eddies are larger than the Rossby radius of deformation, *Nauw et al.* [2006] inferred that the mechanism put forward by *Ou and Gordon* [2002], which involves part of the mixed layer waters entering the thermocline due to a potential vorticity constraint, while the rest is blocked at the surface, should be responsible for the formation of these ITEs.

Being long-lived features during which they could possibly travel from the eastern to the western Indian Ocean, the subsurface eddies retain much of their relatively homogeneous water, with comparable characteristics to their formation areas but distinct from their surrounding thermocline water [*Johnson and McTaggart*, 2010; *Kostianoy and Belkin*, 1989; *Nauw et al.*, 2006]. Mesoscale 'surface' eddies are known to be fundamental in transferring heat and salt across the oceans but since subsurface eddies strongly influence the intermediate and deeper layers of the oceans, they may have a major contribution in the pathways and spreading rates of water masses, and hence on the heat and freshwater fluxes. Additionally, their cores being deeper than the euphotic zone, they may also possibly influence productivity in the open ocean [*Hansen et al.*, 2010; *McGillicuddy et al.*, 2007; *Morales et al.*, 2012].

- **Mesoscale variability south-east of Madagascar**

On the south-eastern side of Madagascar, more specifically in the SICC vicinity, large SSH variability and high EKE prevail. A prevailing frequency of 4-5 times per year and a semi-annual signal [*Morrow and Birol*, 1998] were observed in the eddy variability around Madagascar [*Schouten et al.*, 2002]. *Birol and Morrow* [2003] established that the quasi-semi-annual Rossby waves, with periods between 150 and 180 days, are linked to the eastern boundary pycnocline's variability. In the east Madagascar region, EKE related to the low frequency element of the SSH field suggests a high percentage of the overall EKE variability is associated with mesoscale processes. On

the basis of the *Halliwell et al.* [1994] hypothesis where they suggested that wavelike perturbations can be converted into large eddy structures in a baroclinically unstable system due to nonlinear energy cascade, it is likely that eddy activities observed east and south of Madagascar correspond to the locally generated variability by baroclinic instability in the subtropical Indian Ocean [*De Ruijter et al.*, 2004; *Quartly and Srokosz*, 2004; *Schouten et al.*, 2002]. These features will interact with the SEMC, inducing a bi-monthly (45-85 days) variability in its transport [*Ponsoni et al.*, 2015, 2016].

The main mechanisms related to the variability of biological properties such as nutrients and chlorophyll-a have been described through the dynamics of eddies in the Indian Ocean [*Dufois et al.*, 2016, 2017; *Quartly and Srokosz*, 2004; *Srokosz and Quartly*, 2013]. These can be either upwelling of deep nutrient-rich waters [*Gaube et al.*, 2015; *McGillicuddy et al.*, 2007], horizontal and vertical inputs of nutrients at eddy peripheries [*Gaube et al.*, 2013, 2014; *Lévy*, 2003], or trapped-water rich in organic and inorganic materials which are advected over long distances [*Chelton et al.*, 2011a; *Provenzale*, 1999; *Robinson*, 2012; *Thorpe*, 2007]. These can play a fundamental role south-east of Madagascar, in view of the presence of a biogeochemical feature in the region.

2.2 The South-East Madagascar Bloom

The storage of carbon and the ability to regulate atmospheric carbon dioxide [*Lévy et al.*, 2012], biogeochemical cycling of elements [*Naik et al.*, 2015] and life in the oceans are fundamentally-dependent on primary production. However, compared to terrestrial plants, these oceanic primary producers, namely phytoplankton, are subject to light and nutrient availability, controlled by physical processes of the upper ocean.

2.2.1 General Description

The south-west Indian Ocean, more specifically offshore of the south-eastern coast of Madagascar, is a region of biologically oligotrophic habitat. However, a unique and intriguing aspect of the region is the occurrence, in the Madagascar basin, of a sporadic phytoplankton bloom (Figure 2.8). Known as the South-East Madagascar Bloom, it is one of the most compelling features of interannual variability in ocean color time-series, both in terms of magnitude of the anomaly and the area influenced [*Uz*, 2007; *Wilson and Qiu*, 2008], and hence should have ramifications for the biogeochemistry of the region. The bloom coincides with the presence of the shallow eastward SICC as well as the the wesward-propagating 'eddy-corridor'. On average, the onset of the bloom is in January/February, reaching its maximum in February/March and dissipating by the end of April [*Uz*, 2007]. Thus, it is locked to the austral summer season. When it is fully developed, chlorophyll-a (Chl-a) concentration can reach values greater than 1.0 mg m^{-3}, with some patches reaching 2-3 mg m^{-3} [*Longhurst*, 2001], and can extend up to 70°E, covering an area of almost 2500 km^2. However, from one year-occurrence to another, this dendritic phytoplankton bloom exhibits substantial variability in terms of its temporal and spatial extent, as can be seen in Figure 2.8.

Uz [2007] used a bloom index, by normalizing mean Chl-a concentration in the identified bloom box (48°E-66°E; 24°S-30°S) by that of a similarly-sized box farther east, to convey the occurrence of bloom and non-bloom years (Figure 2.9b). *Wilson and Qiu* [2008] and *Uz* [2007] identified 1999, 2000, 2002, 2004 and 2006 as bloom years, showing its large temporal and spatial variability. *Uz* [2007] mentioned the different timing at which the bloom reaches its maximum, with 1999 and 2000 blooms peaking in March, 2006 bloom in February, and 2004 bloom in April.

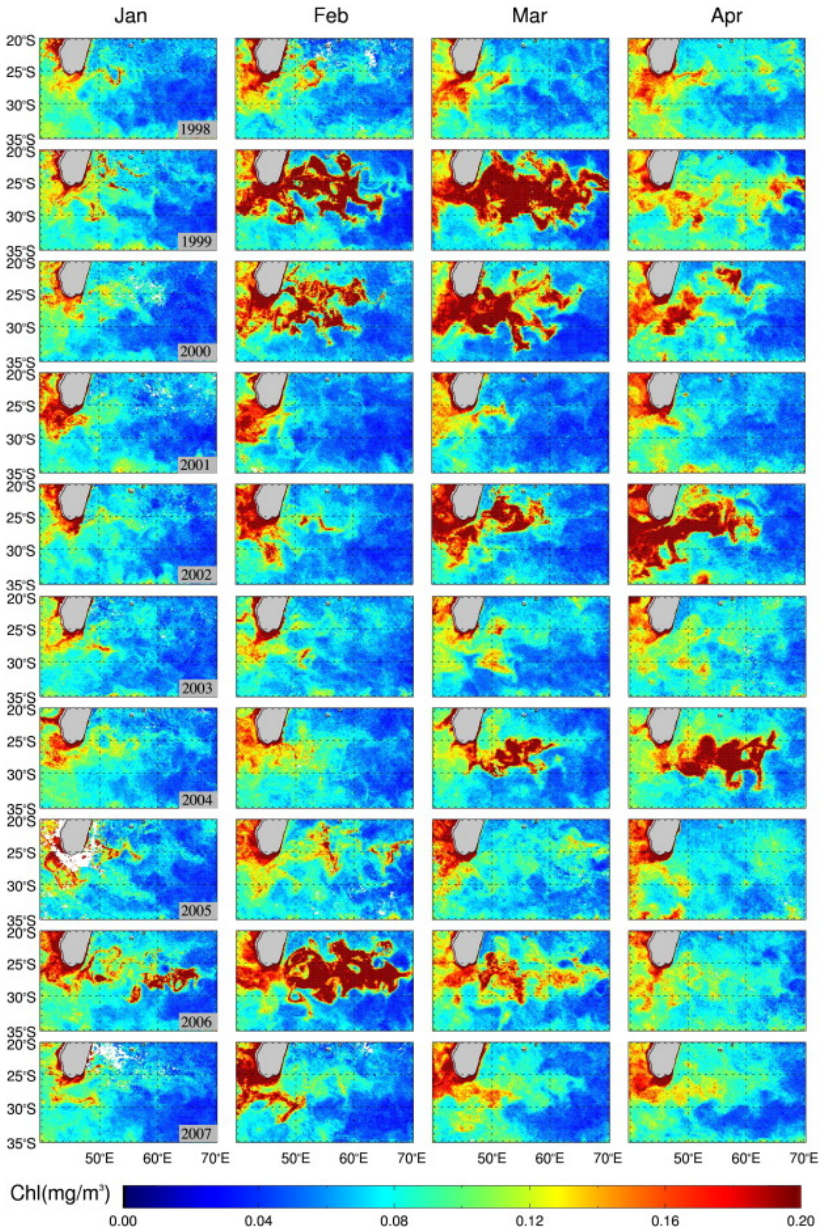


Figure. 2.8 Monthly maps of chlorophyll (mg m^{-3}) for January–April off Madagascar, 20°S–35°S, between 1998 and 2007. [After *Wilson and Qiu* [2008]]

Data from a scientific cruise, which went through a higher Chl-a patch in the region in February 2005, showed that the phytoplankton cells are confined to a shallow mixed layer of ∼30 m [*Srokosz and Quartly*, 2013]. Mostly large nitrogen fixers [> 50 µm] with *Trichodesmium* being more abundant [500-1000 trichomes L^{-1}] in the southern Madagascar waters and *Richelia/Rhizosolenia* diatoms [125-500 cells L^{-1}] dominating

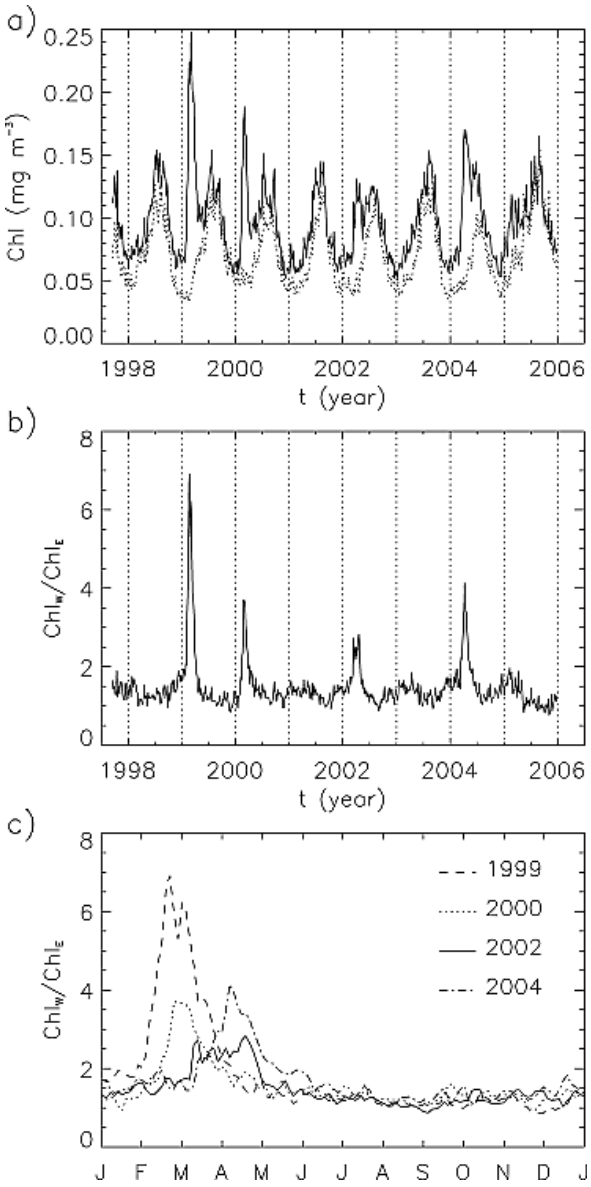


Figure. 2.9 (a) Time series of mean [Chl] from SeaWiFS and MODIS sensors, between 24°S–33°S and 48°E–66°E (solid line) and between 24°S–33°S and 70°E–88°E (dotted line). (b) Time series of the bloom index defined by normalizing mean Chl in the bloom area (solid line in Figure 2.9a to the area farther east (dotted line). (c) The index for the four bloom years plotted together for comparison. [After *Uz* [2007]]

south-east of Madagascar, have been shown to dominate the patch [*Poulton et al.*, 2009]. *Wilson and Qiu* [2008] showed that the bloom does not occur in a region of high trichodesmium occurrence, but on the edge of it. It should also be noted that 2005 was not ascribed as a bloom year by the bloom index from *Uz* [2007].

2.2.2 Hypothesis

Many studies with various outcomes have focused on the physical mechanisms responsible for the onset and distribution of the bloom [*Huhn et al.*, 2012; *Lévy et al.*, 2007; *Longhurst*, 2001; *Raj et al.*, 2010; *Srokosz and Quartly*, 2013; *Srokosz et al.*, 2004, 2015; *Uz*, 2007] but none have been as yet clearly substantiated. Prevailing in a remote and under-sampled region where in-situ and cruise data are very limited, modelling might be necessary to better understand the bloom. Presented here, according to the mechanisms, are the different hypothesis put forward during previous studies of the bloom.

A) Mixed Layer Dynamics

The seasonal evolution of the South-East Madagascar Bloom was first described by *Longhurst* [2001] using Ocean Colour observations from POLDER and SeaWiFS. He noted that the bloom occurs from February to April and proposed a seasonal deepening of the mixed layer depth as a contributing factor to its onset, through entrainment of nutrient-rich waters into the photic zone. Owing to the development of the south-east trade winds during the bloom months, wind stress would increase and together with the associated heat loss by surface fluxes, would induce a deepening of the mixed layer depth to a ∼75-100 m [*Rao et al.*, 1989]. Owing to this deepening, nutrients as well as phytoplankton cells are entrained into the photic zone. These are then upwelled through mesoscale eddies to the surface. *Longhurst* [2001] also associated the complex surface signature of the bloom to the associated eddy-field and hypothesized that nitrogen-fixers, namely *Trichodesmium*, or large eukaryotic cells might dominate the bloom. The bloom seemed to develop during La Niña years (1999) whereas a weakening of the wind in the region, due to the 1997-1998 El Niño event, could explain its absence [*Longhurst*, 2001]. However, the intensity of individual La Niña events does not seem to dictate the intensity and extent of the bloom, and the bloom also did not develop during the La Niña year of 2011. This result shows that even though

seasonal modulation of the mixed layer depth, due to El Niño Southern Oscillation (ENSO)-induced wind changes, may contribute to the bloom, other factors might also be in play.

B) Plankton Wave

Using remotely-sensed ocean colour data, *Srokosz et al.* [2004] proposed the idea of the South-East Madagascar Bloom being the first open ocean plankton wave in the Indian Ocean. This was introduced due to the fact that the bloom has an eastward propagation, against the supposedly dominant westward circulation. Coastal upwelling south of Madagascar [*Lutjeharms and Machu*, 2000; *Machu et al.*, 2002] would bring nutrient-rich waters to the surface, hence inducing enhanced phytoplankton production. This would be advected eastward through the energetic mesoscale eddy field, with the regions of high EKE limiting the north-south extent of the bloom. The eastward advection, linked to the eddy diffusivity processes and against the mean westward propagation of mesoscale eddies and Rossby waves, occurs simultaneously with plankton growth, which utilize the nutrients. Hence, the term plankton wave is used. *Srokosz et al.* [2004] ascribed the diminishing plankton wave in the central Indian Ocean to several factors. As they move eastward, phytoplankton consume nutrients up to a nutrients exhaustion point. A deepening of the mixed layer depth from ∼30 m to ∼70 m occurs with the onset of winter, hence increasing light limitation [*Longhurst*, 2001], which could hinder the bloom. They also proposed a putative theory about the presence of the juncture of the three Indian Ocean Ridge Systems (South-west, Central and South-east), which may impact the mixed layer dynamics or eddy diffusivity in the region.

However, the shallow SICC which has an eastward component, similar to the bloom propagation, was later discovered by *Palastanga et al.* [2007] and *Siedler et al.* [2006]. Hence, the concept of a plankton wave is not required anymore to explain the eastward propagation. Nonetheless, high mesoscale activity prevails in the bloom region and

hence, eddy diffusivity could still play a role in the phytoplankton bloom.

C) Iron Runoff

Uz [2007] studied the phytoplankton bloom using a combination of ocean colour data (SeaWiFS and MODIS), sea surface temperature (SST from the Pathfinder reanalysis of the AVHRR imagery), Argo data and meteorological data (reanalysis winds from NCEP, precipitation fields from CMAP, wind stress curl from NOAA PFEL which is based on the FNMOC numerical model, and best track historical cyclone tracks from the Naval Pacific Meteorology and Oceanography Center, Joint Typhoon Warning Center). *Uz* [2007] put forward a completely new hypothesis for the bloom, which involves the number of tropical cyclones over Madagascar (Figure 2.10) and consequent enhanced river runoff. He proposed that an increased number of tropical cyclones over Madagascar would bring heavy rainfall, increasing river runoff of iron-rich sediments in the coastal waters. These waters are then transported poleward in the EMC and ultimately advected eastward through eddy diffusion. *Uz* [2007] dismissed the mixed layer modulation dynamics presented by *Longhurst* [2001] due to the absence of a direct link between wind forcing and interannual variability of the bloom. He accounted the non-bloom years of 2001, 2003 and 2005 to be due to a decreased number of cyclones passing over Madagascar (Figure 2.10).

Studying the vertical structure of the water column during bloom years indicated the presence of the bloom in a shallow and very stable stratified surface layer [*Uz*, 2007]. A strong pycnocline showed that entrainment of deeper nutrient-rich waters towards the surface did not happen during the bloom period. As a stratified surface layer is also present outside of the bloom, *Uz* [2007] mentioned that it is not a pre-requisite for the bloom. However, *Uz* [2007] agreed with *Longhurst* [2001] about the bloom being simulated by *Trichodesmium* nitrogen-fixation.

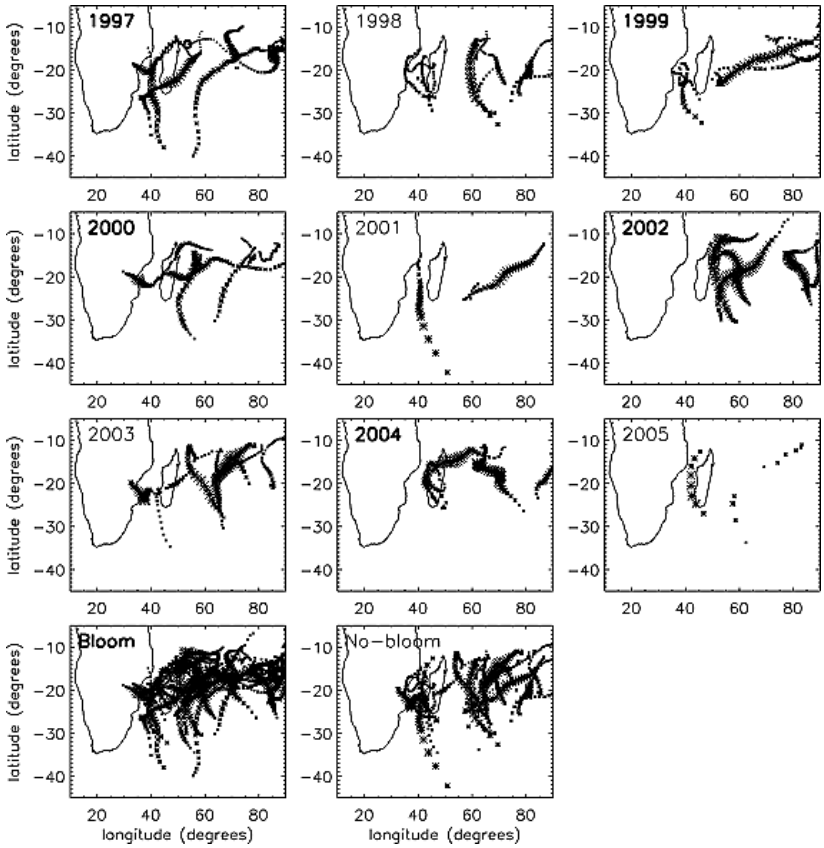


Figure. 2.10 Tracks of cyclones for the first 3 months of years 1997–2005. Symbol size is proportional to maximum sustained wind speed. The year is marked in the upper left of each panel, in bold characters if a strong bloom was observed that year. (bottom) Storms for all of the bloom years (1997, 1999, 2000, 2002, and 2004) and nonbloom years (1998, 2001, 2003, and 2005), respectively. [After *Uz* [2007]]

Nevertheless, some discrepancies exist in the timing of the bloom onset between *Longhurst* [2001] and *Uz* [2007] who stated that the bloom starts in January, and February/March respectively. Another discrepancy noted by *Srokosz and Quartly* [2013] is the presence of a weak bloom in 2005, a year during which the number of cyclones was at its lowest compared to the number of cyclones during ll other non-bloom years. Also, as stated by *Srokosz and Quartly* [2013], the MZC is the end point of most Madagascan rivers, hence river-runoff would be more prominent on the western side compared to the eastern side of the island. Even though these discrepencies dispute the theory of iron bio-availability in modulating the variability of the phytoplankton bloom, they do not completely discard the hypothesis, which might still influence the

bloom.

D) Horizontal advection

Huhn et al. [2012] made use of Finite-time Lyapunov Exponents (FTLE) and Finite-Time Zonal Drift (FTZD) to investigate how the SICC [*Palastanga et al.*, 2006; *Siedler et al.*, 2006] could act as an advective flow for phytoplankton cells. It was not a detailed study on the formation of the bloom but mostly applied to explain its spatial distribution. Zonal jets in the SICC have been shown to be linked to an eastward propagation from the southern tip of Madagascar and the confinement of the phytoplankton cells within a narrow zonal band, with meridional transport boundary being formed by the SICC. *Huhn et al.* [2012] hypothesized that availability of nutrients or phytoplankton cells at the southern tip of Madagascar could be horizontally advected within the zonal jet-like Lagrangian Coherent Structures (LCS).

E) Coastal Upwelling

The hypothesis of coastal upwelling south of Madagascar has been presented by various studies [*Lévy et al.*, 2007; *Raj et al.*, 2010; *Srokosz and Quartly*, 2013] as the main mechanism which triggers the bloom and controls its interannual variability. Investigating the basin-wide seasonal variation of phytoplankton blooms in the Indian Ocean, *Lévy et al.* [2007] proposed that the current-induced upwelling south of Madagascar [*Lutjeharms and Machu*, 2000; *Machu et al.*, 2002] would bring nutrient-rich water to the surface, which would be advected eastward by a possible retroflection of the SEMC [*Quartly et al.*, 2006].

Owing to the findings, from the MadEx Cruise, of nitrogen-fixers being the dominant species south-east of Madagascar, *Srokosz and Quartly* [2013] offered an alternative upwelling hypothesis. They suggested an input of dissolved iron to the surface, coming from sediments on continental shelves, known as a source of iron in coastal areas [*Dale*

et al., 2015; *Jeandel et al.*, 2011; *Johnson et al.*, 1999]. The hypothesis is that iron would be released from the sediments to the surface owing to the current-induced upwelling south of Madagascar [*Lutjeharms and Machu*, 2000; *Machu et al.*, 2002], then advected eastwards in the peripheries of mesoscale eddies, causing enhanced phytoplankton production. As observed during the cruise, the mixed layer is well stratified in the bloom vicinity during this period, and this allows nitrogen fixers to thrive. The consumption of iron in the surface layer of the Madagascar basin will ultimately limit the spread of the bloom. The strength of the upwelling will then control the interannual modulation of the enhanced primary production. *In-situ* Measurements during the MadEx Cruise revealed the presence of a deep chlorophyll maximum (DCM) at a depth of ∼93 m, while the surface production is being modulated by the eddy field. However, different phytoplankton species seems to prevail in the DCM compared to the surface. As stated earlier, it should be noted that the MadEx cruise occurred during a non-bloom year, as observed by *Uz* [2007].

Srokosz et al. [2015] tested the upwelled-iron particles hypothesis, from a Lagrangian technique perspective, using a high resolution [1/12°] eddy-resolving ocean general circulation model. Two spots were chosen, east and south of Madagascar, and 275 particles were released every 5 days, and from these, they demonstrated that in some years, few particles enter the bloom area whereas in other years, significant spatial bloom extent can be covered by the particles. This variability could well explain the spatial distribution of these high phytoplankton patches. Intermittent supply of iron will fertilize the region and have a positive impact on phytoplankton cells. Another important finding from this analysis was that iron particles can be advected sufficiently far to the east, to sustain a bloom in the following year. Investigating the physical mechanisms in play in the region, *Srokosz et al.* [2015] showed that since the mixed layer depth in the region remains relatively shallow throughout the year (< 30 m), light limitation is not a factor which could determine the presence or absence of the bloom, neither its most eastward extent. On the other hand, SST greater than 25°C

could be found during the bloom period with the temperature cooling after the bloom. This effect could be due to the vertical movement of the mixed layer depth and hence this mechanism could play a major role in the bloom [*Srokosz et al.*, 2015].

F) Combination of mechanisms

Raj et al. [2010] did a comprehensive study of the phytoplankton bloom using satellite, reanalysis, model and hydrographic data. They presented various processes which could play a role in the bloom formation mechanisms. Enhanced primary productivity is not only limited to the Madagascar Basin but can also extend into the Mozambique Basin and the Mozambique Channel. In a species context, the NASA Ocean Biogeochemical Model (NOBM) was used to investigate the bloom and the outcome was that cyanobacteria play a major role, having an important effect on nitrogen-fixation, by converting atmospheric nitrogen into nitrogen compounds. Coccolithophores have a secondary role while diatoms contribute the least [*Raj et al.*, 2010]. These cyanobacteria organisms thrive in high temperature [above 25°C], nutrient-rich, and high phosphorous (P) and Nitrogen (N) waters. Another process is the distinct seasonal variability in precipitation, south-east of Madagascar ranging from 260 mm/month in austral summer reducing to a mere 40 mm/month in winter [*Raj et al.*, 2010]. It has been shown in previous studies that increased precipitation induces a decrease in sea surface salinity, hence enhancing the stratification. These conditions are favourable for nitrogen-fixers and can play an important part in the onset of this bloom. Availability of light is crucial for *Trichodesmium* as it is a light-dependent nitrogen-fixer [*Dugdale et al.*, 1961]. Analysis of remotely-sensed photosynthetic available radiation (PAR) displays a definite seasonal variability with a maximum in austral summer (December – February: above 55 Einstein m^{-2}) and a minimum in austral winter [May – July; below 30 Einstein m-2]. *Raj et al.* [2010] also provided evidence of maximum PAR values during strong bloom years (1999, 2000, 2006 and 2008). However, there appears to be no co-occurrence between the biological and climate modes (ENSO and IOD). One of the reasons put forward by *Raj et al.* [2010] towards the absence of a bloom after an El

Niño event is the increased EMC poleward flux, which breaks the connectivity between the Madagascar coast and the mesoscale eddy variability in the south-east region. To summarize, *Raj et al.* [2010] stated that a combination of mechanisms namely the upwelling south of Madagascar, precipitation south-east of Madagascar, light limitation in the bloom region and local mesoscale features, could contribute in a way to the South-East Madagascar Bloom.

2.3 Summary

The South-East Madagascar Bloom, a sporadic phytoplankton bloom in the south-west Indian Ocean, occurs in austral summer and covers an area of approximately 2500 km^2 when it is fully developed [*Longhurst*, 2001]. With one of the strongest interannual variability signals in ocean biology after El Niño and also one of the largest dendroid blooms in the global ocean, it is a compelling case to be better understood. Substantial efforts have been made to discuss the processes governing the South-East Madagascar Bloom [*Huhn et al.*, 2012; *Lévy et al.*, 2007; *Longhurst*, 2001; *Raj et al.*, 2010; *Srokosz and Quartly*, 2013; *Srokosz et al.*, 2004, 2015; *Uz*, 2007]. With almost two decades of remotely-sensed available data, the various hypothesis of the previous studies can be revisited. This observational data, together with a modelling platform, will be needed to acquire a better comprehension of this feature. The regional oceanography around the southern tip of Madagascar needs to be further investigated as the area of bloom initiation. Simultaneously, the ability of the South Indian Ocean's mesoscale features, which occur as surface and subsurface-intensified eddies [*Nauw et al.*, 2006], to advect water from the eastern to the western South Indian Ocean needs to be fully understood. This advection can comprise of trace elements, nutrients or biomass and can possibly have an impact on the South-East Madagascar Bloom. Thus, this thesis will result in an improved understanding of the physics and the biogeochemistry of the South Indian Ocean.

In order to achieve these objectives, specific key research questions are formulated as follows:

1. Can a longer biophysical dataset of 19 years (1998-2016) provide a better insight on the physical-biological interactions involved in the South-East Madagascar Bloom than the earlier data?

2. Using a high-resolution coupled biophysical model, can the physical-biogeochemical mechanisms which trigger the initiation and termination of the South-East Madagascar Bloom be better understood?

3. What are the implications of subsurface-intensified eddies in the South Indian Ocean in terms of their associated heat and freshwater fluxes?

4. Can subsurface-intensified eddies contribute to the South-East Madagascar Bloom?

A set of observational datasets including remotely-sensed data, Argo profiles and an established eddy tracking dataset [*Chelton et al.*, 2011b] are employed in an attempt to answer these questions. An eddy-resolving configuration using the Regional Ocean Modelling System (CROCO) was coupled to the Pelagic Interaction Scheme for Carbon and Ecosystem Studies (PISCES) component and configured to better understand the physical-biogeochemical processes involved in the South-East Madagascar Bloom.

Chapter 3

Materials and Methods

South-east of Madagascar, in the vicinity of the phytoplankton bloom, the oceanic circulation as well as its associated biogeochemical interactions are very complex and poorly understood, as illustrated in the previous chapter. This potentially key region for the surrounding mean circulation and for the biogeochemistry, have been poorly sampled, both temporally and spatially. It includes the South-East Madagascar Current (SEMC), one of the source regions of the Agulhas Current (AC) [*Biastoch and Krauss*, 1999; *Biastoch et al.*, 1999; *De Ruijter et al.*, 2004; *Quartly et al.*, 2006; *Stramma and Lutjeharms*, 1997], and the South-East Madagascar Bloom [*Longhurst*, 2001]. Therefore, alternative tools such as numerical models need to be employed to get a better understanding of the physical-biogeochemical interactions in the area.

The observational datasets used in this study are detailed in section 3.1. In order to investigate the impacts of the physics on the biogeochemical dynamics of the South-East Madagascar Bloom, a coupling between a hydrodynamic model namely the Regional Ocean Modelling System (ROMS) (detailed in section 3.2) and a biogeochemical model namely Pelagic Interactions Scheme for Carbon and Ecosystem Studies (PISCES) (detailed in section 3.3) is performed to simulate the physical and biogeochemical dynamics of the region. The model is configured for the South-West Indian Ocean (SWIO Model; see section 3.4). Section 3.5 evaluates the model's capability in reproducing realistic physical and biogeochemical general patterns in the bloom area.

3.1 Observed Datasets

- **AVISO**

To investigate the sea surface variability, the delayed-time absolute dynamic topography (MADT), sea level anomalies (SLA) and geostrophic velocities datasets are obtained from the gridded data product, produced by SSALTO/DUACS and distributed by AVISO (Archiving, Validation, and Interpretation of Satellite Oceanographic data center; https://www.aviso.altimetry.fr). Altimetric observations from a number of satellites are combined through an interpolation mapping technique [*Ducet et al.*, 2000]. These datasets are available globally as daily averages, objectively analysed on a 0.25° x 0.25° grid.

- **CARS09**

CSIRO Atlas of Regional Seas 2009 (CARS09), a digital climatology of historical subsurface measurements, provides datasets of oceanic water properties such as temperature and salinity [*Ridgway et al.*, 2002]. It is primarily based on data acquired from research vessel instruments as well as autonomous profiling buoys. It is, however, created by interpolating/averaging oceanographic profile data available. Using a locally weighted least square (LOESS) filter, the data are fitted onto a uniform grid while fitting annual and semi-annual harmonics to the data at the same time [*Ridgway et al.*, 2002]. It covers the global ocean at a spatial resolution of 0.5° with its temperature and salinity fields based on numerous datasets available till 2008 such as World Ocean Database 2005 (WOD05), World Ocean Circulation Experiment (WOCE) Program, surface-pressure corrected Argo datasets.

- **WOA13**

World Ocean Atlas 2013 (WOA13) provides an objectively analysed, climatological mean field of various physical and biogeochemical variables in the ocean such as temperature, salinity, dissolved oxygen, nitrate and phosphate. The data is processed by

the National Oceanic and Atmospheric Administration (NOAA) and archived at the National Oceanographic Data Center (NODC). This 2^{nd} version of WOA13 [*Boyer et al.*, 2013] distributes the data on a temporal resolution of annual, seasonal or monthly climatologies. These are interpolated on standard depth levels, with a global spatial resolution of 0.25°. The long-term mean temperature and salinity fields have been computed as the average of six decadal climatologies (1955-2012).

- **AVHRR**

An optimum interpolated high-resolution Sea Surface Temperature (SST) is provided by Advanced Very High Resolution Radiometer (AVHRR) infrared satellite data. These are obtained at a temporal resolution of one day and a spatial resolution of 0.25°. Satellite biases are adjusted on a large-scale using in-situ data from ships and buoys.

- **HadISST**

The Hadley Centre Global Sea Ice and Sea Surface Temperature (HadISST) is a monthly averaged dataset from 1871 till present. At a 1° x 1° resolution, it comprises of SST data from the Marine Data Bank and International Comprehensive Ocean-Atmosphere Data Set (ICOADS), as well as in-situ and adjusted satellite-derived SSTs.

- **QuickSCAT**

The Sea-Winds scatterometer on the Quick Scatterometer (QuikSCAT) provides global wind-fields data, spanning from August 1999 to November 2009. These are Level 3 data on a 0.25° x 0.25° resolution grid. Wind Stress Curl (WSC) as well as the Ekman Pumping (W_{ek}) are derived from this product.

- **Ocean Mixed Layer Depth**

Two different datasets of mixed layer from *de Boyer Montégut* [2004] and *Li et al.* [2017b] are used in this study. The dataset from *de Boyer Montégut* [2004] is an interannual climatology in the Indian Ocean. It is available on a 2°x2° resolution grid from 1969 to 2009 and was computed from approximately 565,000 temperature profiles available from NODC, WOCE, ARGO profiling floats and TAO RAMA Buoys [*Keerthi et al.*, 2012]. The mixed layer depth is calculated as from a fixed threshold criterion of 0.2°C change from the temperature at a reference depth of 10 m.

A longer alternative mixed layer depth dataset in the Indian Ocean is from *Li et al.* [2017b,c]. This product is based on Argo floats and is available on a monthly basis from 2004 to 2016, at a spatial resolution of 1°. For each temperature profile of Argo floats, the mixed layer depth is calculated using the geometry model method proposed by *Chu et al.* [1999].

- **CMAP**

Global oceanic and land precipitation was obtained from the Climate Prediction Center Merged Analysis of Precipitation (CMAP). It consists of a global 5-day (pentad) precipitation estimate, produced on a 2.5° latitude-longitude grid, spanning from 1979 to the present. A combination of gauge station measurements as well as satellite-derived precipitation are combined in this dataset [*Xie and Arkin*, 1997]. The quality of this dataset is largely dependent on the input data, which varies spatially and temporally.

- **ARGO**

The international Argo program consists of a global array of ∼3800 free-drifting profiling floats. These Lagrangian robots are equipped with conductivity, temperature and depth (CTD) instruments and hence provide freely-available data of temperature and salinity

down to 2000 m every ten days (Coriolis Project: http://coriolis.eu.org). In the Indian Ocean, these vertical profiles of temperature and salinity are available from 1999 to 2016.

• **ESA OC-CCI**

Remotely-sensed data of surface chlorophyll-a concentration were provided by the European Space Agency's Ocean Colour Climate Change Initiative (ESA OC-CCI Version 3, see www.oceancolor.org). It is a merged product which combined data from three sensors namely Sea-viewing Wide Field-of-view Sensor (SeaWiFS), Moderate Resolution Imaging Spectroradiometer (MODIS, [*Esaias et al.*, 1998]) and ESA's Medium Resolution Imaging Spectrometer (MERIS, [*Rast et al.*, 1999]). This merging produced a continuous 19 years (1998-2016) of chlorophyll-a concentration data at a spatial resolution of $\frac{1}{24}^{\circ}$ ($\sim$4.5 km) at different temporal scales. In this study, the 8-daily means ESA OC-CCI dataset is used.

• **Eddy Tracking Algorithm**

The 4^{th} release of an eddy dataset, based on an existing eddy tracking algorithm [*Chelton et al.*, 2011b], is used to track mesoscale eddies in the Indian Ocean. Daily sea surface height (SSH) as observed from altimetry in the delayed-time "two-sat merged" product of AVISO, is used in this established algorithm. A simple approach based on *Williams et al.* [2011] is used to locate pixels of maximum/minimum SSH and finding the neighbouring pixels of SSH with decreasing/increasing thresholds, with a threshold increment of 0.25 cm from -100 cm to +100 cm [*Schlax and Chelton*, 2016]. To mark the end of the life of an eddy, E, 5 specific criteria are taken into consideration as follows: (1) E should be connected with less than 2000 pixels, (2) E should be made up of a minimum of 2 interior pixels, (3) pixels of two eddies cannot be neighbours, (4) E should be connected and hence should not have any holes, and (5) the maximum value of d (distance between pixels) over all pairs of edge pixels in E must be less than 400 km. If any of these 5 criteria is violated, this marks the end of the eddy life.

From this dataset, the radius, amplitude, vorticity, propagations speed as well as the start and end locations of the eddy life are obtained and it includes eddies with a lifetime greater than 4 consecutive weeks. This is done so as to decrease the probability of false eddies which may come up from SSH fields' noise. This 4-week factor was chosen since it corresponds to the 35-day e-folding time scale of the Gaussian covariance function, which is used to construct SLA fields of AVISO Reference Series during objective analysis procedure [*Chelton et al.*, 2011b].

3.2 Regional Ocean Modelling System - ROMS

3.2.1 Motivation

In this study, we use the CROCO (Coastal and Regional Ocean COmmunity model) version of ROMS [*Shchepetkin and McWilliams*, 2005] to address our research questions and this is motivated by different reasons associated to some of the models' advantages. Designed specifically to resolve realistically basin-scale and coastal ocean processes, ROMS runs at a relatively low computational cost. This efficiency is guaranteed by the advanced numerical schemes for space and time differencing [*Shchepetkin and McWilliams*, 2005]. Also, its compatibility with the nesting tools (ROMS-AGRIF; *Debreu et al.* [2008, 2012]), a higher resolution sub-domain can be run at relatively low computational costs. The ability of ROMS to conserve water mass properties owing to its isopycnal diffusion (RSUP3 scheme) of tracers [*Marchesiello et al.*, 2009] is important to our region, as well as the coupling possibility with an established biogeochemical component, namely PISCES.

3.2.2 Model Description

ROMS is a split-explicit, free-surface, topographic following coordinate model, that solves the incompressible, hydrostatic, primitive equations on a planetary rotating frame under the Boussinesq and hydrostatic approximations [*Shchepetkin*, 2003; *Shchepetkin and McWilliams*, 2005]. The Boussinesq approximation disregards the seawater density variations in the pressure gradient term as they are insignificant when compared to the buoyancy term. Hydrostatic approximation, in which vertical momentum equation is governed by the pressure gradient and buoyance terms, is used. The model is coupled with a non-linear equation of state and advective/diffusion schemes for potential temperature and salinity. A non-local, K-Profile Parameterization (KPP) boundary-layer scheme [*Large et al.*, 1994] is used to parameterize the subgrid-scale vertical mixing.

• **Equations of motion**

Under Boussinesq and hydrostatic approximations, the primitive equations of motion, solved in ROMS in cartesian coordinates, read as follows:

- the horizontal momentum equations:

$$\frac{\partial u}{\partial t} + \vec{v}.\nabla u - fv = -\frac{\partial \phi}{\partial x} + F_u + D_u \tag{3.1}$$

$$\frac{\partial v}{\partial t} + \vec{v}.\nabla v + fu = -\frac{\partial \phi}{\partial y} + F_v + D_v \tag{3.2}$$

- the advection-diffusion governing the potential temperature T and salinity S:

$$\frac{\partial T}{\partial t} + \vec{v}.\nabla T = F_T + D_T \tag{3.3}$$

$$\frac{\partial S}{\partial t} + \vec{v}.\nabla S = F_S + D_S \tag{3.4}$$

- the hydrostatic ad mass balance:

$$\frac{\partial \phi}{\partial z} = -\frac{\rho g}{\rho_o} \tag{3.5}$$

- the continuity equation for an incompressible fluid:

$$\frac{\partial u}{\partial x} + \frac{\partial v}{\partial y} + \frac{\partial w}{\partial z} = 0 \tag{3.6}$$

- and the equation of state for seawater [*Shchepetkin and McWilliams*, 2005]:

$$\rho = \rho(T, S, P) \tag{3.7}$$

• **Vertical Boundary Conditions**

At the surface and bottom boundary conditions, ROMS introduces external forcing terms through vertical viscosity and diffusivity. These are introduced:

1) at the surface (z=ζ(x,y,t)) as:

- atmospheric wind stress at sea surface, in x and y directions:

$$K_v \frac{\partial u}{\partial z} = \frac{\tau_s^x}{\rho_o}(x, y, t) \tag{3.8}$$

$$K_v \frac{\partial v}{\partial z} = \frac{\tau_s^y}{\rho_o}(x, y, t) \tag{3.9}$$

- thermal and freshwater fluxes at the sea surface:

$$K_T \frac{\partial T}{\partial z} = \frac{Q_T}{\rho_o C_p} \tag{3.10}$$

$$K_S \frac{\partial S}{\partial z} = \frac{(E_v - P_r)S}{\rho_o} \tag{3.11}$$

- vertical velocities associated with the variation of the sea surface:

$$w = \frac{\partial \zeta}{\partial t} \tag{3.12}$$

2) and at the seafloor: z=-H(x,y) as:

- momentum transferred into the ocean by friction at seafloor:

$$K_v \frac{\partial u}{\partial z} = \frac{\tau_b^x}{\rho_o}(x, y, t) \tag{3.13}$$

$$K_v \frac{\partial v}{\partial z} = \frac{\tau_b^y}{\rho_o}(x, y, t) \tag{3.14}$$

- vertical thermal and salt fluxes at the seafloor (which is non-existent):

$$K_T \frac{\partial T}{\partial z} = 0 \tag{3.15}$$

$$K_S \frac{\partial S}{\partial z} = 0 \tag{3.16}$$

- non-crossing of the topography by the flow at seafloor:

$$-w + \vec{v}.\nabla uH = 0 \tag{3.17}$$

The surface wind stress components are given by:

$$\tau_s^x = \rho_{air} C_D \sqrt{u_{10}^2 + v_{10}^2}.u_{10} \tag{3.18}$$

and

$$\tau_s^y = \rho_{air} C_D \sqrt{u_{10}^2 + v_{10}^2}.v_{10} \tag{3.19}$$

The bottom stress is parameterized by a choice between linear, quadratic, or logarithmic terms [*Hedström*, 2009]. Bottom friction is established as:

$$\tau_b^x = (\gamma_1 + \gamma_2\sqrt{u^2 + v^2}).u \tag{3.20}$$

and

$$\tau_b^y = (\gamma_1 + \gamma_2\sqrt{u^2 + v^2}).v \tag{3.21}$$

In the above equations:

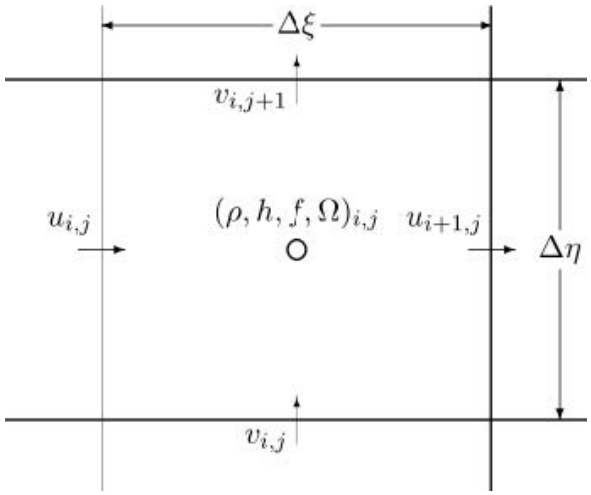
- x,y,z - are the zonal, meridional and vertical directions (m) in the Cartesian coordinate system.
- u,v,w - are the components of the vector velocity $\vec{v}$ (m s^{-1}) in x,y,z respectively.
- t - is the time in seconds (s).
- f - is the Coriolis parameter (s^{-1}).
- ϕ - is the dynamic pressure (m^2 s^{-2}).
- F_u, F_v, F_T, F_S - are the possible forcings terms.
- D_u, D_v, D_T, D_S - are the dissipative terms.
- T - is the potential temperature (°C).
- S - is the salinity (psu)
- $\vec{g}$ - is the acceleration of gravity (m s^2).
- ρ - is the seawater density (kg m^{-3}).
- ρ_o - is the mean seawater density (kg m^{-3}).
- P - is the total pressure (N m^{-2} or Kg m^{-2}).
- ζ - is the sea surface variation (m).
- τ_s^x, τ_s^y - are the surface wind stress (N m^{-2}), in x and y directions respectively.
- τ_b^x, τ_b^y - are the bottom wind stress (N m^{-2}), in x and y directions respectively.
- Q_T - is the surface heat flux (W m^{-2}).
- K_v - is the coefficient of vertical eddy viscosity (m^2 s^{-1}).
- K_T, K_S - are coefficients of vertical eddy diffusivity (m^2 s^{-1}).
- E_r - is the evaporation rate (cm day^{-1}).

- P_r - is the precipitation rate (cm day^{-1}).
- C_p - is the heat capacity of seawater (J kg^{-1} °C).
- H - is the total ocean depth (m).
- u_{10}, v_{10} - are the horizontal components of the wind vector in x and y respectively, measured at 10 m above sea level.
- C_D - is a non-dimensional wind-drag coefficient.
- ρ_{air} - is the density of atmospheric air (kg m^{-3}).
- γ_1 - is the coefficient of linear bottom friction.
- γ_2 - is the coefficient of quadratic bottom friction.

- **Time and space discretization**

ROMS is a free surface model and hence uses a split-explicit time-stepping method to solve the hydrostatic primitive equations for momentum with barotropic (slow) and baroclinic (fast) modes [*Shchepetkin and McWilliams*, 2005]. The barotropic mode includes the barotropic momentum and equation of continuity whereas the baroclinic mode includes the baroclinic momentum and the tracer equations. The free-surface and the vertically integrated momentum equations are advanced using a finite number of barotropic time steps within each baroclinic step. Barotropic terms are time averaged first, and the values are then replaced with longer baroclinic step. This is performed to overcome errors which are associated with the aliasing of frequencies resolved by the barotropic steps but unresolved by the baroclinic step [*Shchepetkin and McWilliams*, 2005]. Thus, ROMS uses large time steps to compute temperature, salinity and baroclinic momentum, but smaller time steps for surface elevation and barotropic momentum. The barotropic model satisfying the 3D continuity equation is performed using a special 2-way time-averaging. For the baroclinic mode discretization, a third-order predictor Leap Frog step, together with an Adams-Molton corrector time-stepping algoritm is used. A substantial increase in the permissible time-step size is allowed through this algorithm [*Shchepetkin and McWilliams*, 2005].

In the horizontal, the Arakawa-C grid [*Arakawa and Lamb*, 1977] is used on which the equations of motion are discretized. Having a characteristic variable-placement scheme, this grid is well suited for problems with a horizontal resolution finer than the first Rossby radius of deformation [*Hedstrom*, 1997]. In Figure 3.1, ρ, h, f and ω are defined in the centre of the grid cell whereas u and v are defined in centres of the respective south/north and east/west cell boundaries, seperated from the grid-centre by half a grid cell. The tracer properties (temperature and salinity), as well as sea surface height, γ, are defined at ρ points.



.

Figure. 3.1 Horizontal distribution of variable points on a staggered Arakawa C-grid [From *Hedstrom* [1997]]

The vertical levels of the Arakawa-C grid are also staggered, as seen in Figure 3.2. The vertical velocity (w) is calculated at the bottom in the centre of the cell, as can be observed in Figure 3.2.

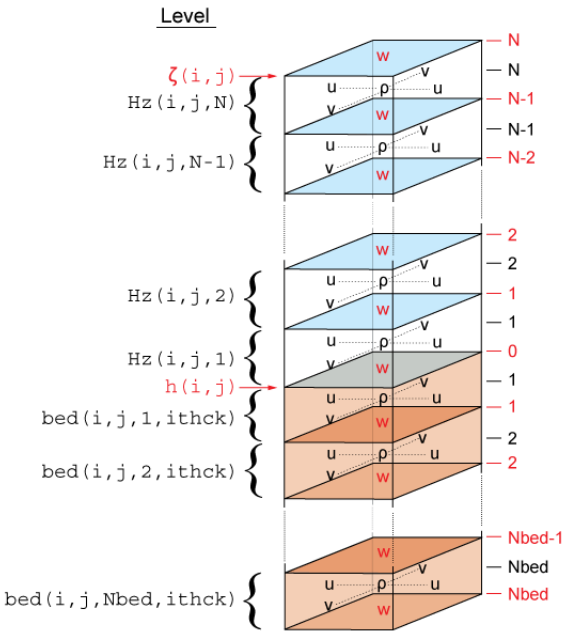


Figure. 3.2 Vertical distribution of variable points on a staggered Arakawa C-grid (From www.myroms.org)

In the vertical, ROMS uses a stretched, terrain-following, σ-coordinate, which improves the representation of the topography, allowing an increase in vertical resolution at the continental shelves [*Song and Haidvogel*, 1994]. The use of this σ-coordinate system implies that the depth of the ocean at all points can be transformed such that:

$$z = z(x, y, \sigma) \tag{3.22}$$

z represents the ocean depth with σ showing the fractional depth of the water column. Following the methodology described in *Song and Haidvogel* [1994], the vertical levels are non-linearly distributed throughout the water column (Figure 3.3). By changing the parameters of θ_b and θ_s, which are set to 0 and 5.5 in this study, respectively, the levels' distribution can be stretched to favour level-density increases near the surface or in the bottom layers. However, in regions of strong slopes and large density gradients, models with σ-coordinates can introduce errors which are related to the discretization of the horizontal pressure gradient. *Shchepetkin* [2003] designed a pressure-gradient algorithm which do not lose as much accuracy with the non-uniform vertical grid. Here,

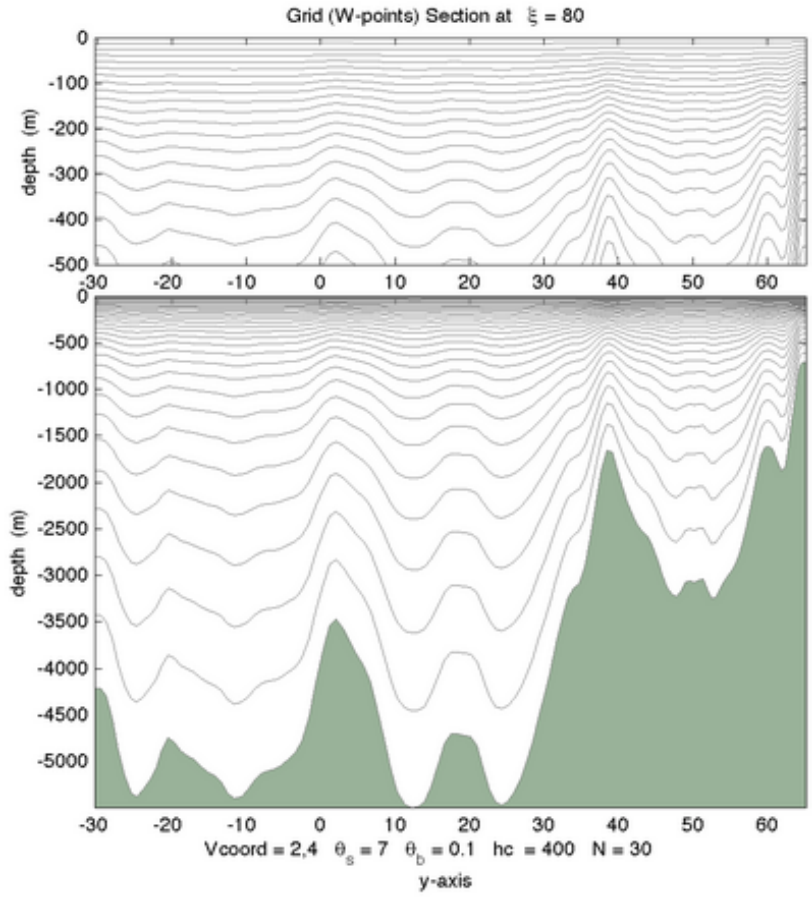


Figure. 3.3 Vertical σ-coordinate system approach in ROMS. [From www.myroms.org]

we use the σ-coordinate version from *Song and Haidvogel* [1994] instead of the most recent one [*Shchepetkin and McWilliams*, 2009].

- **Turbulent closure**

The parameterization of the vertical mixing processes in ROMS is done via a non-local, K-profile planetary (KPP) boundary layer scheme [*Large et al.*, 1994]. Two distinct parameterizations are conducted: one for the ocean interior and one for the oceanic surface boundary layer. The boundary layer depth (h) depends on the surface forcing, the buoyancy and the velocity profile. It is determined by equating a bulk Richardson number relative to the surface to a critical value. Below the boundary layer, the vertical

mixing is regarded as the superposition of three processes: vertical shear, internal wave breaking, and double diffusion. In the surface layer, the diffusivity is formulated to agree with similarity theory of turbulence. At the base of the surface layer, both diffusivity and its gradient have to match the interior values. A non-local convective transport is added to the local down-gradient component. The KPP model has been shown to simulate accurately processes such as convective boundary layer deepening, diurnal cycling and storm forcing.

3.3 Pelagic Interaction Scheme for Carbon and Ecosystem Studies - PISCES

3.3.1 Motivation

CROCO was coupled with the biogeochemical component namely PISCES [*Aumont and Bopp*, 2006]. The choice of PISCES was made as it is an established model that has been used previously in successfully studying the biophysical interactions in the Indian Ocean [*Dilmahamod et al.*, 2016; *José et al.*, 2014, 2016; *Koné et al.*, 2009; *Lévy et al.*, 2007], although it has been coupled with other ocean general circulation model in some of these studies. However, even though nitrogen-fixers might play an important role in the South-East Madagascar Bloom [*Longhurst*, 2001; *Poulton et al.*, 2009; *Srokosz and Quartly*, 2013], the choice of PISCES was made as other biophysical processes apart from nitrogen-fixation might also contribute towards the bloom, and need to be understood. An up-to-date version of PISCES with nitrogen-fixers incorporated was not available at the moment of the study. Other more complex biogeochemical models, for example the HAMburg Ocean Carbon Cycle model (HAMOCC), includes nitrogen-fixers, but is constrained by a possible interface with CROCO and computational costs. On the other hand, a simpler model such as the Nutrients-Phytoplankton-Zooplankton-

Detritus (NPZD) model was not chosen as it has not been used in the South-West Indian Ocean and its ability to correctly resolve the processes in this region is not known yet. It should be noted that the parameterizations in PISCES for this study have been left as default.

3.3.2 Model Description

PISCES was developed to simulate the biological productivity of the ocean, and the associated biogeochemical cycles of carbon and main nutrients [*Aumont and Bopp*, 2006]. Derived from the 5^{th} version of HAMOCC [*Aumont et al.*, 2003], it was built on the assumption that phytoplankton growth is directly restricted by nutrients availability [*Monod*, 1942]. A detailed description of the PISCES model parameterization is described by *Aumont and Bopp* [2006].

PISCES has twenty-four compartments, as seen in Figure 3.4, with four living parts which consist of two phytoplankton size classes which correspond to nanophytoplankton and diatoms; and two zooplankton size classes namely microzooplankton and mesozooplankton. Five modeled limiting nutrients are also present for phytoplankton growth namely Nitrate (NO_3), Ammonium (NH_4), Phosphate (PO_4), Silicate (Si) and Iron (Fe). The molar ratio of carbon to nitrogen to phosphorous, known as the Redfield ratio, is assumed constant, both in the living and non-living components.

- **Phytoplankton and zooplankton dynamics**

Light, temperature and nutrient availability in the water column dictates the growth of phytoplankton cells [*Geider et al.*, 1998; *Sarmiento*, 2013; *Valiela*, 2013]. Phytoplankton take nutrients from the environment and, together with light as a source of energy,

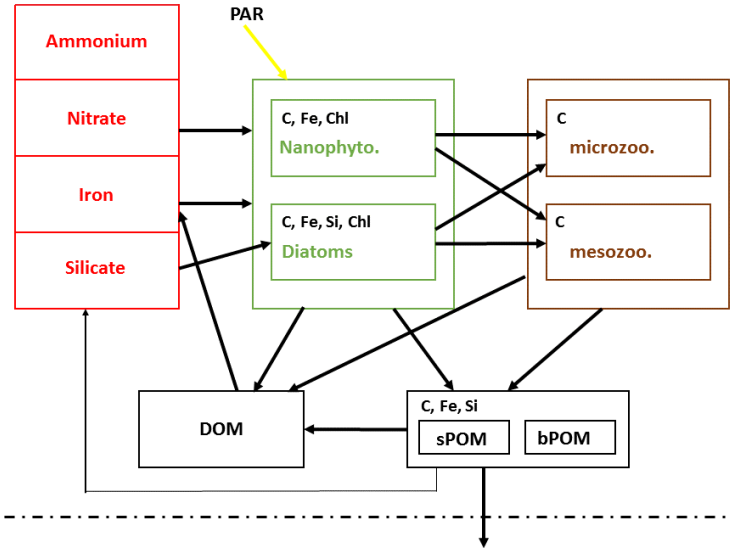


Figure. 3.4 Architecture of PISCES model. C represents carbon, Chl is for chlorophyll, DOM is Dissolved Organic Matter, POM indicates Particulate Organic Matter in big and small forms. From *Aumont and Bopp* [2006].

convert dissolved carbon dioxide to organic matter, a process known as photosynthesis [*Valiela*, 2013]. Temperature influences the process of photosynthesis and controls the uptake rate of nitrogen assimilation [*Geider et al.*, 1998]. Mortality is another fundamental process to phytoplankton productivity and distribution. Mortality includes grazing by zooplankton, death and sinking [*Geider et al.*, 1998; *Sarmiento*, 2013; *Valiela*, 2013]. In PISCES, phytoplankton dynamics are simulated as follows:

$$\frac{\partial P}{\partial t} = (1-\delta^P)\mu^P P - m^P \frac{P}{K_P + P} P - \omega_p^P P^2 - g^Z(P)Z - g^M(P)M \qquad (3.23)$$

where P represents phytoplankton size classes, μ^P is the production rate, δ is respiration rate, m^P is mortality rate, ${\omega_p}^P$ is the aggregation term, K_p is half saturation constant for mortality, grazing of phytoplankton by micro (Z, g^Z) and meso (M, g^M)-zooplankton.

The production rate is controlled by light intensity, temperature and nutrients and is simulated as:

$$\mu^P = \mu_P(1 - e^{\frac{\alpha^P(\frac{Chl}{C})PAR}{\mu_P L^P_{lim}}})L^P_{lim} \tag{3.24}$$

where μ_P represents the growth rate, which is a function of temperature (T) and is given by $\mu_P = \mathrm{ab}^{(c.T)}$. The variables a, b and c are constants for growth rate at 0°C (a), temperature sensitivity of growth (b) and temperature dependence of growth (c); α^P is the slope between photosynthesis and irradiance; $\frac{Chl}{C}$ indicates the balance between light absorption and photosynthetic carbon fixation (C); PAR is photosynthetically available radiation and $\mathrm{L}_{lim}{}^P$ is the nutrient limitation term [*Aumont and Bopp*, 2006].

Phytoplankton is known to be limited by several nutrients. Equation 3.25 and equation 3.26 defined the nutrient limitation terms for nanophytoplankton and diatoms, respectively, as follows:

$$L^P_{lim} = min(L^P_{PO_4}, L^P_{Fe}, L^P_{NO_3} + L^P_{NH_4}) \tag{3.25}$$

$$L^P_{lim} = min(L^P_{PO_4}, L^P_{Fe}, L^P_{NO_3} + L^P_{NH_4}, L^P_{Si}) \tag{3.26}$$

$$L^P_{PO_4} = \frac{PO_4}{K_{PO_4} + PO_4} \tag{3.27}$$

$$L^P_{Fe} = \frac{Fe}{K^P_{Fe} + Fe} \tag{3.28}$$

$$L^P_{NO_3} = \frac{K_{NH_4}NO_3}{K_{NO_3}K_{NH_4} + K_{NH_4}NO_3 + K_{NO3}NH_4} \tag{3.29}$$

$$L^P_{NH_4} = \frac{K_{NO_3}NH_4}{K_{NO_3}K_{NH_4} + K_{NH_4}NO_3 + K_{NO3}NH_4} \tag{3.30}$$

$$L_{Si}^{P} = \frac{Si}{K_{Si}^{P} + Si} \tag{3.31}$$

where K_{PO_4}, K_{Fe}, K_{NH_4}, K_{NO_3} and K_{Si} are the half-saturation constants for nutrient uptake by phytoplankton. In PISCES, diatoms differ from nanophytoplankton by their growth limitation by silicate, as well as their higher half-saturation constants for nitrate and iron uptake. They also exhibit different grazing patterns and sinking properties.

Zooplankton depend on the organic matter produced by phytoplankton [*Valiela*, 2013]. Thus, phytoplankton availability and particulate organic matter (POC) determine zooplankton growth. Their growth is also limited by predation by larger organisms and mortality. Microzooplankton have a higher preference for grazing on nanophytoplankton compared with mesozooplankton. However, microzooplankton depends on phytoplankton and small POC (POC_s) unlike mesozooplankton which can graze on both small and big POC (POC_b), as well as on phytoplankton and microzooplankton [*Bopp et al.*, 2005]. The dynamics of microzooplankton is as follows:

$$\frac{\partial Z}{\partial t} = \in_Z (g^Z(P) + g^Z(D) + g^Z(POC_s))Z - r^Z \frac{Z}{K_Z + Z} Z - g^M(Z) \tag{3.32}$$

where Z is zooplankton, P is nanophytoplankton and D is diatoms. The first term on the right hand side represents the production of zooplankton, the second term is the loss from zooplankton by excretion and the third shows grazing by mesozooplankton. K_Z represents the half-saturation constant for microzooplankton mortality and $\in_Z$ shows the efficiency of microzooplankton growth.

$$\frac{\partial M}{\partial t} = \in_M (g^M(P) + g^M(D) + g^M(POC_s) + g^M(POC_b))M - r^M \frac{M}{K_M +} M - m^M M^2 \tag{3.33}$$

Equation 3.33 detailed the production terms which include the grazing of microzooplankton and big POC by mesozooplankton ($g^M(Z)$) and the predation mortality closure term is given by $m^M M^2$. K_Z is the half saturation constant for mesozooplankton mortality and $\in_M$ represents the efficiency of mesozooplankton growth.

- **Organic matter and nutrient dynamics**

In PISCES model, semi-labile dissolved organic matter, small and big sinking particles form part of the non-living component. The export of dissolved organic matter is done on a time-scale of several weeks to several years. The sinking speed of particles differentiate small from large particles. The sinking speed of the large particle (POC_b) is higher than small particle, varying between 50 m d^{-1} and 200 m d^{-1}. The small particle (POC_s) exhibits slower sinking speeds at about 3 m d^{-1}.

Various nutrient sources are represented in PISCES. These include river discharge, sediment mobilization and atmospheric dust deposition. River discharges of dissolved organic and inorganic carbon (DOC and DIC) are used to obtain Fe, PO_4, NO_3, Si, and C land runoffs by the $Fe/P/N/Si/C$ ratios in the river [*Tagliabue et al.*, 2009]. However, even though the are parameterized in PISCES, they are not included in our configuration as noted in section 3.4. Atmospheric dust deposition contributes to the particulate inorganic iron (FE) distribution, in which Fe is assumed to be 3.5% of the dust [*Tagliabue et al.*, 2009]. Another source of Fe is sediment mobilization [*Aumont and Bopp*, 2006; *Tagliabue et al.*, 2009].

3.4 South-West Indian Ocean (SWIO) CROCO-PISCES configuration

3.4.1 Regional Simulation

The SWIO configuration has been specifically designed to investigate the biophysical processes associated to the South-East Madagascar Bloom. Based on the CROCO version of ROMS, the configuration was coupled to PISCES. It was built using ROMSTOOLS [*Penven et al.*, 2008], and the ROMS-AGRIF two-way embedding procedure was employed to nest a small, high-resolution domain (child domain) within a larger, lower-resolution domain (parent domain; see Figure 3.5). This technique allows the possibility of resolving higher resolution processes of a child domain within reasonable computational costs [*Debreu and Blayo*, 2008; *Debreu et al.*, 2012].

The geographical domain was largely extended further west (0°E) to enclose the main oceanographic features of the Indian ocean namely the greater Agulhas System and the major part of the subtropical gyre of the South Indian Ocean. The parent domain extends from 0°E to 100.25°E and 5.5°S to 47°S (Figure 3.5), with a horizontal resolution of $\frac{1}{4}°$ (∼28 km). The child domain is located from 38.6°E to 80°E and 18°S to 32°S (Figure 3.5), with a horizontal resolution of $\frac{1}{12}°$ (∼9 km). The Madagascar Basin is a region of enhanced Eddy Kinetic Energy (EKE) [*De Ruijter et al.*, 2005; *Halo et al.*, 2014a; *Quartly et al.*, 2006]. With cyclonic and anticyclonic eddies having mean diameters of 139 km and 154 km, respectively, the resolution in the child domain was sufficient to resolve them. [*Halo et al.*, 2014a]. The topography used in this configuration was from the high-resolution 1‘ gridded 2014 version of GEBCO dataset (General Bathymetric Chart of the Oceans: www.gebco.net). To prevent horizontal pressure gradient errors, a smoothing was applied so as to maintain the topographic slope parameter (r) less than 0.2 [*Beckmann and Haidvogel*, 1993].

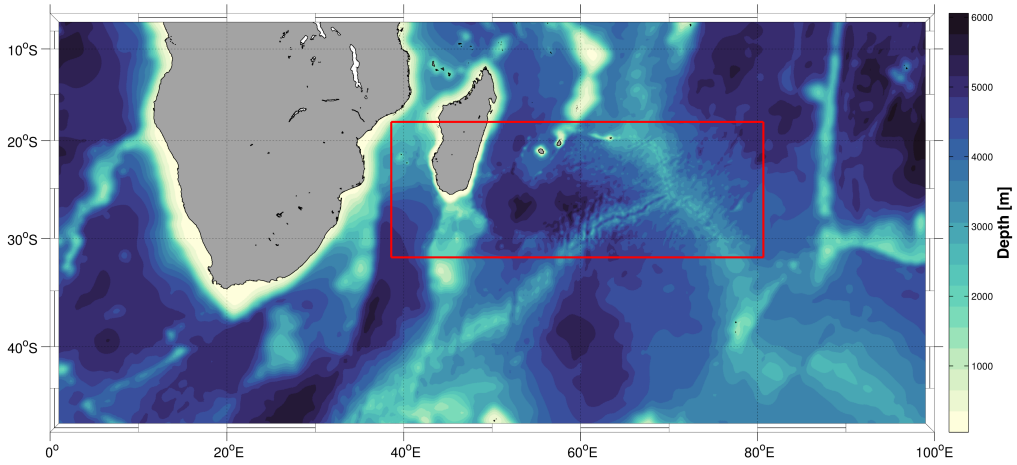


Figure. 3.5 The extension of SWIO child domain (red box), embedded into the parent domain. The bathymetry (m) of the parent and child domains are shown in color. The average resolution over the South-East Madagascar Bloom (child domain) is ∼9 km.

The vertical resolution, in σ-coordinate, consisted of 45 levels, and the following values of surface, bottom and minimum depth-stretching parameters: θ_s=5.5 for the sea surface, θ_b=0 for the bottom, and h_c=10 m [*Beckmann and Haidvogel*, 1993]. This allowed a minimum vertical resolution at the surface of about 0.2 m for a better representation of the upper layer processes.

3.4.2 Surface forcing

The surface layers of SWIO are forced using an online interpolation, using daily means of ECMWF Re-Analysis (ERA-Interim) data [*Dee et al.*, 2011]. This product is a global climate reanalysis from 1979 to date, and which is updated in near real-time. It is produced using a data assimilation system, based on a 2006 release of the Integrated Forecast System (IFS). The variables of interest for SWIO include the 2-meters air temperature, specific humidity, precipitation rate, short wave radiation, downward long wave radiation and wind components at 10 m (U10 and V10), used to force a bulk formula by *Fairall et al.* [1996]. These have a spatial resolution 0.75° (∼83 km). For the biogeochemical component, PISCES, monthly climatological maps [*Tegen and Fung*, 1995] were used to estimate atmospheric dust deposition. Note that river runoff

discharges are not represented in this configuration, so as to prevent an over-estimation of nitrate and phytoplankton concentrations (see section 3.5.2). However, the impacts of river discharges on the South-East Madagascar Bloom can be tested in further studies.

3.4.3 Lateral boundaries and initial conditions

The SWIO configuration, based on CROCO-PISCES, has its four boundaries (East, North, West and South) opened, and was forced with its physical and biogeochemical properties from non-assimilated Global Ocean Reanalysis (GLORYS) data. Carried out in the framework of the European Copernicus Marine Environment Monitoring Service (CMEMS), GLORYS produces and distributes global ocean reanalysis at eddy-permitting ($\frac{1}{4}^\circ$) resolution. This choice was made as the physical component of the non-assimilated GLORYS version includes a corresponding biogeochemical component. Hence, SWIO is forced with consistent physical and biogeochemical variables. Assimilated runs of the physical component could not be employed here as it is known to cause large instabilities in the biogeochemical model.

For lateral forcings, physical variables are obtained through the GLORYS2V3-FREE simulation, the non-assimilated run which is based on ORCA025 (code version: NEMO 3.1). GLORYS2V3 is forced at the surface with 3-hours ERA-Interim data and was initialized using temperature and salinity data from Levitus. With a horizontal resolution of $\frac{1}{4}^\circ$ ($\sim$28 km) and 75 z-coordinate levels, monthly averages of this dataset were used in this study, spanning from January 1993 to December 2014. The biogeochemical component of GLORYS2V3, namely BIOMER GLORYS2V3, was used as lateral forcings for the PISCES component of SWIO. Also a non-assimilated run, this configuration obtained its boundary conditions from daily-means of GLORYS2V3. It was run from 1992-2013, with a spin up of 6 years (1992-1997. Hence, BIOMER GLORYS2V3 was available from January 1993 to December 2013, at monthly averages and with a spatial resolution of $\frac{1}{4}^\circ$.

At these lateral boundaries, a mixed passive-active implicit radiation condition connects the SWIO configuration to the surrounding oceanic environment [*Marchesiello et al.*, 2001]. In case of an outflow conditions, the parent solution is allowed to escape the model domain whereas in an inflow case, the parent solution is nudged towards monthly averages of GLORYS2V3 and BIOMER GLORYS2V3. The parent domain provides the child domain with physical and biogeochemical forcings at the boundaries, and in return, the higher resolution child grid is used to update the parent model solution, through the two-way nesting [*Debreu et al.*, 2008, 2012].

3.4.4 Initialization

SWIO was initialized with GLORYS2V3 and BIOMER GLORYS2V3 prognostic variables. The first three years (1993-1995) of the two boundary forcings dataset were replicated on a time-frame of 1990-1992 and SWIO was then started using variables as from January 1990. The model was run for 24 years (1990-2013), in which the outputs were saved every 5 days. The model had to be limited to 2013 due to the availability of boundary conditions (GLORYS) up to 2013. In the parent domain, the integrated properties of the physical as well as the biogeochemical variables displayed stable conditions quite quickly (Figure 3.6). However, a slight drift can be observed in the volume averaged salt (Figure 3.6) and one of the possible reason for this could be the salt contribution from GLORYS and the absence of river discharges parameterizations in SWIO. However, this drift is of $\sim$0.02 psu which is not consequential.

Diagnostic analysis of both the physical (Figure 3.6) and the biogeochemical component (Figure 3.7) revealed a spin-up time of the simulation after the first 3 years. Hence, the evaluation of CROCO and PISCES will be performed over the 1993-2013 period. A similar time-frame (1993-2013) will be used to investigate the South-East Madagascar Bloom.

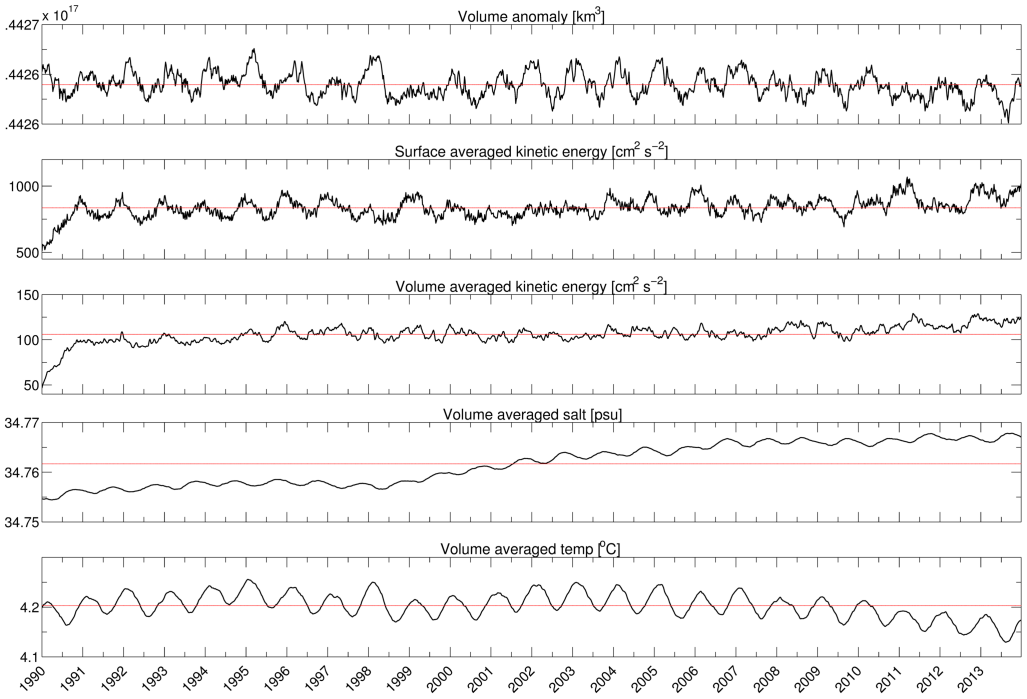


Figure. 3.6 Integrated volume properties, over the parent domain, of physical variables for the 24 years (1990-2013) of model run. The red line shows the mean over the 24 years.

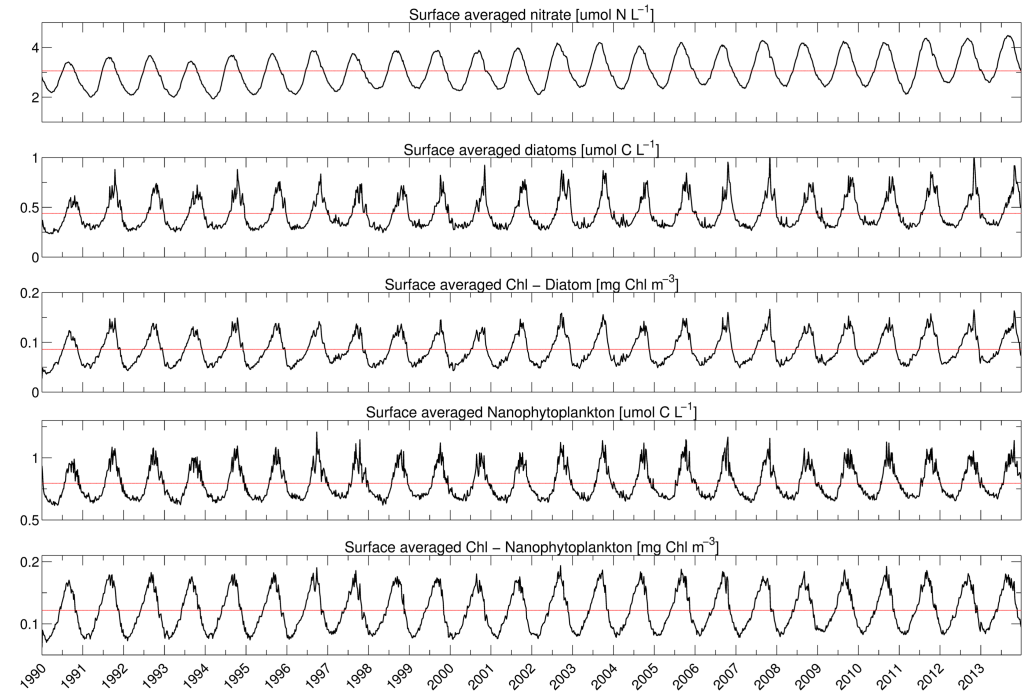


Figure. 3.7 Surface properties of biogeochemical variables, over the parent domain, for the 24 years (1990-2013) of model run. The red line shows the mean over the 24 years.

3.5 Assessing the South-West Indian Ocean (SWIO) configuration

3.5.1 Physical Properties

• Surface tracer distribution

This section analyses the surface and sub-surface tracers' distribution in the whole SWIO model's domain, with a particular focus on the regions around Madagascar. These tracers are influenced by three mechanisms which are the surface forcings applied to the configuration, corresponding tracers' signals from the boundary layers, and the physical processes on the ocean's surface and within the water column. The boundary forcings (GLORYS), playing a major role in governing surface and sub-surface tracers in SWIO, are also assessed during the comparison against remotely-sensed SST and salinity.

Comparison between observational datasets and SWIO (Figure 3.8) shows that the model adequately represents the SST pattern across the Indian Ocean basin. Two distinct features in the domain, which are the incoming warm Pacific Ocean water through the Indonesian Throughflow (ITF) in the eastern Indian Ocean, and the sharp SST gradient around 40°S which indicates the frontal zones of the northern frontier of the Antarctic Circumpolar Current (ACC), are well represented in both SWIO and GLORYS (Figure 3.8).

Much colder coastal waters on the western side of the African continent are indicative of the Benguela Upwelling System (BUS). SWIO under-estimates its intensity, hence inducing less cold water in the surface layer leading to an over-estimation of the SST. The resolution of the parent domain (1/4°) might not be suitable to resolve the local upwelling and mesoscale dynamics [*Penven et al.*, 2006b]. The 20°C thermal imprint of the Agulhas Current also seems to extend further west in SWIO, causing a warming

of the Benguela Current, hence possibly contributing to the over-estimation of SST in the system.

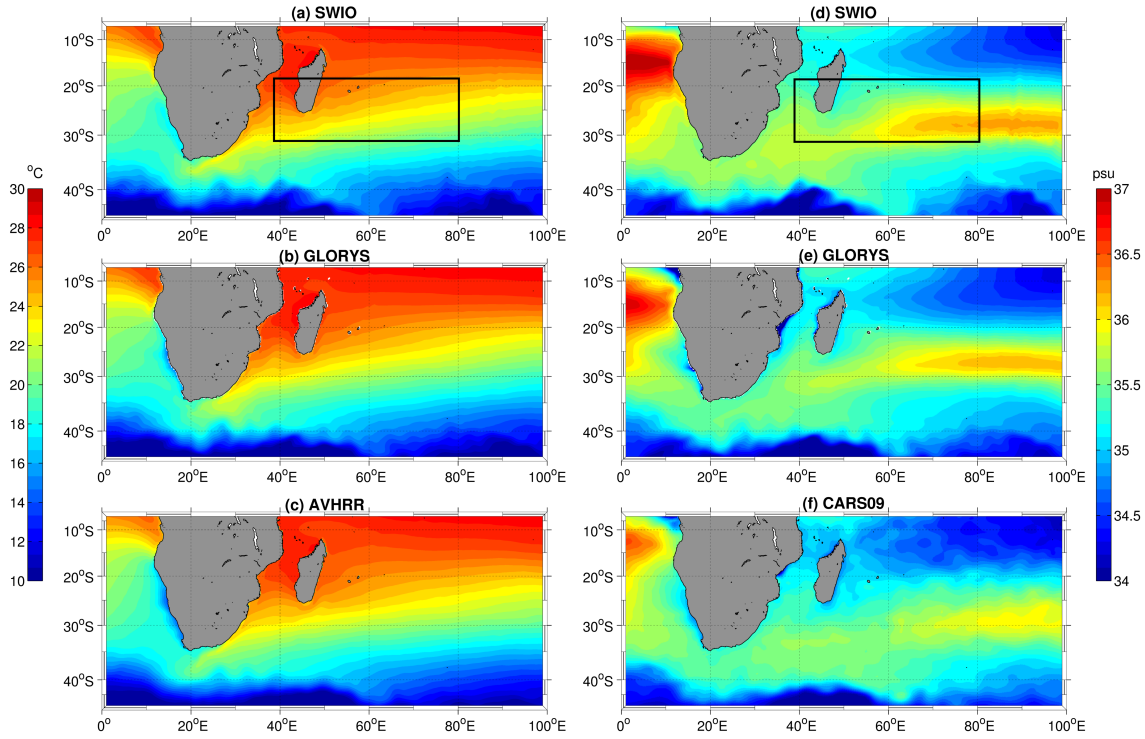


Figure. 3.8 Panels on the left (a, b, c) represent sea surface temperature values (°C), and those on the right sea surface salinities (psu) (d, e, f) for an annual climatology of the last 21 years of the analyzed run (1993-2013). Top panels portray SWIO outputs (a, e), mid panels GLORYS outputs (b, e), and bottom panels are from AVHRR (c) and CARS09 (f).

GLORYS indicates a colder SST in the tropical eastern Indian ocean (Figure 3.9a), when compared to AVHRR. This incoming colder SST signal, from the boundary conditions, is echoed in the model processes, but to a lesser extent, as can be observed in the difference of temperature between SWIO and observations (Figure 3.9b). The SST in the south western region of the Indian Ocean exhibits good agreement with observations, with an anomaly ranging from -0.5°C to 0.5°C, with a 0.5°C under-estimation on the south-eastern coast and southern tip of Madagascar.

Lower sea surface salinity is observed in the eastern Indian Ocean and south of 40°S (Figure 3.8), indicative of incoming ITF water in the Indian Ocean and the

northern extremity of the eastward flow of the ACC respectively. The inability of the parent's horizontal resolution to pick up mesoscale variability and local upwelling in the BUS induces more saline water in the system, compared to observations, as seen in Figure 3.8d and Figure 3.9d. Different factors, such as absence of river discharges, may be at play here to prevent the model from correctly resolving the surface salinity. The western boundary of the model, being quite close to the BUS, hinders the basin-wide adjustment processes, as well as the abnormal saline signal from GLORYS, which are echoed to the model domain. An important aspect of the configuration is the missing Congo River and Orange River, ending in the south-eastern Atlantic Ocean, which also contributes to the anomalously low patch of salinity in the BUS.

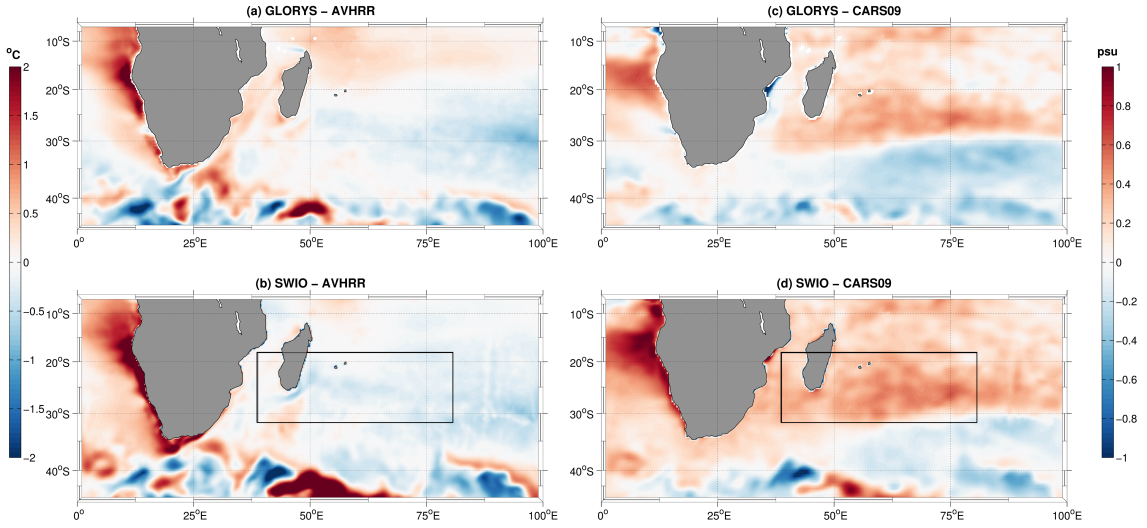


Figure. 3.9 The left column represents the difference in sea surface temperature (°C) between GLORYS and AVHHRR (a, top panel), and between SWIO and AVHRR (b, bottom panel). The right column displays the difference in sea surface salinity (psu) between GLORYS and CARS09 (c, top panel), and between SWIO and CARS09 (d, bottom panel).

While analysing the salinity panels in Figure 3.8d-f, it appears that the peculiar high salinity patch along the latitudinal band of 30°S in the tropical Indian Ocean in SWIO is the resonance of a similar but less intense patch observed in GLORYS. This over-estimation in the South-West Indian Ocean is confirmed in Figure 3.9c and Figure 3.9d, where it is seen to be more intense in SWIO than in GLORYS. Close to

the Madagascar coasts, the over-estimation of salinity is possibly due to the absence of river inputs from PISCES.

• **Subsurface tracer distribution**

The distribution of tracers along the vertical column is compared with observations along two defined transects as shown in Figure 4.21, a zonal transect A along 25°S (47.8°E-80°E) and a meridional transect B along 52°E (6°S-40°S). Figure 3.11 shows the comparison of SWIO, GLORYS and CARS09. The isotherms in SWIO and GLORYS are well represented when compared with CARS09, with temperatures being quite constant throughout the vertical levels from 60°E to 80°E. The 24°C isotherm extends further east in CARS09 compared to SWIO and GLORYS where it extends up to approximately 68°E. Near the coast at 47.8°E, the deepening followed by a shallowing of isotherms represents the signature of the East Madagascar Current (EMC), with high variability in the deeper layers near the coast in SWIO, due to its finer resolution of the child domain compared to the horizontal resolution of GLORYS ($\frac{1}{4}°$) and CARS09 ($\frac{1}{2}°$).

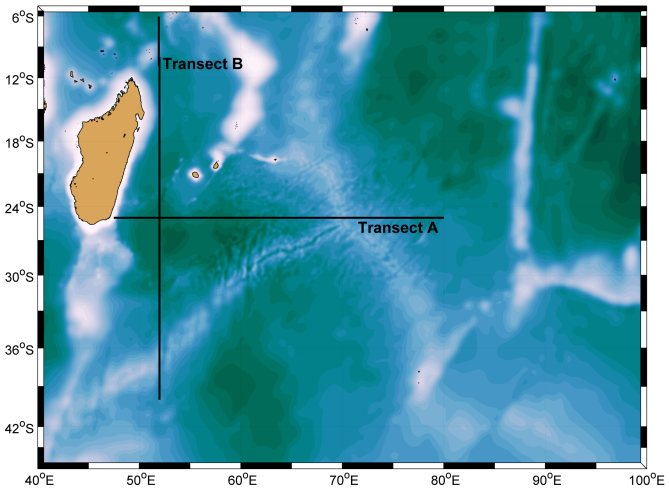


Figure. 3.10 Part of the model's domain indicating the locations of the two main transects: a zonal transect A and a meridional transect B.

Distribution of salt along the model water column, in comparison to temperature, shows greater variation when compared to observations. A distinct more saline signal, as observed in SSS, occurred on the eastern part of transect A in SWIO (Figure 3.11d), a signal which is also present in CARS09 (Figure 3.11f) but at a lower magnitude. This high salinity signal is related to the South Indian Central Waters (SICW). However, the bias in SWIO may be due to the result of a more significant SICW signal in the boundary conditions (GLORYS; Figure 3.11e). A disparity in salt concentration is perceived, close to the coast at 47.8°E in SWIO, with a positive bias of approximately 0.2 psu. In deeper layers of the model, the isohalines are, however, well represented.

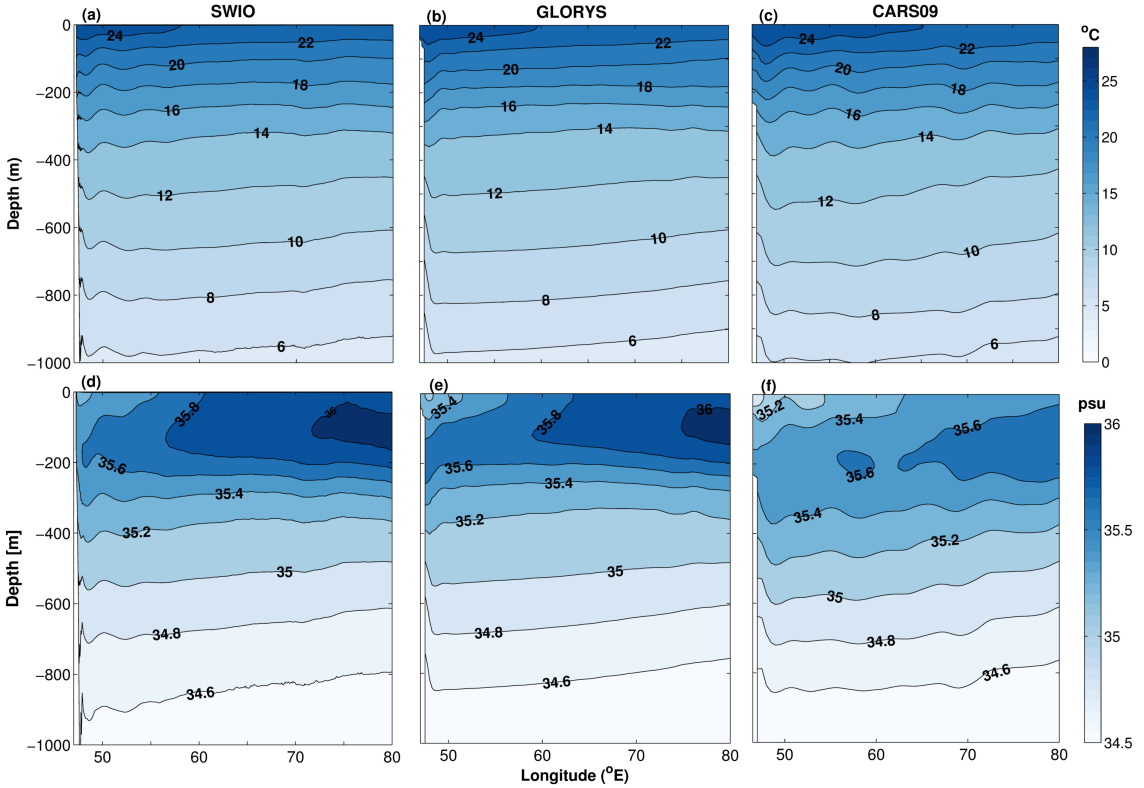


Figure. 3.11 Vertical distribution of temperature (°C) (a, b, c; first row) and salinity (psu) (d, e, f; second row) through the top 1000 m of transect A at 25°S. The first, second and third columns represent the tracers from SWIO, GLORYS and CARS09 respectively.

The density along the vertical water column, which is calculated from potential temperature and salinity fields using the sea water equation of state, $\rho = \rho(S,T,p)$ [*Jackett and Mcdougall*, 1995] is shown in Figure 3.12. The pattern of isopycnals

in SWIO is adequately consistent with CARS09, except close to the surface near Madagascar, where the signature of less dense river waters can be observed. In deeper layers, the isopycnals are largely-spaced, indicative of mixing processes.

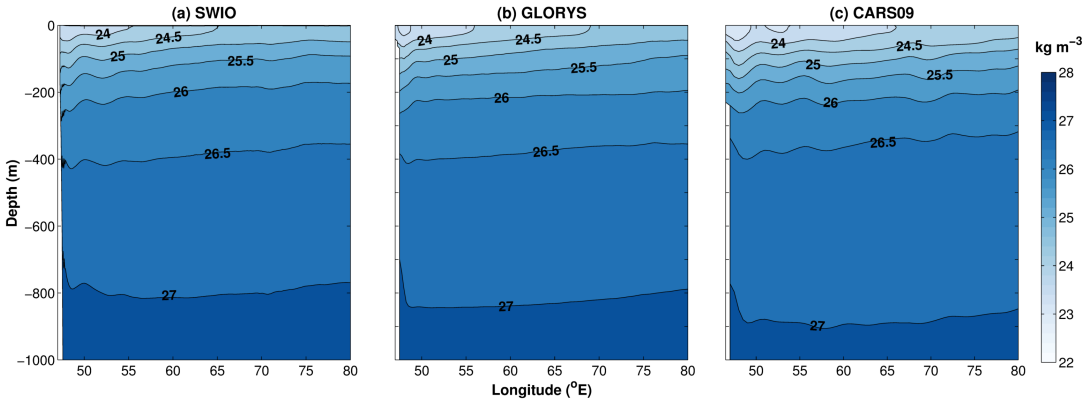


Figure. 3.12 Vertical distribution of density (Kg m^{-3}) along transect A (25°S)from (a) SWIO, (b) GLORYS, and (c) CARS09, respectively.

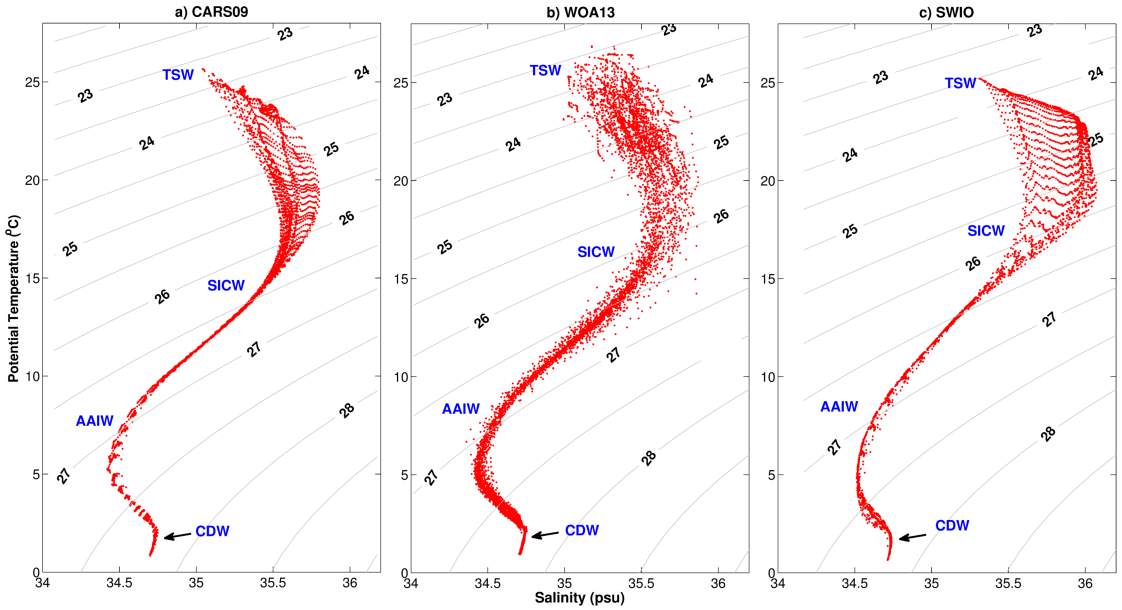


Figure. 3.13 Temperature-Salinity showing water mass properties along the horizontal transect A, spanning from 47.8°E to 80°E for (a) CARS09, (b) WOA13, and (c) SWIO.

The distribution of surface and sub-surface tracers, being quite well reproduced into the configuration means that the major water masses along the transects should also be

well reproduced (Figure 3.13). Circumpolar Deep Water (CDW; 0.1-2°C, 34.62-34.73 PSU) and Antarctic Intermediate Water (AAIW; 2-10°C, 33.8-34.8 PSU) penetrate in the deeper layers along transect A, with South Indian Central Water (SICW; 8-25°C, 34.6-35.8 PSU) dominating the sub-surface layer, and Tropical Surface Water (TSW; 24-30°C, 34.9-35.1 PSU) present in the surface layer, possibly due to the bifurcation of the South Equatorial Current (SEC) into the North-east Madagascar Current and South-East Madagascar Current (Figure 3.12 and Figure 3.13).

Along transect B, a longitudinal band at 52°E extending from latitudes 6°S to 40°S, heat dispersion throughout the vertical column shows great variability, compared to transect A. Overall, compared to observations, SWIO resolves well the isotherms. A maximum in near-surface temperature from 6°S to approximately 20°S(Figure 3.14a-c), possibly related to the TSW. The signature of TSW can also be perceived in the vertical distribution of salt in SWIO, exhibited as a low salinity (Figure 3.14d-f). From 6°S to 12°S, the thermocline deepens with the isotherms closely spaced. This is an indication of deep colder water being upwelling at the surface (Figure 3.14a-c). This specific latitudinal band is in the Seychelles-Chagos Thermocline Ridge (SCTR) [*Hermes and Reason*, 2008], an upwelling region in the South-West Indian Ocean. As from 20°S down to 40°S, the thermocline shoals, with the isotherms becoming largely-spaced.

In Figure 3.14d-f, the main feature is the high salinity tongue observed in SWIO and GLORYS, a feature less significant in CARS. This is indicative of salty Indian Ocean Subtropical Mode Water (IOSMW) which is present in the South Indian Ocean [*Tsubouchi et al.*, 2010; *Wong*, 2005]. The gradient meridional gradient shows the presence of fresh waters from the ITF in the north and highly-saline in the tongue south.

The comparison of isopycnals in Figure 3.15 highlights good agreement between the model and observations. Overall, in a north-south orientation, the isopycnals deepen and become more largely spaced, indicative of higher mixing as we move south.

The closely spaced isopycnals from 6°S to 30°S points to a high stratification of the water column in the first 200 m (Figure 3.15). The shallowing of the pycnocline close to 40°S in Figure 3.15c can be assigned to the Subtropical Surface Water (STSW), not observed in Figure 3.15a as it is found 1° further south in SWIO, but observed in GLORYS (Figure 3.15b) with a lower magnitude.

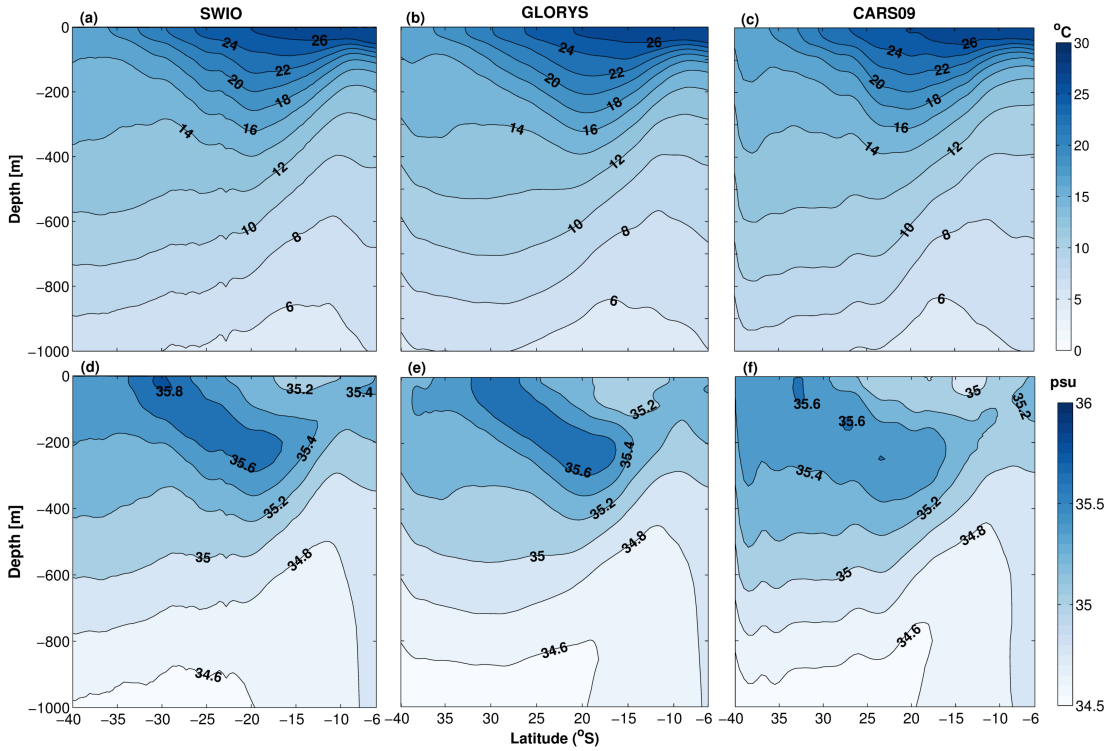


Figure. 3.14 Vertical distribution of temperature (°C) (a, b, c; first row) and salinity (psu) (d, e, f; second row) through the top 1000 m of transect B at 52°E. The first, second and third columns represent the tracers from SWIO, GLORYS and CARS09 respectively.

Similar to transect A, water masses along transect B (Figure 3.16) also exhibit CDW and AAIW in deeper layers, with SICW and TSW in sub-surface and surface layers respectively. Indian Equatorial Water (IEW; 8-23°C, 34.6-35 PSU) is also perfused in the region, owing to its proximity to the equator. An interesting feature is some evidence of Arabian Sea High Salinity Water (ASHSW) which may be occurring in the most northern part of the transect. This water has almost the same temperature as STW but is more saline due to the high evaporation rates in the Arabian Sea [*Tomczak and Godfrey*, 1994]. The consistency of T-S diagrams between SWIO and observations

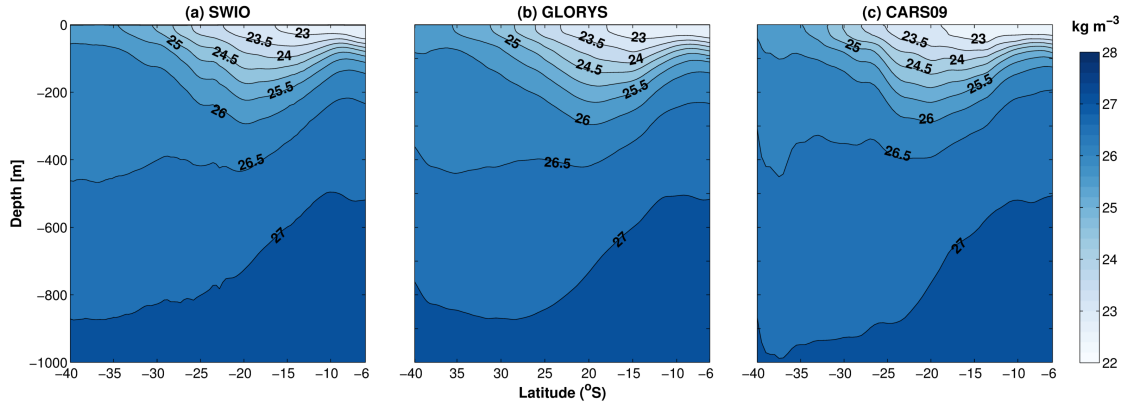


Figure. 3.15 Vertical distribution of density (Kg m^{-3}) along transect B (52°E) from (a) SWIO, (b) GLORYS, and (c) CARS09, respectively.

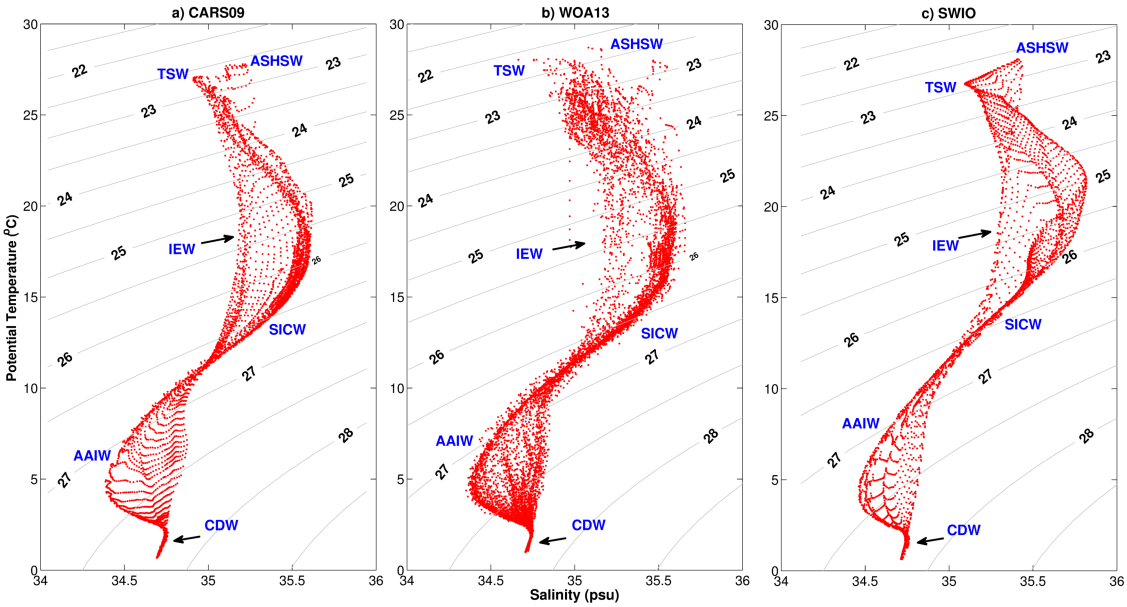


Figure. 3.16 Temperature-Salinity showing water mass properties along the vertical transect B, spanning from 6°S-40°S for (a) CARS09, (b) WOA13, and (c) SWIO.

(CARS09 and WOA13) along both transects demonstrates that the water masses are well-represented in the model. This is probably due to the rotated-diffusion operator which allow the preservation of low dispersion as well as diffusion capabilities, hence conservation of water mass properties [*Lemarié et al.*, 2012; *Marchesiello et al.*, 2009].

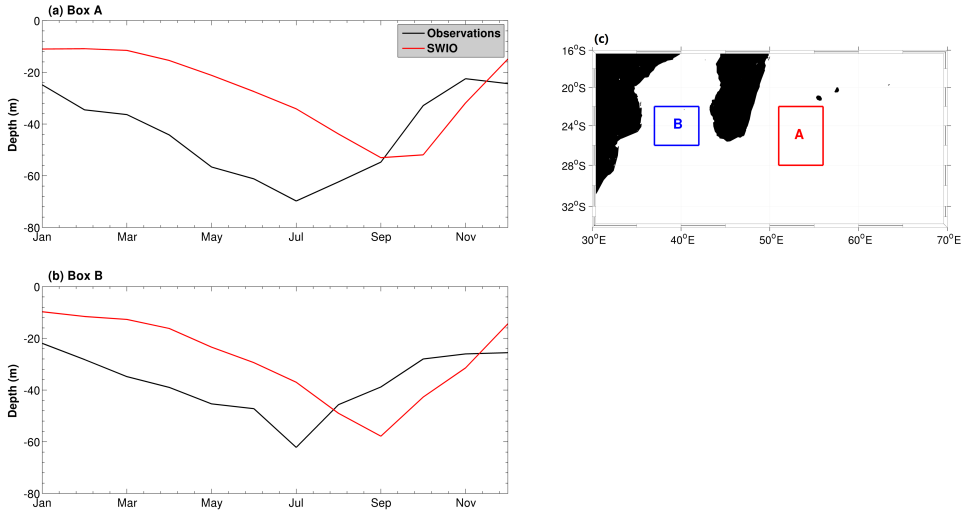


Figure. 3.17 Monthly climatology of mixed layer depth in (a) box A, representative of the bloom region, and (b) box B, representative of the Mozambique Channel region. (c) shows the location of boxes A and B.

The investigation of the mixed layer in the vicinity of the bloom region as well as in the Mozambique Channel reveals an out of phase deepening in austral winter, with the deepest being in July in observations whereas SWIO exhibits maximum depth in September. This out-of phase can be a resultant of a deviation in additional factors such as wind stirring, freshwater fluxes, heat advection, entrainment and mixing influence [**?**]. In austral summer, SWIO under-estimates the mixed layer depth by $\sim$ 10 meters, in both boxes A (Figure 3.17a) and B (Figure 3.17b). This remains the case till August, during which the observed mixed layer is shallower, till November.

- **Mesoscale variability and basin-wide flow circulation**

  A) Surface geostrophic flow and Eddy kinetic energy

SSH streamlines derived from 21 years (1993-2013) of SWIO is compared with remotely-sensed AVISO data. It should be noted that in Figure 3.18b, the EKE with SSH fields are plotted for the parent domain (0.25° resolution) with no child domain, whereas

in Figure 3.18c, the same fields are plotted for the two-way nested parent and child domains. The mean SSH suggests that large-scale circulation exhibited by SWIO is consistant with observations. The westward propagating SEC between 10°S and 20°S bifurcates east of Madagascar (around 18°S) to form the NEMC and SEMC. In the Mozambique Channel (MC), anti-cyclonic southward propagating eddies are observed, together with a southward flow close to the African coast.

On the south-eastern coast of Madagascar, compared to AVISO, the eastward flow, known as the South Indian Ocean Countercurrent (SICC) is shifted north in SWIO by approximately 2° (Figure 3.18b and Figure 3.18c). The termination regime of the SEMC exhibits a retroflection in the average and hence contributes to the SICC, a characteristic flow also observed in remotely-sensed AVISO data. However, a significant part of the extension of the SEMC south of Madagascar follows a westward course with a north-westward route also present in the model as well as observations.

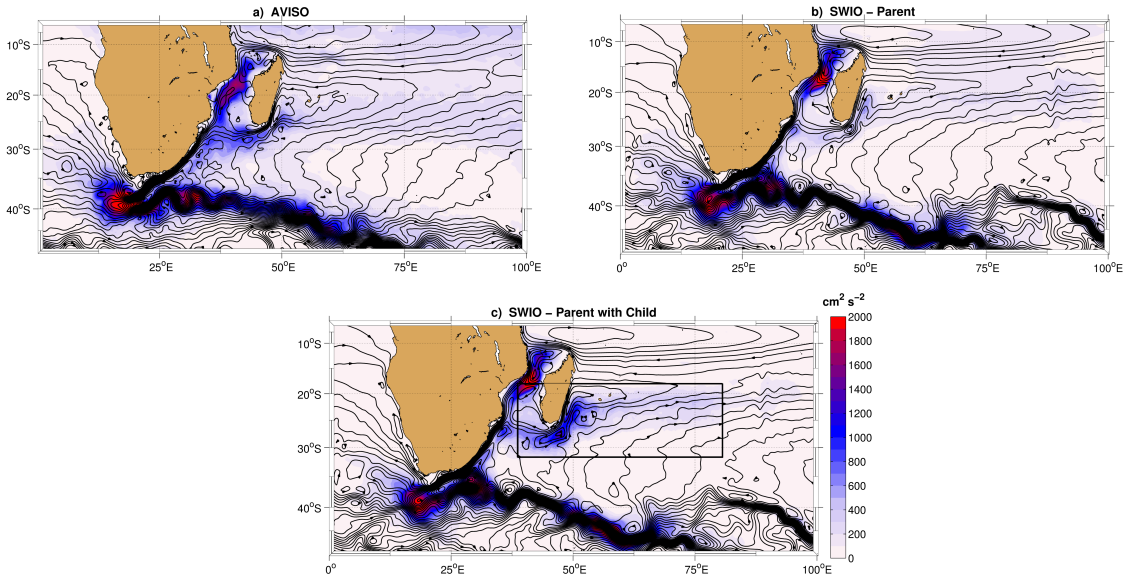


Figure. 3.18 Mean surface geostrophic eddy kinetic energy (EKE; $cm^2\ s^{-2}$) for the 1993-2013 period, derived from (a) AVISO, (b) SWIO without nesting effects and, (c) SWIO with nesting effects. Black contours show the analogous mean sea-surface height fields, with contours indicating 5 cm delineations of SSH.

The location of the Agulhas Retroflection can be observed at a more western point in SWIO, when compared to AVISO. The position of the Agulhas Return Current, which rejoins the Indian Ocean Gyre is, however, adequately resolved in the model from 35°E up to around 75°E where the current seems to reflect off the southern boundary of the configuration to create another intense flow from 75°E to 100°E. This discrepency might be due to the location of the southern boundary, being too close to the return current.

Figure 3.18 also displays the mean EKE from altimetry and SWIO over the same time period (1993-2013). The most significant energetic spot in the configuration's domain in AVISO and SWIO is the Agulhas Retroflection with an energy exceeding 2000 cm^2 s^{-2}. Overall, the EKE in the whole domain is under-estimated in SWIO, except in the Mozambique Channel (MZC), where SWIO exceeds the energy levels. *Halo et al.* [2014b] showed that ROMS produces larger eddies in the MZC and since more energy is present in larger eddies [*Eden*, 2007; *Mcwilliams*, 1985; *Stammer*, 1997], this could explain the higher EKE in MC.

An interesting comparison is presented here between the EKE from the parent domain (Figure 3.18b) and from the parent domain with the two-way nesting effects of the child domain (Figure 3.18c). The south-eastern part and southern part of Madagascar are regions of high mesoscale variability, owing to the mesoscale eddies from the east and the formation of dipoles at the termination regime of the EMC [*De Ruijter et al.*, 2004; *Siedler et al.*, 2009]. In Figure 3.18b, energy levels of westward propagating eddies from the western Australian coast are under-estimated as well as the EKE south-east of Madagascar. However, with the nesting effects (Figure 3.18c), energy associated to mesoscale eddies enhanced within the domain, causing an increase of energy. Therefore, the spatial distribution of turbulent flow is closer to that observed. This suggests that this region is predominantly influenced by mesoscale features which are not appropriately resolved at lower resolution and that a higher resolution configuration is

fundamental for in-depth studies of these regions.

A) Volume transport of main currents

The specific transects designating the location at which the mean volume transports across the main flow structures in the South-West Indian Ocean were computed, are indicated in Figure 3.19. For the SEC, the transect was established at 60°E on a 10°S-20°S zonal band. The SEC bifurcates to form the NEMC and the northern part of South-East Madagascar Current (SEMCn), whose transports were calculated at 49.5°E, 8°S-12°S and 23°S, 48°E-51°E respectively. Volume transport of the southern part of the SEMC known as SEMCs was calculated along 45°E over a zonal band between 25.6°S and 30°S which is over the Madagascar Ridge. On the south-eastern African coast, the transect for the Agulhas Current was established at 32°S, 29°E-32°E, following the transect of *Beal and Bryden* [1997]; *Donohue and Toole* [2003]. The volume transport of the SICC, shown to have shifted around 2° north (Figure 3.18), was calculated along a zonal band from 21°S to 23°S at 54°E.

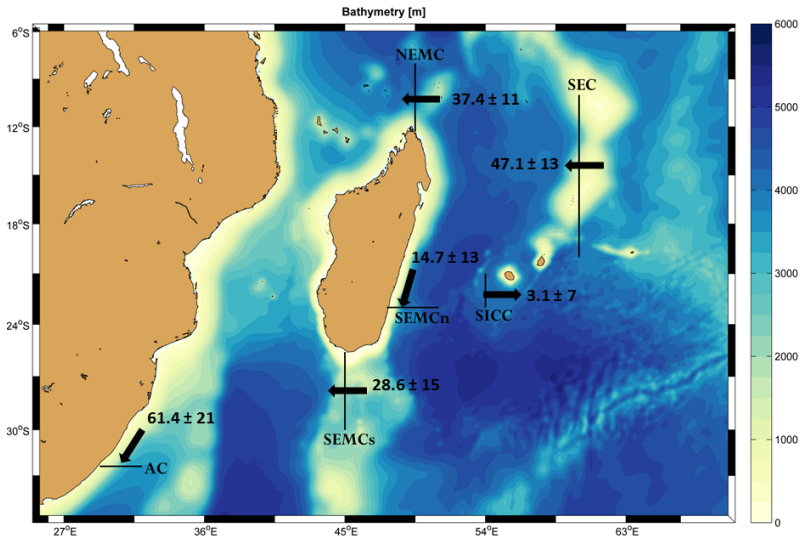


Figure. 3.19 Part of the model's domain indicating the locations of transects through which the volume transport of the main flows of the South-West Indian Ocean is calculated.

It must be noted that the volume transport was calculated by integrating the flow field structures across a 1500 m depth for all the main currents except for the SICC and AC, which were integrated over the upper 300 m and 2000 m depth. Positive values in Figure 3.20 are indicative of an eastward (northward) flow with a reversal flow to the west (south) showing negative values. The calculated volume transport in the upper 1500 m across the SEC presents a mean flow of 47.01 Sv westwards, with deviations of about 13 Sv (Figure 3.20a). This mean transport compares well with in-situ measurements, suggested to range between 40 Sv to 50 Sv [*New et al.*, 2007; *Schott and McCreary*, 2001]. The SEC displays high interannual variability with the flow varying mainly between 30 Sv and 60 Sv, reaching a maximum of approximately 77 Sv occurring during mid-2001 and mid-2013. The westward-flowing NEMC is estimated at 37.39 ± 11.06 Sv (Figure 3.20b), whereas the SEMCn transports 14.66 ± 13.1 Sv (Figure 3.20e) poleward, both in the upper 1500 m. The mean transport flow of SWIO over-estimates the NEMC in relation to hydrographic measurements which indicate transports of 30 Sv [*Schott and McCreary*, 2001; *Swallow et al.*, 1988] and, 26.9 Sv [*Schott et al.*, 1988]. In comparison to *in-situ* observations, which registered a flow of 20 Sv [*Donohue and Toole*, 2003; *Schott and McCreary*, 2001] and 18.3 ± 8.4 Sv [*Ponsoni et al.*, 2016]), the SEMCn is slightly under-estimated. Positive values of transport in SEMCn (Figure 3.20e) can be attributed to eddy-type disturbances in the flow field, a region known to be influenced by westward propagating eddies from the east [*Ponsoni et al.*, 2016; *Siedler et al.*, 2009], also observed in Figure 3.18.

At the southern tip of Madagascar, the average volume transport through the SEMCs transect is 28.56 Sv with a standard deviation of 15.4 Sv (Figure 3.20d). The flow varies mainly between 10 Sv and 60 Sv, with a maximum westward flow of 88 Sv in late 2004. The calculated mean transport of 28.56 Sv is in good agreement with the 32 Sv [*Nauw et al.*, 2008] and 29 Sv [*Donohue and Toole*, 2003] from hydrographic data. However, *Nauw et al.* [2008] presented a flow of approximately 52 Sv, which

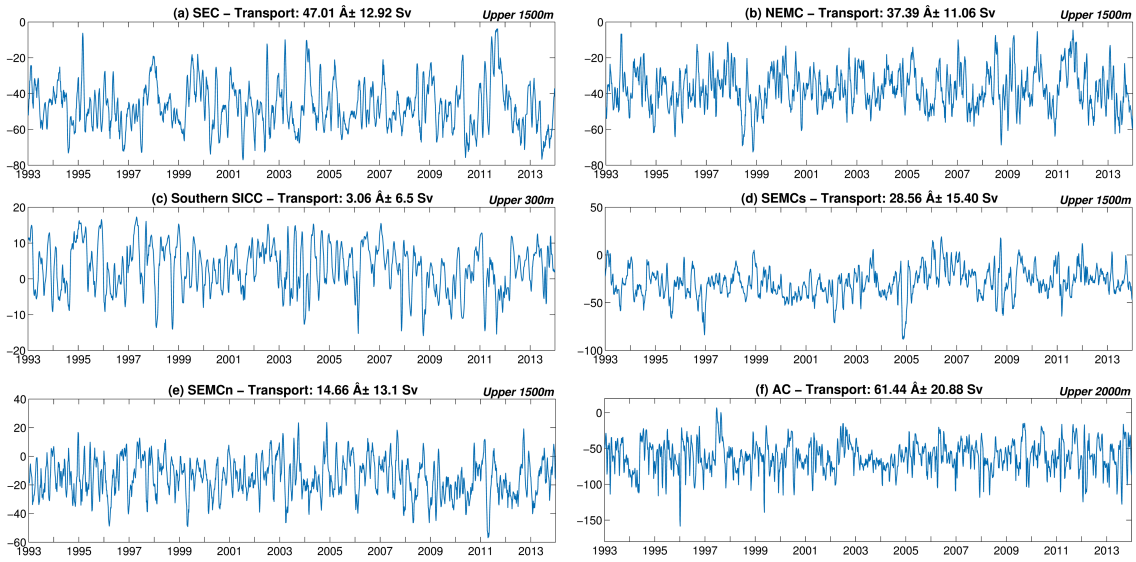


Figure. 3.20 Time series of volume transport calculated across the main South-West Indian Ocean's currents indicated in Figure 3.18 from 1993 to 2013. The mean transport and its standard deviation is given for each flow structure, as well as the depth of the water volume through which the transport is calculated.

they attributed to the eddy variability in the region and this could explain the two maximum westward peaks during early 1997 and late 2005. Reversal of transport (positive values in Figure 3.20d) can also be attributed to eddy flow in this highly energetic area, as can be shown in Figure 3.18.

On the south-eastern coast of Africa, the AC was estimated to have a southward mean transport of 61.44 Sv with deviations from the mean of about ± 20.88 Sv, in the upper 2000 m (Figure 3.20f). The flow varies mainly between 25 Sv and 125 Sv, with anomalous peaks during early 1996 and mid-1999. Volume transport agrees quite well with in-situ observations of 76 Sv [*Donohue and Toole*, 2003], 69.7 ± 4.3 Sv [*Beal and Bryden*, 1997] and 72 Sv [*Gründlingh*, 1987]. Small reversal of the mean flow (∼7 Sv in 1997) can be attributed to mesoscale eddy variability in this highly energetic area (Figure 3.18) [*Rouault and Penven*, 2011; *Rouault et al.*, 2010], as well as strong meandering of the flow [*Lutjeharms and Van Ballegooyen*, 1988]. The mean volume transport of the SICC, which was shown to have shifted approximately 2° north in

SWIO, presents an eastward flow of 2.93 ± 6.32 Sv from the 1/4° parent domain, and a flow of 3.06 ± 6.40 Sv from the 1/12° child domain. These values are consistent with the study of *Menezes et al.* [2014] who calculated a flow of 3-4 Sv from observational data, but are under-estimated when compared to the 10 Sv flow from *Siedler et al.* [2006]. Overall, SWIO does a fairly good job at reproducing the main oceanic currents in the region.

- **Interannual variability**

This section focuses on the comparison of SST interannual variability in the vicinity of the South-East Madagascar Bloom. The SST in a box (50°E-55°E; 24°S-28°S) located within the bloom region is investigated against remotely-sensed AVHRR data. The seasonal cycle, as well as the interannual variability of SST in the bloom region is very well represented by SWIO, with a maximum in austral summer and a minimum in austral winter (Figure 3.21). The most significant difference occurs in austral winter of 2009 where SWIO under-estimates the SST by ∼1°C.

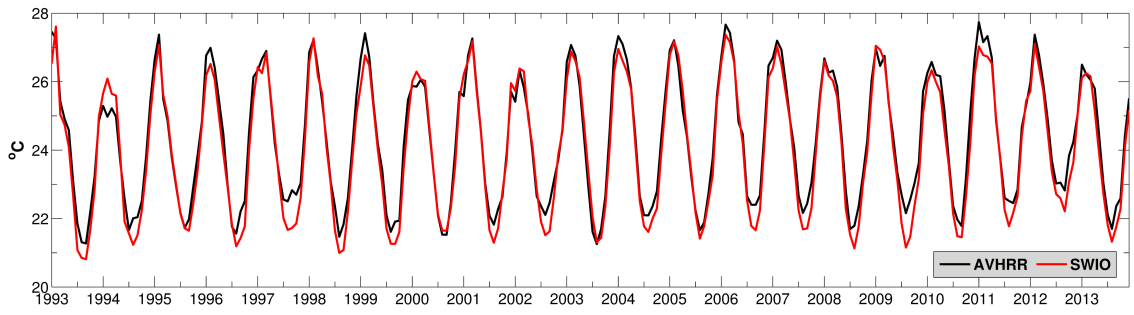


Figure. 3.21 Interannual variability of SST (°C) from AVHRR (black line) and SWIO (red line) in the South-East Madagascar Bloom region (50°E-55°E; 24°S-28°S)

Comparison with climate phenomenon indices indicates how well the large-scale pattern

is well reproduced in the model. Here, the SST is spatially and temporally investigated and expressed as the Subtropical Indian Ocean Dipole (SIOD) which is characterized by a difference of SST in the south-western Indian Ocean (55E°-65°E,37°S-27°S) and the eastern side (90°E-100°E,28°S-18°S) of the basin [*Behera and Yamagata*, 2001].

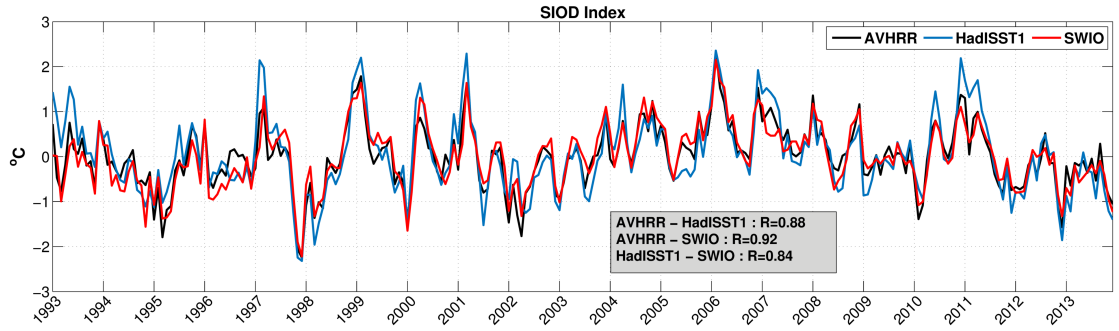


Figure. 3.22 Subtropical Indian Ocean Dipole (SIOD) indices, extracted from remotely-sensed AVHRR (Black line), HadISST (Blue) and the model SWIO (Red). The correlation was performed at a 99% significance level.

The SIOD time series from AVHRR and HadISST1 correlates well with that from SWIO (Figure 3.22), with a correlation coefficient of 0.92 and 0.84 respectively, at a 99% confidence level. The difference in correlation with the two different observational datasets might be due to the fact that HadISST1 is on a 1° latitude-longitude grid whereas AVHRR has been averaged on a 1/4° grid.

3.5.2 Biogeochemical Properties

Following the evaluation of SWIO model to reproduce the physical dynamics of the South-West Indian Ocean, and more specifically in the South-East Madagascar Bloom region, the biogeochemical variables are now compared against observed datasets. The mean surface and subsurface simulated phytoplankton production is first analysed

against remotely-sensed ocean colour data (ESA OC-CCI). Nitrate concentration is an important limiting factor of Chl-a concentration in the Indian Ocean [*Koné et al.*, 2009] and hence needs to be evaluated in the model in comparison with CARS09. Linked to the biological production through photosynthesis and respiration, the oxygen concentration will also be presented. The evaluation focuses mainly on the bloom region and the mean vertical structures of the above-mentioned biogeochemical variables which are investigated along the transect (white) line, shown in Figure 3.23.

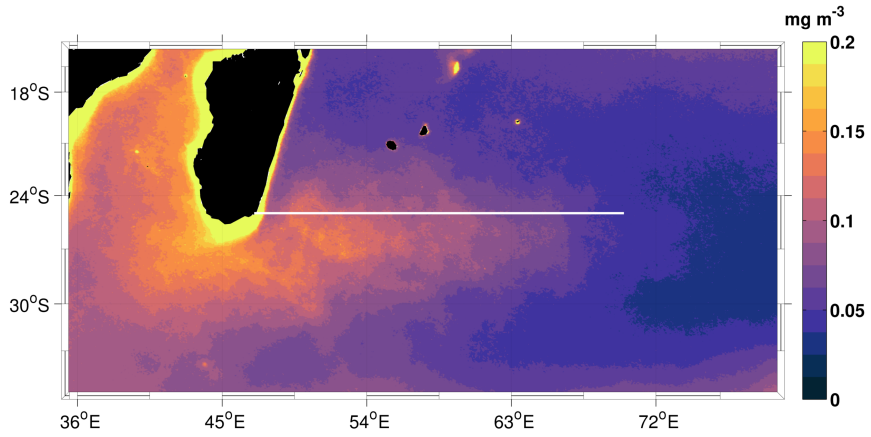


Figure. 3.23 Mean austral summer Chl-a concentration (mg m^{-3}) from ESA OC-CCI averaged over 1998 to 2013. The transect (white line) indicates the location (47°E-70°E; 25°S;) along which the vertical structure of biogeochemical variables are investigated.

- **Surface and subsurface tracer distribution**

Simulated Chl-a concentrations in austral summer and winter are compared to satellite data (Figure 3.24). The most significant signature is the over-estimation of modelled Chl-a in austral winter, in comparison with satellite. The presence of higher nitrate concentrate (as shown in Figure 3.26) in the region can possibly contribute, to some extent, to this over-estimation of Chl0a. The South-East Madagascar Bloom is a feature locked to the austral summer season [*Longhurst*, 2001]. On this basis, comparison of the variables will focus on an extended austral summer season, starting from December to April. The southern coasts of Madagascar exhibit enhanced Chl-a, a feature not present in satellite observations. This implies a stronger coastal upwelling [*Lutjeharms*

and Machu, 2000; *Machu et al.*, 2002; *Ramanantsoa et al.*, 2018a], which is bringing more nutrients to the surface, as can be observed in the mean nitrate concentration in (Figure 3.26). However, in the bloom region, resolving finer-scale processes could play a role in the slight under-estimation of primary production, estimated to be $\sim$ 0.1-0.2 mg m^{-3}. In the Mozambique Channel, low coastal simulated Chl-a can be observed, possibly due to the absence of river discharges in the configuration.

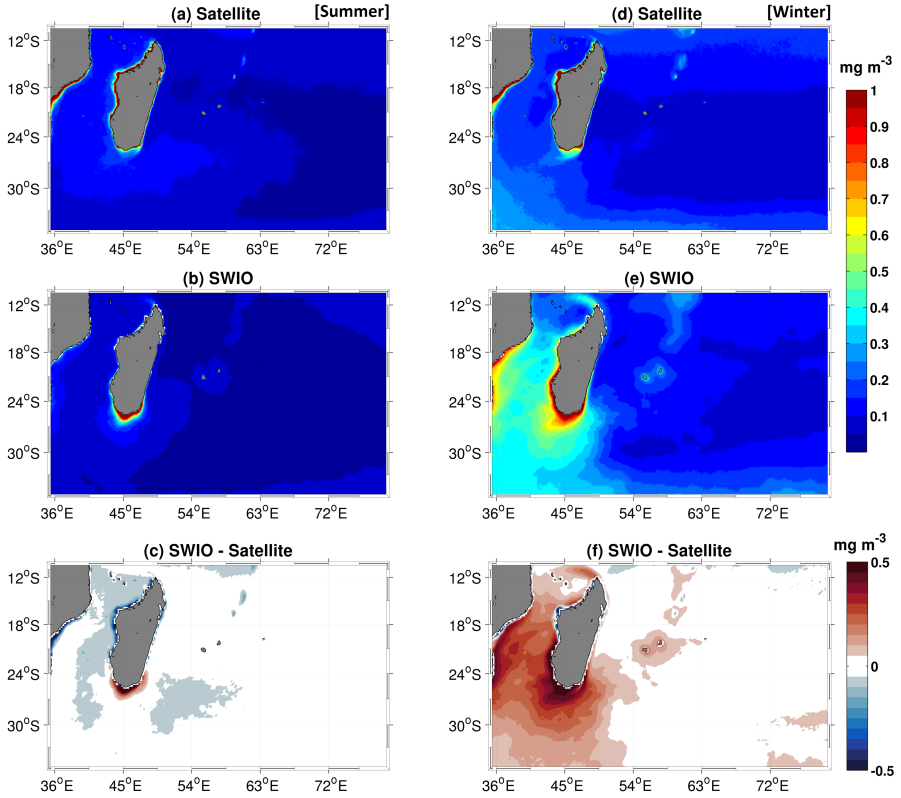


Figure. 3.24 (a) and (d) displays mean seasonal Chl-a concentration (mg m^{-3}) in austral summer and winter from ocean colour dataset (ESA OC-CCI), respectively. (b) and (e) shows mean modelled Chl-a concentration in the surface (0-20 m) layers in austral summer and winter, respectively. The difference between modelled Chl-a and satellite data for (c) austral summer and (f) austral winter, are shown in the last row.

The mean vertical structure of Chl-a displays high surface Chl-a concentration exceeding 0.4 mg m^{-3} near the coasts (Figure 3.25). Towards the open ocean, a deep chlorophyll maximum (DCM) is present which deepens towards the east. This DCM has a mean depth of $\sim$80 (100) m at 55°E (65°E) (Figure 3.25). This corresponds well with SeaSoar data from *Srokosz and Quartly* [2013], which shows a DCM at around 80-100

m depth, from 47°E-51°E in February 2005 (see Figure 3e of *Srokosz and Quartly* [2013]). Hydrographic data south-east of Madagascar in September 2008 confirms the presence of a DCM at 100 m (see Figure S2 from *Voldsund et al.* [2017]). This gives us confidence in SWIO which reproduces the austral summer Chl-a concentration well.

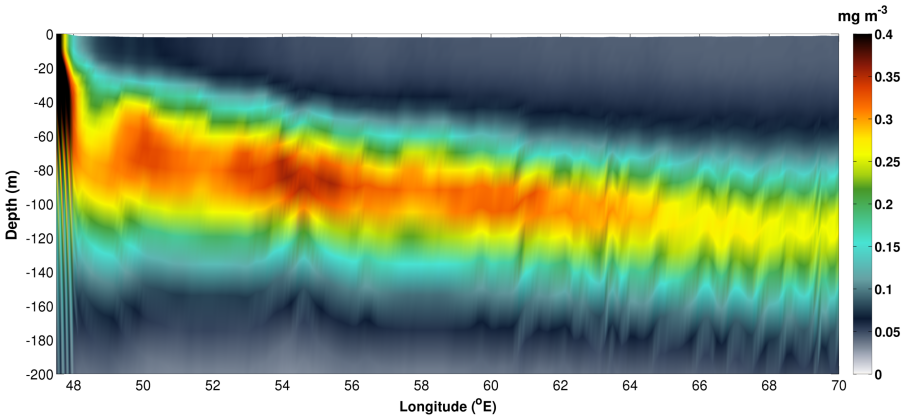


Figure. 3.25 Vertical structure of mean Chl-a concentration (mg m^{-3}) along Transect A, from December to April.

In the vicinity of the bloom, simulated nitrate concentrations (Figure 3.26) are under-estimated in SWIO, with an over-estimation observed on the southern coast of Madagascar. SWIO exhibits nitrate concentration above 0.2 μmol L^{-1}, hence inducing an increased simulated phytoplankton production (Figure 3.24). A stronger coastal upwelling might be responsible for this feature. The nitracline depth, represented as the depth where nitrate concentration exceeds 1 μmol L^{-1}, is 60 m shallower on the south-eastern and southern coasts of Madagascar, compared to CARS09. Owing to this, high nitrate concentration is present at shallower depths, inducing more surface simulated phytoplankton production. A possible influence of this high nitrate-shallow nitracline is the high simulated Chl-a concentration observed close to the Madagascar coast (Figure 3.24). Vertical structures of nitrate (Figure 3.28) show an increase in concentration with depth from 0.1 μmol L^{-1} at the surface to 4 μmol L^{-1} at 200 m depth. Higher concentration is observed near the coasts at 47°E-48°E, with coastal upwelling bringing nitrate-rich waters to the surface. This confirms the presence of higher concentrations at shallower depths in the model.

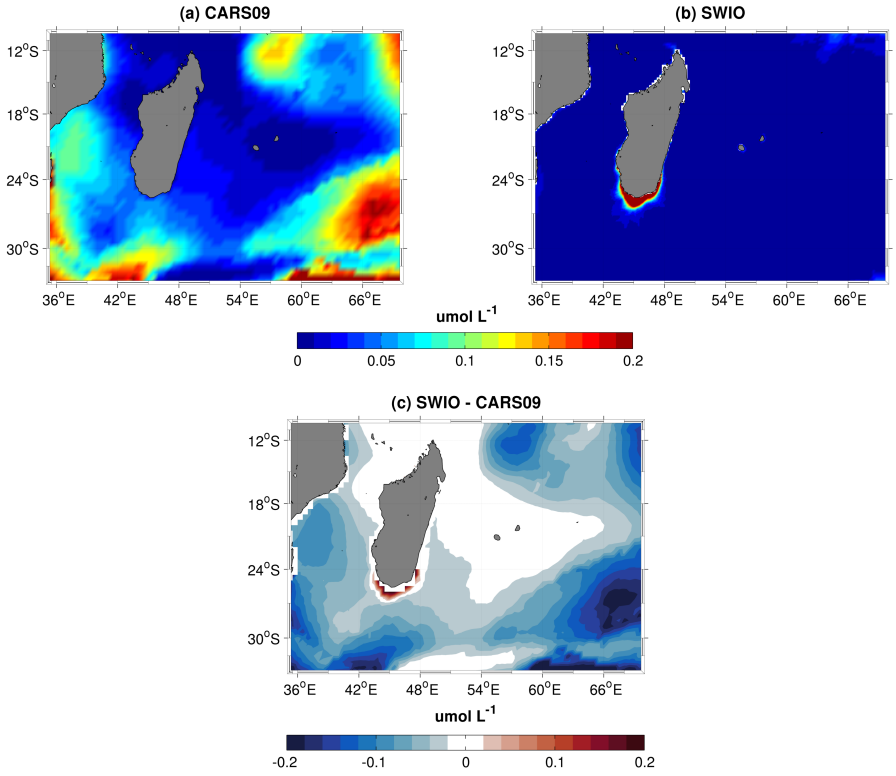


Figure. 3.26 Mean (December-April) surface nitrate concentration (μmol L^{-1}) from (a) CARS09, (b) SWIO and (c) the difference between SWIO and CARS09.

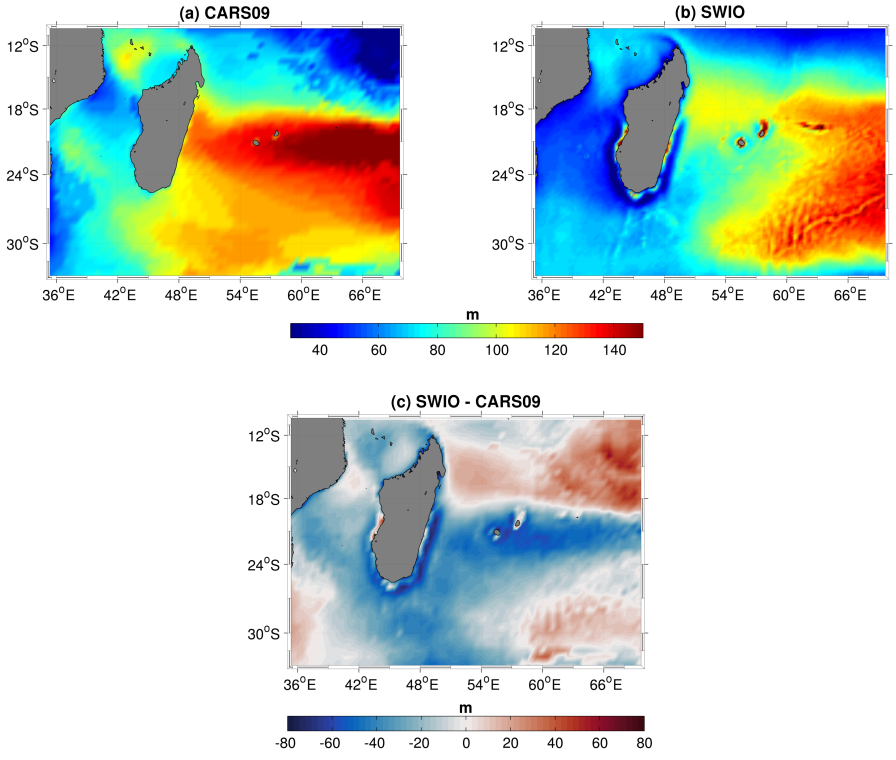


Figure. 3.27 Mean (December-April) nitracline depth (m) from (a) CARS09, (b) SWIO and (c) the difference between SWIO and CARS09.

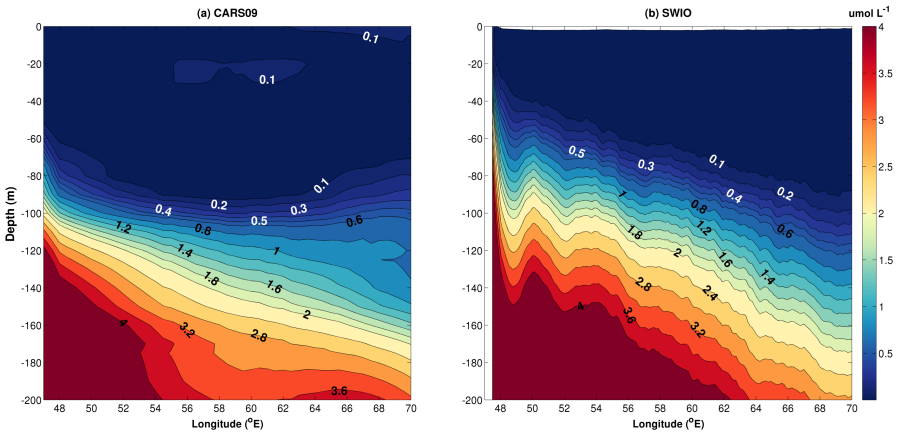


Figure. 3.28 Vertical structure of mean December-April nitrate concentration (μmol L^{-1}) along transect A, from (a) CARS09 and (b) SWIO.

Simulated, as well as observed, dissolved oxygen concentration exhibits a meridional gradient from the northern to the southern part of the domain (Figure 3.29). In the observed dataset, the mean oxygen concentration reaches 240 μmol L^{-1} at 35°S. This meridional gradient is due to the cooler water in the southern domain, which increases oxygen solubility, and consequently oxygen concentration. The model exhibits dissolved oxygen concentrations lower than observations, with a bias of 10 μmol L^{-1}. However, compared to the magnitude of oxygen concentrations, this bias is relatively small. Vertical structures of dissolved oxygen concentration reveal a small over-estimation of oxygen concentration along Transect A. This over-estimation might be related to the higher subsurface salinity present in SWIO, as seen in Figure 3.11d. The lower surface concentration in oxygen levels are representative of low oxygen STSW, as discussed by *DiMarco et al.* [2002].

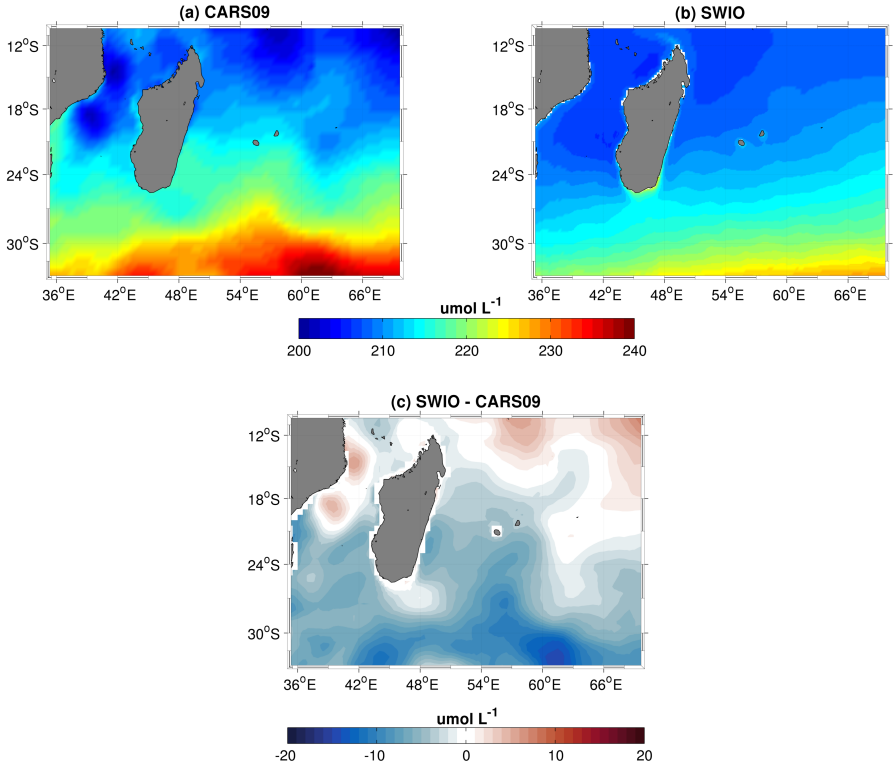


Figure. 3.29 Mean (December-April) surface oxygen concentration (μmol L^{-1}) from (a) CARS09, (b) SWIO and (c) the difference between SWIO and CARS09.

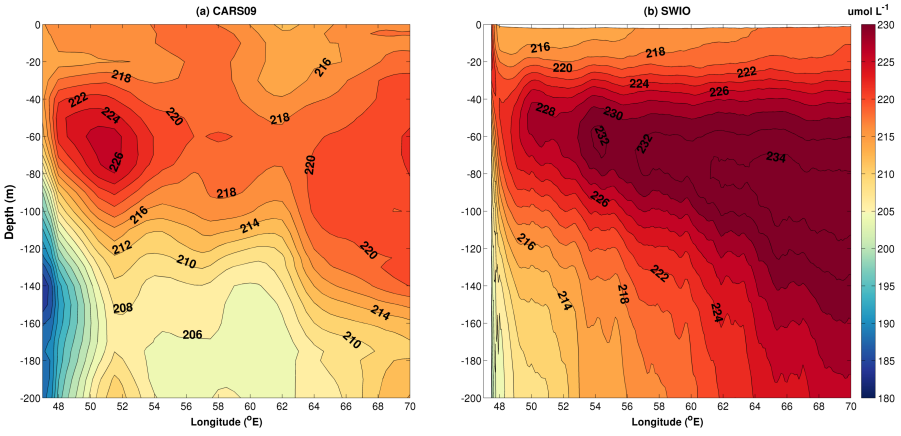


Figure. 3.30 Vertical structure of mean (December-April) oxygen concentration (μmol L^{-1}) along transect A, from (a) CARS09 and (b) SWIO.

3.6 Conclusion

A high resolution coupled ROMS-PISCES model was configured to study the biophysical processes involved in the South-East Madagascar Bloom. This chapter presents the South-West Indian Ocean (SWIO) configuration, and the analysis regarding its ability to resolve the biophysical dynamics in the bloom region.

The mean states for temperature and salinity are adequately resolved by SWIO at the surface and throughout the water column. On the eastern side of the basin, a slight positive salinity bias is observed, possibly due to a similar bias in boundary conditions (GLORYS). The main water masses of the region are well reproduced. The nesting of a higher resolution domain into the coarser one allows SWIO to resolve higher mesoscale processes, consequently increasing the associated EKE south-east of Madagascar. The volume transports of the main currents in the south-west Indian Ocean are well captured. The mean latitudinal band of the SICC is, however, slightly captured to the north.

On the biogeochemical part, when compared to ocean-colour dataset, PISCES shows a large positive bias in simulated Chl-a concentration, possibly due to enhanced nutrients present at the surface. Nevertheless, since the South-East Madagascar Bloom is phase-locked to austral summer season, only modelled outputs from December to April are investigated. In the bloom vicinity, SWIO resolves the processes associated to Chl-a quite well in the region, with a slight negative bias of 0.2 mg m^{-3} observed in the bloom region. However, coastal upwelling is enhanced in SWIO, corroborated by a higher nitrate concentration at the surface and shallower nutricline (> 1 μmol L^{-1}).

Despite some slight discrepencies, the SWIO configuration of the coupled ROMS-PISCEC reproduces the main physical and biogeochemical dynamics of the South-East Madagascar Bloom region. In chapter 5, this simulation will be used to investigate the physical and biogeochemical processes involved in triggering and terminating the

South-East Madagascar Bloom. The influence of the local mesoscale eddy field on nutrient dynamics will also be explored.

Chapter 4

A revisit of the South-East Madagascar Bloom

4.1 Introduction

The area south-east of Madagascar is a complex region of biophysical interactions involving distinct oceanic circulation patterns and zones of enhanced primary productivity. The circulation is dominated by the East Madagascar Current (EMC), an intense and narrow poleward current, rounding the southern tip of Madagascar. The southern part of the EMC (SEMC) exhibits substantial variability south of Madagascar before feeding into the Agulhas Current (AC), through mesoscale eddies, mainly large pairs of counter-rotating eddies or dipoles [*De Ruijter et al.*, 2004; *Ridderinkhof et al.*, 2013] and/or contributions from the downstream mean flow continuation of the SEMC, which on occasions reaches the African western boundary [*Biastoch and Krauss*, 1999; *Biastoch et al.*, 1999; *Stramma and Lutjeharms*, 1997]. A non-persistent retroflection towards the Madagascar Basin also exists and has been attributed to the shedding of anticyclonic eddies [*Halo et al.*, 2014b; *Siedler et al.*, 2009]. This retroflection may act as a possible feeder to the shallow South Indian Ocean Countercurrent (SICC) [*Palastanga et al.*, 2007; *Siedler et al.*, 2006], which connects the western to the eastern tropical Indian Ocean. In the same vicinity, mesoscale eddies migrate in the reverse direction, from the eastern to the western basin, and influence the dynamics and variability of the SEMC [*Ponsoni et al.*, 2015, 2016] and possibly the SICC *Palastanga et al.* [2007]; *Siedler et al.* [2006].

As well as being a complex source of variability within the greater Agulhas Current System, this region exhibits a major sporadic phytoplankton bloom known as the South-East Madagascar Bloom. It was first described as a dendroid bloom by *Longhurst* [2001], owing to its branching shape. It only occurs in austral summer (January, February, March, April), exhibiting substantial temporal variability, and hence has been ascribed as one of the most compelling examples of interannual modulation in ocean biology after El Niño [*Srokosz and Quartly*, 2013; *Uz*, 2007]. Spatially, when fully developped, the bloom can extend eastwards from 45°E to ∼75°E, with a spatial coverage of ∼2500 km^2, showing patches of chlorophyll reaching 2-3 mg m^{-3} [*Longhurst*, 2001]. A biological study of *Poulton et al.* [2009], based on a unique cruise in the high Chl-a patches south-east of Madagascar, has shown that nitrogen-fixers predominate in these patches, specifically *Trichodesmium* which dominates near Madagascar, while *Richelia/Rhizosolenia* were more abundant further east. Taking into consideration the large zonal extent of this feature, the bloom could play an important role in the regulation of atmospheric carbon dioxide [*Lévy et al.*, 2012], biogeochemical cycling of elements [*Naik et al.*, 2015] and oceanic life.

Several studies have focussed on conditions driving the onset, propagation and termination of the bloom. However, it is still debated which physical and biological mechanisms trigger the bloom, and a lack of *in-situ* data in this under-sampled region has impeded a conclusive explanation. The first investigation by *Longhurst* [2001] attributed the onset of the bloom to a co-occurring seasonal deepening of the mixed layer with mesoscale variability in the region. This co-occurrence would drive nutrients, through upwelling, towards the surface and mesoscale eddies would then shape the surface signature of the subsequent enhanced phytoplankton cells. All the following studies also revealed the significance of the highly turbulent circulation in the bloom region, owing to the mesoscale eddies, which disperse nutrients and/or biomass [*Huhn et al.*, 2012; *Raj et al.*, 2010; *Srokosz and Quartly*, 2013; *Srokosz et al.*, 2004, 2015; *Uz*, 2007]. However, *in situ* observations reported by *Srokosz and Quartly* [2013] show that the bloom is

confined to a shallow mixed layer (∼30m), with water temperatures greater than 26.5°C.

Using remotely-sensed ocean colour data, *Srokosz et al.* [2004] described the phytoplankton bloom as the first observed open ocean plankton wave in the Indian Ocean. A combination of plankton growth and an eastward diffusion, against the mean westward flow, due to the mesoscale circulation led to this plankton wave. However, eddies are not necessary for the eastward plankton wave displacement owing to the presence of the shallow eastward flow, the SICC [*Menezes et al.*, 2014; *Palastanga et al.*, 2007; *Siedler et al.*, 2006], which has been shown to occur in this region. Another mechanism put forward was the importance of tropical cyclones passing over Madagascar, which induce an enhanced precipitation on the eastern coast of Madagascar, causing river-runoffs [*Uz*, 2007]. These iron-rich waters could then move eastward through eddy-diffusion, fertilizing the region and triggering the bloom. *Raj et al.* [2010] confirmed the importance of rainfall on the eastern Madagascar region, which they showed to be related to the interannual variability of the bloom, along with light limitation and mesoscale eddies. However, *Lévy et al.* [2007] and *Raj et al.* [2010] also stated the upwelling south of Madagascar to be the source region of nutrients, which would be advected eastward through eddies and hence trigger the bloom.

Srokosz and Quartly [2013] reviewed all the previous hypothesis and stated why they were inadequate. They proposed a new origin of iron particles, upwelled from sediments on the continental shelf, which have been shown to be a source of iron in coastal areas [*Dale et al.*, 2015; *Jeandel et al.*, 2011; *Johnson et al.*, 1999]. These particles could be transported eastward with the bloom ending when all iron particles were exhausted. Consistent with *Srokosz et al.* [2004] and *Srokosz and Quartly* [2013], *Huhn et al.* [2012] related this eastward movement to the presence of zonal jets in the South Indian Ocean and the bloom being shaped by the meridional barrier of these jet-like Lagrangian coherent structures. However, they also concluded that the seasonal and interannual variability of the eastward jets do not match the variability of the bloom. The strength

of the upwelling south of Madagascar may, however, dictate the interannual variability and the size of the bloom, as stated by *Raj et al.* [2010] and *Srokosz and Quartly* [2013]. Opposite to *Longhurst* [2001] hypothesis, a shallowing of the mixed layer, which provides good conditions for nitrogen fixers, may also aid in the bloom [*Capone et al.*, 1997; *Wilson and Qiu*, 2008]. Using an eddy-resolving simulation together with a Lagrangian particle tracking, *Srokosz et al.* [2015] showed that the bloom may be fertilized by iron particles upwelled on the east and south of Madagascar and, as suggested by *Srokosz and Quartly* [2013], the bloom ends after an exhaustion of iron particles. Interannual variability of the spatial extent of the Lagrangian particles in this highly turbulent region could explain the spatial extent of the bloom and that the presence of the SICC is not fundamental to the interannual variability of the bloom [*Srokosz and Quartly*, 2013].

As stated earlier, nitrogen-fixers have been found to prevail in the bloom region [*Poulton et al.*, 2009; *Srokosz and Quartly*, 2013]. However, these conclusions were drawn from a cruise which occurred in 2005, a year which is not characterized as a bloom year [*Raj et al.*, 2010; *Uz*, 2007]. High Chl-a patches were indeed observed during the cruise period but these did not evolve as largely as to be identified as a 'bloom year'. Although nitrogen-fixers can have an influence on the bloom, the possibility of other organisms being predominant during actual bloom years should not be excluded.

A summary of the different hypotheses in the previous studies are:

- Deepening of the mixed layer driven by mesoscale eddies [*Longhurst*, 2001].
- Plankton growth and eddy diffusivity towards bloom region (Plankton Wave) [*Srokosz et al.*, 2004].
- Iron run-off due to enhanced rainfall on the eastern coasts of Madagascar, associated with cyclones [*Uz*, 2007].
- Combination of upwelling south of Madagascar, precipitation along the east of Madagascar, light limitation and mesoscale eddies [*Raj et al.*, 2010].

• Upwelling intensity south of Madagascar bringing either nutrient-rich waters to the surface followed by an eastward advection [*Lévy et al.*, 2007; *Raj et al.*, 2010] or dissolved iron from the continental shelves to the surface and transported eastward [*Srokosz and Quartly*, 2013; *Srokosz et al.*, 2004].

With almost 19 years of remotely-sensed ocean colour (ESA Ocean Colour CCI (ESA OC-CCI)) data available, it is now possible to better examine the different hypotheses which have been presented in previous studies. In combination with other observed physical parameters, this study aims to gain a better understanding of the different variables at play in triggering this sporadic bloom, as well as its termination. Section 4.2 describes the spatial and temporal variability of the bloom, and the vertical structure of the water column where it occurs. Section 4.3 revisits the various existing hypothesis proposed as explanations for the occurrence of the bloom. Section 4.4 looks at a possible relationship with climate modes. Lastly, section 4.5 investigates the relationship of the bloom with the local currents (EMC and SICC). Concluding remarks and a new hypothesis accounting for the bloom generation are discussed in section 4.6.

4.2 Bloom Description

In this section, we revisit the main features of the dentritic South-East Madagascar Bloom. Using a 19-year (1998-2016) ocean colour dataset (see Chapter 3 for further details on this product), we characterize the bloom and detail its associated temporal and spatial variabilities. Based on this long-term dataset, a more comprehensive view of the bloom than previously achievable can be investigated.

4.2.1 Temporal Variability

Uz [2007] described the South-East Madagascar Bloom using a box in the region (24°-30°S and 48°-66°E) which he referred as a 'bloom box'. From this bloom box, a clear bi-annual signal in Chl-a concentration stands out, peaking in summer (end of February) and winter (early July) (Figure 4.1). The winter bloom is recurrent whereas the summer bloom only occurs during some years. *Uz* [2007] proposed a bloom index to unveil the timing of the bloom, removing signal interference from the winter bloom. This index uses two regions of interest, namely, bloom box (W in Fig. 4.2) which captures both the summer and winter blooms, and box E (E in Fig. 4.2; 24°-30°S and 70°-88°E) which captures only the winter bloom. *Uz* [2007] normalized the Chl-a concentration of 'bloom box' by the similarly-sized box E located to the east towards the open ocean. Based on data up to 2005, *Uz* [2007] classified the years of 1999, 2000, 2002 and 2004 (shaded in Figure 4.2) as bloom years. In this study, we have extended the *Uz* [2007] index, up to 2016. The peaks in the index, as shown in Figure 4.2b, display only the summer bloom and give an insight into the temporal variability of this feature, with blooms occurring in the summers of 1999, 2000, 2002, 2004, 2006, 2008, 2009, 2011, 2012, 2013 and 2014. However, the magnitude of the peak varies from one bloom event to the other.

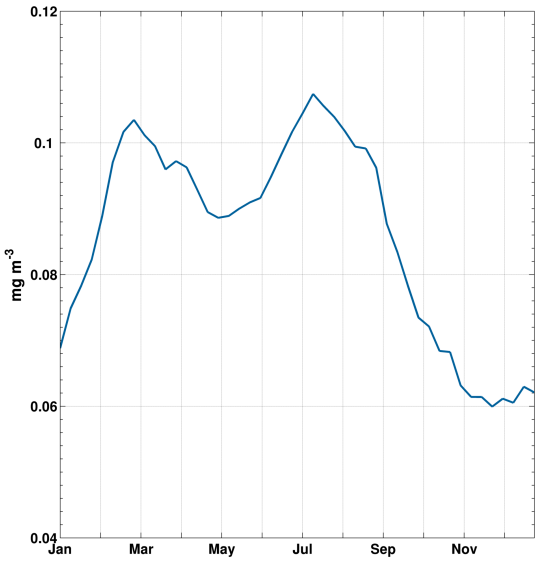


Figure. 4.1 Monthly climatology from 1998-2016 of ESA OC-CCI Chl-a concentration (mg m^{-3}) in a box south-east of Madagascar, defined as the bloom box by *Uz* [2007].

The normalization of Chl-a concentration in the 'bloom box' by box E can be deceptive, as the intensity of the bloom index could be dependent on the intensity of the winter bloom in box E. Normalizing by values close to zero could also lead to a misleading bloom intensity. Therefore, the computation of the bloom index has been redefined by subtracting the Chl-a concentration of box E from 'bloom box' (Figure 4.4b). Even though the bloom index defined by *Uz* [2007] gave a good insight on the bloom timing, this new index provides additional information about the actual intensity of this sporadic bloom. Following this, the new index is referred as 'W-E bloom index' and is used to analyse potential relationships with different physical variables. Weekly data sampling over daily so as to maximise coverage, which might be hindered by cloud cover in the daily data. In addition, weekly data are sufficient to properly capture the temporal structure of the bloom.

The definition of a bloom, however, differs from one region to another in the global oceans. *Richardson* [1997] described a phytoplankton bloom as a rapid growth of one or more species leading to an increase of the species' biomass. Bloom definition based on

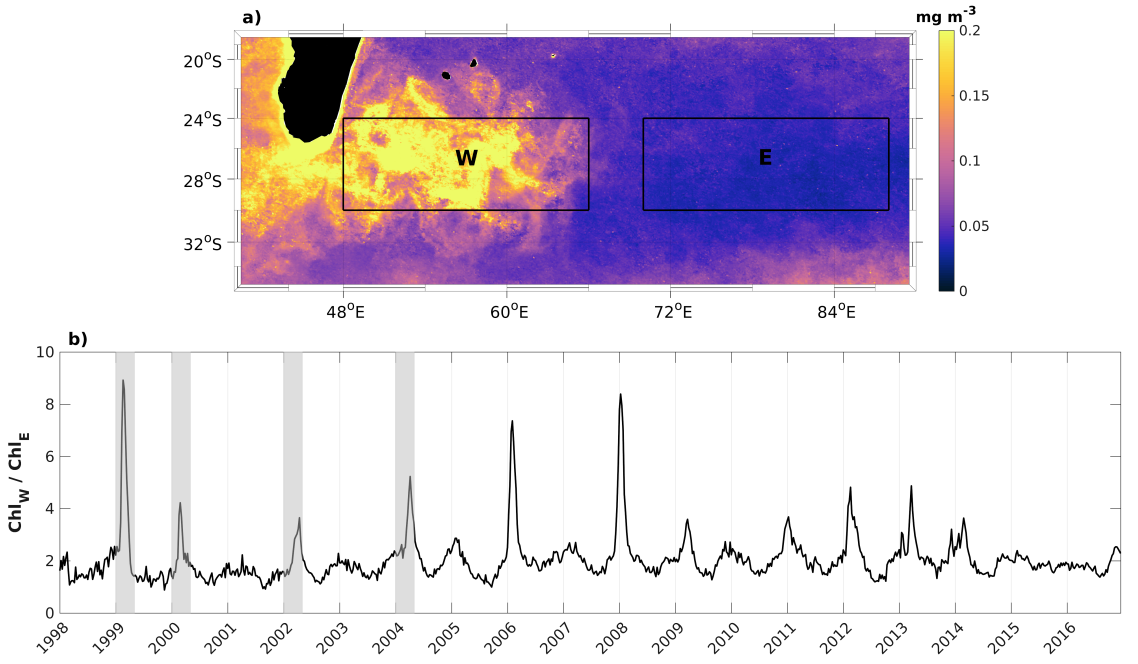


Figure. 4.2 (a) Mean ESA OC-CCI Chl-a concentration in January 1999, overlaid with boxes W and E. (b) displays an extended time series (1998-2016) of the bloom index as defined in *Uz* [2007]. The shading designates the bloom years identified by *Uz* [2007] in their shorter time series (1997-2005). *Uz* [2007] used a composite of SeaWiFS and MODIS Aqua images.

threshold criteria can also be used to quantify a bloom frequency and trend [*Tett*, 1987]. In this study, a histogram of the yearly maximum Chl-a difference ('bloom box' - box E) is used to define a threshold. This difference is computed from January to April only, owing to an austral summer occurrence of the bloom. The occurrence is defined as the first exceedence of a specific Chl-a concentration difference threshold. From Figure 4.3, we can observe a maximum occurrence of Chl-a concentration difference at around 0.05 mg m^{-3}, representative of no bloom. A trough exists at around 0.07 mg m^{-3}, beyond which the occurrence of an enhanced Chl-a difference increases again. Hence, 0.07 mg m^{-3} is considered as a bloom threshold, denoted as a red dotted line in Figure 4.4b. The event peaks again at 0.1 mg m^{-3}, before reaching zero events at 0.14-0.18 mg m^{-3}. From this perspective, a 0.16 mg m^{-3} (blue dotted line in Figure 4.4b) exceedence threshold is assigned to differentiate between normal and major blooms. Respectively, these account for 8 and 3 events. In this context, it means that a bloom is defined

when the Chl-a concentration is higher by 2-3 fold than the mean concentration.

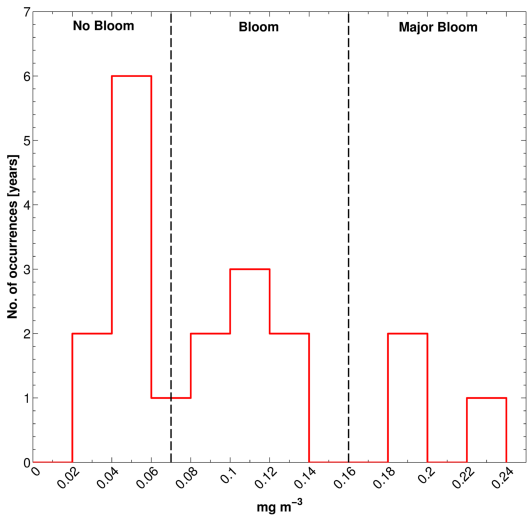


Figure. 4.3 Histogram of maximum difference between 'bloom box' and box E. The vertical dotted black line at 0.07 mg m^{-3} indicates the threshold used to separate bloom from non-bloom years. The line at 0.16 mg m^{-3} separates the normal bloom from major bloom years.

The large temporal variability in the intensity of the austral summer bloom can be observed in Figure 4.4a. As previously noted, the secondary peak in the mean Chl-a concentration is related to the austral winter bloom. Interestingly, during years of austral summer bloom, the latter can be 2 or 3 times stronger than the winter bloom. Using the 'W-E bloom index', 1999, 2000, 2002, 2004, 2006, 2008, 2009, 2012, 2013 and 2014 are defined as bloom years. However, as seen in Figure 4.4b, intensity of the bloom exhibits substantial variability, with the most prominent blooms occurring in 1999, 2006 and 2008 ($>$ 0.16 mg m^{-3}; major blooms), while normal blooms occur in 2000, 2002, 2004, 2009, 2012, 2013 and 2014. These are summarized in Table 4.1. It should be noted that even though the peak in 2011 reaches the 0.07 mg m^{-3} threshold, it was not defined as a typical bloom year, owing to its particular spatial signature, as will be seen later in this chapter.

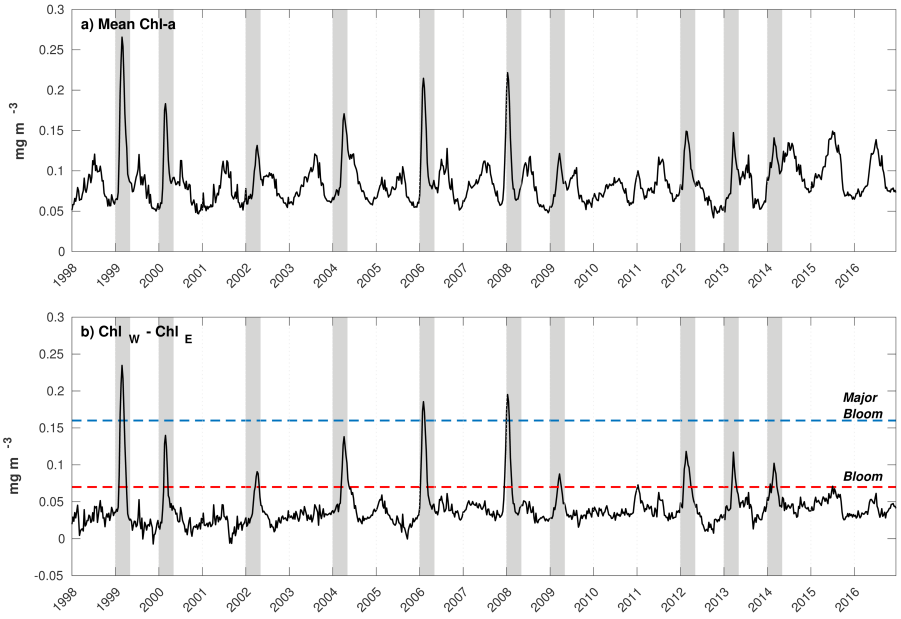


Figure. 4.4 (a) Time series of mean ESA OC-CCI Chl-a concentration in the bloom box. (b) Bloom index computed by subtracting Chl-a of box E from Box W. In (b), the red dotted line indicates the threshold of 0.07 mg m^{-3} (identified in Figure 4.3), which distinguish the bloom years and non-bloom years. Peaks above the blue line (0.16 mg m^{-3}) indicate major blooms. In both (a) and (b) and corresponding later figures, the grey shading indicates the bloom years identified from the red dotted line (0.07 mg m^{-3} of chlorophyll-a difference between boxes W and E).

Another interesting feature of the bloom is that, although it is phase locked to austral summer, it does not always initiate or peak at the same time during that period (Figure 4.4b). Typically, the bloom commences in January, peaking in February and diffusing by March/April. However, variations are observed from one event to the next. During the 3 strongest events, the phytoplankton bloom peaked in January (2008) and February (1999 and 2006). In 2008, the bloom started at the end of the previous year (2007) whereas for 1999 and 2006, it started in January (Figure 4.4b). In other bloom years, the initiation month is delayed, starting in February (2002 and 2004), and peaking later in April. In 2012, 2013 and 2014, the bloom reaches its highest intensity around the end of March. From this, it appears that the South-East Madagascar Bloom lasts for about 3 months. The results also provide an indication that the bloom might be controlled by a mechanism or combination of mechanisms, which should

Table 4.1 Events of bloom and non-bloom years, with bloom years being defined as normal and major blooms. The month at which the bloom is maximum is stated in the fourth column. Bloom years are listed in bold. The '?' indicates the ambiguous classification of 2011.

Years	Bloom		Month of maximum bloom	Non bloom
	Normal bloom [0.07 - 0.16 mg m^{-3}]	Major bloom [>0.16 mg m^{-3}]		
1998				X
1999		X	Feb	
2000	X		Mar	
2001				X
2002	X		Apr	
2003				X
2004	X		Apr	
2005				X
2006		X	Feb	
2007				X
2008		X	Jan	
2009	X		Mar	
2010				X
2011	?	?	?	?
2012	X		Mar	
2013	X		Apr	
2014	X		Mar	
2015				X
2016				X

exhibit similar monthly variability.

4.2.2 Mean spatial structure and variability of the bloom

In addition to the large temporal variability exhibited by the bloom, its spatial extent also varies significantly both meridionally and zonally. The months with maximum Chl-a concentration during identified bloom years, as well as months of non-bloom years, are used to construct a composite Chl-a map of bloom (Figure 4.5a) and non-bloom (Figure 4.5b) periods. This unveils a mean spatial structure of the bloom, with enhanced Chl-a observed around the southern part of Madagascar, and the bloom

identified as an elongated filamentous structure on its south-eastern flank, easterly well out into the open ocean. From this mean structure, a Chl-a concentration of around 0.25 mg m^{-3} in the Madagascar Basin and south of Madagascar can be observed, with patches of lower concentration on the peripheries of the bloom. The mean structure of the feature varies meridionally from 22°S to 32°S and zonally from 50°E to ∼70°E (Figure 4.5a). In the Mozambique Channel, higher concentration of phytoplankton cells can be observed in bloom compared to the non-bloom period, reaching ∼ 0.15 mg m^{-3}. Interestingly, during non-bloom periods, a filamentous structure exists close to the coast with some slight patches of enhanced Chl-a, which however does not extend as far east as in the bloom period (Figure 4.5b). The overlaid box indicates the bloom box which has been used to capture the bloom for every year of its occurrence.

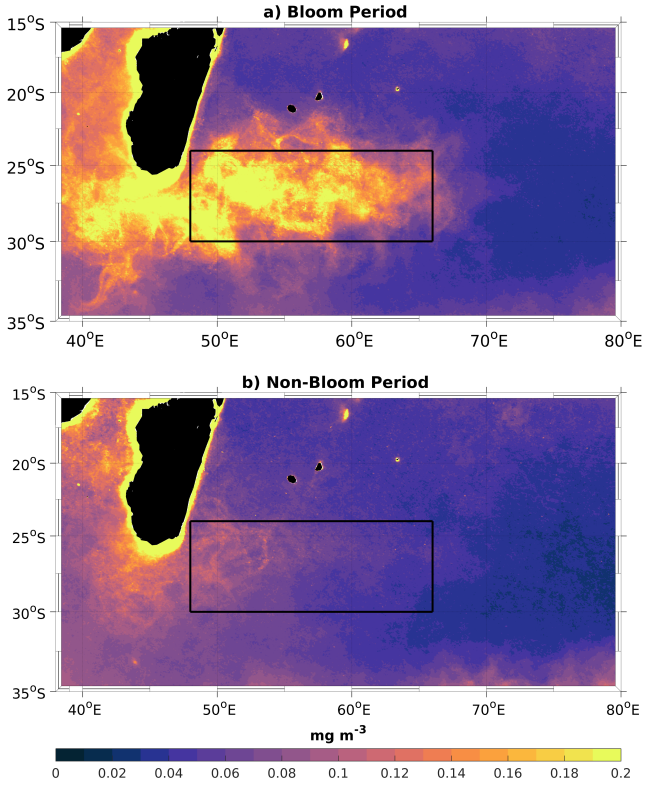


Figure. 4.5 (a) Spatial maps of mean ESA OC-CCI Chl-a concentration (mg m^{-3}) during months of maximum austral summer bloom identified in Figure 4.4b. (b) Same as (a) but during months of minimum Chl-a concentration during austral summer.

As previously advanced, the bloom reaches its highest intensity at different months of austral summer, and it displays strong spatial variability. Figure 4.6 shows the Chl-a distribution for the month which exhibits maximum concentration in the bloom box, for each year from 1998 to 2016. The zonal and meridional extents, as well as the enhanced Chl-a on the south-western and southern parts of the Madagascan coasts, vary from one bloom year to the next (Figure 4.6). A first glimpse from this figure reveals the presence of some patches of Chl-a with higher concentration than the surrounding, during almost every year in the bloom box, except during the identified 'bloom years', during which the enhanced Chl-a patches are exceptional. Note that the bloom years, as identified in Figure 4.4b, are denoted by an asterisk. However, 2011 is denoted by a '?'. Even though enhanced Chl-a patches can be observed during this year, the signature seems to be elongated more south/south-eastward, compared to the zonally elongated signature of a classic South-East Madagascar Bloom. Hence, as mentioned earlier, this year is assigned as neither a bloom or non-bloom year.

A compelling component of the bloom is its connection to the Madagascan coast (Figure 4.6). During some bloom years, enhanced Chl-a signatures appear linked to the south-eastern or southern coast of Madagascar (1999, 2000, 2002, 2006, 2008 and 2012) whereas during other bloom years (2004, 2009, 2013 and 2014), the bloom seems disconnected from the coast by a low Chl-a region (more clearly observed in Figure 4.7). These differences can possibly be associated with a different triggering mechanism between the offshore and coastally-linked blooms. In some non-bloom years, traces of weak Chl-a concentration also develop in the Madagascar Basin (2003, 2005, 2010, 2011, 2015 and 2016; Figure 4.6).

Figure 4.7 gives further insight into the latitudinal and longitudinal variations of the bloom. It displays the bloom anomaly, which is computed by subtracting the mean composite bloom (Figure 4.5a) from the month which exhibits maximum Chl-a concentration for each specific year (Figure 4.7). The longitudinal extent of the bloom,

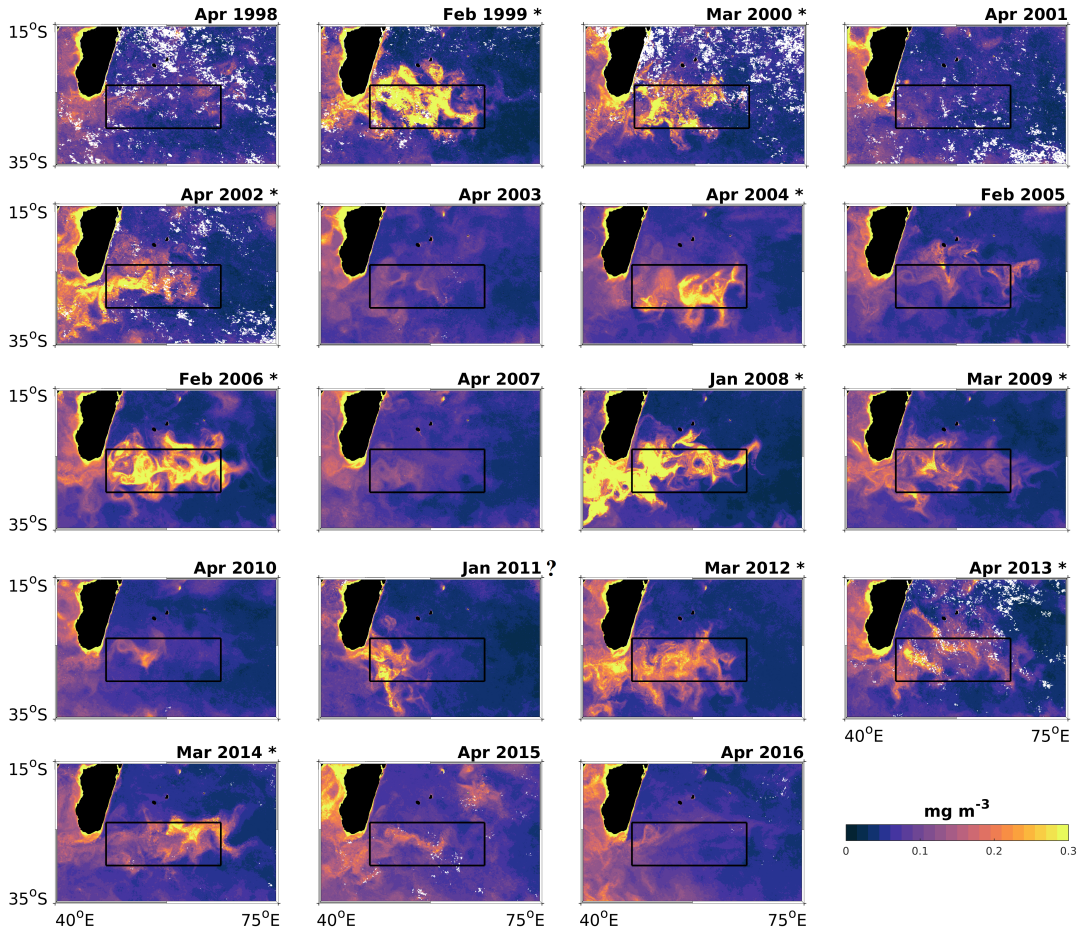


Figure. 4.6 Spatial maps of the months of maximum ESA OC-CCI Chl-a concentration (mg m^{-3}) observed in 'bloom box', from 1998 to 2016. The asterisk* denotes years identified as bloom years from Figure 4.4b.

when fully developed, can reach up to 72°E (1999, 2006 and 2008). However, in other years, it can extend only to about 60°E-65°E. The latitudinal band at which the bloom prevails varies from one bloom year to another. The strongest blooms (1999, 2006 and 2008) appear mostly in the 22°S-30°S band. Comparatively, the 2012 bloom is shifted southward (25°S-34°S).

The bloom occurs in the same region as the eastward shallow SICC. High Eddy Kinetic Energy (EKE) also prevails, associated with mesoscale eddies and the SICC. The latitudinal variations of the bloom, as seen in Figure 4.7, could possibly be altered by the latitudinal variability of the SICC. This latitudinal variability is investigated by

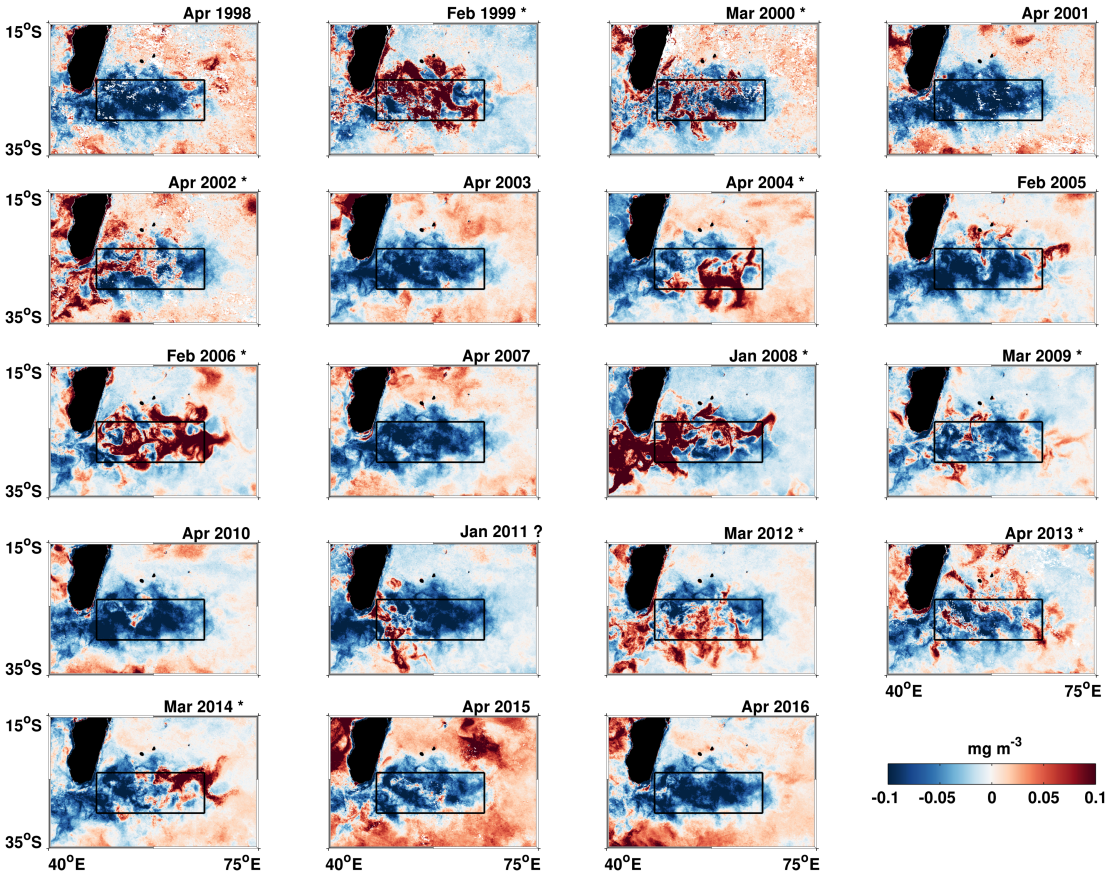


Figure. 4.7 Spatial maps of the difference between months of maximum ESA OC-CCI Chl-a concentration (mg m^{-3}) observed in 'bloom box' and the mean composite bloom, from 1998 to 2016. The asterisk* denotes years identified as bloom years from Figure 4.4b.

performing a hovmöller analysis along an extended SICC transect (20°S-32°S; 50°E) to capture high EKE (significant of the position of the SICC) and the phytoplankton bloom.

The signatures of the austral summer bloom in Figure 4.8b are more captivating compared to the austral winter ones. Also, it is worthwhile noting that the EKE associated with the SICC (Figure 4.8a) does not seem to control the meridional variations of the bloom. Owing to the presence of mesoscale eddies which are a prominent feature of the oceanic circulation in this region, tracks of the eddies, advection along the peripheries of eddies as well as possible biological production in the eddy-cores

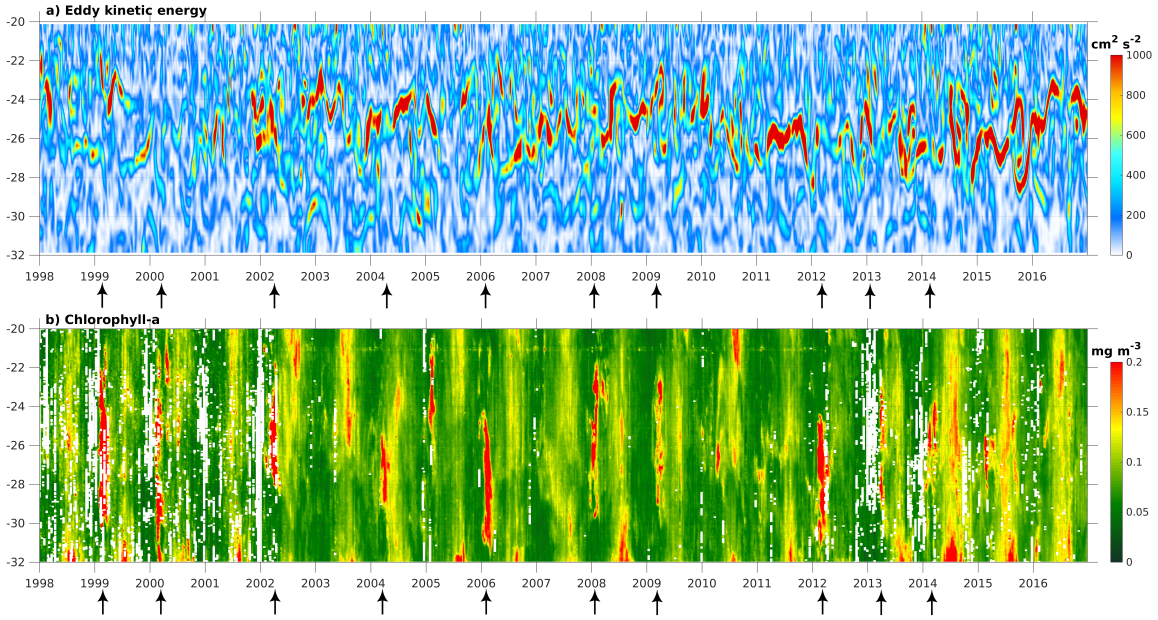


Figure. 4.8 Time-latitude hovmöller of (a) AVISO eddy kinetic energy ($cm^2\ s^{-2}$) along the meridional transect (24°S-28°S; 50°E) which captures the position of SICC, and (b) ESA OC-CCI Chl-a concentration ($mg\ m^{-3}$) along the same transect which caputures both the austral summer and winter blooms.

could be responsible for this northward/southward bloom migration. Some bloom years (1999, 2000, 2008 and 2012) seem to be accompanied by a reduced EKE, whereas during other bloom years, high EKE is present during the bloom initiation.

The phytoplankton bloom co-occurs with enhanced Chl-a concentration south-west of Madagascar in some cases (2002, 2008 and 2012; Figure 4.6 and Figure 4.7). When connected, these two regions of high phytoplankton cells alter the spatial variability of the South-East Madagascar Bloom, giving the view of a possible onset location south or south-west of Madagascar. On this basis, the possible connection, with a delineated box on each side of Madagascar (West and East) is investigated (Figure 4.9). As stated earlier (and which can be seen from Figure 4.9b and c), peaks of Chl-a concentration occur at the same time in both boxes in 2002, 2008 and 2012. However, no significant lag in the concentration can be observed during these specific years, which suggests a simultaneous Chl-a enhancement in both regions. In some years (1999, 2000, 2006, 2012

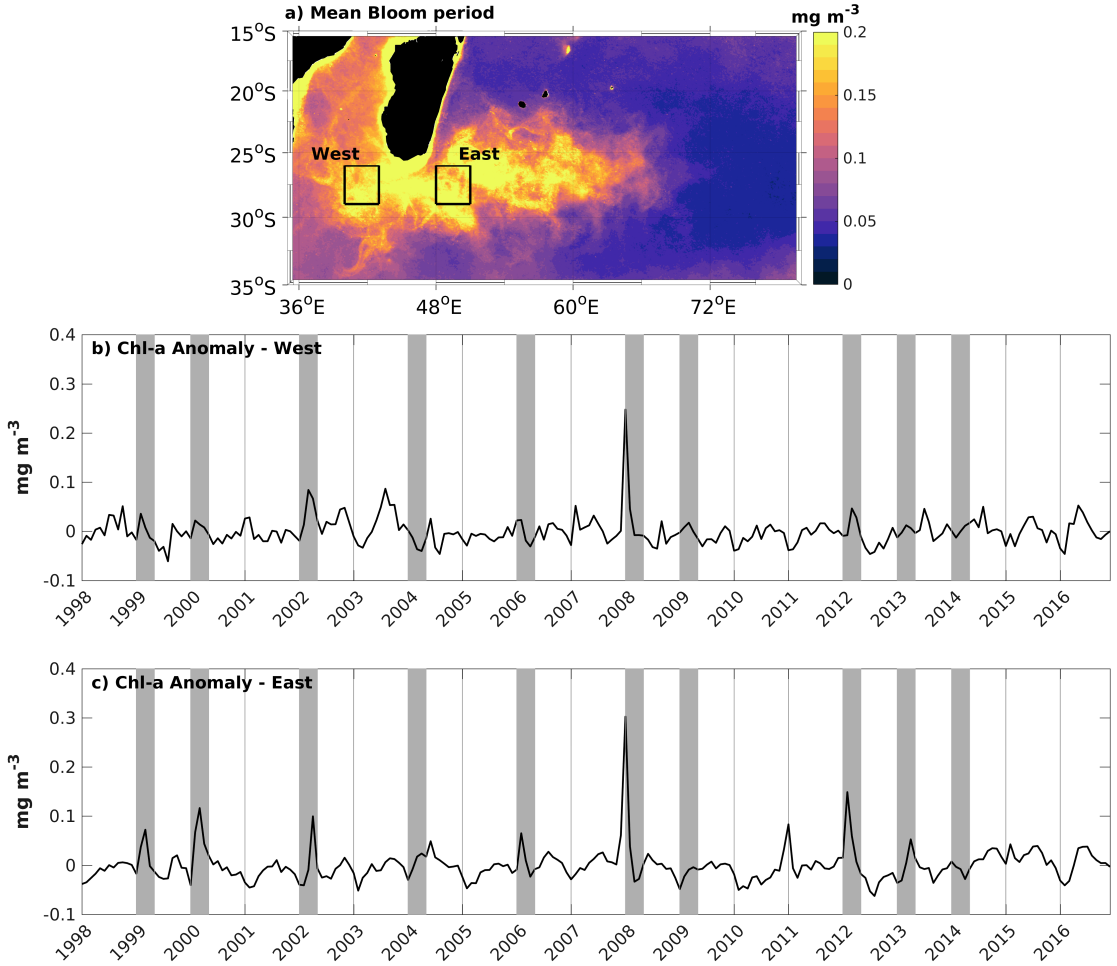


Figure. 4.9 (a) Composite of Chl-a concentration during identified bloom years, overlaid with box West (26°-29°S and 40°-43°E) and East ((26°-29°S and 48°-51°E). (b) and (c) display the Chl-a anomalies in box west and box east respectively, with respect to the 1998-2016 mean Chl-a concentration.

and 2013), a positive Chl-a anomaly is only observed in the eastern box (Figure 4.9b and c), hence showing no connection between the two regions.

4.2.3 Vertical Structure

The mean structure of the water column in the bloom domain is investigated using co-located Argo floats in the bloom box. A threshold of Chl-a concentration greater (less) than 0.27 (0.06) mg m^{-3} is used to identify which float is in a bloom (non-bloom)

spot. These thresholds were chosen to capture patches with high and low chlorophyll contents respectively, and to have an adequate number of Argo profiles in both high and low Chl-a concentration. It should be noted that a surface salinity front (low salinity equatorward and high salinity poleward) is present in the region and in the bloom box, varying interannually. This front is believed to be associated with the SICC [*Menezes et al.*, 2014]. Since the blooms can overlay the mean spatial variability of the salinity front during their occurrence, this could create a bias in the mean haline vertical structure of bloom and non-bloom regions. On this basis, an isohaline of 35.4 psu (green line in Figure 4.10a) is used as a threshold to identify the fresher (less saline) and saltier (more saline) sides of this front. The co-location of Argo-bloom and Argo-non bloom profiles will provide us with a mean water column structure on both sides of the front, without extreme values creating a bias. Henceforth, we refer to Argo profiles in high Chl-a patches as 'bloom profiles', and profiles in low Chl-a as 'non-bloom profiles'.

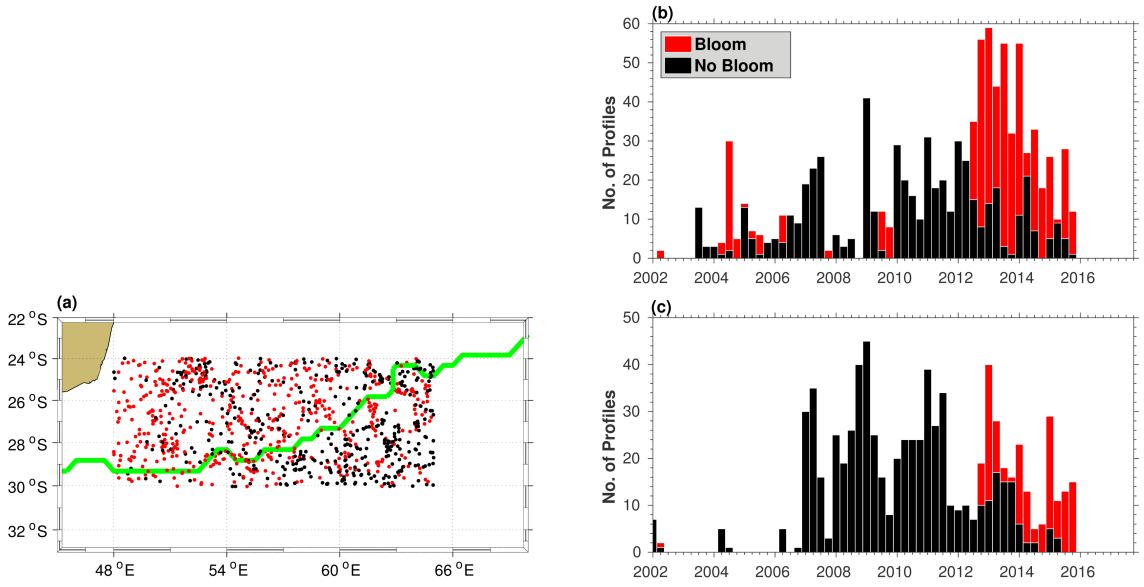


Figure. 4.10 (a) The positions of bloom profiles (red) and non-bloom profiles (black) in the bloom box, separated by the 35.4 psu isohaline (green line). (b) and (c) displays the number of bloom profiles (red) and non-bloom profiles (black) surveyed in each austral summer months (January - April) from 2002 to 2015.

731 (291) bloom profiles and 540 (622) non-bloom profiles were obtained on the fresher (saltier) side of the front (Figure 4.10a). These are well distributed into the bloom box (Figure 4.10a), and are separated onto the fresher (equatorward) and saltier (poleward) side of the 35.4 psu isohaline. From Figure 4.10b and c, we would expect a higher number of bloom-profiles surveyed in bloom years and vice-versa. However, this remains arbitrary as the number of profiles in the ocean increased since the first Argo-float deployment. On the fresher side of the salinity front, non-bloom years of 2005, 2007 and 2010 were mostly surveyed. In 2009, even though a bloom occurs, non-bloom profiles were more abundant, possibly due to the broad distribution of the high Chl-a patches during this year (2009 in Figure 4.6). Frequent profiling occurred in 2012, 2013 and 2014, which have been identified previously as bloom years. On the saltier side of the front, non-bloom profiles are more abundant. This could either mean that the bloom occurs more frequently on the fresher side of the salinity front, or that there were more Argo profiles on the higher saline side of the front during the phytoplankton bloom. The number of profiles in high Chl-a patches were, however, higher in end-2012, 2013 and 2014 (bloom years). The higher number in April 2012 could be due to the southward migration of the bloom during that year(Figure 4.7).

The mean vertical structure of the water column associated with the bloom displays a bloom occurrence in a shallow stratified layer (Figure 4.11), as reported by *Srokosz and Quartly* [2013]. The mean surface temperature in both bloom and non-bloom areas is about 26.2°C (fresher side; Figure 4.11a) and 24.°C (saltier side; Figure 4.11d). Lower surface and subsurface temperatures, analogous to the higher surface and subsurface desntiy, are observed to be associated with bloom profiles on the fresher side of the salinity front. This could be representative of upwelled water bringing nutrient-rich waters to the surface, or shoaling a deep chlorophyll maximum.

No significant differences between the bloom and non-bloom areas are observed in the mean mixed layer depth, from both a temperature and density threshold [*de Boyer*

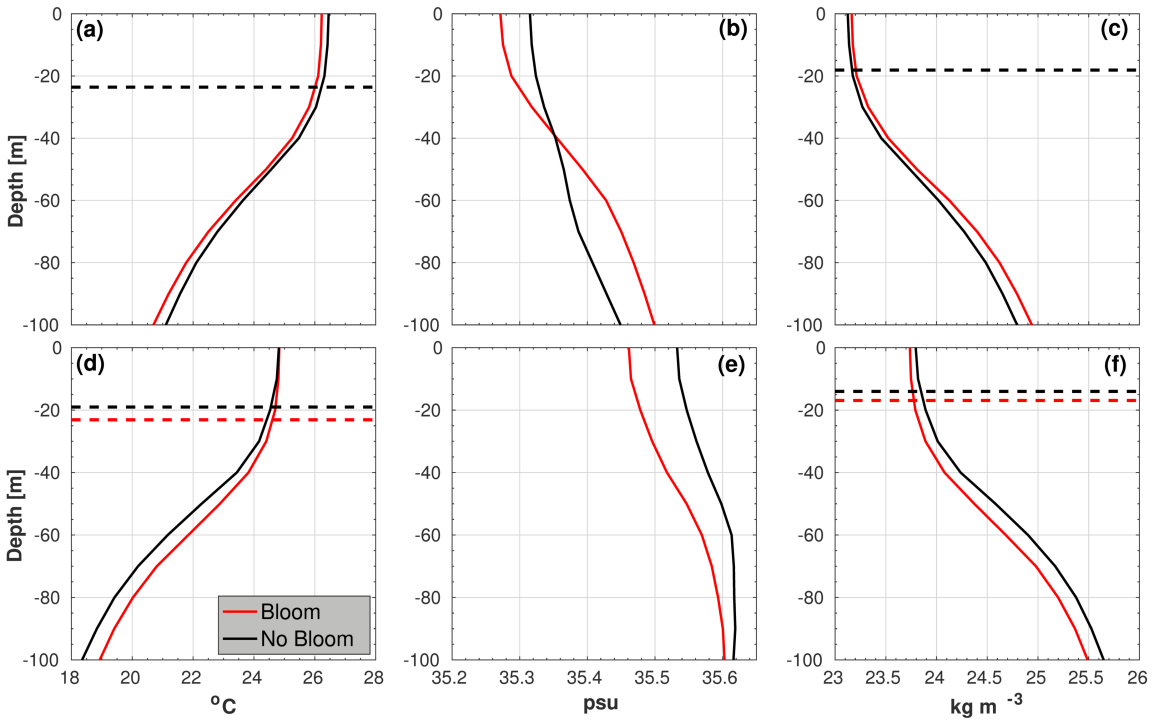


Figure. 4.11 The mean vertical thermohaline structure of the water column associated with bloom (red line) and non-bloom (black line) years on the fresher side (upper panels) and saltier side (lower panels) of the salinity front. The red (black) dotted lines show the mixed layer depth of bloom (non-bloom) era, from a temperature threshold (a,d) and density threshold (c,f).

Montégut, 2004], with a depth of about 23.6 m (Figure 4.11a) and 18.5 m (Figure 4.11c) respectively. On the more saline side, however, the mixed layer is shallower in non-bloom profiles, with a depth of 19 m (Figure 4.11d) and 14 m (Figure 4.11d), while bloom profiles have their mixed layer at 23.1 m (Figure 4.11d) and 16.9 m(Figure 4.11d) depth. Overall, in the bloom box, the mixed layer associated with the bloom remains shallow.

The interesting feature here is that the bloom is confined to surface lower salinity waters on both sides of the front (Figure 4.11b and e), compared to the non-bloom profiles. This gives an indication that low-salinity surface waters are potentially associated with the Madagascar Bloom. The fresher water may be associated with the low salinity EMC, as seen in Figure 4.12, and which could be advected eastward through a mesoscale

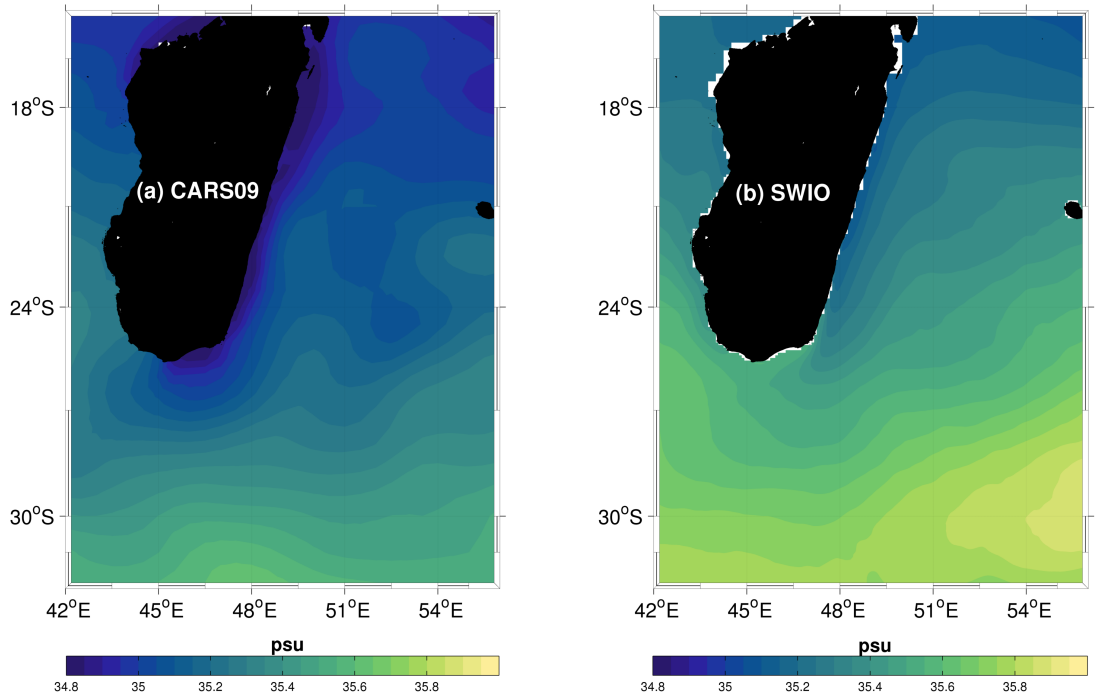


Figure. 4.12 Annual Climatology of sea surface salinity derived from (a) CARS09 and from the (b) SWIO model averaged over the 1993-2013 period.

eddy-field. The low-salinity signature of the SEMC is more pronounced in the CARS dataset compared to the model (SWIO configuration), and this could be due to the absence of river inputs in the model. However, SWIO still exhibits lower salinity in coastal areas.

The mean structures of the water column during the blooms of January 2008 (Figure 4.13) and March 2012 (Figure 4.14) are investigated using individual profiles of Argo floats. Two bloom profiles (denoted as 1 and 2) and two non-bloom profiles (denoted as 3 and 4) are surveyed. As observed in the mean vertical structure (Figure 4.11), the 2008 bloom is confined to a shallow (∼20.4 m) stratified mixed layer depth (Figure 4.13b). However, the vertical haline structure of the two bloom profiles varies, with profile 2 exhibiting higher salinity (∼35.5 psu) in the first 20 m compared to profile 1 (∼35.1 psu). Profile 1 is more equatorward compared to profile 2, and hence can possibly be

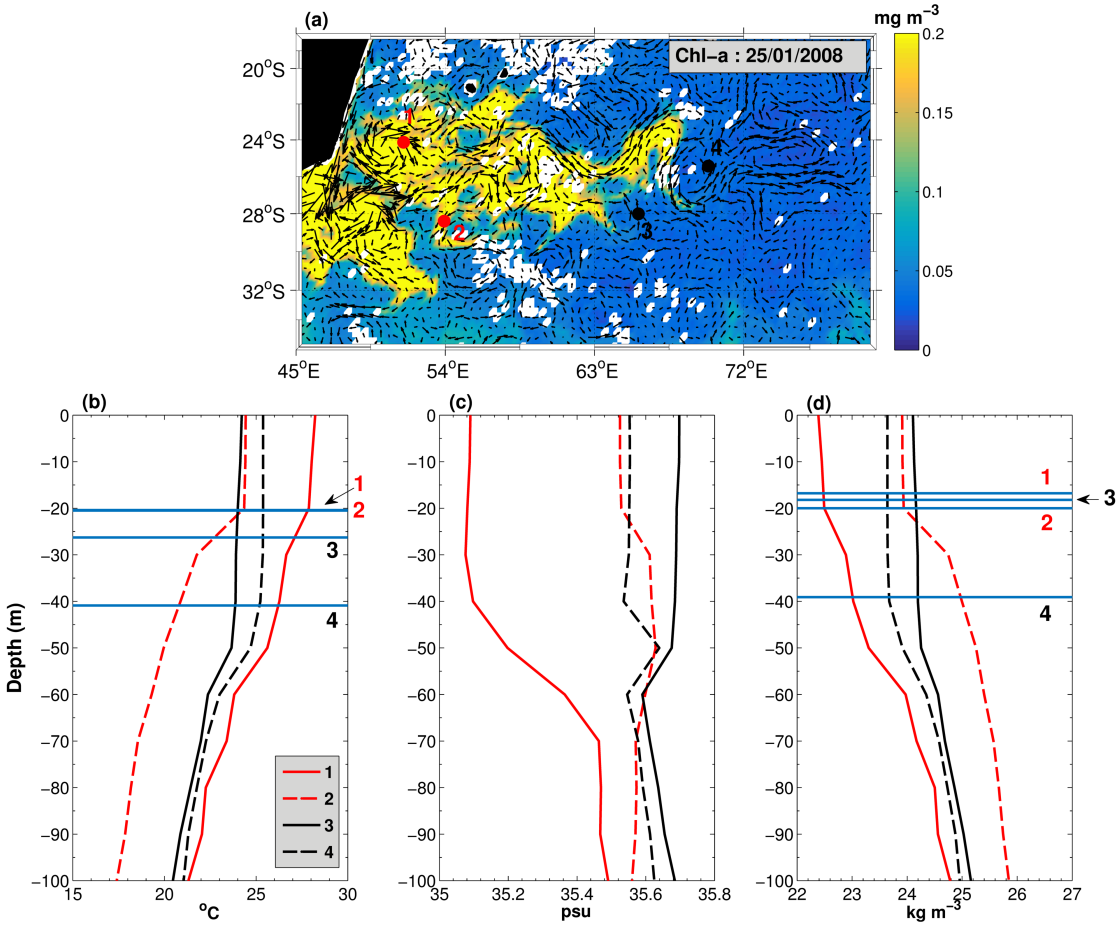


Figure. 4.13 A snapshot of ESA OC-CCI Chl-a data on 25th January 2008, with the positions of 4 floats. Floats 1 and 2 are located in an enhanced Chl-a region (bloom) whereas Floats 3 and 4 are located in a non-bloom region. The bottom pannels give the vertical structure at these 4 floats's location. The assigned blue lines display the mixed layer depth from each profile based on (b) temperature and (d) density threshold.

on the fresher side of the front. It is also located in a cyclonic eddy close to the coast, which could be advecting low-salinity SEMC waters away from the coast. Profile 2 exhibits close surface salinity compared to the mean salinity of the bloom profile on the saltier side of the front (Figure 4.11e). For non-bloom profiles (Profile 3 and 4), a deeper mixed layer (26.3 m for profile 3 and 40.9 m for profile 4) is observed, with a stable haline structure up to 100m depth (Figure 4.13c).

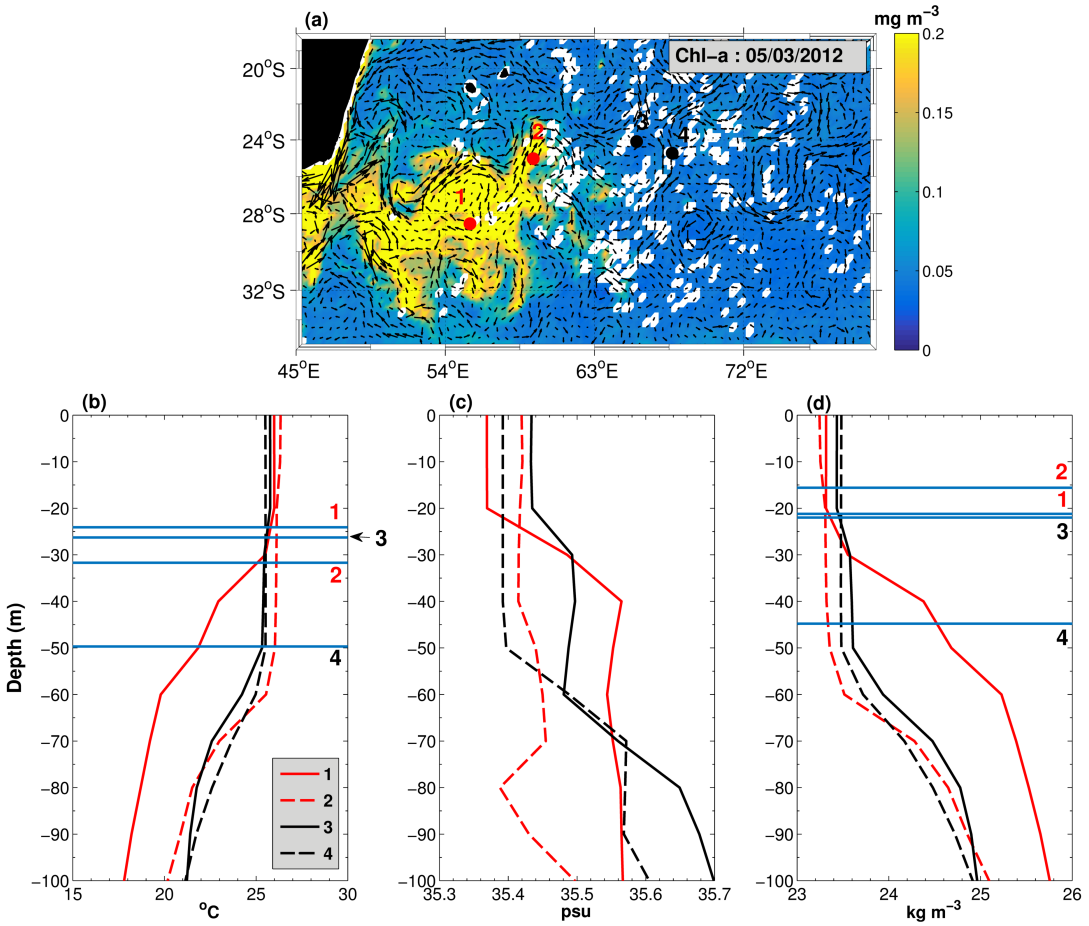


Figure. 4.14 Same as (Figure 4.13) but using a snapshot of ESA OC-CCI Chl-a data on 5th March 2012.

In early March 2012, the 2 bloom profiles exhibit different water column structures (Figure 4.14). Profile 1 shows a shallow stratified mixed layer (∼24.1 m) but enhanced Chl-a in profile 2 occurs within a less shallower mixed layer (∼31.7 m) (Figure 4.14b). As in January 2008, non-bloom profiles are found to have a deep mixed layer (Figure 4.14b), except profile 3 which has a mixed layer depth of 26.3 m (22 m) for the temperature (density) threshold. For the thermohaline structure, no big difference is observed in the salinities between bloom and non-bloom profiles. Profiles 1 and 2 exhibit close salinities, with profile 1 having lower surface salinity values. However, the salinity of profile 1 increases ∼20 m to ∼40 m by 0.2 psu. This is an indication of incom-

ing lower-saline water from the surface. Profile 2 remains quite stable to a depth of 75 m.

4.2.4 Summary

This section has shown that the South-East Madagascar Bloom exhibits substantial temporal and spatial variability. The bloom box used here is identical to the one used in *Uz* [2007] and it seems to be appropriate to capture the maximum spatial coverage of the bloom. We used this box to redefine a bloom index, by subtracting the austral winter bloom occurring in a similar-sized box further east. This new index gives us an insight on the timing, as well as the intensity of the bloom, which varies from month to month in austral summer. Spatially, it has been shown to arise at different latitudinal bands during some years, moving north and south from the mean latitude of 24°S-30°S. This meridional migration is, however, not linked to the SICC position. Its most eastward zonal extent also exhibits large variability, differing by ∼5-10° in longitude in some cases. Some co-occurrence with enhanced Chl-a concentration south-west of Madagascar exists, although a link which could explain the onset of enhanced Chl-a in both regions is not certain. The co-location of Argo profiles and high/low Chl-a patches have revealed that the bloom occurs in a low-salinity surface layer, within a shallow stratified mixed layer depth. This low-salinity signature associated with the bloom, compared to non-bloom profiles, is present on both sides of the salinity front in the bloom box. These fresher waters are speculated to arrive from an eastward advection of the coastally-trapped low saline EMC waters, and/or from upwelling of nutrient-rich waters.

4.3 Hypothesis Testing

Since it was first documented by *Longhurst* [2001], different hypotheses have been suggested to explain the mechanisms responsible for the onset of the South-East Madagascar Bloom. In this section, a quantitative assessment of each hypothesis will be

performed using longer available datasets.

The time-series of Chl-a concentration in the bloom region is a discontinuous one. Hence a continuous correlation between the bloom and the different variables associated with specific hypotheses cannot be performed. On this basis, we use a 'hypothesis-testing model' method to provide an indication of a possible validity of the specific hypothesis. The bloom-months are described as the month at which the bloom peaks during bloom years; whereas non-bloom months are January of each non-bloom year. The hypotheses are tested against the bloom and non-bloom months at zero, one-month, two-months and three months-lag. For each lag, values of the tested hypothesis, coinciding with the bloom/non-bloom months, are assigned and these are compared against different thresholds. The threshold of a specific lag which yields the maximum success rate in terms of occurrence/non-occurrence of the phytoplankton bloom over the 19-year dataset is retained and termed as an 'optimized threshold'. It should be noted that since 2011 was neither described as a bloom nor non-bloom year, it has been omitted in the statistics of this model.

For each figure in which different hypotheses are tested, the blue dotted line indicates the optimized threshold which gives maximum success rate, and the blue dots indicate the months where the hypothesis holds true. The success rate will depend on whether this hypothesis holds in both bloom and non-bloom years.

4.3.1 Mixed Layer Depth

Longhurst [2001] ascribed the bloom to a seasonal deepening of the mixed layer depth (MLD), modulated by the mesoscale eddy field in the region. This will entrain nutrient-rich deeper waters towards the surface, sustaining phytoplankton cells. *Srokosz and Quartly* [2013] showed that chlorophyll was confined to a shallow mixed layer (∼30m) by summer stratification, which could explain blooming of nitrogen-fixers. However, as

previously stated, this study uses data from 2005, a year where some high patches of Chl-a occur but which has not been defined as a bloom year following our threshold. The importance of stratification was further confirmed in the previous section, when analysing the mean vertical structure of the bloom using co-located Argo floats and high Chl-a patches. It should be noted that in the bloom region, the MLD is shallower (∼20-40 m) in the austral bloom period compared to winter when it reaches deeper levels, down to 60 m [*Raj et al.*, 2010]. Here, two MLD products [*de Boyer Montégut*, 2004; *Li et al.*, 2017b] are used to investigate *Longhurst* [2001]'s hypothesis. Due to a paucity of *in-situ* measurements in the region, some gaps in the data exist between 1998 and 2003.

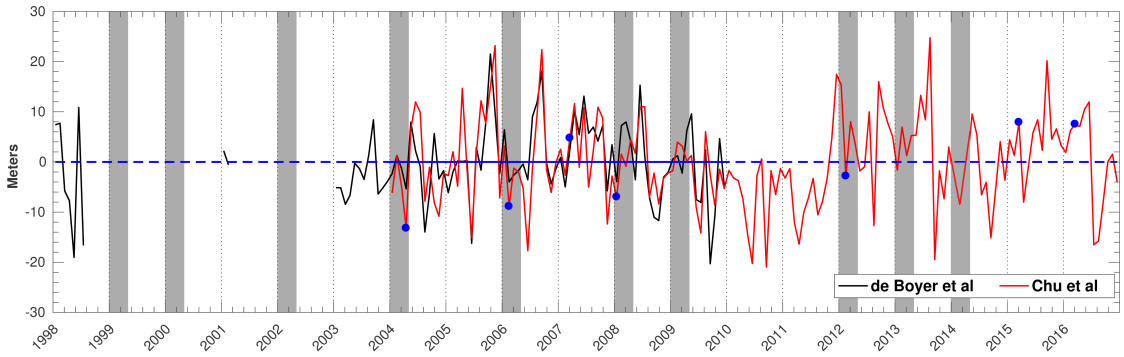


Figure. 4.15 Time series of mixed layer depth anomalies (m) from *de Boyer Montégut* [2004] (black line) and *Li et al.* [2017b] (red line) in the bloom box. The blue dotted line indicates an optimized threshold with the blue dots indicating months when the threshold works.

The hypothesis-testing model returned a success rate of 58% with a threshold of 0 m for the mixed layer depth anomaly, at 0-month lag. In some years during which the bloom occurs, the mixed layer depth gets shallower (2004, 2006, 2008 and 2012; Figure 4.15), indicated by blue dots below the threshold line. 2007, 2015 and 2016 exhibit a deeper mixed layer, consistent with no-bloom during these years. This is in contradiction to the *Longhurst* [2001] seasonal mixed layer deepening hypothesis, but consistent with *Srokosz and Quartly* [2013]. It should be noted that these are monthly averages and a better insight may require mixed layer depth data at higher temporal

resolution. Mesoscale eddies in the region could also modulate the MLD, variability which would be captured in monthly-averaged data.

Hence, it can be concluded that the bloom occurs in a shallower mixed layer compared to non-bloom years, as shown by *Srokosz and Quartly* [2013]. However, it should be questioned that if the MLD is the controlling factor of the bloom, why does it not occur in other years exhibiting shallow mixed layer, as per the optimized threshold? This apparent paradox implies that other mechanisms are likely to be important.

4.3.2 Plankton wave

Srokosz et al. [2004] described the South-East Madagascar Bloom as the first observed open ocean plankton wave which originates in the enhanced Chl-a region south of Madagascar. They described the bloom as a rapid eastward spread, with a combination of plankton growth and eddy diffusivity playing a role. If fast enough, this eastward propagation, related to eddy diffusion, would propagate against the typical mean flow, supposed here to be westward at the time of the study. However, the SICC was later revealed by *Siedler et al.* [2006] and *Palastanga et al.* [2007] and hence, the eastward plankton wave propagation is not against the mean flow as reported by *Srokosz et al.* [2004]. *Wilson* [2003] described a similar feature as *Srokosz et al.* [2004] in the oligotrophic North Pacific region, where advective effects are at play in a mean eastward flow. Nonetheless, the bloom regions remain a high mesoscale activity area and eddy diffusivity could still play a role.

To help assess the influence of eddies, an eddy diffusivity parameterization (A_H) in the bloom region (Figure 4.16) is computed from satellite altimetric observations of EKE. Generally, the product of the eddy length scale L_e and eddy velocity U_e is used to give an eddy diffusivity coefficient [*Sallée et al.*, 2008]. *Stammer* [1998] found a correlation between the dominant eddy scale and the deformation radius. Hence, the eddy length scale, L_e is approximated by the baroclinic Rossby radius of deformation, L_d [*Sallée*

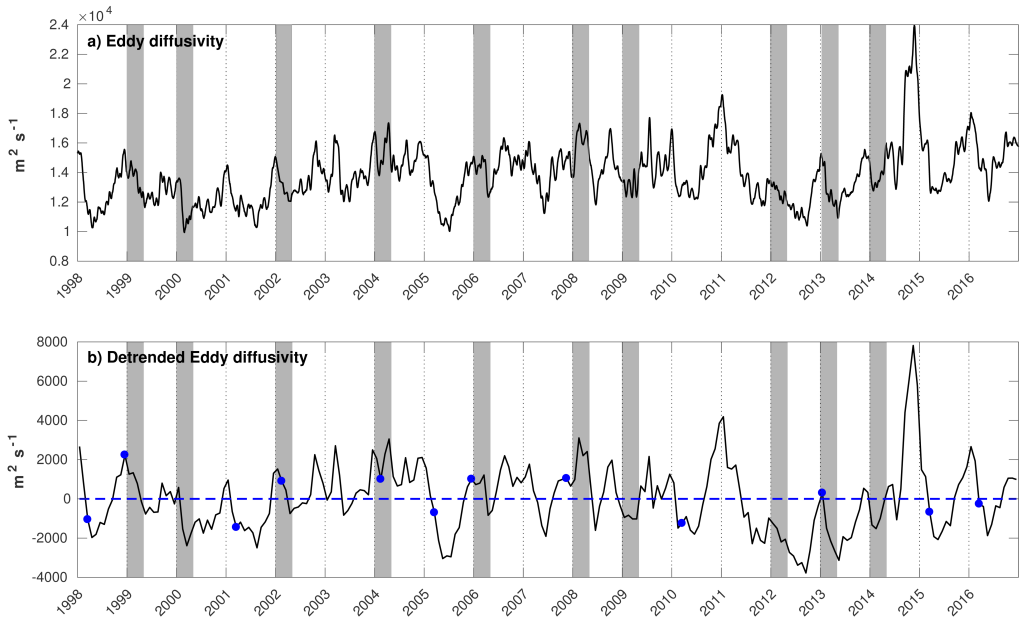


Figure. 4.16 (a) Daily and (b) detrended monthly time series of eddy diffusivity(A_H; m^2 s^{-1}) in the bloom box.

et al., 2008]. The square root of the EKE, $\sqrt{EKE}$, yields the eddy velocity.

Following [*Sallée et al.*, 2008], an eddy diffusivity coefficient can be inferred as follows:

$$A_H = \alpha \times \sqrt{EKE} \times L_d \tag{4.1}$$

Sallée et al. [2008] used an α value of 1.35 in the Southern Ocean. This value holds in energetic areas, with EKE higher than 0.015 [m^2 s^{-2}]. High EKE is observed south-east of Madagascar and hence this specific α could be used in this study. A high eddy diffusivity is expected to occur during bloom years, which would transport upwelled nutrients and subsequently growing plankton eastward, compared to non-bloom years. Owing to an increasing trend observed in the eddy diffusivity time series (Figure 4.16a), the dataset is detrended by its mean value, before applying the hypothesis-testing model.

A 67% success rate is observed, when the eddy diffusivity value for bloom (non-

bloom) months exceeds (does not exceed) a threshold of 0 at 1-month lag. The eddy diffusivity in 1999, 2002, 2004, 2006, 2008 and 2013, denoted as blue dots in Figure 4.16b, exceeds the optimized threshold and this could possibly contribute to the phytoplankton bloom. Lower diffusivity is observed in 1998, 2001, 2005, 2010, 2015 and 2016, in accordance to these being no-bloom years.

However, the high eddy diffusivity during 2011 could be responsible for the enhanced Chl-a patches, although it was neither characterized as a bloom nor a non-bloom year, due to the south-eastward propagation of Chl-a patches. Eddy diffusivity might play a role in the apparent eastward movement of some bloom events. Nevertheless, the presence of the mean eastward flow, namely the SICC, could have a more prominent impact on a possible eastward propagation of the high Chl-a signatures.

4.3.3 Iron Runoff

The hypothesis described by *Uz* [2007] suggested that an increased number of tropical cyclones hitting the eastern part of Madagascar will induce enhanced rainfall, ultimately contributing to the South-East Madagascar Bloom. Excess rainfall would induce river runoff, hence washing dissolved iron into the open ocean, which would then be transported poleward by the SEMC and advected eastward through the eddy field south-east of Madagascar. With nitrogen-fixers supposed to be dominant into the bloom region, these phytoplankton cells will utilize the incoming iron from river runoff and hence may bloom.

Using a longer dataset than *Uz* [2007], we investigated the concentration of rainfall in the region (47.5°E-52.5°E, 12.5°S-25°S). A lag between high (low) rainfall and the occurrence (non-occurrence) of the bloom is expected due to the time taken for the iron particles from land to be washed into the ocean, transported southwards by the SEMC and ultimately ending in the bloom vicinity. Through Lagrangian analysis, 2-3

months were calculated as the time taken for particles to propagate from the south-east Madagascar coast to the bloom region (see Figure 6 in [*Srokosz et al.*, 2015]).

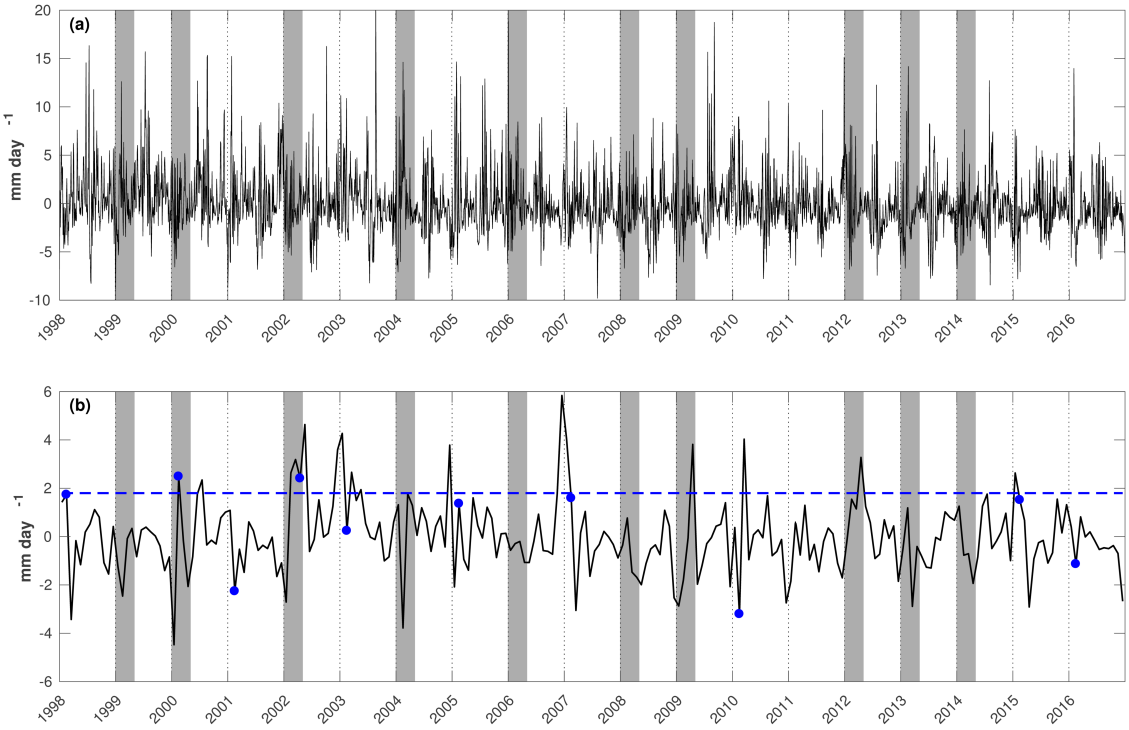


Figure. 4.17 Time series of CMAP (a) pentad precipitation anomalies (mm day^{-1}) and (b) monthly precipitation anomalies averaged over 47.5°E-52.5°E and 12.5°S-25°S, as in *Uz* [2007].

Peaks of CPC Merged Analysis of Precipitation (CMAP) pentad (5-days) rainfall anomalies are present in 1999, 2004, 2006, 2012 and 2013 (Figure 4.17a), co-occurring with the bloom period. The other years identified as bloom occurrence years do not seem to take place during high rainfall and its associated excess of river runoff. Using a monthly anomaly of precipitation in the box of interest (47.5°E-52.5°E and 12.5°S-25°S), our hypothesis-testing model yields a 56% success rate with a threshold of 1.8 mm day^{-1}, at a 2-month lag. This success rate, however, includes mostly the years of non-bloom occurrence (1998, 2001, 2003, 2005, 2010, 2015 and 2016; Figure 4.17b) compared to the occurrence ones (2000, 2002). The other years identified as bloom years do not seem to occur during high rainfall which would cause excess of river runoff.

The box used to define the bloom is quite large and hence the lag between the high rainfall and enhanced Chl-a would vary by a couple of months, depending on the advection speed in the vicinity. It should however be noted that since the CMAP rainfall uses a combination of satellite data, rain gauge and model output, rainfall may be underestimated to some extent.

4.3.4 Ekman Pumping

Ekman pumping (W_{ek}) represents the vertical velocities induced by wind stress curl at the base of the Ekman layer. Positive W_{ek} (positive vertical velocities) leads to an uplift of isotherms and colder, nutrient-rich waters being brought to the surface. On the other hand, a negative W_{ek} is associated with a deepening of the isotherms. *Uz* [2007] and *Raj et al.* [2010] stated that the W_{ek} in the region is too small to have any influence on the bloom. Nevertheless, this region is prone to tropical cyclones in austral summer, and these climatic events are known to largely influence the W_{ek} and eventually the primary production [*Chacko*, 2017; *Lin et al.*, 2003]. The W_{ek} is calculated as:

$$W_{ek} = \frac{1}{\rho_w f} curl\tau \tag{4.2}$$

where ρ_w is the density of sea water (1025 kg m^{-3}), f the Coriolis parameter and τ is the wind stress component.

QSCAT data are only available from 2000 to 2009, whereas ERA-Interim, being a reanalysis product, is available throughout the whole time series of interest. QSCAT data exhibit W_{ek} of higher intensity compared to ERA-Interim (Figure 4.18) (refer to *Collins et al.* [2012] for comparison). This difference could be due to the higher spatial resolution of QSCAT as well as the smoothing in the ERA-Interim data. A running

mean of 2 weeks is performed on the daily values of the two datasets, to observe any episodic wind events which might lead to upwelling. Larger W_{ek} prevails in the bloom region in austral summer compared to austral winter (Figure 4.18a). The main signal, however, is the highly positive W_{ek} in 2004, which could possibly play a major role in the 2004 bloom. 2005 seems to exhibit high W_{ek} too but was not accounted as a bloom year by our threshold.

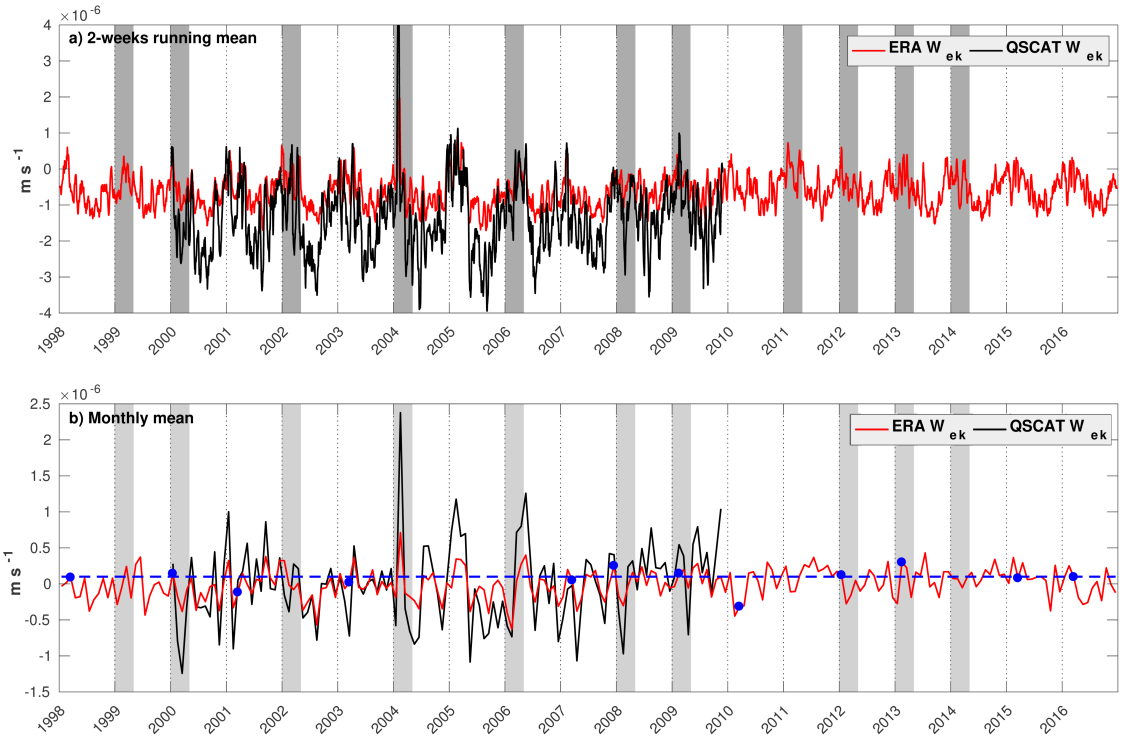


Figure. 4.18 Time series of (a) 2-weeks running mean of daily W_{ek} (m s^{-1}) and (b) monthly anomaly of W_{ek}, computed from QSCAT data (black line) and ERA-Interim data (red line) in the bloom region

Although, higher frequency winds could have an important impact on the bloom, the hypothesis-testing model is applied on monthly means of W_{ek} (Figure 4.18b), as a monthly integrated view is of interest here. A W_{ek} threshold greater than 0.1x10^{-6} m s^1 for bloom and non-bloom occurrence at 1-month lag yielded a 67% success rate from the hypothesis-testing model. Five years, namely 2000, 2008, 2009, 2012 and 2013, were correctly hypothesized by the optimized threshold as bloom years. A significant peak

is observed in 2004, a year of bloom occurrence. This peak was, however, picked at a 2-month lag of W_{ek}. During this year, the bloom peaks in April with the W_{ek} happening in February. The enhanced vertical velocities in the bloom region may have largely contributed to the bloom by upwelling nutrient-rich waters. This is consistent with the fact that the 2004 bloom seems to be disconnected from the coast of Madagascar.

4.3.5 Upwelling South of Madagascar

Current-induced upwelling south of Madagascar has been hypothesized by various studies [*Lévy et al.*, 2007; *Raj et al.*, 2010; *Srokosz and Quartly*, 2013] to be the main mechanism that contributes to the bloom and which controls its interannual variability. This upwelling can influence the bloom through two different ways. It will bring deep nutrient-rich waters to the surface, which will be advected eastwards through the mesoscale eddy field [*Lévy et al.*, 2007; *Raj et al.*, 2010]. In addition, owing to the possible presence of nitrogen fixers namely *Trichodesmium* and *Rhizosolenia/Richelia*, dominating near the Madagascar coasts and further to the east respectively suggests the importance of dissolved iron in the region. *Srokosz and Quartly* [2013] suggest an input of iron from the sediments found on the continental shelves east and south of Madagascar, which are then upwelled to the surface and transported eastward towards the bloom region. *Srokosz et al.* [2015] tested this hypothesis using Lagrangian particles and demonstrated that the spatial dispersion of the advected particles have a significant interannual variability, as is the case for the phytoplankton bloom. However, using a non-assimilated high-resolution model for the Lagrangian tests, they could not replicate the interannual variability of the phytoplankton cells dispersion, as observed in remotely-sensed data.

Two upwelling indices are used to investigate possible relationships between the upwelling south of Madagascar and the phytoplankton bloom. The first one is a sea surface temperature (SST) based coastal upwelling index (CUI) (Figure 4.19a), as in

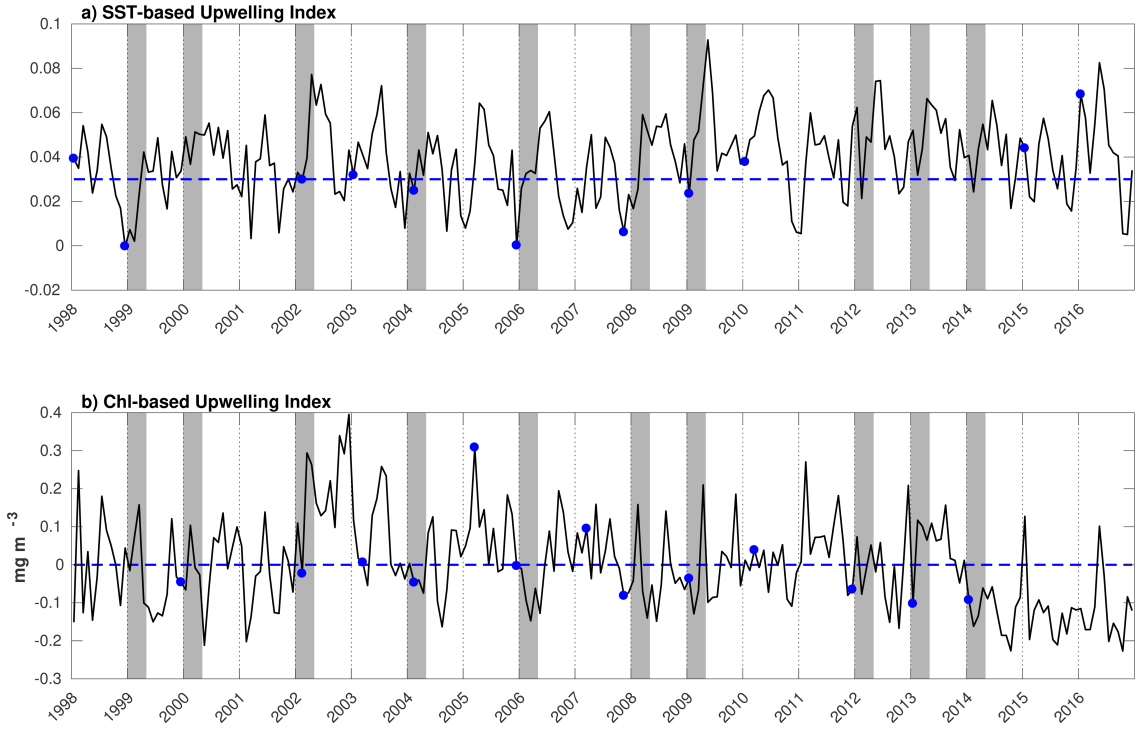


Figure. 4.19 (a) Upwelling index computed from sea surface temperature as in *Ramanantsoa et al.* [2018a]. (b) Chl-a anomalies (mg m^{-3}) around the southern tip of Madagascar, on the continental shelves.

Ramanantsoa et al. [2018a], in which the box chosen was adapted to report the SEMC influence on the coastal upwelling. The second index was based on the Chl-a concentration anomaly on the continental shelves south of Madagascar, inshore of the SEMC. Chl-a concentration is analogous to upwelling as nutrient-rich waters being brought to the surface would infer an increase in surface phytoplankton cells concentration. It should be noted that we do not expect any relationship between the two indices, given the larger spatial area considered for the Chl-based upwelling index. As suggested by previous studies [*Lévy et al.*, 2007; *Raj et al.*, 2010; *Srokosz and Quartly*, 2013], upwelling in this region will eventually lead to the South-East Madagascar Bloom. Given the very turbulent mesocale field in the region, associated with the SICC, one would expect a lag between the upwelling and the bloom. With the SICC having a mean speed of 9-18 cm s^{-1} [*Menezes et al.*, 2014] in the region, a lag of 1-4 months between the upwelling and the onset of the bloom would be expected, depending on the current speed in the region.

One would expect a higher upwelling intensity, hence bringing nutrient-rich or dissolved iron particles to the surface and triggering the bloom. The SST-based CUI produces a 61% success rate of bloom/non-bloom occurrence, observed at 2-months lag when the CUI is lower than an optimized threshold of 0.03, contrary to expectation. 1999, 2002, 2004, 2006, 2008 and 2009 were bloom years when CUI was lower than the threshold 2 months before. Interestingly, the upwelling intensity was at its lowest during the 3 major blooms (1999, 2006 and 2008; Figure 4.19a). This leads to an important question as to which mechanism is responsible for a decreased upwelling in this region, and if this mechanism can influence the South-East Madagascar Bloom. The structure and intensity of the SEMC might possibly be responsible for this upwelling dampening.

For Chl-based upwelling intensity, 72% success rate was observed at 2-months lag with the bloom, having a threshold of lower (higher) than 0 mg m^{-3} for bloom occurrence (non-occurrence). Lower Chl-a concentration is observed on the continental shelf south of Madagascar, 2 months before the occurrence of the bloom. This is in contradiction with previous hypothesis but consistent to SST-based CUI (Figure 4.19a), where a decrease in upwelling intensity south of Madagascar seems to be associated with the South-East Madagascar Bloom.

4.4 Influence of large-scale climate modes

This section investigates the possible impacts of large-scale climate phenomena such as the El Niño Southern Oscillation (ENSO), Indian Ocean Dipole (IOD) and Subtropical Indian Ocean Dipole (SIOD) on the Madagascar Phytoplankton bloom. Oceanic and atmospheric anomalies due to large scale climate modes will impact the Indian Ocean [*Reason et al.*, 2000; *Saji et al.*, 1999] and can exert substantial influence on the variability of biogeochemical processes in the western Indian Ocean [*Currie et al.*, 2013;

Dilmahamod et al., 2016; *Vinayachandran et al.*, 2007]. In the South Indian Ocean, the SIOD [*Behera and Yamagata*, 2001; *Reason*, 2001], which exhibits warmer SST and associated anticylonic wind anomalies when its positive phase south of Madagascar, could possibly also influence the biogeochemistry of the region.

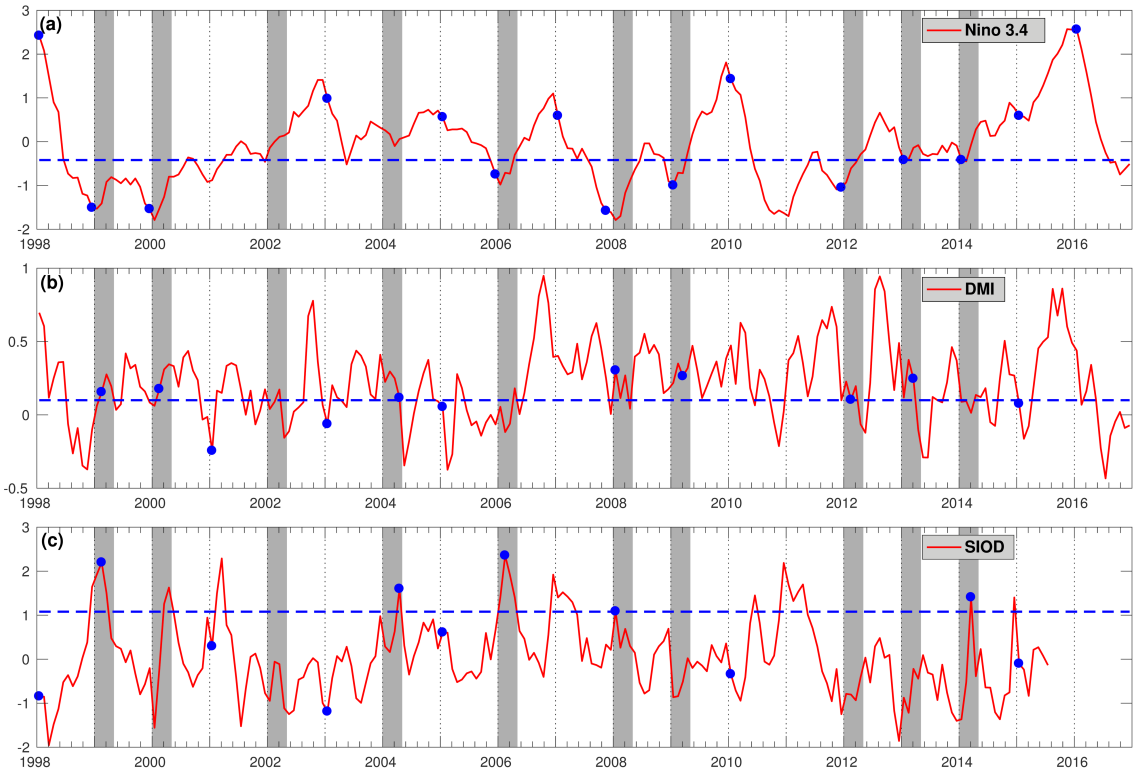


Figure. 4.20 Time series of (a) Nino 3.4 Index (b) Dipole Mode Index and (c) SIOD Index, against years of bloom occurrence (gray) shading.

El Niño (La Niña) events have been shown to induce anticyclonic (cyclonic) wind stress curl in the eastern Indian Ocean. This in turn will generate downwelling (upwelling) westward propagating Rossby waves at a speed of ~ 0.24 m s^{-1} [*Gnanaseelan and Vaid*, 2010] which may lead to a thermocline deepening (shallowing) in the western Indian Ocean, south of 10°S [*Rao and Behera*, 2005; *Yu et al.*, 2005], and may eventually influence phytoplankton biomass. The IOD is also associated with westward propagating Rossby waves, which deepen the thermocline in the western Indian Ocean during its positive phase [*Chakravorty et al.*, 2014; *Trenary and Han*, 2012].

The relationships between the three climate modes modulating the Indian Ocean and the South-East Madagascar Bloom are investigated using the hypothesis-testing model. Interestingly, the Nino 3.4 index yields an 84% success rate at 1-month lag, with a threshold of less than -0.4°C for bloom occurrence, corresponding to La Niña events (Figure 4.20a). 7 out of the 8 non-bloom years occur during a Nino 3.4 index lower than -0.4°C , with 8 out of 10 bloom events occur with Nino 3.4 index less than -0.4°C (weak and strong La Niña). 1999 and 2008, two of the three major bloom events occur during strong La Niña events. A 58% success rate is achieved at a 0-month lag with the Dipole Mode Index (DMI) (Figure 4.20b), with a threshold greather than 0.1°C for bloom occurrence. The hypothesis-testing model produces a 63% success rate with SIOD at 0-month lag, with a threshold greater than 1.8°C for a bloom year to occur.

These climate modes are known to modulate the oceanic circulation around Madagascar [*Palastanga et al.*, 2006]. During La Niña and negative IOD, the tropical gyre strengthens and/or migrates southwards. Hence the South Equatorial Current (SEC) is increased, and subsequently the SEMC gets stronger, with a lag of 13 to 25 months [*Palastanga et al.*, 2006]. The opposite occurs during El Niño and positive IOD. However, due to the delayed-lag between the onsets of the phenomena, the influence of La Niña or negative IOD is subtle on the bloom even though there seems to be a relationship in Figure 4.20a.

4.5 Local currents: SEMC and SICC

The South-East Madagascar Bloom is found in a region of complex oceanic circulation with two main mean flows namely the south EMC, the southern part of the EMC after it rounds the southern tip of Madagascar and the SICC (Figure 4.21). Their intensity, apart from being modulated by large scale climate modes [*Palastanga et al.*, 2006;

Siedler et al., 2009] and mesoscale eddies [*Menezes et al.*, 2014], can possibly have an impact on the bloom.

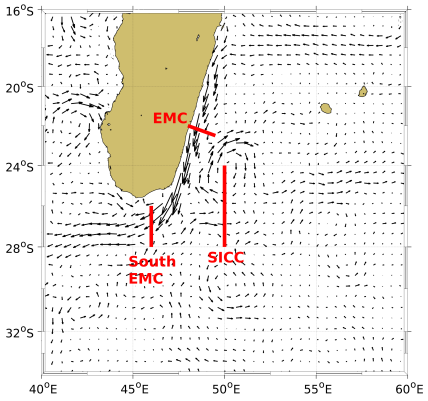


Figure. 4.21 Mean AVISO geostrophic velocities (m s^{-1}) during the bloom period. The red lines indicate the location of the different transects; the EMC (as per *Ponsoni et al.* [2015, 2016]), South EMC and SICC.

In 2000, 2012 and 2014, the intensity of the poleward-EMC decreases during the bloom months (Figure 4.22a), although the signature is not very clear. However, in other years, no significant differences are observed. Interestingly, during some of the bloom years (1999, 2002, 2004, 2012, 2013 and 2014), a more offshore equatorward flow is observed. This reduction in EMC and the more-offshore equatorward flow is likely due to mesoscale eddies interacting with the current. This could disrupt the EMC and advect nutrients or phytoplankton biomass offshore towards the bloom region. This mechanism would be in accordance with the fresher waters found to be associated with the high Chl-a patches (see section 4.2.3), which was hypothesized to be sourced from the low-salinity EMC waters.

Analysing Figure 4.22b shows no clear connection between the south-EMC and the bloom, except in 1999 and 2004 during which westward flow is weakly reduced, with eastward transport along the southern part of the transect. The region exhibits shedding of eddies from the EMC and these can induce a reduced intensity or opposite flow

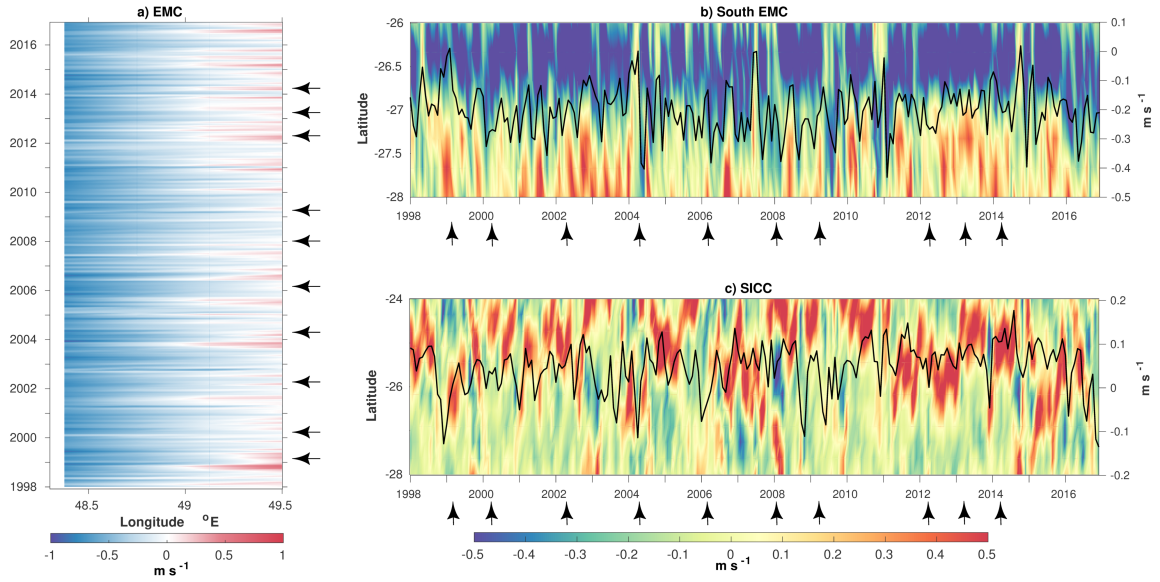


Figure. 4.22 Hovmöller of (a) alongshore geostrophic velocities (m s^{-1}) of the EMC at around 22°S; (b) zonal component of the South EMC with the mean velocity (black line) overlaid; and (c) zonal component of the SICC with its mean velocity (black line) overlaid. The mean velocities are calculated over the specific latitude ranges for each transect. The arrows indicate the bloom years.

of the EMC. The SICC lies in the bloom region and varies latitudinally (Figure 4.22c). Due to the arrival of westward-propagating eddies in the Madagascar Basin, the SICC is disconnected in some periods and varies significantly in intensity. In 1999, 2004 and 2006, the SICC is reversed with a mean flow towards the west, and this co-occurred with the phytoplankton blooms during these 3 years. However, no other direct correlation with other bloom years exists. It should be noted that the vicinity of the bloom region is dominated by the main currents as well as incoming mesoscale eddies. Hence, the mean current-eddy interaction could hinder any clear relationship of the mean flows and the bloom years.

The different hypothesss which have been documented in previous studies to explain the initiation of the South-East Madagascar Bloom are summarized in Table 4.2. The bloom intensities are defined as normal (+) and major bloom (++) (Figure 4.4b). The years for which the hypothesis can elucidate the occurrence and non-occurrence of the bloom are labelled by a '✓'. The hypothesis-testing model we used here gave an

optimized threshold of the physical variable at play in each hypothesis, at different lags. These are labelled by a '✓'. The success rate of the specific threshold for predicting bloom and non-bloom occurrence is also displayed. It should be noted here that if we hypothesize that all years are bloom (non-bloom) occurrence (a null hypothesis), this will yield in a success rate of 56% (44%). Hence, the different hypotheses with a success rate close to less than these values can be discarded.

Table 4.2 A summary of the different hypotheses linked to the South-East Madagascar Bloom, with the bloom intensity denoted by + (Normal Bloom) and ++ (Major Bloom). Hypotheses which hold true, according to the optimized threshold in the hypothesis-testing model, during bloom and non-bloom occurrence are denoted as ✓. The lag at which the hypothesis holds and their specific success rate are also stated. Bloom years in the first column are listed in bold and absence of data for some years are denoted as 'N/A'

Years	Bloom Intensity	MLD	Plankton Wave	Iron/River Runoff	W_{ek}	CUI - SST	CUI - Chl	ENSO	IOD	SIOD
1998		N/A	✓	✓	✓	✓		✓		✓
1999	++	N/A	✓			✓		✓	✓	✓
2000	+	N/A		✓	✓		✓	✓	✓	
2001		N/A	✓	✓	✓				✓	✓
2002	+	N/A	✓	✓		✓	✓			
2003		N/A		✓	✓	✓	✓	✓	✓	✓
2004	+	✓	✓			✓	✓		✓	✓
2005			✓	✓			✓	✓	✓	✓
2006	++	✓	✓			✓	✓	✓		✓
2007		✓		✓	✓		✓	✓		
2008	++	✓	✓		✓	✓	✓	✓	✓	✓
2009	+				✓	✓	✓	✓	✓	
2010			✓	✓	✓	✓	✓	✓		✓
2011	?	?	?	?	?	?	?	?	?	?
2012	+	✓			✓		✓	✓	✓	
2013	+		✓		✓		✓	✓	✓	
2014	+						✓	✓		✓
2015		✓	✓	✓	✓	✓		✓	✓	✓
2016		✓	✓	✓	✓	✓		✓		
Lag		0	1-month	2-months	1-month	2-months	2-months	1-month	0	0
Success Rate		58%	67%	56%	67%	61%	72%	83%	61%	61%

Although some of the hypotheses can explain some of the bloom events, there is not one hypothesis which can explain all the bloom events. La Niña came out with the most success rate, together with the upwelling index (Chl-a based) south of Madagascar. W_{ek} and the eddy diffusivity coefficient also seem to play a role. A very important signal is the occurrence of the major bloom (1999, 2006 and 2008), 2 months after the upwelling intensity (SST-based; *Ramanantsoa et al.* [2018a]) is almost completely dampened. Either a combination of physical processes or another hypothesis which

has not yet been described, is responsible for the onset of this sporadic bloom.

4.6 Discussion and Summary

The South West Indian Ocean exhibits an intriguing biophysical feature, known as the South-East Madagascar Bloom. Occurring in austral summer, the bloom displays substantial temporal and spatial variability. Using a 19-year time-series of ocean colour satellite data, this chapter provides an updated characterization of the bloom. A new bloom index is defined, based on *Uz* [2007], by subtracting the Chl-a concentration in a box further offshore from the bloom box shown in *Uz* [2007]. This new index provides a clear and improved diagnosis of the timing and intensity of the South-East Madagascar Bloom.

From this bloom index, a minimum Chl-a concentration threshold of 0.07 mg m^{-3} was assigned, from which bloom and non-bloom years were differentiated. Bloom years were further subdivided into normal and major blooms, by a 0.16 mg m^{-3} threshold, with three major events occurring in 1999, 2006 and 2008. However, no clear evidence of a specific initiation or dissipation month could be perceived, with enhanced Chl-a starting and reaching its climax at different months for different bloom years. The filamentous nature of this bloom varies significantly with the mean bloom structure occurring at a mean latitude of 24°S-30°S, and a mean zonal extent from the coasts to ∼65°E. This spatial extent displays some variability with the 2008 bloom extending up to ∼75°E, whilst the 2012 bloom is located more poleward (25°S-34°S). The bloom co-occurs in a region of salinity front, which varies latitudinally from year to year. High Chl-a patches are found to be mostly on the fresher side but are also observed on the saltier side of this front. An analysis of co-located Argo profiles and high/low Chl-a patches confirmed that the bloom develops in a shallow mixed layer, and exhibits low salinity at the surface on each side of the front. This low-salinity water could possibly

be due to an inflow from the SEMC.

This extended Chl-a time series, together with other physical variables is used to review the different hypotheses which have been presented by previous studies. *Longhurst* [2001] suggested a deepening of the mixed layer, associated with the mesoscale eddies in the region. This is consistent with previous studies [*Kumar et al.*, 2014; *Lévy et al.*, 2007; *Resplandy et al.*, 2009] where a deepening of the MLD erodes the nutricline, bringing nutrient-rich waters to the surface and promoting phytoplankton production. However, in the South-East Madagascar Bloom region, the study of *Srokosz and Quartly* [2013] as well as the analysis of the mean vertical structure of the water column (section 4.2.3) (Figure 4.11) showed that the feature occurs within a shallow mixed layer. This behaviour is more representative of high-latitude blooms where phytoplankton biomass are preserved in nutrient rich and well-lit stratified waters, occurring due to seasonal warming [*Yoder and Kennelly*, 2003]. A shallow mixed layer south-east of Madagascar may possibly be associated with vertical stability, allowing phytoplankton density to accumulate at the surface [*Niu et al.*, 2016]. The hypothesis-testing model displayed a correct prediction of shallowing (deepening) of MLD during bloom (non-bloom) years at only 58% over 13 years of dataset. Associated environmental factors, such as wind mixing may contribute to the episodic shallowing/deepening of the MLD, hence stratifying or de-stratifying the water column. This episodic variation in the MLD could not be investigated in this study due to the lack of a higher temporal frequency mixed layer depth dataset [*Gregg and Conkright*, 2001; *Yoder et al.*, 1993].

Wind stress events have been shown to influence phytoplankton blooms in other parts of the ocean [*Koné et al.*, 2009; *Yamada et al.*, 2004; *Zhang et al.*, 2016]. Episodic wind events will influence the mixed layer, hence the stratification, as well as induce positive/negative W_{ek}, impacting the input of nutrients into the euphotic zone, and this potentially playing a role in the South-East Madagascar Bloom. The hypothesis-testing model correctly predicted the bloom and non-bloom occurrence at 67% with a 1-month

lag. The highly-significant 2004 positive W_{ek} was observed 2 months prior to the peak of the bloom. Enhanced vertical velocities will bring nutrients to the surface, hence promoting phytoplankton production. It is important to note that this event did not induce a deepening of the MLD, as expected.

Srokosz et al. [2004] proposed the phytoplankton bloom as a plankton wave feature against the mean westward flow. However, it was later found that the main oceanic circulation in this region is dominated by the shallow, eastward flowing SICC [*Palastanga et al.*, 2007; *Siedler et al.*, 2006]. Hence, a plankton wave is still possible but not necessary to explain the eastward propagation of the bloom, consistent with the mean flow in the region. The SICC is modulated by mesoscale eddies [*Menezes et al.*, 2014] and hence associated eddy diffusivity, together with simultaneous plankton growth, could be important. 67% of the events (bloom and non-bloom) were successfully predicted at a 1-month lag. The three major blooms exhibit high eddy diffusivity compared to the normal blooms. No bloom occurs in 2015 although the strongest eddy diffusivity signal occurs in December 2014. Coastal upwelling as a bloom initiation mechanism [*Lutjeharms and Machu*, 2000; *Srokosz et al.*, 2004], might possibly hinder the enhancement of coastal phytoplankton and hence hamper a bloom during high eddy-diffusivity no-bloom years.

Uz [2007] described a hypothesis involving tropical cyclones which would bring positive rainfall anomalies over Madagascar. These would then increase river runoff into the ocean together with iron particles, thereby fertilizing the bloom region. A lag of 2-3 months [*Srokosz et al.*, 2015] is expected between the peaks of rainfall and the onset of the bloom for this hypothesis to be valid. The highest success rate was obtained at two-months lag, accounting for 56% of correct prediction. Poleward transport by the SEMC followed by an eastward advection through the mesoscale eddies could be the common route taken by the iron particles after river run-off. A quicker route, in the case of an early destabilization of the SEMC, could ultimately bring these elements quicker

into the bloom region, contributing to the onset of the enhanced Chl-a concentration.

The highest success rate yielded from the hypothesis-testing model results from La Niña, at 83%. The impact of climate modes on the region involves the strengthening or weakening of the main currents in the vicinity. ENSO can influence the intensity as well as the position of the South Indian Ocean tropical and subtropical gyres, hence modulating the flow of the SEMC [*Palastanga et al.*, 2006]. This increase/decrease in the intensity of the SEMC may eventually influence the upwelling south-east and south of Madagascar [*Lutjeharms and Machu*, 2000; *Machu et al.*, 2002]. This upwelling has been suggested to be the source of nutrients or dissolved iron particles [*Lévy et al.*, 2007; *Raj et al.*, 2010; *Srokosz and Quartly*, 2013]. Nonetheless, the upwelling index, based on SST [*Ramanantsoa et al.*, 2018a], intensity seems to be weak prior to the bloom (Figure 4.19a), and hence does not corroborate these studies.

A revisit of the different hypotheses presented in preceding studies concluded that either combination of different physical mechanisms are at play in initiating and sustaining the South-East Madagascar bloom, or a new hypothesis needs to be proposed to explain the bloom. Analysing composites data of AVISO mean sea level anomalies and geostrophic velocities during bloom and non-bloom years (Figure 4.23) reveals a compelling feature. An eddy dipole (cyclonic and anticyclonic) exists near the south-eastern coast of Madagascar during the bloom, a feature which is completely absent during non-bloom years. This dipole characteristic suggests a new hypothesis which consists of an early destabilization of the SEMC before it reaches the southern tip of Madagascar, hence advecting nutrient/trace elements/phytoplankton biomass into the Madagascar Basin.

The results of this chapter corroborate with this new hypothesis. The occurrence of the phytoplankton bloom has been shown to arise within a shallow-stratified layer, with a low salinity signature at the surface compared to the surroundings. The SEMC

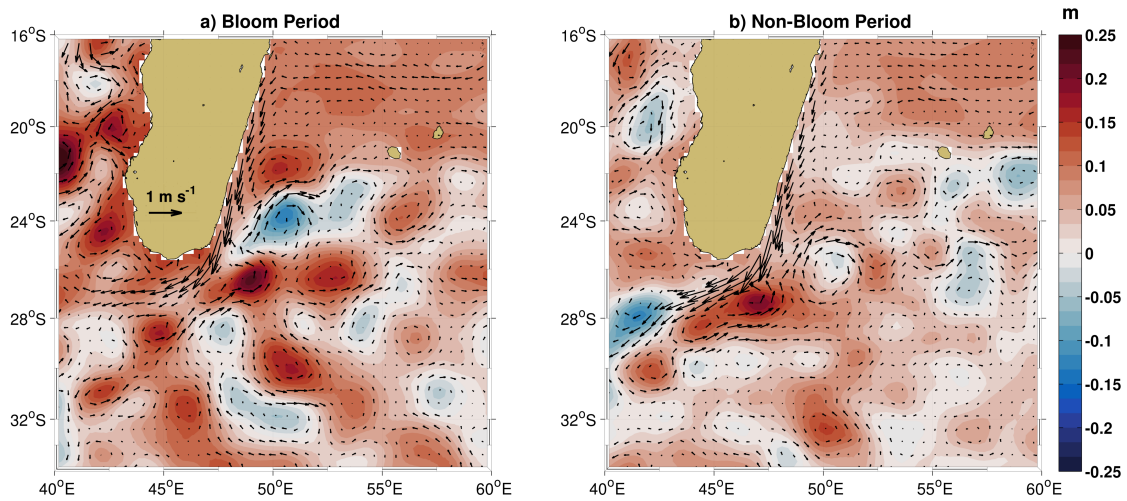


Figure. 4.23 Mean sea level anomaly (SLA; m) overlaid with surface geostrophic velocities from AVISO, (a) one month before and during peak month of major bloom years identified by our threshold; and (b) January-February of non-bloom years.

exhibits low salinity waters (Figure 4.12), which, through a possible destabilization by the dipole structure, will induce an eastward advection of this water mass into the bloom region, before it reaches the southern tip of the island. The SEMC is known to largely influence the coastal upwelling south of Madagascar [*DiMarco et al.*, 2000; *Lutjeharms and Machu*, 2000; *Machu et al.*, 2002; *Ramanantsoa et al.*, 2018a]. Hence a destabilization of the SEMC further north means a reduced current-driven upwelling south of Madagascar. This is consistent with our results of hypothesis-testing between the CUI and the bloom, with a reduced upwelling intensity occurring during 6, out of 10 bloom years (Figure 4.19a). The upwelling intensity is also observed to be at its minimum during 1999, 2006 and 2008, years described as major bloom occurrence. This destabilization process could also be consistent with the hypothesis of *Uz* [2007], with increased river runoff brining more nutrients into the SEMC, which could then be transported into the bloom region without passing through the southern tip of Madagascar.

This chapter has demonstrated the conflicting results of the previous bloom hypotheses and highlighted the potential importance of mesoscale eddies for the South-East

Madagascar Bloom. The presence of these features south-east of Madagascar can possibly destabilize the local regime of the SEMC and advect particles (nutrients or trace elements or phytoplankton biomass) into the bloom region, hence driving it. Simultaneously, mesoscale eddies can impact the vertical structure of the water column by inducing upwelling. Using a high-resolution coupled biophysical model together with observational data, the new hypothesis presented here will be investigated in the next chapter.

Chapter 5

Local Influences of the South-East Madagascar Current on the South-East Madagascar Bloom

5.1 Introduction

A unique and intriguing aspect of the biologically oligotrophic South-West Indian Ocean is the occurrence, in the Madagascar Basin, of a sporadic phytoplankton bloom, the South-East Madagascar Bloom. Prevailing in austral summer, this dendritic feature shows substantial variability in terms of temporal and spatial extent. With respect to ocean biology, it has been described as one of the most compelling features of interannual variability, after El Niño [*Srokosz and Quartly*, 2013; *Uz*, 2007]. When fully developed, chlorophyll-a concentration (Chl-a) can reach values greater than 1 mg m^{-3}, with some patches reaching 2-3 mg m^{-3} [*Longhurst*, 2001], and can extend up to the coast up to 70°E, covering 1% of the world's ocean surface area. The importance of blooms lies in their role in carbon storage and their ability to regulate atmospheric carbon dioxide [*Lévy et al.*, 2012], biogeochemical cycling of elements [*Naik et al.*, 2015] and life in the oceans.

Previous studies with various outcomes have addressed the physical mechanisms responsible for the onset and distribution of the bloom [*Huhn et al.*, 2012; *Lévy et al.*, 2007; *Longhurst*, 2001; *Raj et al.*, 2010; *Srokosz and Quartly*, 2013; *Srokosz et al.*, 2004, 2015; *Uz*, 2007], but none have been as yet clearly substantiated. A review of previously

introduced physical mechanisms associated with the bloom was proposed by *Srokosz and Quartly* [2013]. *Longhurst* [2001] was the first to describe the seasonal modulation of the bloom, ascribing it to a co-occurring mixed layer deepening and strong mesoscale eddy-field, which regulates the input/entrainment of nutrients into the photic zone and hence causing a Chl-a enhancement. Subsequent studies confirmed the importance of the highly energetic mesoscale field south-east of Madagascar in dispersing nutrients or biomass [*Huhn et al.*, 2012; *Srokosz and Quartly*, 2013; *Srokosz et al.*, 2015; *Uz*, 2007].

Using cruise datasets, *Poulton et al.* [2009] showed that nitrogen-fixing phytoplankton cells namely *Trichodesmium* and *Richelia/Rhizosolenia* are present in the bloom region. However, this cruise occurred in 2005 and following the bloom index by *Uz* [2007], this specific year was defined as a non-bloom year. *Uz* [2007] proposed that washed off riverine iron particles, modulated by the passage of tropical cyclones over Madagascar, would flow poleward with the South-East Madagascar Current (SEMC) and would be advected eastward through mesoscale eddies, hence fertilizing the bloom area. *Srokosz and Quartly* [2013] questioned the origin of these iron particles as major Madagascan rivers flow into the Mozambique Channel. Thus, they proposed the continental shelves east and south of Madagascar as new sources of dissolved iron. Previous studies have shown that continental shelves can be a primary source of iron in coastal areas, and to the open ocean through current/eddy interactions [*Dale et al.*, 2015; *Jeandel et al.*, 2011; *Johnson et al.*, 1999]. Using an eddy-resolving simulation together with a Lagrangian particle tracking scheme, *Srokosz et al.* [2015] showed that sediments could be advected from Madagascar coasts to the open ocean, with the advection variability dictating the interannual variability of the bloom.

In chapter 4, a new bloom index was defined, based on the index initially proposed by *Uz* [2007], by subtracting the mean Chl-a concentration in a box further offshore from the bloom box shown in *Uz* [2007]. This allowed us to grasp a better diagnosis of the timing and intensity of the South-East Madagascar Bloom. Occurring at a mean

latitude range of 24°S-30°S, the bloom extends from the coast up to ∼65°E. However, it exhibits large zonal and meridional variability, with a more poleward bloom in 2012, at latitude 25°S-34°S, and extending up to ∼75°E in 2008. An analysis of co-located Argo profiles and high/low Chl-a patches revealed the bloom to be confined to a shallow-stratified mixed layer, exhibiting low-salinity water at the surface. This could possibly be due to an intrusion of the low-salinity EMC waters. The various hypothesis proposed by previous studies were assessed using a hypothesis-testing model, with the main outcome being that the bloom occurred mostly at a one-month lag during La Niña events, at a success rate of 83%. Another interesting outcome from the hypothesis-testing experiments was that the major blooms (1999, 2006 and 2008) co-occurred preferably with a dampening of the current-driven coastal upwelling (sucess rate of 72%) south-east of Madagascar [*Lutjeharms and Machu*, 2000; *Machu and Garçon*, 2001; *Ramanantsoa et al.*, 2018a]. Investigating composites of AVISO sea level anomalies revealed the prevalence of a dipole feature close to the coasts, during bloom months. This could de-stabilize the SEMC, bringing low-salinity, nutrient/phytoplankton cell rich waters into the bloom area, and consequently reducing the coastal upwelling south-east of Madagascar. This mechanism was proposed as a new hypothesis which could be driving the South-East Madagascar Bloom.

Occurring in a remote and under-sampled region where in-situ and cruise data are very limited, uncertainties still surround the drivers of the bloom. This chapter presents the first high-resolution numerical study of the South-East Madagascar Bloom, used to investigate whether the local circulation in the bloom region could result in a de-stabilization of the SEMC and, consequently provides a quicker route for nutrient-rich coastal waters to be advected directly into the bloom region. A coupled biophysical model, CROCO-PISCES, was set up with a configuration of the South-West Indian Ocean (SWIO model), including a high-resolution ($\frac{1}{12}$°) subdomain spanning from 38°E-80°E and 18°S-32°S. SWIO was forced with a physical non-assimilative GLORYS2V3-FREE simulation and its corresponding biogeochemical

component namely BIOMER GLORYS2V3, at its boundaries, and ERA-Interim for its surface forcings. Chapter 3 provides an evaluation of the SWIO, which reproduced reasonably well the main physical and biogeochemical dynamics in the South-East Madagascar Bloom region.

Using the computation of the bloom index employed in Chapter 4, a 'model bloom index' will be assessed and a mean description of the temporal and spatial variability of the modelled South-East Madagascar Bloom will be provided, as well as its associated mean vertical structure. The model will then be used to test the aforementioned hypothesis. This chapter is structured as follows: Section 5.2.1 describes the detection of a simulated South-East Madagascar Bloom, focussing on its temporal as well as spatial variability; and its mean vertical physical properties. Section **5.2.2** explores the mean local oceanic circulation associated with the bloom, and its corresponding influence on nitrate (NO_3) fluxes from the coasts and from the subsurface levels (upwelling). A Lagrangian particle analysis is also presented in this section. Section 5.3 highlights the main findings and a summary is provided in section 5.4.

5.2 Results

5.2.1 Simulated South-East Madagascar Bloom

• Detection of a South-East Madagascar Bloom in the model simulation

SWIO reproduces the mean oceanic circulation in the vicinity of the South-East Madagascar Bloom, as seen in Chapter 3. The complex circulation in the bloom region includes the shallow eastward South Indian Ocean Countercurrent (SICC; *Palastanga et al.* [2007]; *Siedler et al.* [2006]). In the model, this feature is observed to have shifted slightly north, compared to observations (Figure 5.1). This variability in the meridional

position of the SICC could possibly have an influence on the bloom.

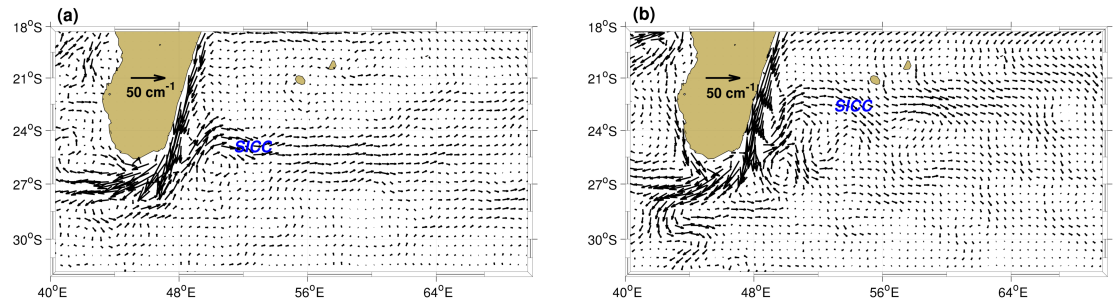


Figure. 5.1 Averaged surface geostrophic velocities on a 1993-2013 time frame in (a) AVISO and (b) SWIO model. SICC illustrates the latitudinal band of the South Indian Ocean Countercurrent.

Using the bloom box proposed by *Uz* [2007] and in Chapter 4, the mean Chl-a concentration in the first 20 m (optical depth) is explored for a possible austral summer bloom. Although the signal is dominated by winter blooms, three small austral summer peaks are observed, during 1999, 2004 and 2006 (Figure 5.2). It should be noted that 1999 and 2004 were ascribed bloom years in the previous chapter. However, these peaks remain small (< 0.0075 mg m^{-3}), compared to the intensity of the peaks observed in the ocean colour dataset. Exploring the Chl-a concentration in the subsurface levels (20-40 m) reveals the presence of a much more pronounced bloom, south-east of Madagascar, as seen in Figure 5.3. In February-March 2004 and December 2009 (Figure 5.3), surface blooms are not evident but the subsurface blooms exhibit a similar eastward propagation as the observed South-East Madagascar Bloom, and at a higher intensity. On this basis, a further investigation of this subsurface bloom is performed. SWIO presents a summer phytoplankton bloom, a feature more significant in the model subsurface levels (20-40 m) compared to the surface levels (0-20 m). Two distinct events, in February-March 2004 and December 2009 (austral summer month of 2010), where a slight increase in surface Chl-a occurs concurrently with a significant increase is subsurface (Figure 5.3), occur. In February-March, the subsurface bloom south-east of Madagascar extends further offshore up to 55°E, with patches of $\sim$0.5 mg m^{-3}, near

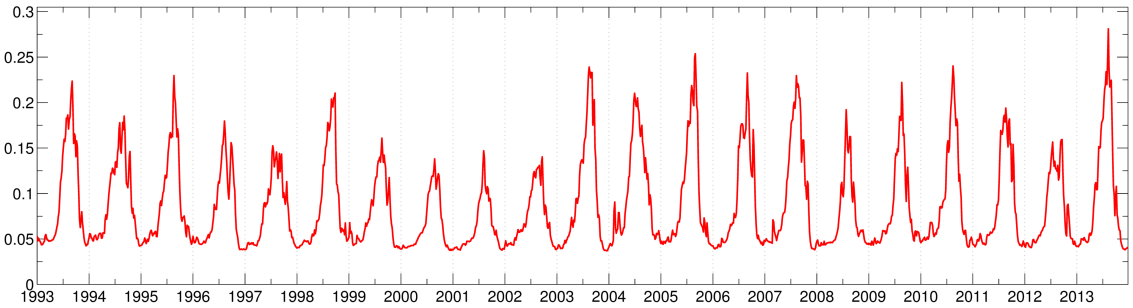


Figure. 5.2 Time series of simulated Chl-a concentration (mg m^{-3}) in the bloom box proposed by *Uz* [2007], from 1993 to 2013.

the coasts (Figure 5.3c). In December 2009, this Chl-a enhancement occurred again in the subsurface levels, extending till ∼58°E (Figure 5.3d). During these two events, a slight increase in Chl-a concentration is also observed at the surface, but not as strong as in the subsurface levels (Figure 5.3a and b).

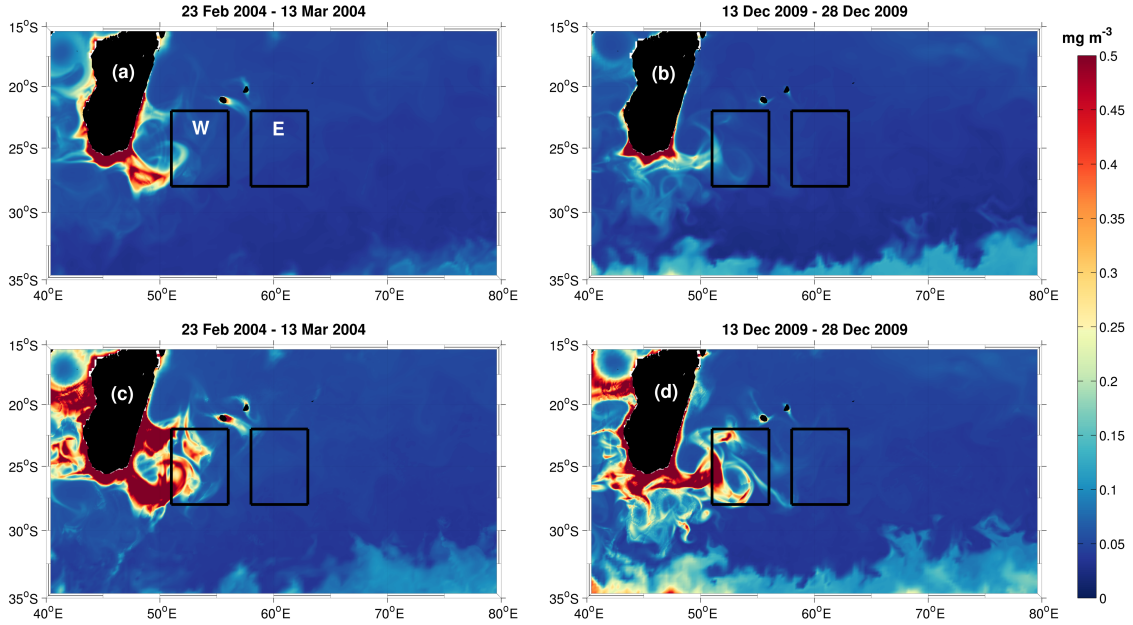


Figure. 5.3 Mean (upper row, a and b) surface (0-20 m) and (lower row, c and d) subsurface (20-40 m) Chl-a concentration (mg m^{-3}) from 23/02/2004 to 13/03/2004 (first column) and 13/12/2009 to 28/12/2009 (second column). The two delineated overlaid boxes define the regions where the modelled bloom occurs (bloow W). A box further east (box E) captures the winter bloom.

As in the previous chapter, a 'model bloom index' needs to be defined, to allow the identification of years of bloom occurrence. However, a significant over-estimation of modelled phytoplankton concentration is observed in austral winter in the Mozambique Channel as well as around the southern coasts of Madagascar (see Figure 3.24 in Chapter 3). This enhanced, coastally-confined Chl-a will consequently influence the computation of the bloom index (box W - box E), as it will hinder the removal of the seasonal cycle. To overcome this austral winter's non-homogeneity in surface Chl-a in the Madagascar Basin, a western box W was defined out of the high austral winter bloom (51°E-56°E; 22°S-28°S), as much as possible. The austral summer bloom should, however, be captured by box W. A box further east, box E (58°E-63°E; 22°S-28°S), was placed close to box W, so as to capture a similar austral winter bloom intensity as box W, but not the austral summer one. From these two boxes, the 'model bloom index' is defined.

In both boxes W and E, the monthly climatology of Chl-a concentration is dominated by the aforementioned very strong signal in austral winter (Figure 5.4), which is ∼0.05 mg m^{-3} stronger in box W. Owing to this more intense austral winter Chl-a in box W, computing the bloom index, as suggested earlier, might not remove the seasonal cycle of Chl-a completely. In comparison to the surface levels, subsurface levels exhibit higher concentration of phytoplankton cells in austral summer by ∼0.035 mg m^{-3}. This feature is not present in box E. This shows that the position of box W is able to capture the austral summer bloom of the region. Phytoplankton cells concentration increased as from early December, peaking at the end of December- early January, and eventually dissipating towards April. Hereafter, unless stated otherwise, a South-East Madagascar (summer) bloom entails enhanced Chl-a concentration averaged between the December of the previous year and April of the actual year.

A bloom threshold in the model has to be defined, to differentiate between the occurrence of bloom and non-bloom years. Owing to the Chl-a concentration starting to

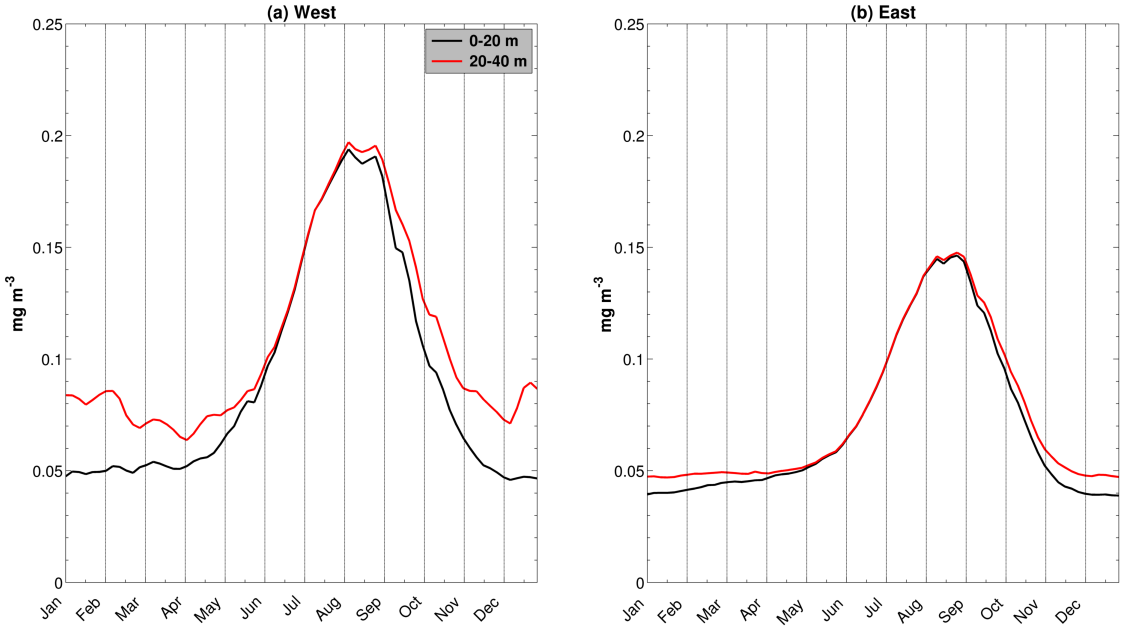


Figure. 5.4 Monthly climatology of Chl-a concentration (mg m^{-3}) averaged along the 0-20 m (black line) and 20-40 m (red line) depth ranges, in (a) box W and (b) box E.

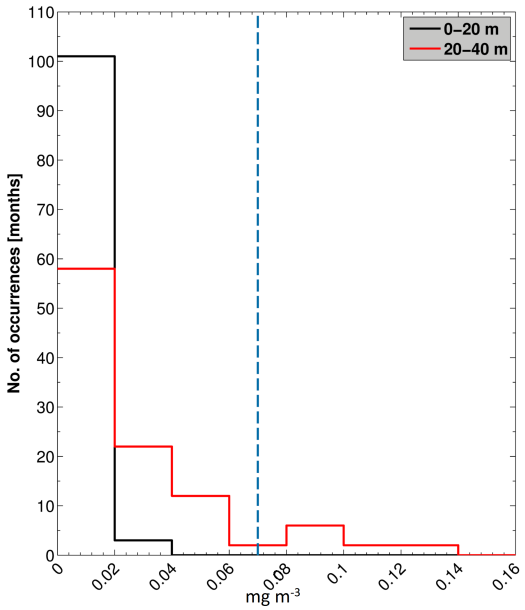


Figure. 5.5 Histogram of occurrences (months) of monthly maximum Chl-a differences (mg m^{-3}) between box W and box E, in the surface (black line) and subsurface (red line) levels. The vertical dotted blue line at 0.07 mg m^{-3} indicates the threshold used to separate bloom from non-bloom years.

increase as early as December, a focus will be made on the December-April period. Maximum in monthly Chl-a differences (box W - box E), at both surface and subsurface, are used to build a histogram, from which a threshold is defined (Figure 5.5). Contrary to the yearly maximum Chl-a difference used in Chapter **4**, a monthly maximum Chl-a difference is used here, owing to the small duration of the simulated bloom. It can be observed that the surface levels exhibit maximum Chl-a difference between 0-0.02 mg m^{-3} (black line in Figure 5.5). This small range of maximum Chl-a difference demonstrates the absence of an austral summer bloom in the surface levels. From the subsurface perspective, maximum Chl-a difference occurrences peak in the 0-0.02 mg m^{-3} range, with a decreasing trend to about two months between 0.06-and 0.08 mg m^{-3} (red line in Figure 5.5). From this range, the number of occurrences increases again before stabilizing on 2 months from 0.1mg m^{-3} to 0.14mg m^{-3}. Hence, a bloom threshold of 0.07 mg m^{-3} (blue dotted line in Figure 5.5) is assigned, beyond which a peak of subsurface Chl-a concentration indicates a bloom year. This threshold is similar to the 0.07 mg m^{-3} threshold used in the previous chapter to identify bloom years from satellite observations. Henceforth, the study will focus only on the subsurface levels, with the occurrence of a bloom year designating a bloom in the subsurface levels.

- **Temporal variability of the simulated bloom**

The 'model bloom index' is shown in Figure 5.6b, with the blue dotted line indicating the 0.07 mg m^{-3} threshold, beyond which a year is assigned as a bloom year. The model produces a sporadic Chl-a bloom, as observed in satellite data. However, the years of increased Chl-a concentration in the model do not match those in satellite data. This could possibly be due to a signature of the turbulent and chaotic processes associated with a bloom appearance, and could also explain the failure of some of the different hypothesis put forward by previous studies, as shown in Chapter 4.

From Figure 5.6b, eight years namely 1994, 1995, 1996, 2004, 2005, 2006, 2008 and 2010 have been identified as bloom years. The model reproduces a bloom during some years

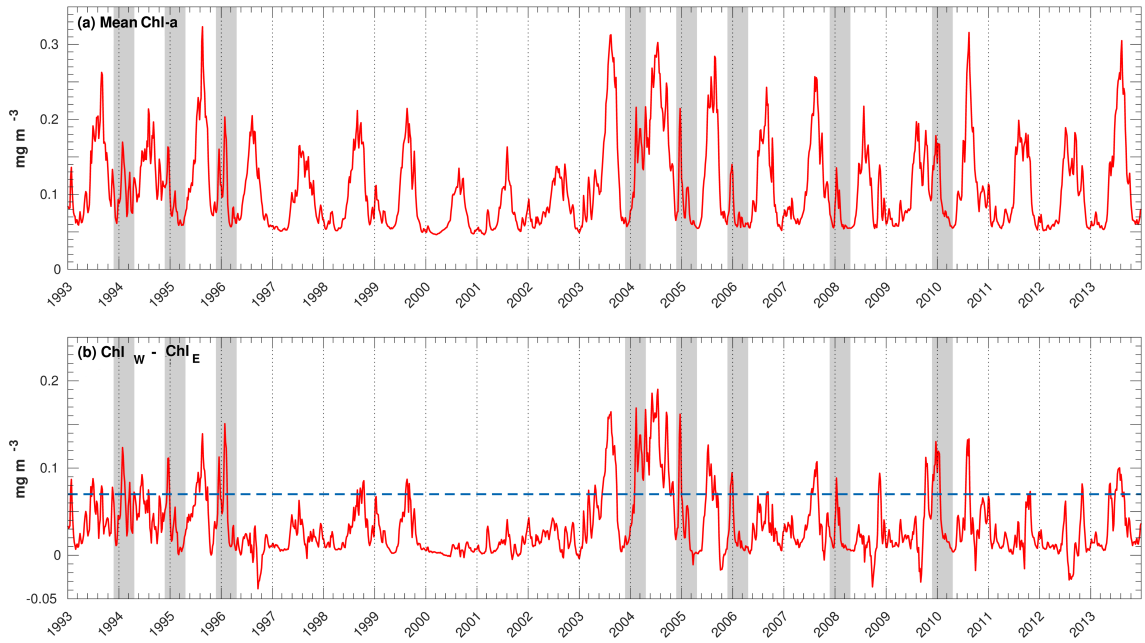


Figure. 5.6 (a) Mean Chl-a concentration (mg m^{-3}) in box W, and (b) time series of the difference of Chl-a concentration between box W and box E. The gray shadings indicate austral summer months (December-April). The blue dotted line indicates a threshold value of 0.07 mg m^{-3} from which bloom years can be separated from non-bloom years.

(2004, 2006 and 2008) which were also identified as bloom years in ocean colour dataset. The initiation and termination, as well as the peak of the bloom, vary significantly on temporal scales. In 1994 and 1996, enhanced production starts late December of the previous year (1993 and 1995 respectively) and peaks by the end of January, reaching a maximum concentration of ∼0.17 mg m^{-3} and ∼0.2 mg m^{-3}, respectively. The austral summer bloom of 1995 initiates early December of the previous year (1994) and reaches its maximum intensity (∼0.16 mg m^{-3}) by end of December 2004.

The two strongest blooms occur in 2004 and 2005, both reaching a maximum concentration of ∼0.21 mg m^{-3}. The onset in 2004 occurs at the end of January and peaks in March, whereas the 2005 one initiates at the end of November 2004 and peaks in December 2004. Both the 2006 and 2008 blooms peak at ∼0.14 mg m^{-3}, in December 2005 and January 2008, respectively. The onset of the 2010 bloom occurs at the end of November 2009, and reaches a maximum intensity of ∼0.17 mg m^{-3} by the end of

Table 5.1 Events of bloom and non-bloom years, with bloom years listed in 'bold'. The month at which the bloom is maximum is stated in the third column.

Years	**Bloom**	**Month of maximum bloom**	**Non Bloom**
1993			X
1994	X	Jan-94	
1995	X	Dec-94	
1996	X	Jan-96	
1997			X
1998			X
1999			X
2000			X
2001			X
2002			X
2003			X
2004	X	Feb-04	
2005	X	Dec-04	
2006	X	Dec-05	
2007			X
2008	X	Jan-08	
2009			X
2010	X	Dec-09	
2011			X
2012			X
2013			X

December 2009. However, the bloom persists till mid-January 2010.

50% of the years ascribed as bloom occurrence years, peak in December, with the remaining 4 years peaking in January (3 events) and February (1 event). 1996, 2004 and 2005 are the strongest bloom years, with mean Chl-a concentration in box W, reaching an excess of 0.2 mg m^{-3} concentration. The details of bloom-occurrences are summarized in Table 5.1.

• **Horizontal structure of the simulated bloom**

As shown in Chapter 4, the South-East Madagascar Bloom also exhibits large variability meridionally and zonally. A composite of mean Chl-a concentration during months of maximum Chl-a bloom and no bloom occurrence, in both satellite and the model, is constructed and shown in Figure 5.7. The mean spatial structure of the modelled bloom reveals higher productivity near the coasts, compared to satellite data (Figure 5.7a and c). This high Chl-a concentration also extends from the coast to 54°E, with a mean concentration exceeding 0.4 mg m^{-3} (Figure 5.7c). However, one should keep in mind that this over-estimation of the bloom could be a result of the bloom being concentrated in the subsurface levels.

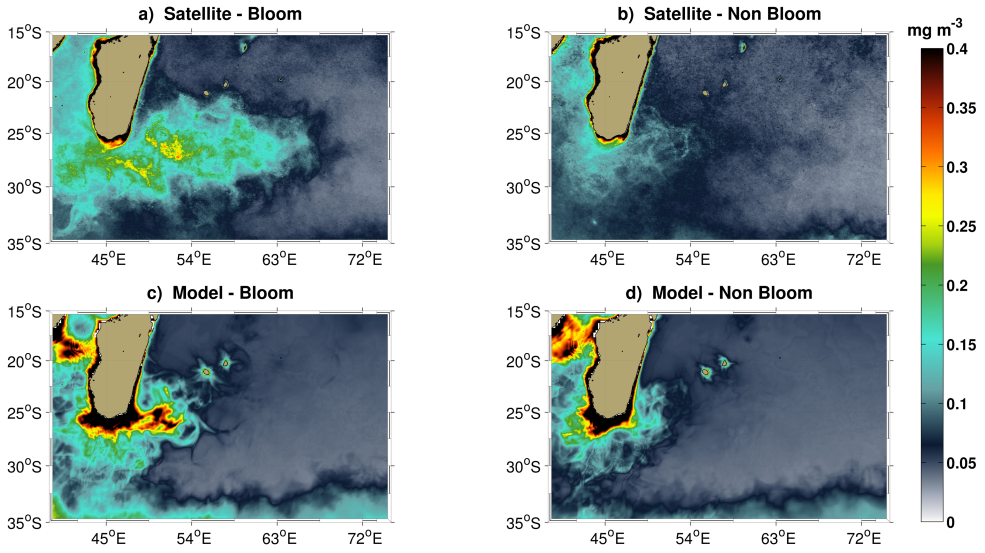


Figure. 5.7 Spatial maps of mean Chl-a concentration (mg m^{-3}) during months of maximum bloom occurrence (left column), identified in Figure 5.6, and months of non-bloom occurrence (right column). The first row shows Chl-a from remotely-sensed ESA OC-CCI data and the second row shows Chl-a data, in the subsurface levels, from SWIO.

The mean meridional extent of the bloom, observed within a latitudinal band of 22°S-29°S, compares quite well to that of satellite data (24°S-30°S; Chapter 4). However, the zonal extent of the modelled bloom is underestimated (Figure 5.7d). It presents an elongated high Chl-a patch till 58°E (Figure 5.7d), whereas in the satellite data,

it extends up to 65°E. An interesting feature is the link between the coasts and the most offshore point of the high Chl-a patches. In satellite data, a high patch of Chl-a can be observed at around 52°E-53°E, but not connected to the Madagascar coasts (Figure 5.7a). Within the model, the south-eastern region of the Mozambique Channel is dominated by the high Chl-a concentration, linked to high productivity in the coastal areas, a feature not present in satellite. During non-bloom years, some patches of high Chl-a are observed in the bloom region, with a concentration of ∼0.15 mg m^{-3}, similar to satellite data.

As shown earlier, the bloom in the model reaches its peak at different months of austral summer and the spatial pattern varies greatly. For each year ascribed as a bloom year, the month which exhibits the most intense bloom in the 'model bloom box' is shown in Figure 5.8. These display the filamentous ('dendritic') structure of the bloom, as described by *Longhurst* [2001]. The blooms in 1994, 1996, 2005 (end-2004), 2006 (end-2005) and 2008 show an elongated structure connected to the coast. In 1995 (end-1994), this structure extends zonally up to 53°E whereas in 2005 (end-2004), it extends up to ∼60°E. This elongated structure varies latitudinally for each of these years, with a mean latitude of 25°S for 1994, 1996 and 2008, whereas in 2005 (2006), it exhibits a south-eastern (north-eastern) propagation.

In 1995, 2004 and 2009, the mean bloom structure exhibits large variability. The 1995 bloom co-occurs with a bloom south of Madagascar, to which it looks connected through a possible retroflection of the mean circulation. The 2004 event exhibits an eddy-type structure, with high phytoplankton cells on the peripheries. In 2009, high patches of Chl-a are found in the bloom box, linked to the Madagascar coasts, and co-occurring with a bloom south and south-west of Madagascar. This shows the large spatial variability of the modelled South-East Madagascar Bloom.

- **Mean vertical physical properties associated with the simulated bloom**

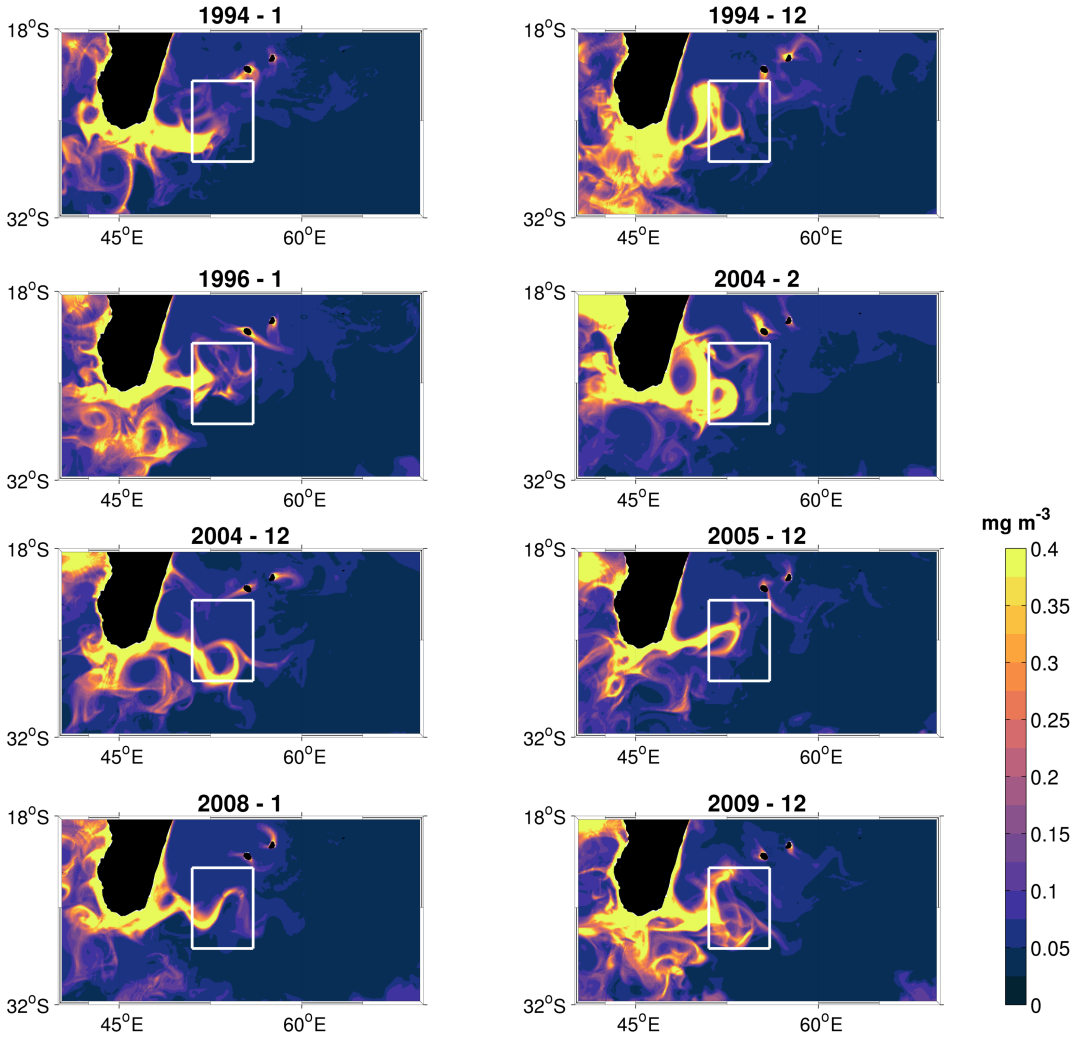


Figure. 5.8 Spatial maps of the months of maximum simulated Chl-a concentration (mg m^{-3}) observed in box W during bloom years. The white box shows the location of the 'model bloom box'.

The mean thermohaline structure of the water column, associated with high Chl-a patches during bloom years, is investigated. A bloom threshold of 0.12 mg m^{-3} is used to identify spots of high Chl-a, with a concentration lower than 0.06 mg m^{-3} designating no-bloom spots. These thresholds were chosen so as to capture only profiles in high and low Chl-a spots in all bloom years. The temperature and salinity profiles in these patches are used to construct mean bloom and non-bloom water column structures. The mean profiles related to bloom and non-bloom patches will be referred to as 'bloom profiles' and 'non-bloom profiles', respectively. A salinity front, co-located

with the South Indian Ocean Countercurrent (SIIC; [*Menezes et al.*, 2014]) is present in this region, as can be seen in Figure 5.9. The 'model bloom box' is crossed by four isohalines denoting 35.4, 35.5, 35.6 and 35.7 psu. The 35.6 isohaline crosses the middle of the 'model bloom box' and hence, is used to separate the fresher and saltier side of the this specific front. The mean water column structure is investigated on both sides of the front, so as to prevent any bias in surface salinity. Note that the fresher coastal water is representative of the poleward SEMC.

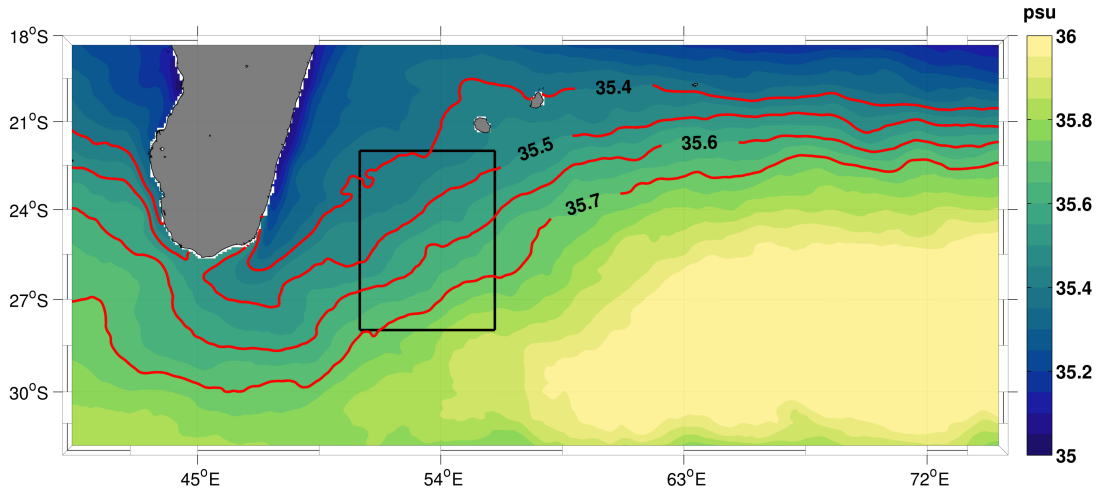


Figure. 5.9 Mean (December-April) modelled salinity (psu), averaged over the first 40 m, from 1993 to 2013. The red lines denote the isohalines crossing the bloom box namely the 35.4, 35.5, 35.6 and 35.7 psu isohalines. The black box shows the position of the 'model bloom box'.

The mean vertical structure of the water column reveals bloom occurrence in a shallow stratified layer (Figure 5.10), as shown with co-located Argo-bloom patches in Chapter 4. This feature was also reported by *Srokosz and Quartly* [2013], using cruise data. On the fresher side of the front, the mean temperature associated with the bloom profiles is ∼0.8°C lower than non-bloom profiles (Figure 5.10a). This is coupled to the higher (lower) density (Figure 5.10c) water observed linked to the bloom (non-bloom) profiles and could be representative of colder, nutrient-rich water being upwelled towards the surface, and hence inducing high production of phytoplankton cells. High and low

Chl-a patches are present in a shallow mixed layer of ∼15.2 m.

On the saltier side of the front (poleward-side), higher temperature is found to be associated with the bloom, compared to non bloom (Figure 5.10d), with a difference of ∼0.8°C at the surface. The associated mixed layer depth sits at approximately the same depth in both cases (∼13.2 m). The density profiles, however, exhibit less dense water in bloom areas compared to non-bloom areas (Figure 5.10f).

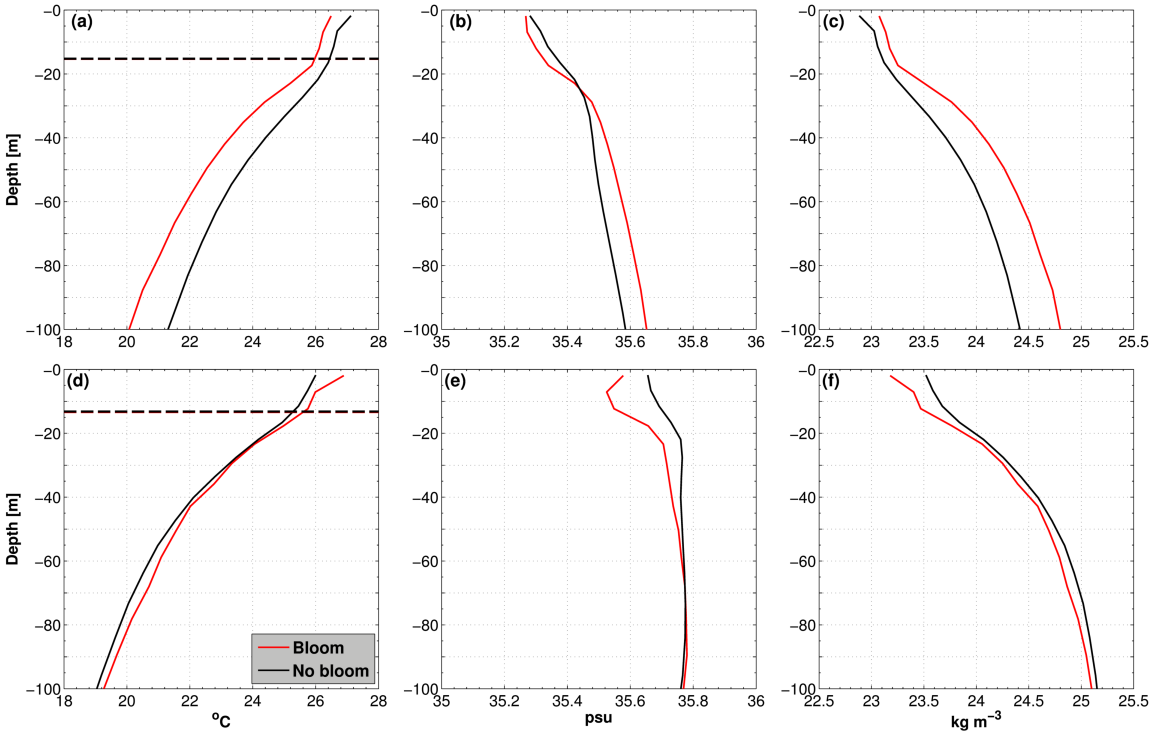


Figure. 5.10 The model mean water column structure associated with bloom (red line) and non-bloom (black line) years on the fresher side (upper panels) and saltier side (lower panels) of the 35.6 psu salinity front. The red (black) dotted line shows the mixed layer depth during bloom (non-bloom) months (a and d).

As is seen in observational data, the bloom is confined to surface layers of lower salinity on both sides of the salinity front (Figure 5.10b and e), highlighting the similarities in potential processes associated with the simulated and observed bloom. This low-salinity water is observed in the first 20 m on the fresher side of the front with a difference of

∼0.04 psu in the first 20 m. On the saltier side, this low salinity is present from the surface to ∼60 m depth. The difference is ∼0.08 psu at the surface, increasing to a maximum of 0.16 psu at 10 m deep. This corroborates with the new hypothesis put forward in the last chapter (Chapter 4), where it is stated that advection of fresher, nutrient-rich coastal SEMC waters could fertilize the bloom.

5.2.2 Mean circulation associated with the bloom

Composites of the mean circulation associated with the bloom and non-bloom periods, in both satellite altimetry and SWIO are investigated (Figure 5.11). The regional austral summer mean sea level anomaly (SLA) was subtracted from the AVISO SLA product so as to present only the local fluctuations of the circulation (Figure 5.11a and b). South-east of Madagascar, the sea surface variations in SWIO compares quite well with AVISO. However, the mean circulation exhibits contrasting features during bloom and non-bloom periods, in both AVISO and SWIO.

During bloom months, the mean circulation south-east of Madagascar exhibits vortex-like features, in both AVISO and SWIO. Remotely-sensed data clearly exhibits an anti-cyclonic circulation, with positive SLA, and two cyclonic circulations also visible: one to the south (S2) and one to the north (S3) (Figure 5.11a). The simulated SLA captures the anticyclonic feature of the mean circulation (S1) as well as the cyclonic circulation (S2) south of S1 (Figure 5.11c). A less-intense elongated cyclonic flow (S3) is also observed north of S1. However, the simulated vortex circulation, compared to altimetry, is shifted slightly north, and this could be associated with the northward shift of the SICC (Figure 5.1). During non-bloom period, these vortex circulations close to the SEMC are shifted southward. Individual bloom years were also assessed and these features occur repeatedly and are not simply an artifact of one strong feature in the time period aliasing the composite.

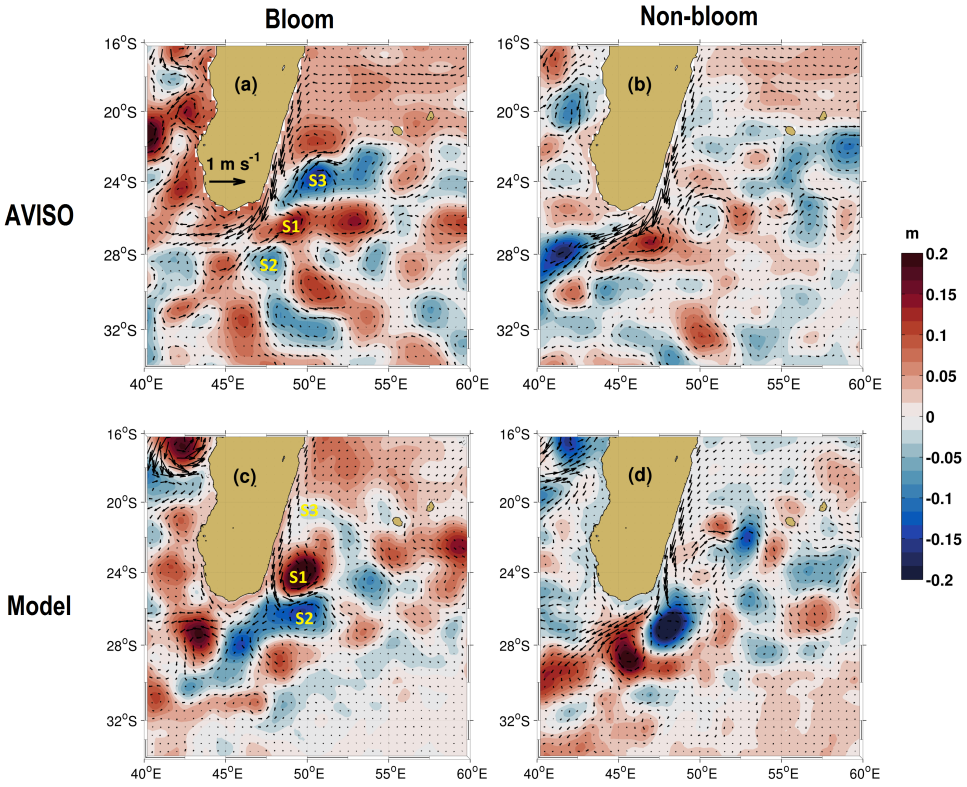


Figure. 5.11 Comparisons between the remotely sensed sea level anomalies (m) from AVISO (first row) and the simulated sea surface height anomalies by SWIO (second row), during (a and c) bloom and (b and d) non-bloom periods. The surface geostrophic velocities were overlaid. S1, S2 and S3 denote structures of the mean circulation.

Owing to these features, the observed SEMC partly retroflects and moves in a north-eastern direction due to S3 and S1 during bloom months (Figure 5.11a). However, the mean circulation associated with the non-bloom period reveals no retroflection, with the SEMC exhibiting a stronger south-westward flow after rounding the southern tip of Madagascar (Figure 5.11b), compared to the bloom period. This is consistent with a dampening of the current-driven upwelling south-east of Madagascar [*Lutjeharms and Machu*, 2000; *Machu et al.*, 2002; *Ramanantsoa et al.*, 2018a] during bloom months, owing to the lower intensity of the SEMC. In SWIO, the simulated SEMC also partly retroflects and flows eastward, as a result of S1 and S2 (Figure 5.11c), with the mean flow south of Madagascar exhibiting a weak south-westward direction. In contrast, during the non-bloom period, although a slight retroflection might exist as

a result of the cyclonic circulation centered at 48°E-27°S,a strong SEMC flows in a south-westward direction. This fate of the SEMC, south-east and south of Madagascar, could be associated with the local effect of oceanic turbulence. Hence, the prediction of the bloom as well as the testing of some of the hypotheses in 4 is complicated due to the chaotic processes of the local circulation.

Nonetheless, the bloom in the observed dataset and in SWIO seems to be related to a vortex-like circulation south-east of Madagascar, which would induce a retroflection of the SEMC, along with a weakened SEMC south of Madagascar. These features may influence the South-East Madagascar Bloom, by horizontally advecting low-salinity, nutrient-rich SEMC waters into the bloom region, hence triggering the bloom, or through a vertical flux of nutrients and phytoplankton biomass from the subsurface layers. To investigate the response of upwelling intensity and nutrients delivery from the coasts, a nitrate (NO_3) flux analysis is performed in the 'model bloom box' during the bloom events over the first 40 m of the upper layers. These are divided into an incoming flux from the Madagascan coast, and a net vertical flux from the subsurface levels. In a biogeochemical context, a net positive incoming flux from the coasts (hereafter referred as 'Eadv') would be indicative of nutrients input into the 'model bloom box', whereas a net positive vertical flux (hereafter referred as 'Vadv') would quantify the amount of nutrient supply owing to upwelling. However, local biogeochemical recycling could also result in an increase in nutrients in the upper layers [*Zhang et al.*, 2016]. In line with a possible intrusion of fresher SEMC waters into the bloom region, the mean vertical structure of the salinity is also explored. This analysis was performed separately, as case events for each bloom year.

- **Simulated Nutrient Flux Analysis**

In 1994, an increase in Chl-a concentration is observed since early January, co-occuring with an increase in NO_3 concentration (Figure 5.12a). Eadv dominates the region as

from early January 1994 but starts to decrease mid-January (Figure 5.12b). Vadv takes over, increasing from 8^{th} January 1994 and reaching its maximum on the 28^{th}, simultaneously with the peak in Chl-a concentration. Although Eadv plays a major role at the start of the bloom, Vadv contributes to the NO_3 concentration, sustaining the bloom which reaches its maximum on the 28^{th} of January 1994. The peak in Eadv brings in lower salinity water (Figure 5.12c), which are rapidly mixed in the 'model bloom box'.

The 1995 event accounted for a bloom which occurred in December 1994. Nitrate concentration increases as from end of November 1994, reaching a maximum on 18^{th} December, at the same time of maximum bloom (Figure 5.12d). Similar to the 1994 event, this specific bloom is triggered by an incoming of NO_3 concentration from the western boundary of the bloom box and sustained by upwelling (Figure 5.12e). However, the incoming western boundary flux does not account for a low-salinity water signature (Figure 5.12f).

The 1996 bloom exhibits a maximum concentration of $\sim$0.2 mg m^{-3}, simultaneously with the NO_3 concentration (Figure 5.13a). This event is triggered by nutrients input from the coast (Eadv) as well as from the subsurface levels (Vadv) (Figure 5.13b), which increase and peak at the same time, contributing to a net NO_3 of 14.5 μM m^2 s^{-1}. The increase in NO_3 coincide with a decrease of salinity of $\sim$0.2 psu, indicative of fresh water associated with high nutrients. The source of this low-salinity high-nutrient water could possibly be the nutrient-rich coastal EMC waters.

The 2004 event is one of the strongest blooms. The region is oligotrophic throughout January 2004, and as from early February 2004, the mean concentration of NO_3 started to increase, concurrently with Chl-a (Figure 5.13d). The NO_3 flux into the 'model bloom box' is dominated by vertical fluxes, which confirms that upwelling, rather than horizontal advection, played a major role in nutrient supply (Figure 5.13e). It peaked on the 8^{th} of February from 1.8 x 109 μMm^2s^{-1} to 7.5 x 109 μMm^2s^{-1} before decreasing

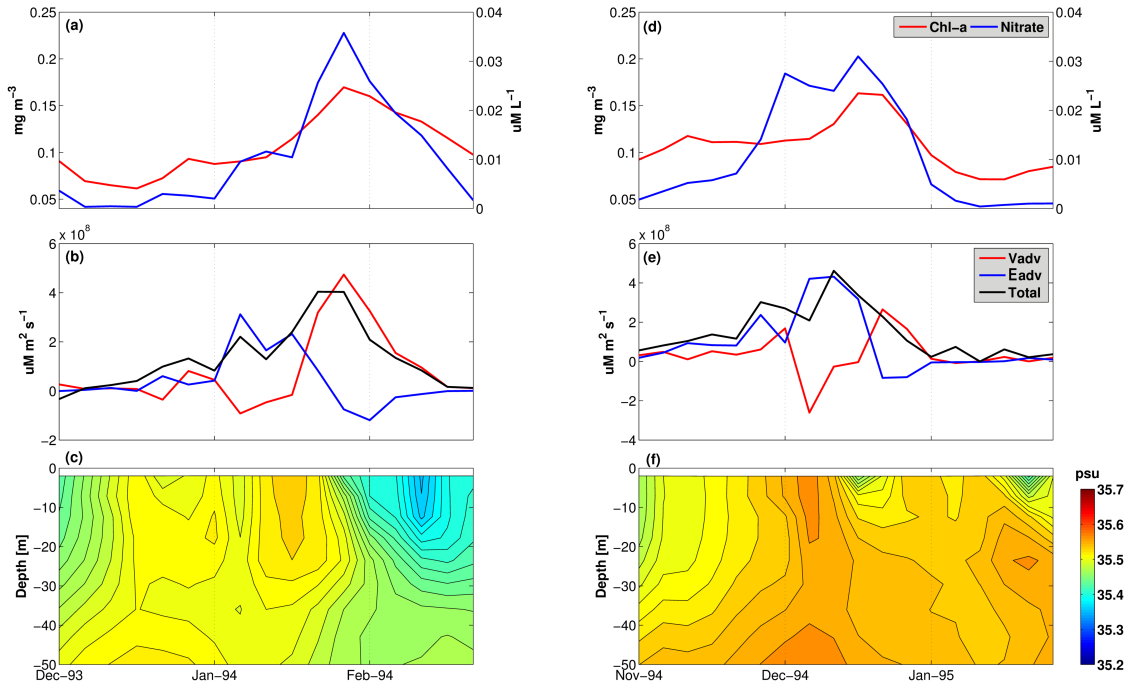


Figure. 5.12 Time series of averaged simulated Chl-a and NO_3 concentration observed in the bloom box, in the upper 40 meters (a and d) for the 1994 (first column) and the 1995 (second column) events; simulated NO_3 fluxes per unit area, over the first 40 m (b and e), with the red and blue lines indicating flux from the subsurface (Vadv) and from the Madagascan coast (Eadv). The Total flux (horizontal + vertical) is shown by the black line. Hovmöller of the mean vertical structure of salinity in the 'model bloom box' for the (c) 1994 and (f) 1995 events are displayed.

again (Figure 5.13e). Upwelling brought high concentrations of NO_3 (0.23 μM L^{-1}), hence sustaining high productivity. The bloom reaches its maximum intensity 5 days later ($\sim$0.21 mg m^{-3}) and then decreases gradually until April 2004.

2004 was described as a bloom year in both the observations and the model. In the previous chapter (Chapter 4), a significant peak in Ekman pumping (W_{ek}) was observed in 2004, with the hypothesis testing showing (W_{ek}) to be successful at 67% at a one-month lag. With (W_{ek}) being representative of the vertical velocities induced by wind stress curl (WSC) at the base of the Ekman layer, the wind stress curl in the model is investigated (Fig. 5.14). SWIO reproduced the observed WSC early February 2004, but at a smaller magnitude (Fig. 5.14c). This feature is associated

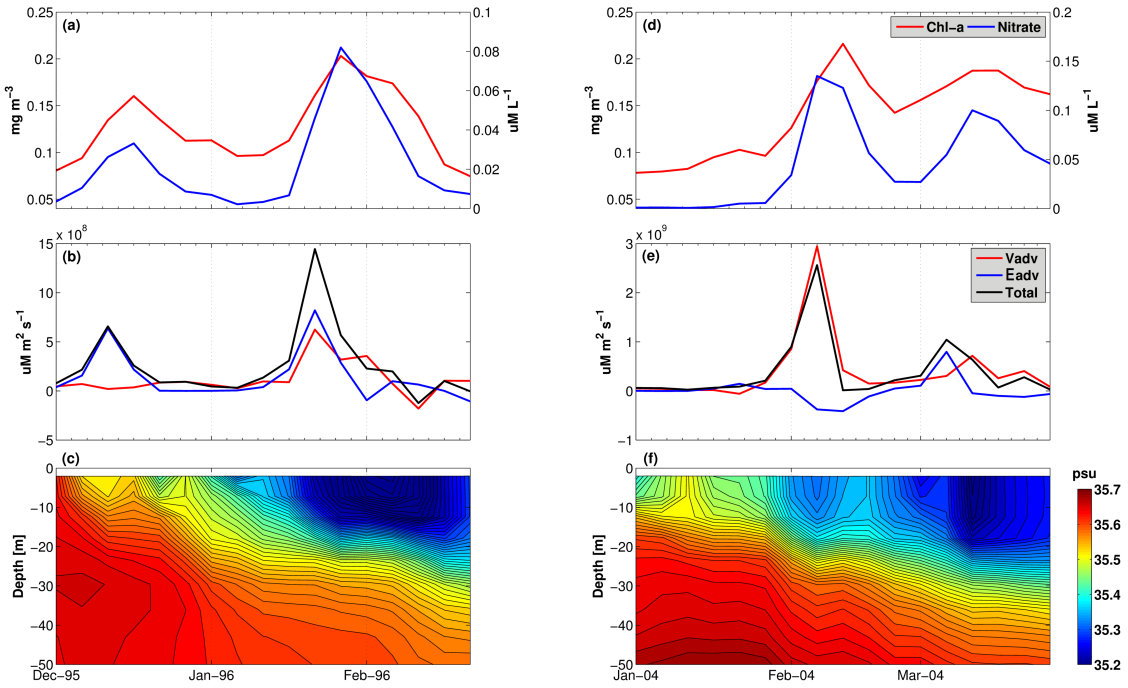


Figure. 5.13 Same as Figure 5.12 but for the 1996 (first column) and 2004 (second column) events.

with the initiation of the simulated 2004 bloom. However, the bloom started 5 days after the peak in WSC (Fig. 5.14d), whereas in QSCAT, the bloom peaked about one month later (Fig. 5.14b), corroborating the one-month lag detected from the hypothesis-testing. It can be concluded that when atmospherically-forced, the model reproduces the phytoplankton bloom. It should be noted that the observed negative WSC in early February is due to the presence of the tropical cyclone, Elita, in the region at the same time.

Both 2005 and 2006 events have their maximum Chl-a concentration during the end of December of the previous year (2004 and 2005 respectively) (Figure 5.15a and d). The productivity was controlled by the high NO_3 concentration at the same time. In these two cases, the NO_3 fluxes are dominated by horizontal advection from the west, which represents advection of high-nutrient waters from the eutrophic coastal regions. However, these also occur simultaneously with a slight increase in upwelling intensity

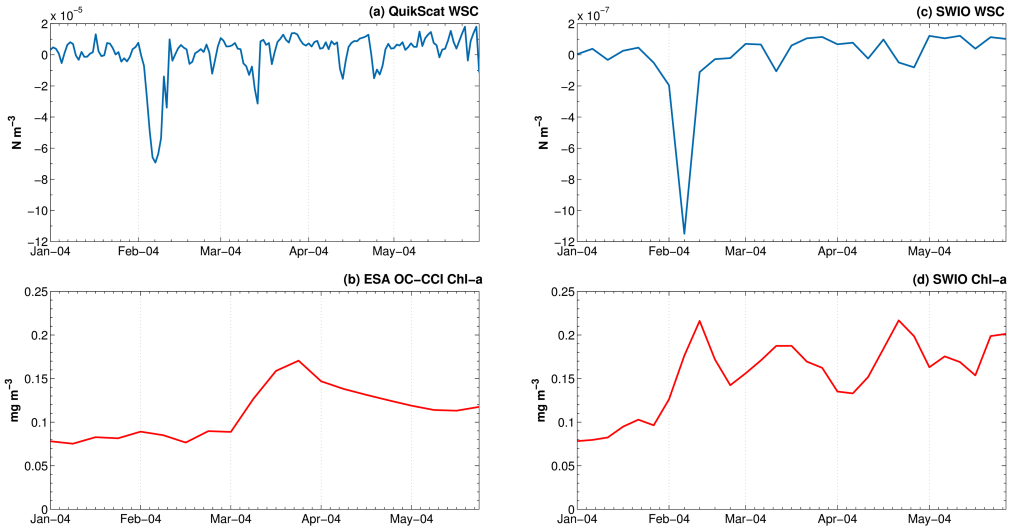


Figure. 5.14 Time series of wind stress curl computed from (a) QSCAT and (b) SWIO; and associated Chl-a concentration from (c) ESA OC-CCI and (d) SWIO, from January 2004 till May 2004.

(Vadv) (Figure 5.15b and e). As expected, the eastward inflow of nutrients is also evident by the low-salinity signature (Figure 5.15c and f), representative of the coastal SEMC water being advected into the bloom region through the vortex-like structure in the mean local circulation (Figure 5.11).

The bloom region in late 2007 is oligotrophic, until a peak in NO_3 (Figure 5.16b) flux from the west initiates a Chl-a bloom which peaks early January 2008 (Figure 5.16a). This influx of nutrients from the west co-occurs with a dampening of the Vadv. Comparable to previous events (1996, 2005 and 2006), intrusion of low-salinity water coincides with the increase in Eadv (Figure 5.16c). Enhanced productivity is sustained for almost one month during the 2010 event, with high concentrations from mid December 2009 to 23^{rd} January 2010 (Figure 5.16d). This is due to a contribution of NO_3 from both Eadv, which peaks mid December 2009, and Vadv which peaks early January 2010 (Figure 5.16e). Hence, Eadv contributes to the onset of the bloom with Vadv bringing nutrients to sustain it for a longer time. Eadv is associated with a decrease in the

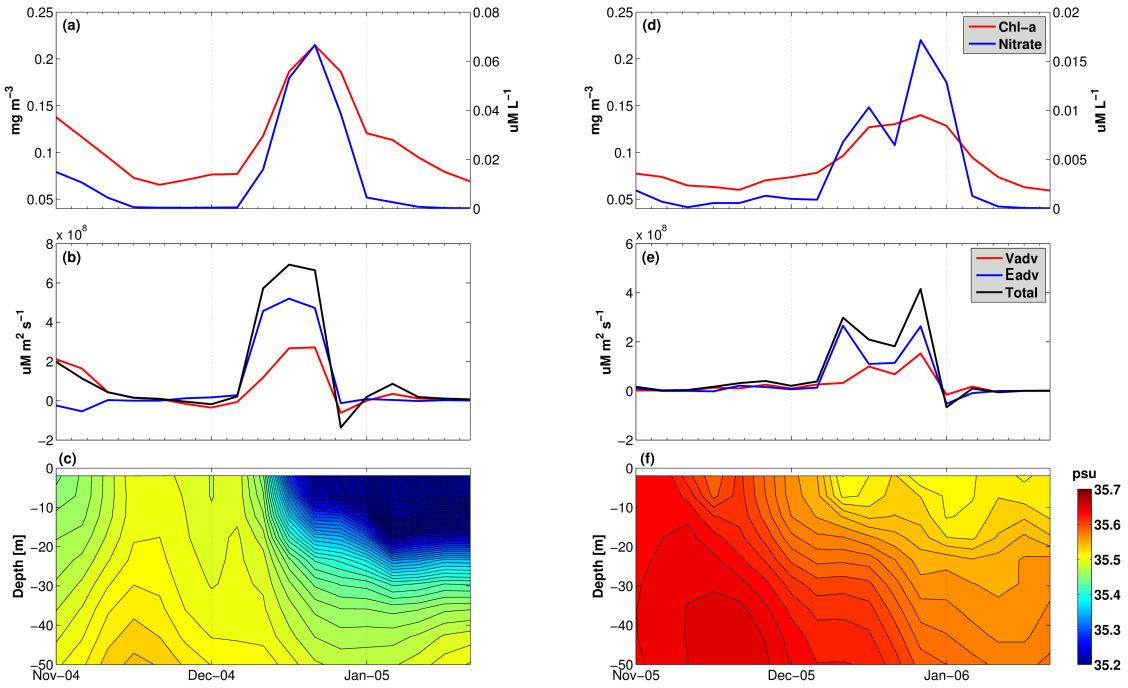


Figure. 5.15 Same as Figure 5.12 but for the 2005 (first column) and 2006 (second column) events.

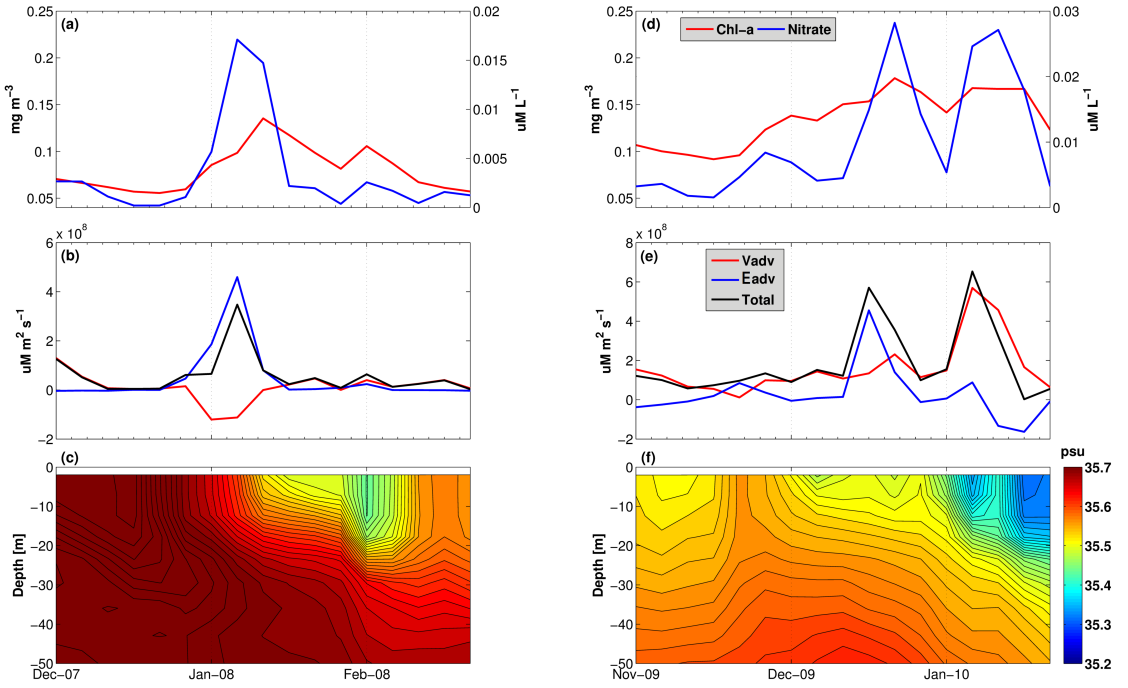


Figure. 5.16 Same as Figure 5.12 but for the 2008 (first column) and 2009 (second column) events.

salinity in the 'model bloom box' (Figure 5.16f).

Table 5.2 Summary of which bloom event is dominated by incoming eastward fluxes or vertical fluxes of NO_3.

Bloom Years	**Vertical Advection NO_3 flux**	**Eastward Advection NO_3 flux**
1994	X	
1995		X
1996		X
2004	X	
2005		X
2006		X
2008		X
2010		X

Table 5.2 provides a summary of the dominant fluxes (Eadv or Vadv) associated with each bloom event. Two bloom events namely 1994 and 2004 were mostly influenced by the vertical fluxes of NO_3, owing to the WSC. The 2004 event, ascribed as a bloom year in both observations and the model, have been shown to be associated with a negative WSC, which initiated the simulated bloom. This negative WSC is also present in satellite data, with a bloom initiating with a one-month lag. This demonstrates the ability of SWIO to correctly reproduce a bloom triggered by atmospheric forcing. The response of Chl-a was, however, quicker in the model compared to the observational dataset. During 6 out of 8 events, inputs of NO_3 through the western boundary of the 'model bloom box' controlled the productivity in the region, although upwelling of nutrient-rich waters from the subsurface levels could still play a minor role. This eastward influx is also associated with low-salinity water. This confirms the possibility of a new hypothesis put forward in the previous chapter, where fresher, nutrient-rich SEMC water close to the coast can be advected into the bloom region through the vortex-like mean local circulation, and hence initiates a phytoplankton bloom.

- **Lagrangian Particle Tracking**

To investigate the possible advection of low-salinity, nutrient-rich SEMC waters into the bloom region, the Lagrangian transport model, Ichthyop [*Lett et al.*, 2008], is used in combination with the high resolution ($\frac{1}{12}^{\circ}$) domain of SWIO. Ichthyop is a model developed to study the effects of physical and biological factors of marine particles [*Lett et al.*, 2008]. 500 particles are released, every month, in the surface layers of the SEMC (Figure 5.17). These particles have a lifetime of 90 days, after which they are assumed 'dead'. This choice was made as 90 days is considered sufficient time for the particles to reach either the 'model bloom box' or the box south of Madagascar (Figure 5.17), as shown by *Srokosz et al.* [2015]. This experiment is repeated monthly, from 1993 till 2013, and the percentages of particles arriving in the 'model bloom box' and south of Madagascar are assessed. A higher percentage of particles in the bloom region would be representative of an advection of coastal waters which could fertilize the South-East Madagascar Bloom.

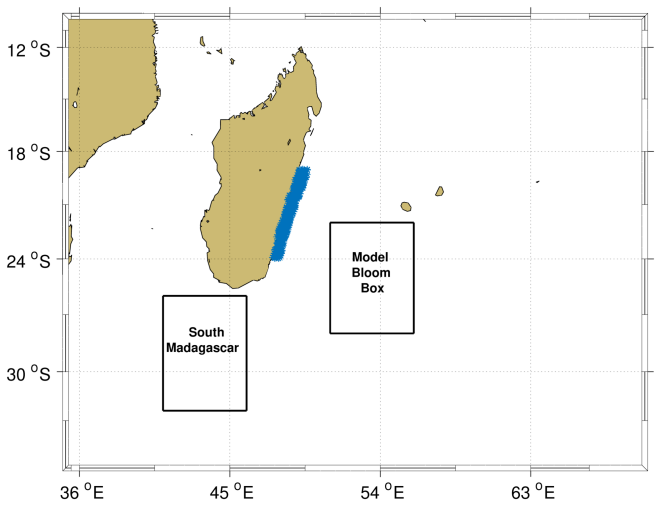


Figure. 5.17 The release area of langrangian particles in the SEMC, as represented in SWIO. The two delineated boxes indicate the region through which the langragian particles are tracked

The number of particles entering the 'model bloom box' exhibits large variability from year to year, a feature possibly due to the chaotic processes at play in the region (Figure 5.18a). This initial result shows that particles released in the coastal SEMC can be advected offshore south-east of Madagascar. In addition, the significant interannual variability associated with the percentage of particles entering the 'model bloom box' could possibly dictate the intermittent supply of low-salinity, nutrient-rich SEMC waters, hence fertilizing the South-East Madagascar Bloom. These results would support the hypothesis stated at the beginning of the chapter.

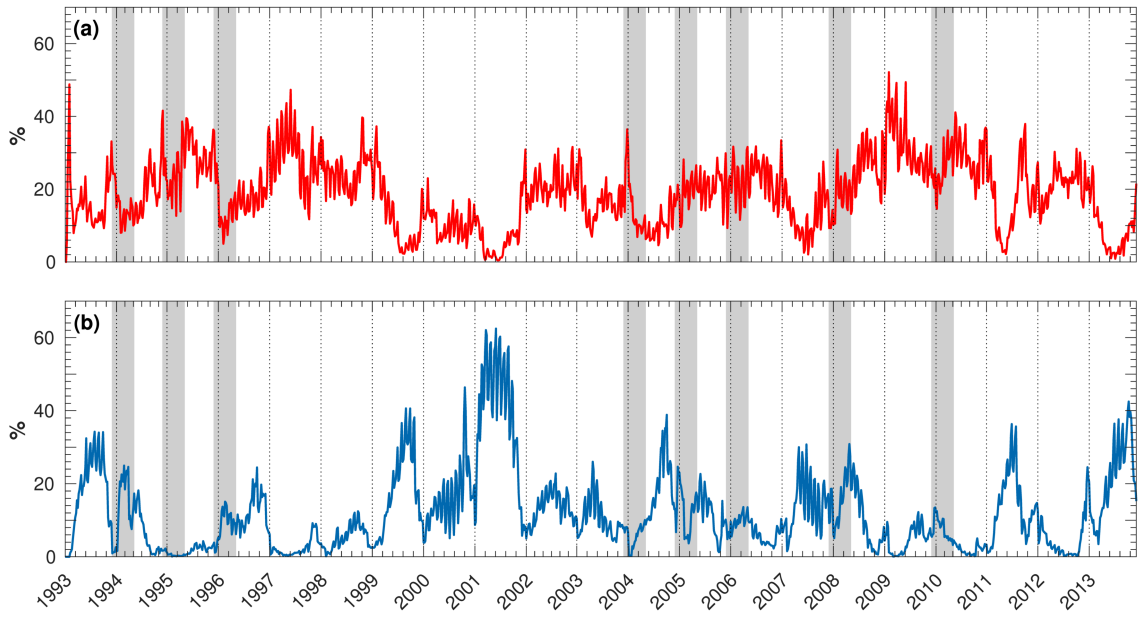


Figure. 5.18 Time series of the percentage of lagrangian particles arriving in the (a) 'model bloom box' and (b) south of Madagascar region.

During the first three bloom events (1994, 1995 and 1996), Langragian particles are observed in the bloom area, with peaks of high percentages occurring prior to the bloom (Figure 5.18a). The 1994, 1995 and 1996 events were characterized by ∼37%, 41% and 39% of particles in the box. Simultaneously, the box south of Madagascar exhibits low number of particles (Figure 5.18b). This confirms that coastal SEMC waters have been advected offshore, hence contributing to an input of NO_3 particles which will aid

in fertilizing the simulated South-East Madagascar Bloom. Interestingly, the lower percentage of particles present in the bloom area is observed in 1994 (Figure 5.18a), a year which was mostly characterized by a dominant input of NO_3 from the subsurface levels.

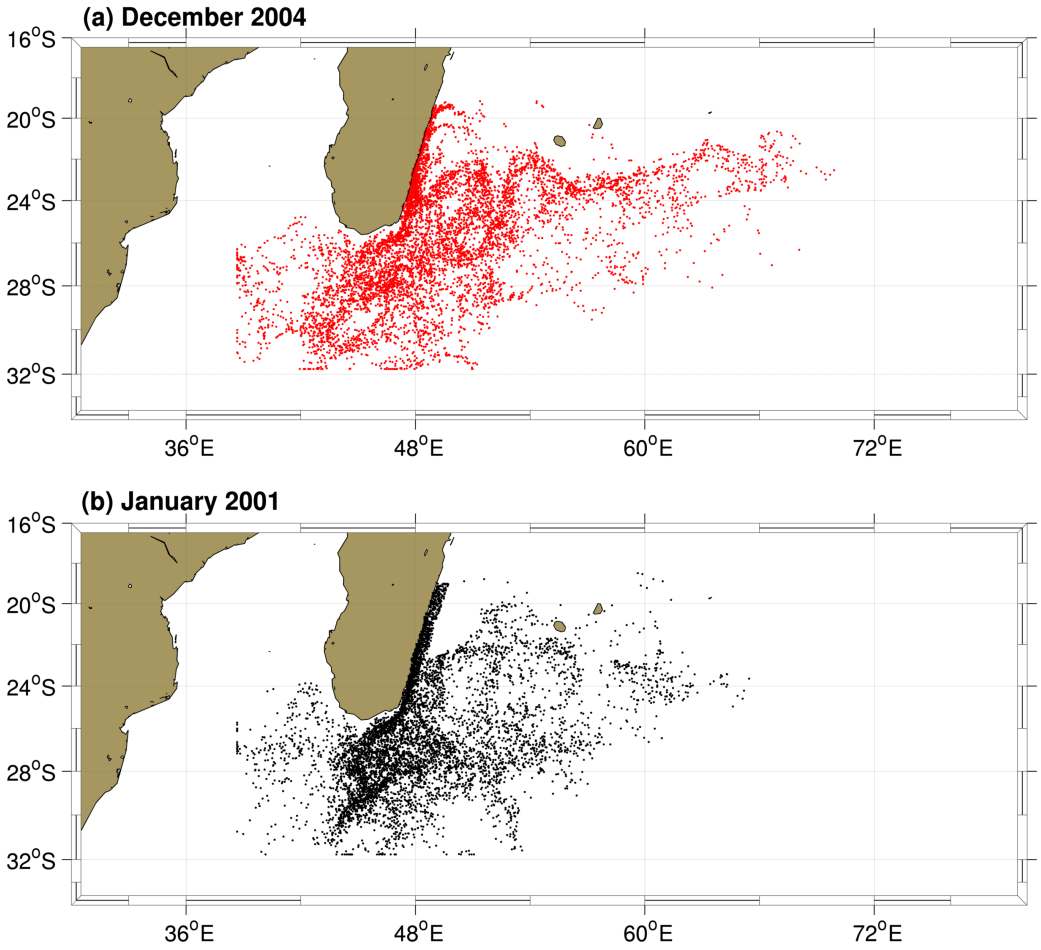


Figure. 5.19 Location of particles during (a) bloom event of December 2004, and (b) non-bloom event of 2001.

The 2004 event has been shown to be due to upwelling driven by negative WSC, owing to the presence of the tropical cyclone Elita in the region (Figure 5.14b). The associated vertical velocities are enhanced, inducing a stronger upwelling which brings nutrient-rich waters into the surface layers, triggering and sustaining the simulated 2004

bloom. However, a peak in the amount of Lagrangian particles is seen early January 2004, although this does not have an apparent influence on the input of NO_3 particles (Figure 5.13e). December 2005 and January 2001 were characterized by smaller percentages of particles in the 'model bloom box' (Figure 5.18a). These fewer particles could still indicate nutrient concentration which would influence the blooms. The 2005 and 2010 events are characterized by few particles entering the bloom region, co-occurring with even smaller numbers in the box south of Madagascar. These small portions in the bloom area could still be representative of coastal SEMC waters advected offshore. An important note is that an increase in number of particles in the 'model bloom box' co-occurs mostly with a decrease south of Madagascar, and vice-versa (Figure 5.18a and b).

The spread of the particles during two events, one of bloom occurrence (December 2004) and one of non-bloom occurrence (January 2001) are investigated (Figure 5.19). A clear difference between their dispersion is observed, with a preferential eastward advection during December 2004 (Figure 5.19a) compared to a more south, south-westward, after rounding the southern tip of Madagascar, during January 2001 (Figure 5.19b). These favoured eastward pathways could bring coastal, nutrient-rich waters into the bloom region, fertilizing it.

5.3 Discussion

The South-East Madagascar Bloom is investigated using a high-resolution biophysical CROCO-PISCES model (SWIO). SWIO has been shown to correctly resolves the mean physical properties in the region, but with a SICC position shifted slightly north. This northward shift is also apparent in a high resolution (0.1°) Parallel Ocean Program (POP) model by *Lambert et al.* [2016], who studied the connection between the SICC and the Indonesian Throughflow. In the Mozambique Channel and around the southern coasts of Madagascar, compared to observational datasets, SWIO simulates higher

productivity in austral winter whereas in austral summer, a slight over-estimation is observed in the bloom vicinity. Investigating the concentration of phytoplankton cells in the upper layers (0-20 m) of the water column, SWIO does not reproduce an austral summer bloom. However, in the subsurface layers (20-40 m), a bloom occurs south-east of Madagascar, exhibiting a sporadic interannual variability as observed in the ocean colour dataset. Spatially, the bloom displays a filamentous structure, as described by *Longhurst* [2001]. However, although the bloom is not confined to the surface layers, the irregular enhancement of Chl-a in the subsurface levels needs to be understood.

Accounting for the high austral winter productivity, a 'model bloom box' (51°E-56°E; 22°S-28°S) is delineated which is offshore enough to prevent interference from the austral winter signal, but which still captures the bloom. An eastern box (58°E-63°E; 22°S-28°S), further offshore is outlined, for the computation of a model bloom index. The bloom index computation method (box W - box E), presented in the previous chapter, is used to build a 'model bloom index'. From a histogram of maximum monthly Chl-a concentration from 1993 to 2013, a bloom threshold is defined and it is similar to the bloom threshold defined from ocean colour dataset in the previous Chapter (0.07 mg m^{-3}). The combination of the 'model bloom index' and the bloom threshold allows the identification of bloom and non-bloom years occurrences. Eight bloom years are described namely 1994, 1995, 1996, 2004, 2005, 2006, 2008 and 2010. The bloom years of 2004, 2006 and 2008, reproduced by SWIO, were also bloom years in Chapter 4. The simulated bloom exhibits substantial temporal variability, with the 2004 and 2005 events being the strongest ($\sim$0.21 mg m^{-3}). Maximum bloom intensity is reached during different months. Events of 1994, 1996 and 2008 present maximum bloom in January, and 1995, 2005 and 2010 reaching highest intensity in December of the previous year. The 2004 bloom is strongest in February of the same year.

The simulated South-East Madagascar Bloom also presents large variability in terms of its zonal and meridional extent. The mean latitudinal band at which it occurs

(22°S-29°S) compares quite well with the observed mean bloom, which occurs within a range of 24°S-30°S. The zonal extent is however underestimated, with the mean simulated bloom extending as far as 58°E, whereas in satellite data, the bloom extends up to 68°E. The spatial coverage of the bloom, during specific events exhibits differences in their shape. An elongated shape, initiating at the coast and extending further offshore, is observed in the bloom years of 1994, 1996, 2004, 2006 and 2008. The offshore extent, however, varies for each year. On the other hand, the 1995, 2004 and 2009 blooms display more vortex-like structures, possibly associated with mesoscale eddies. Exploring the mean vertical physical properties of the water column associated with bloom and non-bloom patches reveals a similar low-surface salinity signature during bloom years, as observed in the previous Chapter. This could possibly indicate a similar process associated with the simulated and observed bloom.

The mean local circulation, from satellite altimetry, associated with the bloom years has been shown to exhibit vortex-like structure with an anticyclonic circulation south-east of Madagascar, bounded by cyclonic circulation north and south. Similar local fluctuations of SLA are observed in SWIO. During non-bloom years, after rounding the southern tip of Madagascar, the SEMC displays a strong south-westward mean flow, whereas the mean flow is eastward during bloom months. This feature is also observed in satellite altimetry data, with a strong (weak) south-westward flow of the SEMC during non-bloom (bloom) months. This simulated eastward flow south-east of Madagascar creates a local retroflection whereas in the AVISO dataset, this retroflection flows mostly in a north-eastward direction. The fact that the coupled biophysical model simulates a sporadic subsurface phytoplankton bloom, associated with similar mean vertical physical properties within the water column and quite similar mean local circulation, allows further investigation of the causes of this bloom. A new hypothesis was put forward in the previous chapter, which states that the mean local circulation south-east of Madagascar during bloom months, could induce an advection of low-salinity, nutrient-rich waters into the bloom region. This would corroborate

with the low-salinity signature observed within bloom patches, as well as a dampening of the current-driven, coastal upwelling south-east of Madagascar [*Lutjeharms and Machu*, 2000; *Machu et al.*, 2002; *Ramanantsoa et al.*, 2018a].

A NO_3 flux analysis is performed to investigate the influence of vertical advection of nutrients from the subsurface, which would be representative of upwelling, as well as the horizontal advection of nutrients from the western boundary of the 'model bloom box', which would indicate influx of NO_3 from the coasts. From the 8 identified bloom events, 6 years (1995, 1996, 2005, 2006, 2008 and 2010) were found to be largely dominated by the influx of NO_3 from the western border of the 'model bloom box'. Associated low-salinity signature was also observed, hence representative of the fresher coastal SEMC waters. However, vertical uplift of nutrients towards the surface also play a minor role in contributing to the net NO_3 flux during those years. 1994 and 2004 were mostly dominated by vertical advection of NO_3. *Frajka-Williams et al.* [2009] also described the advection of low-salinity, nutrient-rich waters from West Greenland in playing a role in the spring phytoplankton bloom in the Labrador Sea. Similar to the south-east of Madagascar, the Labrador Sea is influenced by strong eddies which impact the separation of a boundary current [*Frajka-Williams et al.*, 2009].

SWIO simulates a bloom in 2004, also defined a bloom year from observed dataset, during which a significant positive W_{ek} was observed in the previous chapter. SWIO reproduces a significant but less intense WSC early February 2004, as observed from QuikSCAT data. This signature in WSC is a result of the tropical cyclone Elita, in the region. Tropical cyclones are known to alter the productivity in oligotrophic regions [*Lin et al.*, 2003; *Shi and Wang*, 2007; *Subrahmanyam et al.*, 2002]. Their associated intense wind induces stirring and divergent geostrophic currents. These result in a deepening of the mixed layer depth, and enhanced nutrients injected into the surface layer, triggering increased productivity [*Lin et al.*, 2003; *Shi and Wang*, 2007]. In the South China Sea, 20-30 % of the annual primary production are suggested to be

associated with tropical cyclones [*Subrahmanyam et al.*, 2002]. In SWIO, the bloom initiates 5 days after the peak in WSC whereas a one-month lag is seen in observational datasets. This indicates a quicker response in the surface dynamics in SWIO. The one-month lag associated with the observed 2004 bloom is corroborated by the success rate of 67% of W_{ek} at a one-month lag, from the hypothesis-testing model. Hence, SWIO seems to resolve correctly a bloom associated with the atmospheric variability, south-east of Madagascar. *Zhang et al.* [2016] showed that the effect of local transient wind-driven upwelling on vertical fluxes can dictate an increased phytoplankton biomass on the continental shelf off Ningaloo Reef, north-western Australia, during austral spring-summer.

The intrusion of low-salinity SEMC was further investigated using Lagrangian particles. 500 particles were released every month in the SEMC region and their occurrence in the 'model bloom box' and another box south of Madagascar were studied. As shown by *Srokosz et al.* [2015], particles from the SEMC can get advected offshore in the bloom region and hence fertilizes the bloom. The significant interannual variability associated to the number of particles in the bloom area could also illustrate the intermittent supply of nutrient-rich coastal waters, hence inducing the sporadic interannual variability of the bloom. It is observed that during the first four events (1994, 1995, 1996 and 2004), large numbers of particles arrived in the 'model bloom region', and hence could be representative of an influx of low-salinity coastal SEMC waters, bringing nutrients and consequently triggering a phytoplankton bloom. However, in 2004, the high percentage of particles did not influence the bloom, which was shown to be locally-driven by the wind. No significant peaks are observed during the other bloom months, but simultaneously, the number of particles south of Madagascar were relatively low. Hence, this more significant number of particles in the 'model bloom region', compared to the south of Madagascar, could still indicate high-nutrient SEMC waters advected offshore and initiating the phytoplankton bloom. *Srokosz et al.* [2015] explored the possibility of iron-advection from the sediments in coastal waters into the bloom region

using a combination of a high resolution ($\frac{1}{12}^{\circ}$) and a Lagrangian Particle model [*Blanke and Raynaud*, 1997]. They concluded that iron particles can be advected east, through mesoscale eddy field, and hence supporting the bloom during the specific year and the next year. *Srokosz et al.* [2015] also showed the significant spatial variability in the dispersal of the particles which could explain the substantial interannual variability in the spatial extent of observed blooms. Our analysis however, provides evidence of the significant temporal variability which could control the sporadic feature of the South-East Madagascar Bloom.

5.4 Summary

The high resolution biophysical model (SWIO) used in this study resolves a sporadic South-East Madagascar Bloom but in the subsurface layers. This simulated feature shows some bloom years (2004, 2006 and 2008) in agreement with the ocean colour dataset. It also exhibits large spatial and temporal variability and it is found to be confined within a shallow mixed layer, with fresher surface waters. This is in agreement with observations and indicates a possible similar mechanism at play. A hypothesis was put forward in the previous chapter, which implies the advection of fresher coastal SEMC waters, rich in nutrients, offshore and hence triggering the South-East Madagascar Bloom. SWIO is employed to test this hypothesis. It is shown that advection of this water-mass concurrently occurs with the simulated South-East Madagascar Current, with its interannual variability driving the sporadic phytoplankton enhancement of the region. The southern SEMC appears to act as a gate allowing the water to flow towards the African continent or switching into a retroflection loop, diverting the water into the South-East Madagascar Bloom region. Such behaviour is consistent with the description made by *Siedler et al.* [2009] and might explain the controversy for an existence or not of a retroflection of the SEMC [*Lutjeharms*, 1988; *Quartly and Srokosz*, 2002].

Chapter 6

Subsurface intensified eddies in the South Indian Ocean

6.1 Introduction

Mesoscale eddies are ubiquitous features of the world oceans and play a fundamental role in transferring physical and biological properties across different spatial and temporal scales [*Chaigneau et al.*, 2011; *Chelton et al.*, 2011a; *Dufois et al.*, 2017; *Qiu and Chen*, 2005; *Zhang et al.*, 2014, 2015]. The paradigm of a mesoscale eddy, known as a surface-intensified eddy, features the occurrence of a maximum geostrophic velocities at the surface. However, mesoscale eddies with their cores in subsurface layers, and hence maximum geostrophic velocities in their subsurface, have also been shown to occur in the ocean [*Kostianoy and Belkin*, 1989; *Mcwilliams*, 1985]. These are known as subsurface eddies or subsurface vortices. Depending on the depth of their cores, they can further be classified as subthermocline eddies (STEs), with the core below the thermocline, and intrathermocline eddies (ITEs), with the core between the seasonal and permanent thermoclines [*Barceló-Llull et al.*, 2017; *Li et al.*, 2017a; *Nauw et al.*, 2006; *Pelland et al.*, 2013; *Zhang et al.*, 2015]. This study focuses on surface and subsurface-intensified eddies in the South Indian Ocean, without distinguishing between the different subsurface eddy-types.

Surface signature associated with a subsurface eddy may be evident in some cases, whereas in others, it may be weak or event absent. A peculiarity of subsurface cyclonic (anticyclonic) vortices is their bowl (dome)-shaped isopleths in the shallower levels, and

dome (bowl)-shaped isopleths in the deeper levels. The cyclonic-associated shape has been termed as 'thinny' by *McGillicuddy* [2015]. These features trap vertically homogeneous water properties [*McGillicuddy et al.*, 2007] similar to their area of origin. A key attribute, however, is their longevity, during which they trap water representative of their formation area and advect these thousands of kilometers away [*Nauw et al.*, 2006]. This process could represent an important contribution to the oceanic heat and salt budgets as well as transport of biological tracers [*Ledwell et al.*, 2008; *Thomsen et al.*, 2016].

Subsurface eddies have been investigated in different parts of the global oceans, most extensively in the North Atlantic [*Barceló-Llull et al.*, 2017; *Bower et al.*, 1997, 2013; *McDowell and Rossby*, 1978] and North Pacific Oceans [*Collins et al.*, 2013; *Li et al.*, 2017a; *Oka et al.*, 2009; *Pelland et al.*, 2013; *Zhang et al.*, 2015] compared to the south-eastern Pacific Ocean [*Johnson and McTaggart*, 2010], the North-western Indian Ocean [*Shapiro and Meschanov*, 1991] and South Indian Ocean [*Nauw et al.*, 2006]. The most common are the Mediterranean water eddies, also known as Meddies, which are deep, warm and salty lenses drifting south-westward from the Mediterranean outflow to the northern Atlantic Ocean. They are 500-1000 m thick with a 40-150 km diameter [*Bashmachnikov et al.*, 2015; *Carton et al.*, 2010; *Hebert et al.*, 1990; *L'Hégaret et al.*, 2014] and play an integral part in redistributing high salinity water in the North Atlantic Ocean. Another common group of subsurface eddies are the Cuddies (California Undercurrent eddies), which have an average radius of 20.4 km. A study by *Pelland et al.* [2013], using 5.5 years of Seaglider data, showed that up to 40% of the heat and salt loss of the California Undercurrent can be attributed to Cuddies.

The formation mechanisms of subsurface eddies vary in nature, depending on their genesis area in the world ocean. The two main subsurface vortices, namely Meddies and Cuddies, have been shown to be formed as a result of baroclinic instabilities of their undercurrents, the Mediterranean Undercurrent and California Undercurrent, respectively [*Bashmachnikov et al.*, 2015; *Carton et al.*, 2010; *Collins et al.*, 2013; *Garfield et al.*,

1999; *Hebert et al.*, 1990; *L'Hégaret et al.*, 2014]. Another mechanism is the reduction of potential vorticity in frontal regions associated with opposite-directed winds on the frontal jet [*Thomas*, 2008]. A numerical study on the generation mechanisms of ITEs in the Japan Sea, by *Hogan and Hurlburt* [2006], deduced three main mechanisms: 1) subduction of winter surface mixed layer water at frontal convergence; 2) advection of stratified water capping a pre-existing eddy and; 3) a restratification of the upper layers in a pre-existing eddy due to solar heating. *McGillicuddy* [2015] proposed that eddy-wind interaction can drive a local upwelling so intense that it induces doming of isopycnals in anticyclonic eddies. A recent study by *Gordon et al.* [2017] suggested a new mechanism, where interactions between a tropical cyclone and a surface-intensified eddy can result in an ITE. A tropical cyclone will influence the upper layers of the eddy by removing heat, with the deeper part of the eddy subducting into the stratified thermocline. Further interactions will be hindered, with the ITE isolated from air-sea interactions, and its periphery being stable to shear instability [*Gordon et al.*, 2017].

In the Indian Ocean, two anticyclonic subsurface eddies, termed as ITEs, were surveyed south-east of Madagascar during the Dutch-South African ACSEX programme (Agulhas Current Sources EXperiment) [*Nauw et al.*, 2006]. Characterized by a subsurface maximum in salinity exceeding 35.8 psu, these flat homogeneous water lenses had oxygen-rich cores. They exhibited horizontal and vertical extent of 180 km and 150 m respectively, with maximum azimuthal velocities of about 0.2-0.3 m s^{-1} observed on the edge of the eddy-core, at 200 m depth. Using the cruise datasets as well as data from World Ocean Circulation Experiment (WOCE), World Ocean Database (WOD) and ARGO profiles, *Nauw et al.* [2006] tracked these anticyclonic eddies through their water mass properties, namely, the Subtropical Underwater (STUW), up to their generation area. High evaporation associated with low precipitation in the eastern South Indian Ocean induce an increase in sea surface salinity. The subsurface eddies appear in this high surface salinity region, which is also an important shear zone between the shallow eastward South Indian Ocean Countercurrent (SICC) [*Jia et al.*, 2011a; *Palastanga*

et al., 2007; *Siedler et al.*, 2006] and the underlying westward South Equatorial Current. Owing to local instabilities between the currents, this highly saline water subducts in deeper layers, hence creating a subsurface salinity maximum. Interannual modulations of the eddy kinetic energy (EKE) in this zonal band (15°S-35°S) was shown to result from the variation of large-scale wind forcing by the Southern Annular Mode [*Jia et al.*, 2011b]. Anomalous gyre-scale upwelling or downwelling induces slackening or steepening of the isotherms and thus reduced or enhanced baroclinic instabilities and eddy activities, also at seasonal time scale [*Jia et al.*, 2011b].

Following the study of *Nauw et al.* [2006], which reported for the first time the presence of anticyclonic subsurface vortices in the South Indian Ocean, no other work has explored further the implications of these features to the Indian Ocean circulation and its possible link to the biogeochemistry. Some open questions remain: 1) What is the actual role of subsurface eddies within the context of heat and salt redistribution at mid-depths of the South Indian Ocean?; and 2) Do subsurface cyclonic eddies also exist in the South Indian Ocean? To answer these questions, a blended analysis of matching Argo float profiles and satellite altimetry-detected eddy signals is used to construct an average eddy field. Based on some previous knowledge about the vertical structure of a prototypical subsurface eddy [*Nauw et al.*, 2006], a subsurface eddy-identification method is developed to distinguish between surface and subsurface eddies. Finally, a three-dimensional eddy census and statistical characterization of subsurface eddies in the South Indian Ocean is presented, along with the first climatological estimates of their associated volume, heat and freshwater transports.

The rest of this document is structured as follows: The different datasets as well as the regions of interest and the subsurface eddy-identification method are detailed in section 6.2. The results are presented in 6.3 with section 6.3.1 giving a statistical description of surface and subsurface eddies in the studied regions, as well as their mean vertical thermohaline structure. The mean vertical characteristics of the subsurface

eddy cores including their dominant water masses and propagation are detailed in section 6.3.2. Section 6.3.3 comprises of a description of the heat and salt transport associated with the different eddy-types. Finally, the main findings of this work are summarized in section 6.4.

6.2 Data and Methods

6.2.1 Eddy Available Potential Energy (EAPE)

The Eddy Available Potential Energy (EAPE) in the ocean is an energy budget, different from the kinetic energy reservoir, which indicates mesoscale turbulence at depth [*Roullet et al.*, 2014]. Indicative of active baroclinic instabilities, this dataset is based on ∼830,000 Argo profiles spanning from 2002 to 2013. Anomalies in the vertical isopycnal displacements are used as a proxy to compute the intensity of the mesoscale subsurface turbulence. A practical method of computing EAPE is:

$$EAPE = -\frac{g}{2\rho_0}\overline{\zeta'\rho'} \tag{6.1}$$

where ζ' is the vertical isopycnal displacement, ρ' the density anomaly associated with this displacement, g is the gravitational acceleration (9.81 m s^{-2}), ρ_0 the potential density of seawater (1024 kg m^{-3}) and the bar referring to a long-term time averaging. However, internal tides and waves, as well as the seasonal modulation in mixed layer can affect the signal. Consequently, it should be considered in regions remote to internal tides generation. From the maps shown by *Arbic et al.* [2012], it can be inferred that the eastern box is not influenced by internal tides. Although the western box is found on the southern boundary of internal tides hotspots (Mascarene Plateau), it is not greatly influenced by these features either. Further details on this product are provided by *Roullet et al.* [2014].

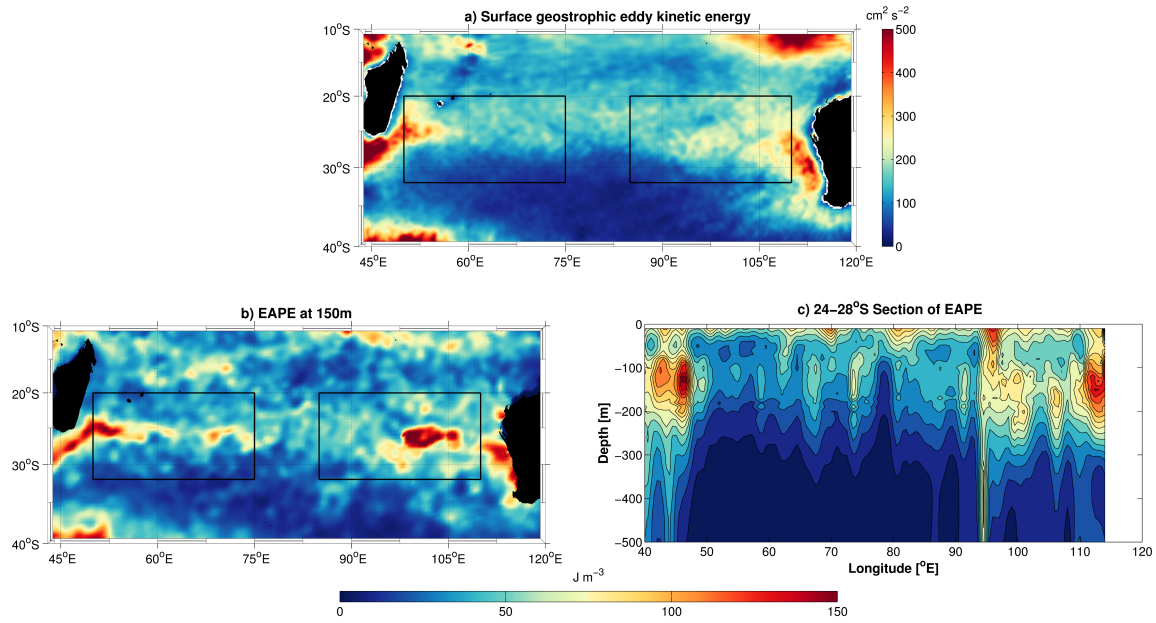


Figure. 6.1 (a) Mean surface geostrophic eddy kinetic energy (EKE; cm^2 s^{-2}) calculated from 12 years (2002-2013) AVISO data. **(b)** Mean EAPE (J m^{-3}) at 150 m depth with two black boxes delineating regions of interest. **(c)** shows a mean latitudinal (24°S-28°S) vertical section of EAPE across the South Indian Ocean (40°E to 120°E).

A peculiarity of the South Indian Ocean is its level of eddy energy in its eastern basin, in agreement with *Jia et al.* [2011a], as is apparent in Figure 6.1a. An enhanced EAPE signature, as well as EKE, are evident in both the eastern and western boundary current systems, namely the Leeuwin Current and the South East Madagascar Current. It should be noted that the EAPE is shown in Figure 6.1b at 150 m depth, where *Nauw et al.* [2006] observed the eddy core of subsurface eddies. The boxes outlined in Figure 6.1a and b indicate the two study regions: an 'eddy generation region' (eastern box at 85°E to 110°E) proposed by *Nauw et al.* [2006], and an 'eddy arrival region' (western box at 50°E to 75°E), where two subsurface eddies have been previously observed [*Nauw et al.*, 2006], both at a latitude range of 20°S-32°S.

The eastern box encloses the region where subsurface eddies have been shown to be generated via subduction of high-salinity water. This eddy generation site is

collocated with the enhanced signal of EAPE near 100°E, shown within the box in Figure 6.1b. The western box was based on the observations reported by *Ponsoni et al.* [2015, 2016], which suggest that altimeter-detected eddies drive a significant variability of the volume transport carried by the EMC. In accordance with these findings, the western box was located in the open ocean, before interaction with the EMC, so that the properties of the eddies are captured prior to their arrival to the western boundary. This western box forms part of an 'eddy-corridor' described by *Quartly et al.* [2006], and which has been associated with the westward-propagating mesoscale eddies. These two distinct zones are separated by the low subsurface EAPE signature observed at approximately 78°E (Figure 6.1b) and are located well into the open ocean.

6.2.2 Eddy Tracking Algorithm

In this study, the 4^{th} release of an existing eddy global dataset [*Chelton et al.*, 2011b] was used to identify and study mesoscale eddies in the South Indian Ocean. This dataset is established from an automated algorithm which tracks eddies based on daily sea surface height (SSH), as seen from altimetry in the delayed-time 'two-sat merged' product of AVISO. See 'Eddy Tracking Algorithm' in section 3.1 of Chapter 3 for more details about this algoritm.

The eddies in the two regions of study were selected based on two different criteria. In the eastern box, mesoscale eddies with their genesis occurring within the box were taken into consideration. In the western box, all eddies passing through it were considered, either locally or remotely generated.

6.2.3 Argo Float Data

Initially designed for large-scale climate studies [*Riser et al.*, 2016], the international Argo program which consists of almost 3800 autonomous Lagrangian profiling floats, has recently been used to study oceanic mesoscale eddies in different parts of the

world oceans [*Chaigneau et al.*, 2011; *Li et al.*, 2017a; *Yang et al.*, 2015; *Zhang et al.*, 2014]. Argo floats provide data of temperature and salinity from the surface to as deep as 2000 m. These data have been made freely available by the Coriolis Project (http://coriolis.eu.org). For the three-dimensional study of surface and subsurface eddies propagating in the South Indian Ocean basin, temperature and salinity profiles from August 2000 till December 2015 are used. These data have undergone automatic pre-processing and quality control measures by the Argo Data Centre [*Böhme and Send*, 2005; *Owens and Wong*, 2009; *Wong et al.*, 2003]. To ensure that only good data is retained, the following requirements based on the quality control flags and sampling characteristics of the Argo data are employed: (1) only temperature, salinity and pressure data with quality flag 1 and 2 (good and potentially good respectively) are considered; (2) the shallowest and deepest data should be between the surface and 20 m, and below 1500 m respectively; (3) the temperature and salinity difference from one depth to the next should not exceed 3°C and 1 psu respectively, after interpolating on a regular 10 m vertical resolution grid.

The above criteria were applied after an eddy-Argo collocating analysis was performed. Assuming a perfect circle eddy-shape, all Argo profiles located within the eddy-radius distance from the eddy-core are taken into consideration. At this stage, Argo profiles are also identified as either anticyclonic or cyclonic, depending on the eddy altimeter database. In the eastern Indian Ocean region, this technique provides 1232 and 1191 profiles in anticyclonic (AE) and cyclonic eddies (CE) respectively, whereas in the western region, this yields 1232 profiles for AE and 1451 profiles for CE. The combined 5106 T/S profiles were interpolated on a regular 10 m vertical grid from the surface down to 1500 m depth. The temperature, salinity and density anomalies of each profile associated with the two eddy categories (AE and CE) are then calculated by removing the climatological values from the CSIRO Atlas of Regional Seas 2009 (CARS09) dataset [*Dunn and Ridgway*, 2002; *Ridgway et al.*, 2002], which have been spatially and temporally interpolated to match the exact day in year and positions

of Argo profiles. This enables the quantification of the eddy properties that make them different from the background field and, therefore their potential role in the redistribution of heat and salt in the ocean.

6.2.4 Subsurface Eddies Identification Method

The combination of the Argo and eddy-database led to 5106 Argo profiles co-located to altimeter-detected eddies. However, among these Argo profiles, the signal of either surface or subsurface eddies may be evident; the latter type only when they also have a surface signature. The challenge is to set an automated algorithm which will assign the above number of Argo profiles to surface or subsurface eddies. To this aim, first their steric dynamic height anomaly is computed. The variability in steric change is due to changes in either the subsurface temperature profiles (thermosteric component) and/or in the subsurface salinity profiles (halosteric component). For each profile, the *Steric Dynamic Height Anomaly (SDHA)*, h', was computed using a reference level at 1500 dbar, following the definition by *Gill and Niiler* [1973] and *Tomczak and Godfrey* [1994]:

$$h' = \int_{-1500}^{0} \delta\rho \, dz \tag{6.2}$$

where $\delta\rho$ is the density anomaly of the profile, relative to CARS09, and dz is the vertical grid resolution. 1500 dbar has been commonly referenced as no-motion in former studies in this region [*Yang et al.*, 2015]. For any co-located Argo-eddy profile, a dynamic height anomaly more significant in the subsurface compared to the surface layers, would be representative of subsurface maximum in velocities associated with the eddy, hence a subsurface-intensified eddy. It should be noted that steric height anomalies may represent the signature of internal tides. The implication of internal tides on the two boxes of interests have been discussed in section 6.2.1.

Applying this specific criterion to identify subsurface eddies, 474 CEs and 135 AEs profiles in the eastern South Indian Ocean, and 368 CEs and 168 AEs in the western

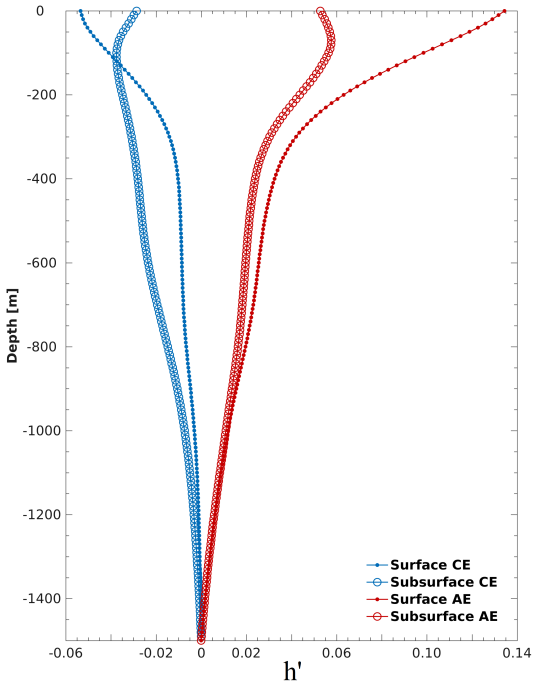


Figure. 6.2 Steric Dynamic Height anomaly, h', (m) for surface (small dots) and subsurface (large dots) intensified cyclonic (blue) and anticyclonic (red) eddies

part were characterized as subsurface-intensified. Figure 6.2 illustrates the difference in steric dynamic height anomalies of surface and subsurface eddies in the South Indian Ocean. Cyclonic profiles characterized as subsurface cyclonic eddies displayed more negative steric dynamic anomalies in their subsurface layers. For subsurface anticyclonic eddies, the profiles exhibited more positive anomalies of steric dynamic height in their subsurface levels. On the other hand, surface-intensified profiles are very distinct with large anomalies at the surface, representative of maximum velocities at the surface. However, it is worthwhile recalling that in Figure 6.2, only subsurface eddies with a surface signature are included since they were altimeter-detected. Concurrently, submesoscale eddies account for 54% of the total number of eddies in the South Indian Ocean [*Zheng et al.*, 2015] and are not considered here, given the spatial resolution of the altimeter product. These imply an underestimation of the total number of surface and subsurface eddies.

It is worthwhile noting that the accuracy of this method relies on the characteristic vertical distance between surface and subsurface anomalies of steric dynamic height. A high vertical resolution of temperature and salinity is required such that the characteristic difference between SDHAs is well resolved. In this study, the mean vertical sampling resolution of Argo floats in the eastern and western Indian Ocean was 8.7 ± 1.4 m and 8.4 ± 1.6 m, respectively; whereas mean vertical distances between surface and subsurface peaks in SHDA were 80 (110) m for AEs (CEs). Based on the latter, one can reasonably argue that these are well above the requirement to resolve indistinctly the difference between surface and subsurface eddies. The applicability of this eddy identification method to other regions of the global oceans will depend on the above discussed relationship between vertical scales of surface against subsurface eddies and vertical sampling rates of temperature and salinity data.

6.2.5 Eddy Composition

To reconstruct the 3-dimensional structure (temperature, salinity and potential density) of each eddy-type, a rotationally symmetric eddy with cylindrical shape is assumed. The zonal and meridional distances (Δx and Δy respectively) are defined relative to the eddy centre, where ΔX=ΔY=0. For the eddy composites, a normalized coordinate system is used, where the distance of each Argo profile to the eddy centre, denoted as 'r', is normalized by the eddy radius, R.

For each level of depth (z), the variables and their respective anomalies are transformed onto a normalized horizontal eddy-coordinate system (ΔX, ΔY). These are then mapped onto a regular 0.5° X 0.5° grid using the Barnes objective analysis [*Barnes*, 1973]. This method consists of an inversed distance weighting interpolation and has previously been used in mesoscale eddy structures studies [*Yang et al.*, 2013, 2015]. The variables are then extracted in 1-D as a function of the distance r/R to the eddy centre.

A regression fitting curve, LOESS (Locally Weighted Scatter-plot Smoother) [*Cleveland and Devlin*, 1988] is then applied to the 1-D dataset at each level z to prevent the presence of any discontinuity in the composites. Eventually, all the variables, v (r,z), are mirrored to v (-r,z) for graphics.

From the composite vertical potential density, $\bar{\rho}$ (r,z), the composite vertical rotational speed ($\bar{v}$) is calculated using the thermal wind balance equation:

$$\bar{v}(r,z) \;=\; -\frac{g}{f}\int_{-1500}^{z}\frac{\partial\rho\,(r,z)}{\partial r}\,dz \tag{6.3}$$

where f is the mean Coriolis parameter (-0.64 x 10^{-4} s^{-1}) over the latitudinal band.

6.3 Results

6.3.1 Eddy Statistics and Vertical Structure

In this section, the statistics and typical three-dimensional structure of the four eddy-types (cyclonic/anticyclonic and surface/subsurface), for both the eastern and western South Indian Ocean regions, are presented.

• Eastern Indian Ocean

The mean statistical characteristics of the different eddy types generated in the eastern South Indian Ocean region are displayed in Table 6.1. Surface AEs have been more often detected than surface CEs, and this is consistent with a higher occurrence of AEs in the Eastern South Indian Ocean [*Zheng et al.*, 2015]. The number of Argo profiles tracked in surface eddies is also greater than for subsurface eddies, as one might expect. The weaker, and sometimes even absent surface signal of subsurface eddies enables the collocation of a lower number of Argo profiles as compared to the number of Argo profiles in surface eddies: 43% (11%) of the total of profiles corresponded to cyclonic (anticyclonic) subsurface eddies. In this context, limited information is available to

Table 6.1 Statistical characteristics of surface and subsurface eddies in the Eastern South Indian Ocean. ± refers to the standard deviation from the mean.

Eastern Indian Ocean	**Surface**		**Subsurface**	
	CE	AE	CE	AE
Number of profiles	779	1190	605	151
Lifespan (days)	185 ± 169	175 ± 158	217 ± 189	223 ± 168
Amplitude (cm)	9.0 ± 4.7	9.6 ± 4.7	10.0 ± 5.9	7.6 ± 4.1
Radius (km)	115.3 ± 36.3	115.8 ± 32.1	103.9 ± 39	111.7 ± 31.1
Rotational Speed (cm s^{-1})	25.0 ± 8.9	25.6 ± 7.6	26.8 ± 9.6	22.3 ± 7.0
Translational Speed (cm $^{-1}$)	4.5 ± 1.7	4.7 ± 1.9	4.6 ± 1.7	4.5 ± 1.4

argue that the lower percentage of subsurface AE profiles compared to CE profiles respond to either an actual lower percentage of subsurface AEs or to a lower retention capacity of the subsurface AEs. Remarkably, subsurface eddies outlive surface eddies, with a mean lifespan of approximately 217 (CEs) and 223 days (AEs) compared to 175 (CEs) and 185 (AEs) days for surface eddies. This supports the suggestion of the important role of subsurface eddies for the re-distribution of ocean properties as their natural tendency to propagate westward from the east will take them towards the western margins of the basin.

The mean rotational and translational speeds of the different eddy-types exhibit no major differences in these statistical characteristics. They present similar mean radius ranging from 100-115 km. Considering the standard deviation from the mean, their amplitudes also reveal no great variation among the different eddy-types, with surface CE (AE) exhibiting amplitudes of 9.0 (9.6) cm and subsurface CE (AE) presenting amplitudes of 7.6 (10.0) cm. However, the mean amplitude for cyclonic subsurface vortices is slightly higher compared to subsurface anticyclones.

Temperature and salinity anomalies of the four distinct eddy-types in a cross section passing through the centre of the composite eddies (at ΔY =0) were analysed (Figure 6.3). Note that the two subsurface AEs surveyed by *Nauw et al.* [2006] in 2001

near Madagascar, whose origin were suggested to be in the eastern South Indian Ocean, were characterized by subsurface positive salinity anomalies in their cores. In agreement with this, the subsurface eddy-identification method used in this study reveals a positive salinity anomaly in the subsurface levels of these eddies [see Figure 6.3d [CE] and Figure 6.3h [AE]]. This vertical salinity structures give confidence in the eddy-identification method.

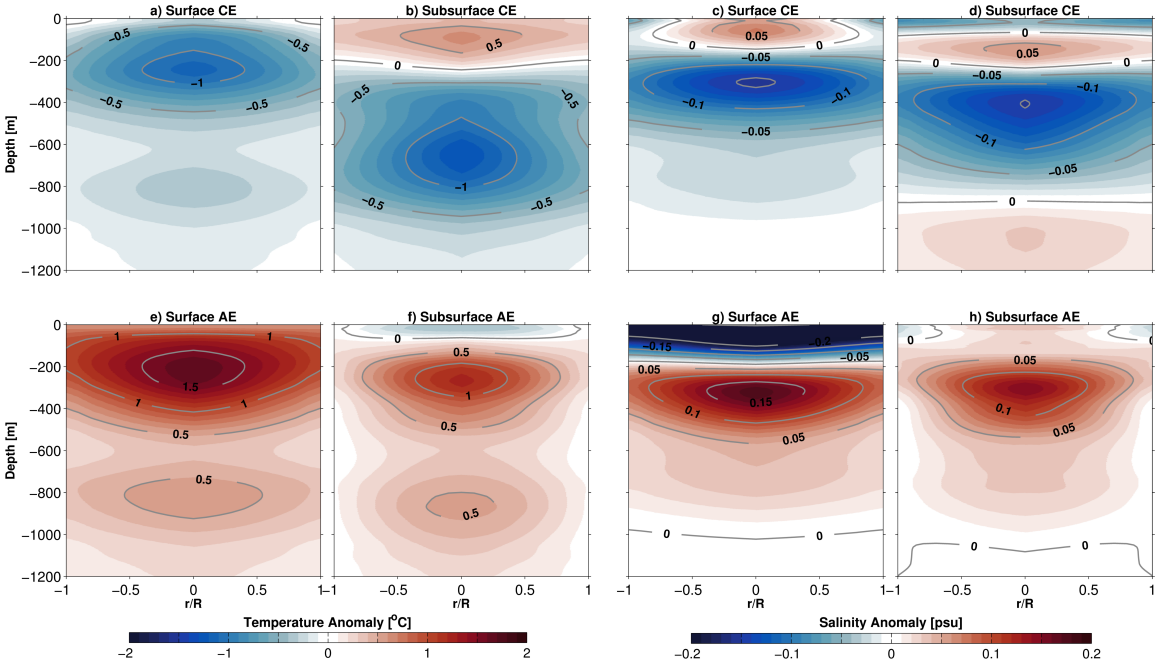


Figure. 6.3 Vertical sections of potential temperature (°C; 1^{st} and 2^{nd} columns; a,b,e,f) and salinity anomalies (psu; 3^{rd} and 4^{th} columns; c,d,g,h) across composite cyclonic (top) and anticyclonic (bottom) surface and subsurface eddies, at ΔY=0, in the eastern South Indian Ocean, over the box shown in Figure 6.1a.

The composite vertical structures of surface and subsurface eddies, after performance of the automated identification algorithm, agree well with expectation according to their associated vertical displacements. Thus, composite eddies present a positive salinity maximum at subsurface levels when vertical movement subducts surface high salinity water at depth. This occurs at almost the same depth ($\sim$ 300 m) in both surface and subsurface AEs (Figure 6.3g and h). The vertical extent of this positive anomaly

goes down to 900 m for subsurface AEs, compared to it being concentrated between the 200-900 m layers for surface AEs. Interestingly, surface AEs differ in the upper layers from subsurface AEs with a salinity minimum, absent in the latter (Figure 6.3h). Also as expected in subsurface CEs, a positive subsurface salinity maximum occurs at ∼150 m depth, with significant negative anomalies in the deeper layers (∼400 m; Figure 6.3d). On the other hand, surface CEs showed a slightly positive surface salinity anomaly (0-200 m depth), and a strong subsurface negative salinity anomaly from 200 m to ∼900 m depth.

The eddy-vertical temperature structures also follow expectations from their associated vertical displacements, with both surface and subsurface CEs (AEs) being responsible in moving colder (warmer) waters. Both surface CEs and AEs exhibit the same polarity in temperature anomalies throughout the vertical column, with negative and positive anomalies, respectively (Figure 6.3a and e). They both present two cores of temperature anomalies along their structure, with a shallower one at ∼200 m depth and the deeper one at ∼800 m depth. Interestingly, subsurface eddies also exhibit two cores of temperature anomalies, but of different polarities. Subsurface CEs display positive anomalies in their surface and negative anomalies in their subsurface layers. The contrary occurs in subsurface AEs, with negative and positive anomalies in their surface and subsurface layers, respectively. The negative core of subsurface CEs is located at around ∼650 m, deeper than subsurface AEs positive core which is found at ∼300 m.

The mean vertical structure of rotational speed associated with each different eddy-type in the eastern South Indian Ocean is calculated using the thermal wind balance (Equation 6.3) and is shown in Figure 6.4. As expected, maximum rotational speeds prevail in the deeper levels for subsurface CEs and AEs (Figure 6.4b and d), compared to surface CEs and AEs which exhibit maximum speed at the surface (Figure 6.4a and

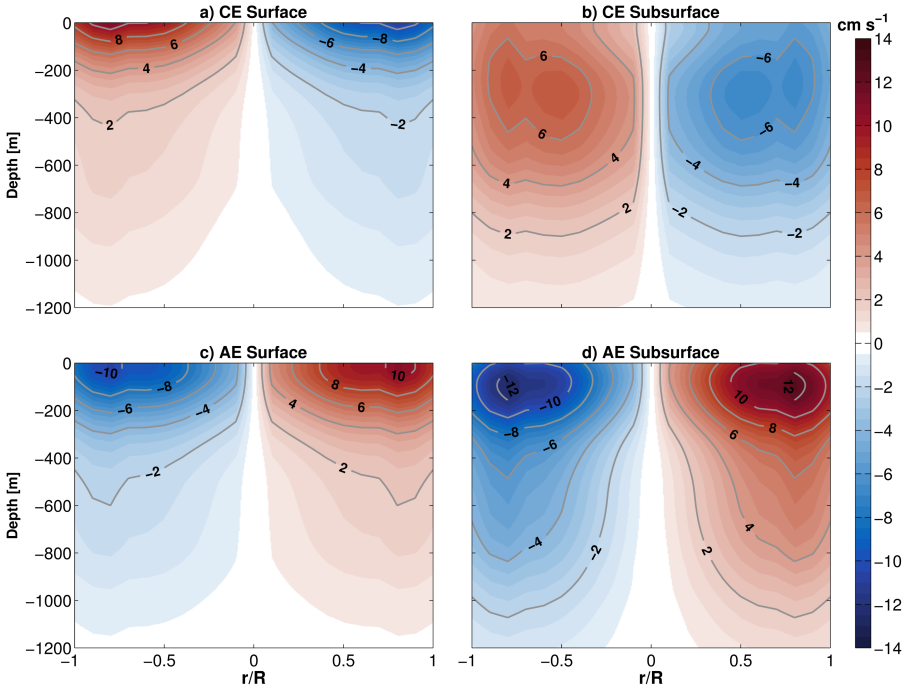


Figure. 6.4 Vertical sections of the rotational speed anomaly (cm s^{-1}) of the composite surface CEs (a) and AEs (c) and subsurface CEs (b) and AEs (d) in the eastern Indian Ocean.

c). This shows that the identification method of subsurface eddies, using the steric dynamic height anomaly, works well in pinpointing out profiles within eddies having subsurface maximum velocities, as one would expect for a subsurface-intensified eddy.

Rotational speeds of subsurface AEs are generally stronger than subsurface CEs, but with the vertical extent of enhanced speed being smaller and shallower. Note that the former exhibits almost two times the rotational speed of subsurface CEs. Maximum magnitudes of 12.6 cm s^{-1} and 6.8 cm s^{-1} occur at ∼100 m and ∼300 m depth for subsurface AEs and CEs respectively, compared to a surface magnitude of 10-11 cm s^{-1} for surface AEs and CEs. The rotational speed of surface eddies extends down to ∼1000 m, compared to subsurface eddies which influence deeper levels, sometimes down to 1200 m.

• **Western Indian Ocean**

Statistical characteristics of the different eddy-types in the western South Indian Ocean are displayed in Table 6.2. Compared to the eastern box, more (less) subsurface AEs (CEs) are tracked in the western box, accounting for a total of 14.9% (28.8%) of all western AEs (CEs) profiles. As observed in the eastern South Indian Ocean, these subsurface features are longer-lived compared to surface ones. Considering the altimetric expression of the different eddy-types, no major differences are observed, with a mean radius of the order of 100 km and mean amplitude of ∼8.5 cm. However, the mean translational speeds in the western box exceed those in the eastern box by almost 0.75 cm s^{-1}.

Generally, the thermohaline vertical structures of the distinct eddy-types in the western South Indian Ocean Figure 6.5) are analogous to the eastern region (generation site; Figure 6.3), with similar vertical structures but at weakened intensities. Subsurface eddies are characterized by positive salinity anomalies, with surface AEs differentiating from subsurface AEs with a negative surface salinity anomaly. Owing to their associated upwelling (downwelling) mechanisms, as expected, CEs (AEs) display negative (positive) temperature anomalies. However, as observed in the eastern region, their subsurface forms exhibit two cores of opposite polarities. Their respective surface signature is characterized by a negative sign of the surface paradigm (Figure 6.5b and c), and only the subsurface water column is consistent with the expected uplift/downlift of isotherms. This peculiarity of opposite vertical temperature polarities associated with subsurface eddies needs to be taken into consideration when investigating the biogeochemical implications associated with subsurface eddies in the South Indian Ocean.

The magnitude of the rotational speed associated with surface eddies in the western South Indian Ocean (Figure 6.6) remains quite coherent, when compared to the eastern

Table 6.2 Statistical characteristics of surface and subsurface eddies in the Western South Indian Ocean. ± refers to the standard deviation from the mean.

Western Indian Ocean	**Surface**		**Subsurface**	
	CE	AE	CE	AE
Number of profiles	1158	1304	469	229
Lifespan (days)	161 ± 123	150 ± 113	171 ± 128	158 ± 124
Amplitude (cm)	8.8 ± 4.7	9.3 ± 4.5	8.2 ± 4.3	7.8 ± 4.0
Radius (km)	116.0 ± 33.1	119.8 ± 33	118.4 ± 34.0	115.4 ± 31.4
Rotational Speed (cm s^{-1})	23.5 ± 8.9	23.8 ± 7.5	22.2 ± 8.3	21.2 ± 6.7
Translational Speed (cm $^{-1}$)	5.3 ± 2.6	5.4 ± 2.7	5.4 ± 2.5	5.3 ± 2.3

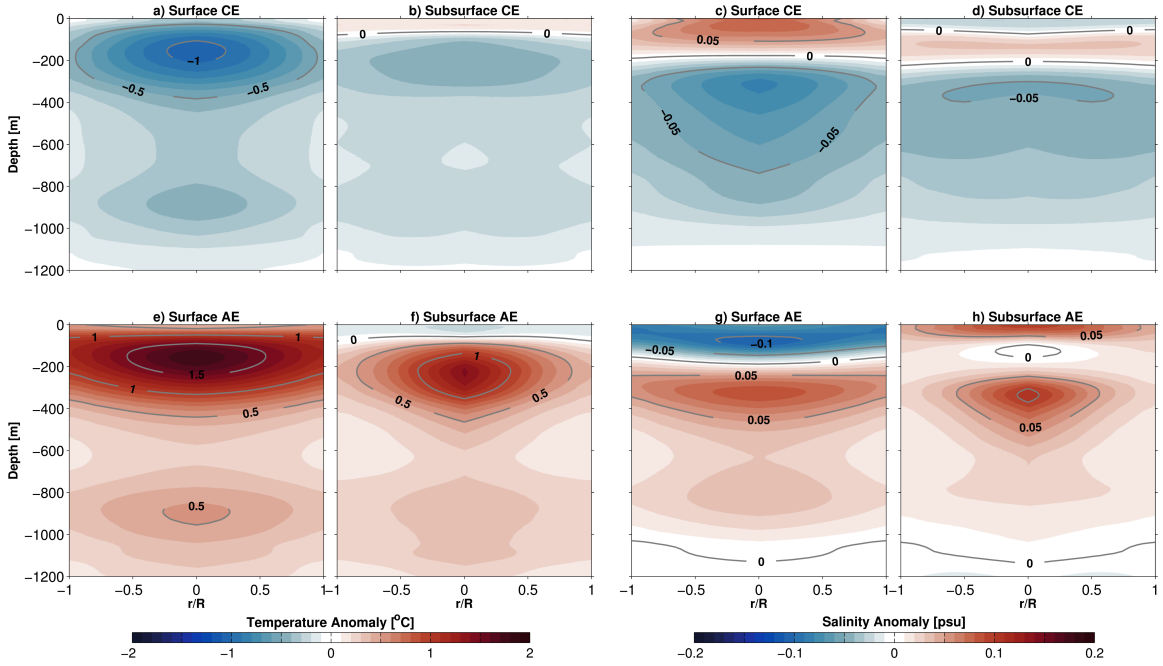


Figure. 6.5 Vertical sections of potential temperature (°C; 1^{st} and 2^{nd} columns) and salinity anomalies (psu; 3^{rd} and 4^{th} columns) across composite cyclonic (top) and anticyclonic (bottom) surface and subsurface eddies in the western Indian Ocean.

box (Figure 6.4). On the other hand, subsurface eddies, especially CEs, decrease in strength. They exhibit maximum magnitudes of 3 cm s^{-1} and 11 cm s^{-1} for subsurface CEs and AEs respectively, and a vertical extent down to 800 m. However, subsurface CEs have maximum speeds closer to the surface, compared to the maximum being at ∼50 m depth for AEs. This maximum is closer to the eddy-center, compared to the subsurface AEs in the eastern box. This may be due to the long-lived dynamics of subsurface eddies, which lose their rotational speeds' intensity far from their generation

site. Collectively with shorter lifetimes and comparable rotational speeds, this supports the idea that most surface eddies are originated either locally or in adjacent areas.

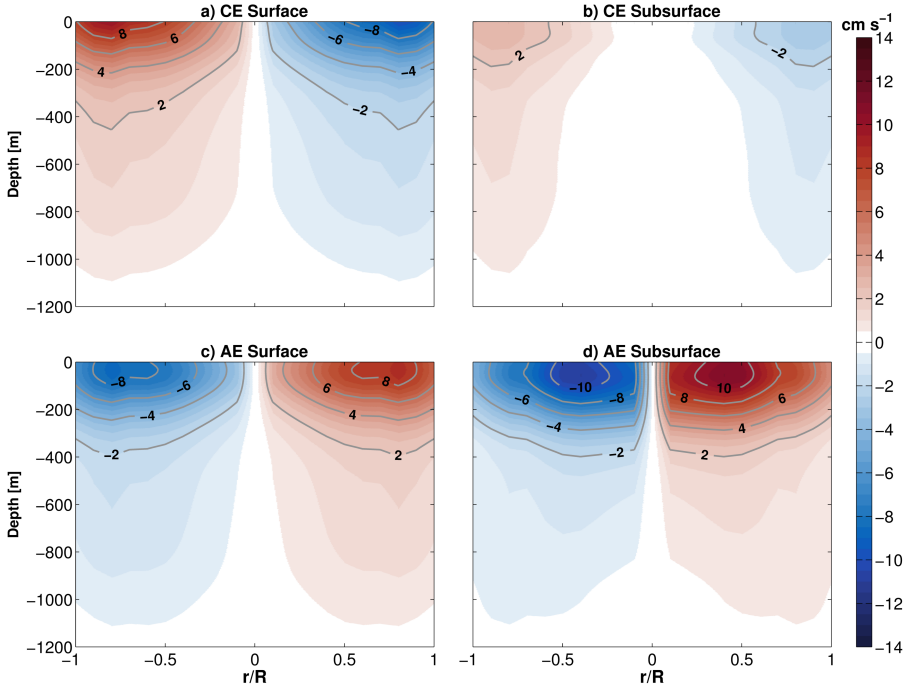


Figure. 6.6 Vertical sections of the rotational speed anomaly (cm s^{-1}) of the composite surface CEs (a) and AEs (c) and subsurface CEs (b) and AEs (d) in the western Indian Ocean.

A band of high EKE occurs at 25°S in the South Indian Ocean, linking the eastern to the western basin [*Jia et al.*, 2011a]. Along this band, mesoscale eddies, which are referred to here as 'SIDDIES' (South Indian ocean eDDIES), propagate westward towards Madagascar. Apart from their cyclonic and anticyclonic vorticity contrast, SIDDIES can occur as two distinct features; namely, surface-intensified and subsurface-intensified SIDDIES. Adding to the 'eddy-zoo', hence these two eddy-types are referred to as 'surfSIDDIES' and 'subSIDDIES', respectively. These eddies, travelling in a preferential latitudinal band (15°S-35°S), forms an eddy corridor between the eastern and western South Indian Ocean, as shown in the following section.

6.3.2 SubSIDDIES vertical characteristics and propagation

This section investigates subSIDDIES vertical characteristics, including their dominant water masses, and how these features propagate westward from the eastern South Indian Ocean basin. Based on *Nauw et al.* [2006] as well as on Figure 6.3 and Figure 6.5, the depth at which maximum positive salinity anomalies prevail, for Argo profiles falling within the subsurface vortices category are considered. This is referred to as the 'maximum salinity depth'.

Figure 6.7 displays the θ/S diagram, constructed from the mean Argo profiles of each type, in the eastern and western boxes. The diagram reveals the presence of high temperature and saline waters at $\sim$ 200 m and $\sim$ 120 m depth for subsurface AE (Figure 6.7a) and CE (Figure 6.7b) in the eastern box, with salinity approaching 35.8 psu. This high salinity water, present in high evaporation regions of subtropical oceans, is known as the STUW [*Hanawa and D.Talley*, 2001; *O'Connor et al.*, 2005], identified with a salinity range of 35.41-35.7 and potential temperature range of 18.2-21.1°C. In the western region, the maximum salinity is observed at a slightly deeper levels for anticyclonic subSIDDIES, but at approximately the same depth for cyclonic subSIDDIES. The associated eddy-surface layers exhibit warmer waters in the western South Indian Ocean compared to the eastern part.

The water characteristics at the maximum salinity depth are investigated and it can be observed that in both the eastern and western South Indian Ocean, the preferential maximum salinity depth lies between 75 and 150 m with $\sim$42% ($\sim$60%) of AEs (CEs) being in this depth range. Subsurface AEs have a secondary deeper preferential maximum salinity depth with almost 30% lying between 200-300 m and 250-350 m in

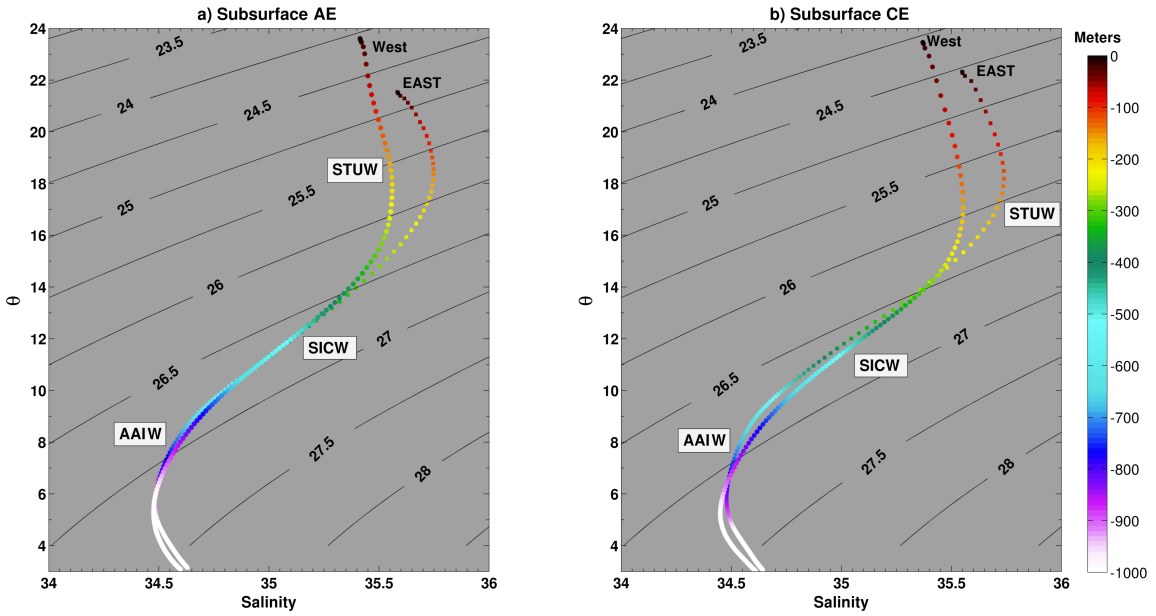


Figure. 6.7 Mean θ/S diagrams of (a) anticyclonic subSIDDIES and (b) cyclonic subSIDDIES, in the western and eastern regions of interest. Subtropical Underwater is indicated as 'STUW, South Indian Central Water as 'SICW' and for Antarctic Intermediate Water as 'AAIW'.

both the eastern and western South Indian Ocean, respectively (Figure 6.8a and c). This is in agreement with upwelling/downwelling which will push (drag) the maximum salinity depth to shallower (deeper) levels. For cyclonic subSIDDIES, preferential salinity depths are found to not vary significantly between both study regions.

Potential densities corresponding to the maximum salinity depth in the eastern region range from 26-26.8 kg m^{-3} for AEs and 25.8-26.2 kg m^{-3} for CEs (Figure 6.8b), with 44% (33%) of subsurface AEs (CEs) being in the 26.2-26.6 (26-26.4) kg m^{-3} range. The associated upper and lower bounds are within the domain of the highly saline STUW [*Hanawa and D.Talley*, 2001; *O'Connor et al.*, 2005]. In the western region, the potential density in cyclonic subSIDDIES is more spread from 25.4-26 kg m^{-3}, with another peak between 26.6-26.8 kg m^{-3} (Figure 6.8d). However, 60% of AEs potential density ranges from 25.8 to 26.4 kg $^{-3}$. Generated in a region of water mass formation

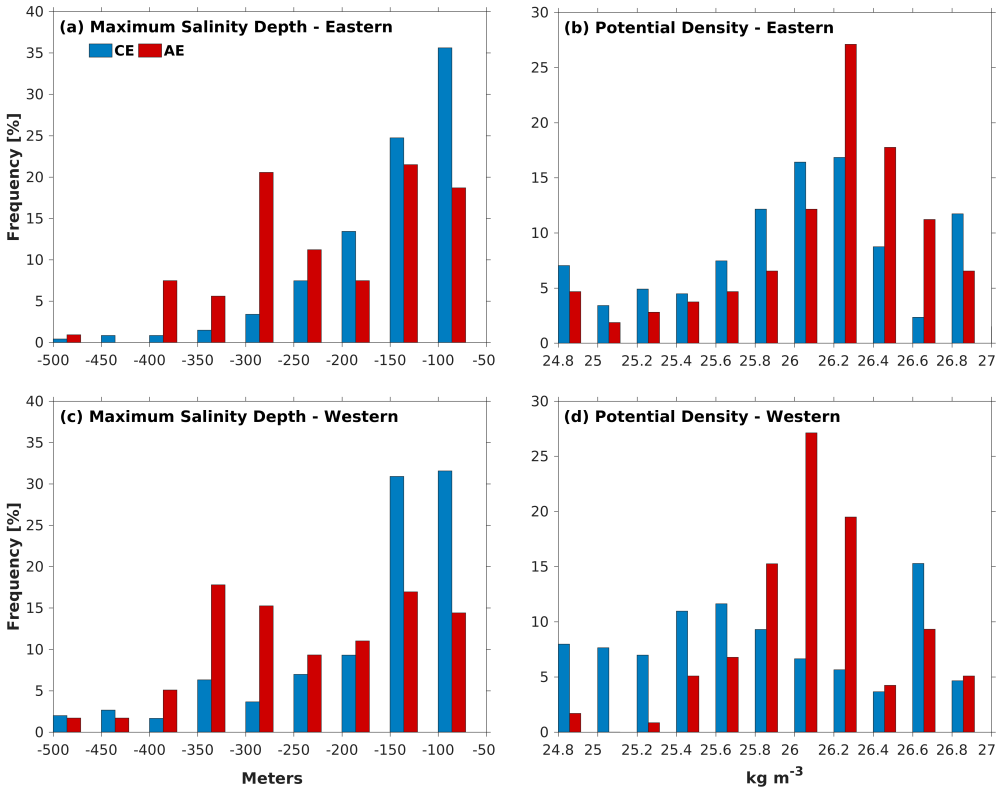


Figure. 6.8 Histogram distribution of maximum positive salinity depths and their corresponding potential density of subSIDDES in the eastern Indian Ocean (a, b) and western Indian Ocean (c, d).

(eastern box), eddies would trap waters with distinct water mass properties. However, AEs appear to be more coherent while propagating westward, retaining greatly their original water mass properties (Figure 6.8b and d). Observed differences might be the response to diffusion processes, interannual variations in the θ/S properties of the water masses of origin as proposed by *Nauw et al.* [2006], or because of eddies surveyed in the western box being generated far from the eastern box.

Following the assumption that subsurface lenses migrate along isopycnal surfaces and consequently conserve their water mass properties during this propagation [*Mcwilliams*, 1985], the favoured isopycnal depths and their tracks are investigated. Subsurface CEs and AEs in the western South Indian Ocean have potential density ranges of

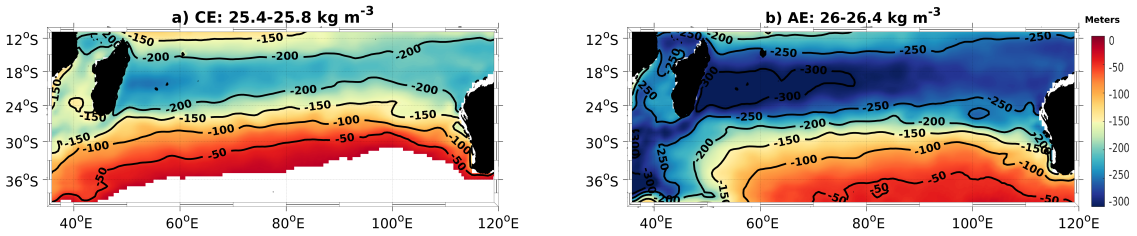


Figure. 6.9 Depth of isopycnal layers corresponding to favoured water mass properties of (a) cyclonic and (b) anticyclonic subSIDDIES.

25.4-25.8 kg m^{-3} and 26-26.4 kg m^{-3}, accounting for 23% and 46% respectively. The low percentage of CEs in the given density range might be attributed to the spread of the eddy core over a wider potential density range (Figure 6.8d). Figure 6.9a reveals the favoured CE isopycnal layers which links the eastern to the western South Indian Ocean at 200 m, 150 m and 100 m depth, accounting for 75% of CEs having their maximum salinity depth within that range. On the other hand, denser water present in the AE deeper layers links the two regions at 250 m, 200 m and 150 m depth, accounting for 75% of CEs having their maximum salinity depth within that range. On the other hand, denser water present in deeper layers links the two regions at 250 m, 200 m and 150 m depth. 37% of AEs have their maximum salinity within these depths, with 38% being at shallower depths. This variability can possibly be explained through the seasonal modulation of the depth of isopycnal layers in the region.

These pathways are further confirmed when investigating the generation sites as well as the trajectories of the subSIDDIES in the eastern (Figure 6.10a and b) and western (Figure 6.10c and d) South Indian Ocean. One important note is that these are only eddies with surface signatures and which have been surveyed at least once by an Argo profile, hence leading to an underestimation of the subsurface eddy tracks. SIDDIES connect the eastern box to the western box. When focussing on eddies generated in the eastern South Indian Ocean (Figure 6.10a and b), there are more cyclonic subSIDDIES propagating up to the western box. With eddies in the western region,

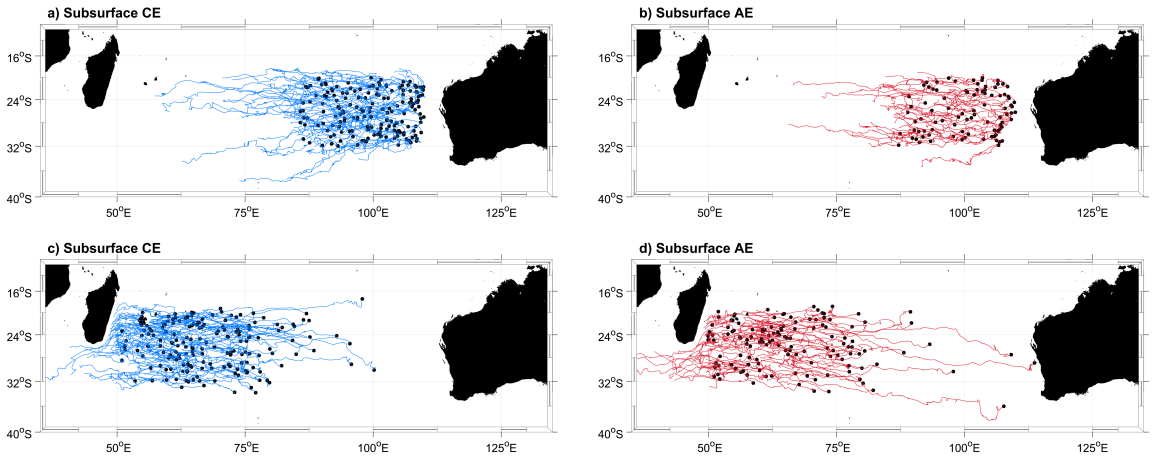


Figure. 6.10 Tracks of subSIDDIES studied in the (c,d) eastern and (d,f) western South Indian Ocean, with blue (red) indication CE (AE). The black dots show their formation location.

more anticyclonic subSIDDIES are observed, generated in the eastern South Indian Ocean and which move till the western region. As observed in the previous sections, this could suggest a more coherent anticyclonic structure in the region. In this section, Figure 6.10 revealed that pathways exist from the eastern to the western South Indian Ocean for isopycnal surfaces of 25.4-25.8 kg m^{-3} and 26-26.4 kg m^{-3}.

Surface as well as subsurface eddies connect the eastern to the western South Indian Ocean basins, along isopycnal layers. These pathways, corroborated by the eddy tracks in Figure 6.10c to f, are suggestive of a continuous eddy corridor between Australia and Madagascar, coinciding with the high zonal EKE band at 25°S (Figure 6.1a) where large eddies (R>100 km) are observed [*Zheng et al.*, 2015]. This is a preferential latitudinal band of propagation for SIDDES and, therefore, this latitudinal band in the South Indian Ocean has been termed the 'Corridor of SIDDIES', analogous to the Canary Eddy Corridor [*Sangrà et al.*, 2009]. This corridor suggests a possible key role of these features (surfSIDDIES and subSIDDIES) in the redistribution of warm and fresh water, as well as other variables such as nutrients and trace elements.

6.3.3 Heat and Freshwater Fluxes

The ocean's role in the global heat balance is fundamental due to its ability to transport excess heat from the tropics towards the poles. The oceanic circulation is responsible for most of this poleward heat transport, partly through mesoscale eddies [*Dong et al.*, 2014; *Robinson*, 1983; *Volkov et al.*, 2008]. This section estimates the heat and freshwater fluxes associated with the four eddy-types of study. *Flierl* [1981] suggested that the volume of trapped water in an eddy is dependent on the ratio of its rotational and translational speeds, also known as the nonlinearity parameter, with a ratio exceeding 1 implying a coherent eddy structure during its propagation [*Chelton et al.*, 2007, 2011b]. Accordingly, the mean vertical structures of nonlinearity for cyclonic/anticyclonic surfSIDDIES/subSIDDIES in both western (Figure 6.11a) and eastern (Figure 6.11b) regions, are computed.

In the eastern South Indian Ocean, the deep vertical stretch of cyclonic and anticyclonic subSIDDIES associated with the existence of subsurface eddy-cores results in a large vertical area of trapped fluid, down to 630 m and 780 m respectively, compared to their analogous surface eddies with trapped fluid extending down to 190 m and 260 m respectively. Generally speaking, the extent of trapped water in the western side of the basin is much lower, with a depth of 250 m for anticyclonic subSIDDIES, and 160 m (190 m) for cyclonic (anticyclonic) surfSIDDIES. However, the non-linearity parameter associated with cyclonic subSIDDIES reveals no trapped fluid, owing to their low rotational speed, as seen in Figure 6.6b. However, it must be noted that the rotational speed is underestimated in this case, since only the geostrophic component of the eddy is considered, and not the ageostrophic one. *Penven et al.* [2014] and *Barceló-Llull et al.* [2017] showed that the ageostrophic part could contribute to 30-40% of the geostrophic component of anticyclonic eddies. Only absolute *in-situ* measurements of this eddy-type will help to better elucidate its non-linearity parameter.

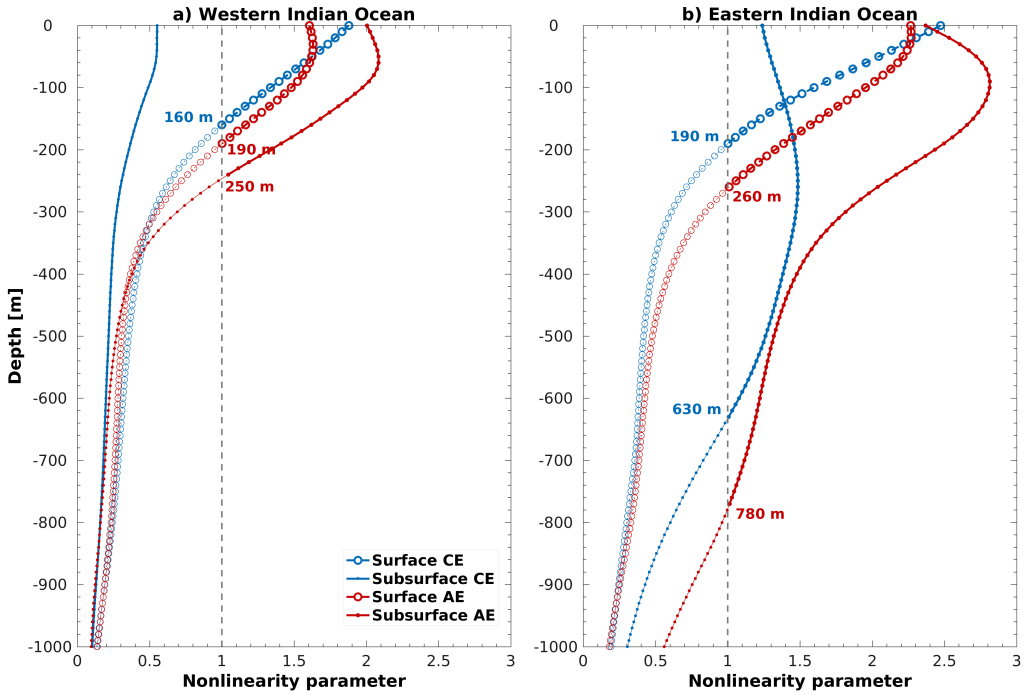


Figure. 6.11 Mean vertical profiles of the nonlinearity parameter of the four eddy-types (surface and subsurface CEs and AEs) for the western (a) and eastern (b) South Indian Ocean.

Overall, this results in a more significant volume advected through subsurface eddies compared to surface features, and hence will have a greater impact on the warm and fresh water distribution in the South Indian Ocean. The available heat and salt content anomalies (AHA and ASA respectively) of the four eddy-types are computed, as in *Chaigneau et al.* [2011], to estimate how much warm and fresh water is being transported.

The AHA and ASA are derived from the following equations:

$$AHA \;=\; \int_{Ztrap}^{0} \int_{0}^{Rc} \rho_0 \; Cp \; \theta' \; (2\pi r) \; dr \; dz \tag{6.4}$$

$$ASA \;=\; 0.001 \int_{Ztrap}^{0} \int_{0}^{Rc} \rho_0 \; S' \; (2\pi r) \; dr \; dz \tag{6.5}$$

where C_p is the specific heat capacity [4000 J kg $^{-1}$ K $^{-1}$] and R_c the mean eddy radius. The temperature and salinity anomalies (θ' and S$'$ respectively) are integrated over the eddy-core area by assuming a circular symmetrical shape, and then vertically integrated over the trapping depth (Z_{trap}). Integration is also performed radially from the eddy centre to the eddy-core is also performed, with R_c being the mean eddy radius of the four distinct eddy-types. A 0.001 factor is used for ASA so as to convert salinity to salinity fraction (kg of salt per kg of seawater).

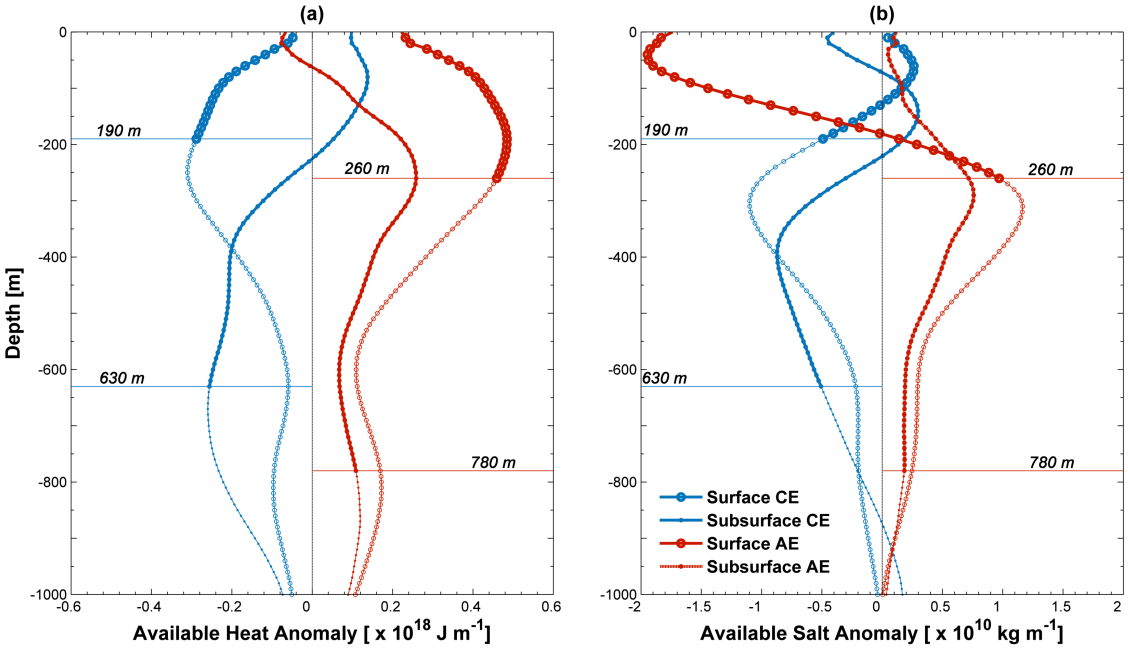


Figure. 6.12 Mean available heat anomaly (J m^{-1}; left column) and available salt anomaly (Kg m^{-1}; right column) associated with the four eddy-types in the eastern South Indian Ocean.

Focusing on the 'eddy-generation region' namely the eastern South Indian Ocean, the vertical profile of AHA (Figure 6.12a) reveals more significant negative (positive) anomalies associated with surface CEs (AEs) compared to their subSIDDIES counterpart. Cyclonic surfSIDDIES exhibit a maximum AHA of ∼-0.3 x 10^{18} J m^{-1} at 190 m whereas anticyclonic surfSIDDIES display a maximum of ∼0.5 x 10^{18} J m^{-1} at

200 m. Owing to their pecular thermohaline structure, cyclonic subSIDDIES show positive AHA from the surface till ∼225 m depth and then negative AHA down to 630 m. This feature is present in anticyclonic subSIDDIES too which display negative (positive) AHA in their surface (subsurface layers). When integrating from the surface to the trapping depths, subsurface CEs advect larger AHA values (-5.1 x 10^{18} J) compared to surface CEs (-3.8 x 10^{18} J) (Table 6.3) due to deeper trapping depths. Furthermore, surface AEs carry larger AHA, owing to their more significant positive surface anomalies compared to subsurface AEs.

For the available salt content anomalies, subSIDDIES play a more influential role on the total salt redistribution in the South Indian Ocean, primarily due to their positive/negative salt content and larger vertical extent of trapped volume (Figure 6.12b), although ASA associated with anticyclonic surfSIDDIES being highly negative in the first 190 m. Surface AEs show salt deficiencies (-19.8 x 10^{10}Kg) with respect to the background water mass, whereas subsurface AEs transport a surplus of saline water (27 x 10^{10} Kg). Moreover, surface CEs carry a slight excess salt (0.6 x 10^{10} Kg) with subsurface CEs being deficient in salt (-25.6 x 10^{10} Kg) (Table 6.3).

In the western Indian Ocean, cyclonic subSIDDIES do not seem to play a significant role in the heat and freshwater advection (Figure 6.13) owing to their weak rotational speed, with no apparent capacity to transport water (Figure 6.11a). The other eddy-types show similar AHA and ASA vertical structures to the eastern region but with shallower trapping depths. As seen in sections 6.3.1 and sectio 6.3.2, SIDDIES lose their characteristics partially during the westward migration and this could explain the lower integrated AHA and ASA. Anticyclonic surfSIDDIES are again shown to correspond to freshwater content whereas both cyclonic surfSIDDIES and anticyclonic subSIDDIES have positive salt content anomalies.

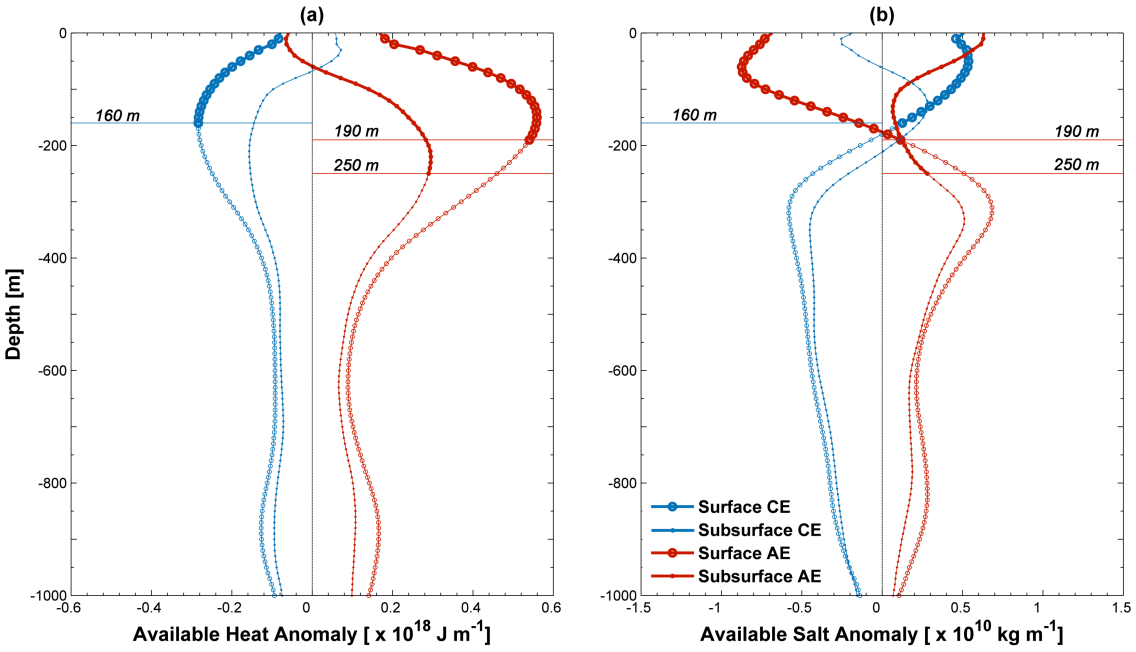


Figure. 6.13 Same as Fig. 6.12 but for the western South Indian Ocean.

The respective zonal heat and salt transports (Zonal Q_{eh} and Zonal Q_{fw}) as well as their meridional components (Meridional Q_{eh} and Meridional Q_{fw}) for each eddy-type are computed for the eastern and western South Indian Ocean boxes (Table 6.3). This is investigated through longitudinal (97.5°E for eastern and 62.5°E for western region) and latitudinal (26°S) sections centered on the 2 boxes. The associated total time-mean fluxes are estimated by multiplying the average eddy properties by their respective population density number, N_e, where N_e is the total number of each eddy-type passing through the longitudinal and latitudinal sections divided by their corresponding time length, as in *Duncombe Rae et al.* [1996] and *Chaigneau et al.* [2011]. Salt transport is interpreted as freshwater flux (unit: Sv), with Q_{fw} = - Q_{es} /$\rho_0 S_o$, where S_o = 35 psu (salt mass fraction) is the mean upper ocean salinity. It should also be noted here that the associated eddy-fluxes are from the surface down to the specific trapping depth of each eddy-type.

The resultant fluxes associated with each eddy-type as well as the net eddy fluxes are also displayed in Figure 6.14. The mass flux of all eddy types is representative

Table 6.3 Vertical extent, volume, thermohaline contents and associated heat/freshwater flux of 4 distinct eddy-types in the western and eastern Indian Ocean regions.

	Western Indian Ocean				**Eastern Indian Ocean**			
	Surface		**Subsurface**		**Surface**		**Subsurface**	
	CE	AE	CE	AE	CE	AE	CE	AE
Vertical Extent [m]	0 - 160	0 - 190	-	0 - 250	0 - 190	0 - 260	0 - 630	0 - 780
Volume [x 10^{12} m^3]	6.8	8.6	-	10.5	7.9	11	21.4	30.6
AHA [x 10^{18} J]	-3.3	8.4	-	3.8	-3.8	10.8	-5.1	9.4
Zonal Q_{eh} [TW]	-0.62	1.7	-	0.4	-0.6	1.7	-0.6	0.8
Meridional Q_{eh} [TW]	-0.06	-0.02	-	-0.04	0.04	0.12	0.04	0.07
ASA [x 10^{10} Kg]	6.7	-10.8	-	6.1	0.6	-19.8	-25.6	27
Zonal Q_{fw} [Sv]	-0.4	0.6	-	-0.2	-0.02	0.9	0.8	-0.7
Meridional Q_{fw} [Sv]	-0.03	-0.007	-	0.02	0.002	0.06	-0.05	-0.06

of their westward displacement, with slightly equatorward (poleward) deflections for anticyclonic (cyclonic) surfSIDDIES and subSIDDIES in the eastern South Indian Ocean, as expected. This westward migration of the cyclonic and anticyclonic eddies induces a zonal heat transport, that tend to offset each other to some extent, due to their opposite signs. Meridional heat transport, however, will combine to give larger values. Comparatively with freshwater fluxes, this is not always the case.

In the eastern region, anticyclonic subSIDDIES advect 50% less heat (0.81 TW) compared to anticyclonic surfSIDDIES (1.7TW), whereas cyclonic subSIDDIES (0.6 TW) and surfSIDDIES (0.6 TW) display quite similar heat transport. A net equatorward heat flux towards a temperature up-gradient is observed in the eastern Indian Ocean (Figure 6.14b), owing to the preferential equatorward movement of anticylonic vortices, and their associated large vertical trapping depths (Figure 6.11b). In the western Indian Ocean, the same phenomenon is observed with AEs, with their surface

form moving warmer water (1.7 TW) compared to their subsurface form (0.41 TW). The net eddy heat flux here is slightly poleward.

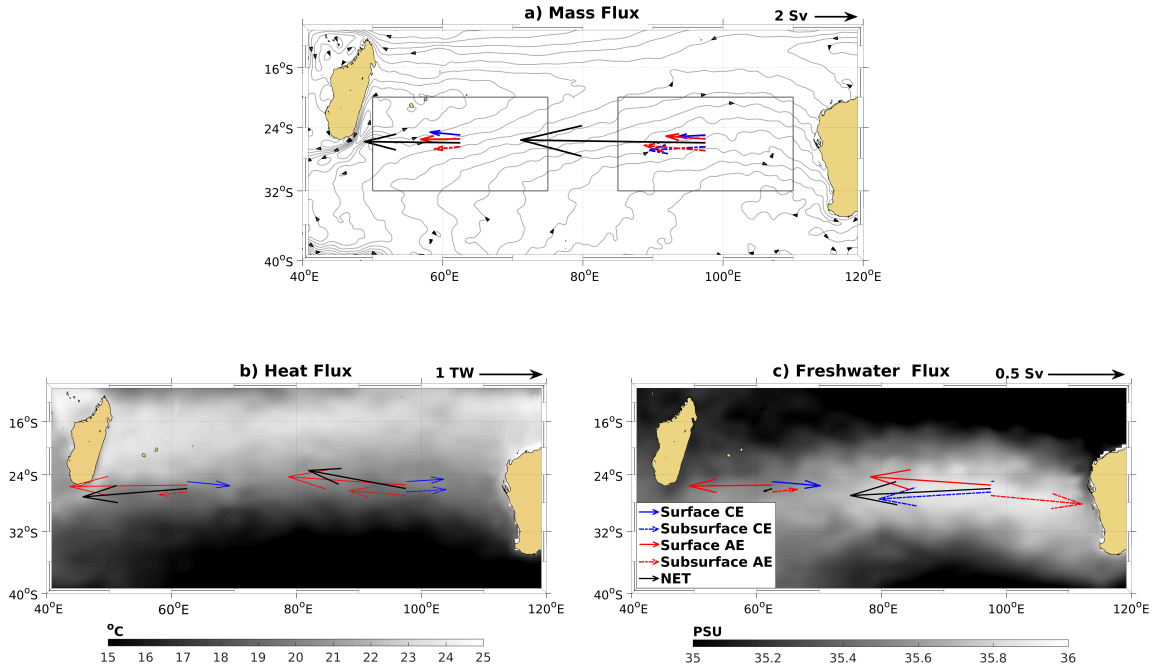


Figure. 6.14 Resultant vectors associated to the mass (a), heat (b) and freshwater flux(c) of each eddy-types (see legend), in the eastern and western South Indian Ocean region. The background displays (a) streamlines of sea surface height representing geostrophic mean circulation, (b) salinity and (c) temperature, both salinity and temperature averaged between 50 and 150m depth.

An interesting feature of the South Indian Ocean is the presence of high subsurface salinity in the eastern basin. One might expect that mesoscale eddies formed in this region would advect this high salinity water westward. However, a westward freshwater flux through eddies is predominant. This flux is associated with all eddy-types, except anticylonic subSIDDIES (Table 6.3), and is largely controlled by the extent of their trapping depths. A shallow trapping depth of 260 m for anticyclonic surfSIDDIES infer fresher surface water advection compared to the deeper saltier water (Figure 6.3g). On the other hand, anticyclonic subSIDDIES move parcels of saltier water (23.3 x 10^3 Kg s^{-1}), in their subsurface layers, towards the western margin, a feature that has been

surveyed for the ITEs in the western Indian Ocean [*Nauw et al.*, 2006]. The shallow trapping depths associated with cyclonic surfSIDDIES in both eastern and western areas, and their surface positive salt content result in freshwater flux in an eastward direction, although this flux is small in the eastern region. The westward freshwater flux associated with anticyclonic surfSIDDIES in the western box is compensated by the eastward salt flux exhibited by cyclonic surfSIDDIES and anticyclonic subSIDDIES. The net eddy freshwater flux is however westward in both regions and slightly equatorward (poleward) in the eastern (western) South Indian Ocean regions, but of lesser magnitude in the western basin (Figure 6.14c).

6.4 Discussion and Summary

The South Indian Ocean is characterized by a zonal band of high EKE, the only one occurring at a subtropical eastern boundary of the global oceans [*Jia et al.*, 2011a]. Among other features, this enhanced EKE is attributed to westward-propagating South Indian Ocean eddies, which are termed in this study as 'SIDDIES'. SIDDIES can occur in two forms namely surface-intensified or subsurface-intensified. On the basis of an eddy tracking scheme [*Chelton et al.*, 2011b] and available Argo profiles, a novel subsurface eddy identification method, based on their steric dynamic height anomalies, has been devised. This study has characterized, for the first time, a mean vertical thermohaline structure of cyclonic and anticyclonic surface and subsurface eddies in the eastern (genesis area) and western South Indian Ocean, where only two subsurface AEs have been previously surveyed [*Nauw et al.*, 2006]. This allows the investigation of their ability to transport properties to remote regions. The eddy-subsurface identification method was successful in distinguishing between Argo profiles collocated in surface eddies and subsurface eddies. Hence, it is proposed that surface-intensified and subsurface-intensified eddies to be referred as 'surfSIDDIES' and 'subSIDDIES'.

SubSIDDIES were characterized by subsurface salinity maximum signatures, with their mean cores at ∼150-200 m in cyclonic (Figure 6.3d and Figure 6.5d) and ∼250-300 m in anticyclonic forms (Figure 6.3h and Figure 6.5h). A recent subsurface anticyclonic eddy surveyed south of the Canary Islands in the North Atlantic Ocean [*Barceló-Llull et al.*, 2017], as well as anticyclonic eddies in the South Pacific Ocean [*Chaigneau et al.*, 2011] have quite similar vertical haline structure as anticyclonic subSIDDIES. Characterized by a warm-water lens in subsurface layers, they exhibit a small cap of cold water at the surface, consistent with *Barceló-Llull et al.* [2017], where they suggest it to be due to the seasonal thermocline shoaling. Hence, the key attributes of anticyclonic subSIDDIES are a slight (significant) positive salinity anomaly at the surface (subsurface levels), accompanied by a negative (positive) temperature anomalies at the surface (subsurface levels). This structure is in agreement with the PUMP eddy structure [*Barceló-Llull et al.*, 2017]. Although less observed in open ocean, cyclonic forms of subsurface eddies do occur in the South Indian Ocean. However, compared to anticyclonic subSIDDIES, their positive subsurface salinity signature is weaker. Cylonic surfSIDDIES have been shown to exhibit surface salinity anomalies, a feature associated with the vertical displacements in CE, which draw high salinity water upwards [*Castelao*, 2014]. The mean statistical study shows that surfSIDDIES and subSIDDIES exhibit a mean radius ranging from 100-115 km, consistent with *Dufois et al.* [2014], who also showed averaged eddy radius of the order of 100 km in the South Indian Ocean. However, the mean amplitude for cyclonic vortices are higher compared to anticyclonic ones. This is in agreement with *Chelton et al.* [2011b] who showed larger amplitudes associated with CEs in the Southern Hemisphere, a feature linked to a rotational speed greater than 20 cm s^{-1}.

The dominant water mass at the preferential depths of eddy-cores is the STUW *Hanawa and D.Talley* [2001]; *O'Connor et al.* [2005]. This water mass is more distinct in eddies generated in the eastern South Indian Ocean. In this region, high evaporation

associated with low precipitation causes an increase in surface salinity which, due to local instabilities of the South Equatorial Current, is then subducted in deeper layers, hence creating a subsurface salinity maximum. *Nauw et al.* [2006] suggested the origin of the two surveyed subsurface-intensified AE in the western South Indian Ocean to be from this eastern saline subtropical mixed layer water. They proposed that the variability in the subsurface-intensified eddies, characterised by high salinity patches in their core, is linked to the interannual variations in the θ/S properties of the subtropical surface winter mixed layer. The difference in water characteristics of subsurface eddies between the eastern and western South Indian Ocean could be partly due to these interannual variations, as well as a diffusion mechanism where the water masses characteristics are lost to some extent during their westward propagation towards the western South Indian Ocean. SubSIDDIES display higher surface temperature in the western South Indian Ocean (Figure 6.7) compared to the eastern part, and this is due to the warmer water prevailing over the western branch of the subtropical gyre.

Formed in the eastern basin, these lenses migrate westward through preferential isopycnal layers to link the eastern to the western basin (Figure 6.10a and b). The equatorward (poleward) tendencies of AEs and CEs, observed are due to their propagation on a β-plane, and the meridional drift of the eddies which is induced by the change in relative and planetary vorticities on their flanks [*Morrow et al.*, 2004]. Cyclonic (Anticyclonic) subSIDDIES prefer density layers of 25.4-25.8 (26-26.4) kg m^{-3}, consistent with the density ranges of Peru-Chile Current System (PCCS) eddies where CE (AE) cores correspond to 25.2-26 (26-26.8) kg m^{-3} [*Chaigneau et al.*, 2011]. The pathways, corroborated by the eddy tracks in Figure 6.10c to e, are suggestive of a continuous eddy corridor between Australia and Madagascar, as shown by *Zheng et al.* [2015]. This preferential latitudinal (15°S-35°S) band is referred to as the 'Corridor of SIDDIES', where both surfSIDDIES and subSIDDIES prevail.

The thermohaline structure of surfSIDDIES and subSIDDIES allow the estimation

of the heat and salt content associated with each eddy-type. However, in contrast to subsurface vortices in other regions, anticyclonic subSIDDIES display higher available heat content (9.4 x 10^{18} J respectively) than the PUMP eddy (2.9 x 10^{18}J) [*Barceló-Llull et al.*, 2017] , Cuddies (0.36 x 10^{18}J) [*Pelland et al.*, 2013] and PCCS eddies (8.7 x 10^{18}J) [*Chaigneau et al.*, 2011]. For the cyclonic counterpart, they exhibit almost similar heat anomalies (-5.1 x 10^{18}J) to PCCS eddies (-5.5 x 10^{18}J) [*Chaigneau et al.*, 2011]. This difference in heat content can be dependent on the radius of the eddy, which is larger for subSIDDIES (∼115 km) compared to PUMP (∼30 km), Cuddies (∼20 km) and PCCS eddies (∼60 km), as well as the much deeper associated trapping depths. Anticyclonic subSIDDIES, compared to other eddy-types in the region, transport large salt content anomalies (27 x 10^{10} Kg), which is of the same order of salt content of AEs in PCCS (23.8 x 10^{10} Kg) [*Chaigneau et al.*, 2011].

SIDDIES have the ability to advect mass, heat and freshwater in distinct depth layers, depending on the ratio between their rotational and translational speeds. Consistent in terms of direction, the net-eddy heat flux is, however, of a lesser magnitude compared to *Volkov et al.* [2008] and *Dong et al.* [2014], owing to a basin-wide context in their studies. In the eastern region, anticyclonic subSIDDIES advect 50% less heat (0.81 TW) compared to anticyclonic surfSIDDIES (1.7TW). This is due to the colder water in the surface layers of anticyclonic subSIDDIES compared to the warmer water for surfSIDDIES. Cyclonic subSIDDIES (0.76 TW) display slightly higher heat transport than their surface counterparts (0.55 TW). Anticyclonic (cyclonic) surfSIDDIES advect 6 (3) times more heat compared to PCCS anticyclonic (cyclonic) eddies which advect 0.28 (-0.17) TW [*Chaigneau et al.*, 2011]. A net equatorward heat flux towards a temperature up-gradient is observed in the eastern Indian Ocean (Figure 6.14b) owing to a preferential equatorward movement of anticyclonic vortices (and poleward movement of CEs) [*Chelton et al.*, 2007; *Morrow et al.*, 2004], and their associated large vertical trapping depths (Figure 6.11b). SubSIDDIES have a net eddy-heat flux of approximately 3% of the total global northward heat component (50-60 TW),

between the latitudinal band of 20°S-32°S [*Dong et al.*, 2014; *Jayne and Marotzke*, 2002]. In contrast, net eddy heat and salt fluxes (Figure 6.14b and c respectively) are slightly poleward in the western region and this can be attributed to the presence of the shallow SICC [*Palastanga et al.*, 2007; *Siedler et al.*, 2006] which flows against the volume mass (Figure 6.14a), as well as the sub-gyre east of Madagascar, which can interact with the mesoscale eddies and their poleward/equatorward affinities. The 1.5 TW eddy-heat flux in this region could contribute to the 100 TW conveyed by the Agulhas Current [*Volkov et al.*, 2008] and the 62 TW transported by the Agulhas rings [*Souza et al.*, 2011] into the South Atlantic Ocean. This inter-ocean exchange of heat and salt, on longer timescales, could alter the variability Meridional Overturning Circulation [*Beal et al.*, 2011; *Biastoch et al.*, 2008].

With positive salt content anomalies along their trapping depths, anticyclonic subSIDDIES are found to be the sole saline-water eddy-conveyor towards the western region. This is consistent with the two anticyclonic subSIDDIES surveyed close to Madagascar in 2001 [*Nauw et al.*, 2006]. *Dong et al.* [2014] reported a freshwater flux of -0.1 Sv to -0.2 Sv, at latitudes 20°S and 32°S respectively, with a positive freshwater flux (0.1 Sv) observed at ∼25°S. The net eddy-freshwater flux in the eastern region (0.98 SV) accounts for almost 10 times more than reported [Dong et al., 2014]. A more important number of subSIDDIES would imply a greater influence on the main oceanic currents in the vicinity, and eventually on the Agulhas Current System. The western South Indian Ocean region, being the 'eddy-arrival region', is expected to reveal different fluxes compared to the eastern part. This may be due to various factors namely: 1) more coherent structures of mesoscale eddies in the east generate more significant fluxes; 2) freshwater input from the Indonesian Throughflow into the eastern region significantly influences the salt advection; 3) the presence of the SICC and the sub-gyre south-east of Madagascar can interact and influence incoming eddies and/or shed its own eddies; and finally 4) the loss, to some extent, of the eddy properties during their long-lasting life.

SubSIDDIES are found to contribute largely to the distribution of heat and salt in the South Indian Ocean. 58% (32%) of the total heat flux is attributed to cyclonic (anticyclonic) subSIDDIES in the eastern Indian Ocean whereas 58% is attributed to the total in the western region. In terms of fresh water, anticyclonic subSIDDIES account for 42.5% (24%) of the total freshwater fluxes in the eastern (western) regions, but in the opposite direction. It is important to note that some uncertainties are associated with the fluxes. These are because only surface-detected eddies are taken into consideration, the computation of rotational speed is based on a level of no-motion which is not always the same in different part of the global ocean, and the ageostrophic component of the eddy is not being accounted for. Hence, in the western basin, cyclonic subSIDDIES could still advect water even when our current results suggest otherwise. From these, stronger fluxes than stated here could be inferred.

The results in this study highlight the importance as well as the contribution of subsurface-intensified eddies in the redistribution of warm and fresh water in the South Indian Ocean, and hence suggest that they might have an important role in the regional western boundary current system namely the Greater Agulhas Current System. The interesting dipole temperature structure associated with these subSIDDIES are worthy of further investigation due to its possible importance on the spatial distribution of SST and eventually on the ocean surface current feedback on the atmosphere [*Renault et al.*, 2016]. The influence of eddies on the distribution of chemical tracers through horizontal and vertical advection have also been previously reported [*Chelton et al.*, 2011b; *Gaube et al.*, 2013, 2014; *Iskandar et al.*, 2010; *McGillicuddy and Robinson*, 1997]. Several studies have shown that high Chl-a maximum can be observed in the core of subsurface-intensified anticyclonic eddies [*Hansen et al.*, 2010; *Kim et al.*, 2012; *Ledwell et al.*, 2008; *McGillicuddy et al.*, 2007; *Thomsen et al.*, 2016]. *McGillicuddy et al.* [2007] proposed an eddy-wind interactions to enhance vertical flux in mode-water eddies, and these are responsible for large biomass concentration in subsurface vortices.

Ledwell et al. [2008] measured this upward flux, at a rate of 0.4 m d^{-1}, and suggested that 40% of the nitrogen flux required for new production in Sargasso Sea is supplied by this flux of inorganic nitrogen. Another study by *Thomsen et al.* [2016] showed that subsurface anticyclonic eddies stir local tracers and then advect biological properties such as oxygen and nitrate from the PCCS slope towards the offshore open ocean where an oxygen minimum zone is present. Hence, it will be important to the biogeochemical community to investigate how these special eddies, with their cores in the subsurface, transport nutrients or biomass during their long-lived journeys across the South Indian Ocean, and how they interact with the presence of the deep chlorophyll-maximum or the South-East Madagascar Bloom.

Chapter 7

Summary and future research

The region south-east of Madagascar is complex in terms of its mean circulation and its biogeochemistry. The South-East Madagascar Bloom, one of the largest blooms in the global ocean, co-exists with the poleward flowing South-East Madagascar Current (SEMC), the eastward flowing South Indian Ocean Countercurrent (SICC) as well as westward-propagating surface and subsurface eddies. To explore the mechanisms linked to the bloom, the regional oceanography around the southern coast of Madagascar needs to be understood. This thesis employs a set of observational datasets to study the oceanographic regime in the area, as well as to grasp further insights into the bloom. In addition, for the first time, a South-West Indian Ocean (SWIO) configuration of a high resolution ($\frac{1}{12}^\circ$) coupled biophysical model (CROCO-PISCES) has been configured to help in understanding the physical and biogeochemical processes associated with the initiation of this sporadic bloom.

An extensive evaluation of the physical and biogeochemical tracers of SWIO has been performed in Chapter 3. The mean state of surface and subsurface tracers was fairly well reproduced by SWIO, when compared to observational datasets. However, SWIO displayed a slight positive salinity bias in the domain, north of 30°S. This feature could be attributable to the non-assimilated, $\frac{1}{4}^\circ$ horizontal resolution, boundary conditions GLORYS, which exhibited a similar bias.The T-S diagrams showed that SWIO correctly reproduced the main water masses in the region, as a result of the advection scheme proposed by *Marchesiello et al.* [2009]. The SSH streamlines in SWIO, compared to AVISO, were well represented, except for the position of the SICC, which was located slightly north, and this has also been observed in the physical model

Parallel Ocean Program [*Lambert et al.*, 2016] in the region. With the introduction of the child domain, mesoscale turbulence was enhanced, and was fairly comparable to observed eddy kinetic energy (AVISO). In addition, the volume transports across the main currents were well captured by SWIO.

The biogeochemical component of the model, PISCES, exhibited higher than observed productivity in austral winter. Since the South-East Madagascar Bloom is a feature locked to the austral summer season, evaluation of PISCES was focussed only on the December to April period. SWIO reproduces successfully the large-scale surface Chl-a concentration in the domain, except for a higher simulated productivity around the southern coast of Madagascar. In the bloom vicinity, a patch of lower Chl-a ($\sim$0.2 mg m^{-3}) concentration was observed. The mean vertical structure of phytoplankton cells was, however, well represented when compared to *in-situ* measurements. In SWIO, higher than observed nitrate concentration occurred around the southern coast of Madagascar, together with a shallower nutricline. This could explain the higher coastal productivity in SWIO. Overall, SWIO resolved reasonably well the physical and biogeochemical processes in the vicinity of the bloom. This provided confidence in using the coupled biophysical model to investigate the mechanisms associated with the South-East Madagascar Bloom.

Chapter 4 provided an updated description of the spatial and temporal variability of the sporadic South-East Madagascar Bloom. A new bloom index was defined by subtracting the austral winter bloom occurring in a box further east, from a similar-sized box defined by *Uz* [2007], in the bloom region. This index provided an improved diagnosis of the timing and intensity of the bloom, from which a bloom threshold of a minimum Chl-a difference (0.07 mg m^{-3}) was assigned to distinguish between bloom and non-bloom years. Another threshold of 0.16 mg m^{-3} was used to characterize normal and major blooms. The bloom occurred within a mean latitudinal range of 24°S-30°S, extending from the Madagascan coast till $\sim$65°E. However, its initiation and

termination months exhibited large variability. Analysing the mean vertical structures within high/low Chl-a patches revealed the presence of low-salinity waters at the surface levels, during the bloom. The possibility of advected SEMC waters emerged from this low-salinity water signature. A review of previous hypotheses in the literature were performed and one of them, which would sustain the possible advection of SEMC waters, was quite robust, namely the intensity of the current-driven upwelling south of Madagascar [*DiMarco et al.*, 2000; *Lutjeharms and Machu*, 2000; *Machu et al.*, 2002; *Ramanantsoa et al.*, 2018a]. A dampening of the upwelling was observed during months of bloom occurrences, with it being at its lowest intensity during the major blooms of 1999, 2006 and 2008. Analysing the mean regional circulation during the bloom months unveiled a dipole feature more prevalent close to the SEMC. These threads of previously unknown and important information converged towards a possible new hypothesis put forward in this thesis. This hypothesis stated that the South-East Madagascar Bloom would develop owing to the local circulation inducing an early destabilization or a retroflection of the SEMC, hence advecting low-salinity, nutrient-rich coastal SEMC waters eastward, thereby fertilizing the bloom.

In **Chapter 5**, the high resolution coupled biophysical model, SWIO, was used to study the bloom and to test the aforementioned new hypothesis. Surface (0-20 m) blooms were not observed in SWIO but further investigation revealed sporadic subsurface (20-40 m) blooms. Similar to the previous chapter, two boxes were delineated to capture both the simulated bloom as well as the austral winter Chl-a signal. A 'model bloom index' was computed and a bloom threshold of 0.07 mg m^{-3}, similar to the threshold in ocean colour dataset, was used to identify bloom years. Eight bloom years (1994, 1995, 1996, 2004, 2005, 2006, 2008 and 2010) were identified, and they showed large temporal variability, with maximum blooms occurring either in December (1995, 2005 and 2010), January (1994, 1996 and 2008) or February (2004). The meridional extent of the bloom, however, compared well with observations, as it occurred in a latitudinal range of 22°S-29°S. Zonally, the model bloom did not extend as offshore as

the observed bloom. The vertical water characteristics in bloom patches revealed a low-salinity surface signature, comparable to the observational dataset. This proved similar processes could be at play in governing the bloom. The mean local circulation during bloom years exhibited quite similar features compared to observations, with a dipole feature close to the SEMC. This feature creates a retroflection of the SEMC during bloom years whereas a significant south-westward flow to the SEMC occurred during non-bloom years. This corroborated with the new hypothesis stated earlier, and hence was tested using a nutrient fluxes analysis and a Lagrangian tool. Nitrate fluxes from the subsurface which are indicative of upwelling, and from the west, indicative of nutrient-rich, advected SEMC waters, were tested. Two bloom years (1996 and 2004) were linked to wind-driven vertical pumping. The 2004 bloom was associated with a possible wind stress event, namely a tropical cyclone. SWIO was therefore capable of reproducing an atmospherically-forced phytoplankton bloom, south-east of Madagascar. The remaining six years (1995, 1996, 2005, 2006, 2008 and 2010) were mostly attributed to incoming flux of nitrate from the Madagascan coast. This was further confirmed by tracking the number of particles, released in the SEMC, in the 'model bloom box' and comparatively, south of Madagascar. Bloom years were characterized by more particles in the 'model bloom box'. The interannual variability observed in the dispersion of particles in the 'model bloom box' could also explain the intermittent supply of nutrients into the bloom region, fertilizing it. This new hypothesis suggests the fertilization of the simulated South-East Madagascar Bloom occurs concurrently with the retroflection/de-stabilization of the SEMC [*Siedler et al.*, 2009].

Surface and subsurface-intensified eddies form part of the local circulation south-eastvof Madagascar [*Nauw et al.*, 2006], in the South-East Madagascar Bloom vicinity. These originate west of Australia and migrate westward towards Madagascar and can potentially impact the bloom. However, only one study to date has focussed on the subsurface-intensified eddies in the South Indian Ocean (SIO) [*Nauw et al.*, 2006].

Using a co-located eddy tracking dataset together with Argo profiling floats, **chapter 6** provided a detailed analysis of these features. A subsurface eddy identification method was devised, based on their steric dynamic height anomalies, to distinguish between Argo profiles captured in surface from subsurface-intensified eddies. Adding to the 'eddy-zoo', these features, in all their forms, were termed South Indian ocean eDDIES (SIDDIES). Analysing the mean thermohaline structure of these eddies revealed a positive salinity anomaly throughout their water column, more significant in the subsurface levels. This featured in the eddy-cores, and is shallower (∼150-200 m) cyclonic, and deeper (∼250-300 m) in anticyclonic subsurface-intensified eddies. They exhibited preferential density layers, 25.4-24.8 (26-26.5) kg m^{-3} for cyclonic (anticyclonic) vortices, along which they propagate from the eastern to the western SIO. SIDDIES, in their surface (surfSIDDIES) and subsurface-intensified (subSIDDIES) forms, migrate at a latitudinal band ranging from 15°S to 35°S, which was termed the 'SIDDIES Corridor'. Analysing the associated heat fluxes, cyclonic and anticyclonic subSIDDIES have been found to contribute up to 58% and 32%, respectively, of the total eddy-heat flux in the eastern SIO, and a combined 58% of the total in the western. In terms of freshwater fluxes, anticyclonic subSIDDIES were shown to be the sole conveyor of high-salinity water towards the western region. These features could possibly advect nutrients or biomass through their long-lived journeys across the SIO, and therefore, influence the South-East Madagascar Bloom.

Regarding the scientific questions addressed in this thesis, their corresponding conclusions are:

Chapter 4

- Can a longer biophysical dataset of 19 years (1998-2016) provide a better insight into the physical-biological interactions involved in the South-East Madagascar Bloom than the earlier data?

These longer datasets allow for the spatial and temporal characterization of the South-East Madagascar Bloom. Results about the mean vertical properties and local oceanic circulation associated with the bloom suggest that a new process could be playing a fundamental role in triggering the bloom. The hypothesis involves the advection of low salinity, nutrient-rich SEMC waters into the bloom region owing to a de-stabilization of the SEMC.

Chapter 5

- Using a high-resolution coupled biophysical model, can the physical-biogeochemical mechanisms which trigger the initiation and termination of the South-East Madagascar Bloom be better understood?

The high-resolution model reproduces a sporadic South-East Madagascar Bloom, but located more in the subsurface (20-40 m) than in the surface levels. The mean vertical water structure associated with the simulated bloom also exhibits a low-surface salinity signature, suggestive of possible similar mechanisms at play in the model and observations. A nutrient flux analysis as well as a Lagrangian particle experiment confirm the link between the low-salinity, nutrient-rich SEMC waters and the South-East Madagascar Bloom. The high-nutrient coastal SEMC waters can trigger the South-East Madagascar Bloom.

Chapter 6

- What are the implications of subsurface-intensified eddies in the South Indian Ocean in terms of their associated heat and freshwater fluxes?

South Indian Ocean eddies, termed 'SIDDIES', occur as surface eddies (surfSIDDIES) and subsurface eddies (subSIDDIES) and they migrate over a preferential latitudinal band (SIDDIES Corridor) from the eastern to western South Indian Ocean. On average, they account for ∼50% and ∼35% of the total eddy-heat flux and freshwater fluxes in both the eastern and western SIO.

- Can subsurface-intensified eddies contribute to the South-East Madagascar Bloom?

Subsurface-intensified eddies have been shown to carry warm and fresh (as well as salty) waters across the SIO. It can be hypothesized that nutrients can also be advected in the subsurface-eddy cores and this can potentially impact the South-East Madagascar Bloom. This impact has, however, not been quantified at present.

7.1 Perspectives

The CROCO-PISCES based configuration was designed to simulate the coupled bio-physical processes in the region of the South-East Madagascar Bloom. Although the main oceanographic features were reasonably well-resolved, some major issues were detected. In the bloom region, the position of the shallow eastward SICC is shifted slightly north. A further investigation of the SICC dynamics needs to be performed to understand which processes control the simulated SICC and why it is shifted north. A possible causative factor can be the resolution ($\frac{1}{4}^{\circ}$) of the boundary forcing, GLORYS model data, which will not resolve the small scale features at the eastern boundary of SWIO. The SICC can be altered by these boundary conditions since it occurs in a high eddy kinetic energy band.

In a biogeochemical context, the large-scale bias of Chl-a concentration during winter in the region is associated to an enhanced level of nitrate concentration at the surface. Compared to observations, the simulated mixed layer depth is, however, shallower during this period. Hence, it is of fundamental importance to understand the processes driving a higher nitrate input in the surface layer. Understanding this bias can be helpful for further biogeochemical studies in the region.

In relation to the South-East Madagascar Bloom, it will be interesting to perform a similar coupled simulation, with a version of PISCES which resolves nitrogen-fixer species. From this, other questions could be addressed such as: What will be the large-scale impact of this added feature, in the south-west Indian Ocean? How much of the results, in the bloom region, will change with nitrogen-fixers included? How much of the bloom is associated with nitrogen-fixers? This will be important in a further description and investigation of this sporadic bloom. In addition, SWIO has been configured with no influence from river discharges and therefore, the effect of rivers on the surrounding biogeochemistry, as well as the bloom, still needs to be investigated.

Finally, the South-East Madagascar Bloom has been shown to last for approximately two to three months. Occurring in the Exclusive Economic Zone of Madagascar, Mauritius and Reunion Island, these islands can benefit from the bloom occurrence in terms of fisheries. Thus, if the years of bloom occurrences could be predicted, dedicated scientific cruises, departing from one of those countries could be organized. Given the temporal and spatial variability of this feature, multiple cruises should be done in the area, during bloom months as well as non-bloom months. Such an observational programme will allow scientists to get a grasp of all the physical as well as biogeochemical processes at play in the South-East Madagascar Bloom and the surrounding region.

- **Critical point in the South-West Indian Ocean**

Oceanic phytoplankton contributes to approximately half of the biosphere's net primary productivity, through photosynthesis. These microscopic plants fix more than a hundred million tons of carbon, in the form of CO_2, into organic material each day [*Behrenfeld et al.*, 2006]. At the same time, phytoplankton provide the necessary energy to fuel marine food webs and hence contribute to the whole ecosystem. The importance of the South-East Madagascar Bloom lies in its proximity to Madagascar and the Mascarene Islands. Providing energy to sustain fish population, the bloom can be beneficial to these islands which are largely dependent on the fisheries industry.

In a climate change era where the western tropical Indian Ocean has been observed to be warming up at a rate faster than any other region of the tropical oceans [*Roxy et al.*, 2014], concurrently, a decline in ocean productivity is observed [*Behrenfeld et al.*, 2006; *Boyce et al.*, 2010; *Roxy et al.*, 2014]. Over the last six decades, a decrease at an alarming rate of 20% in marine phytoplankton has been revealed in the tropical Indian Ocean [Roxy et al., 2016]. This decrease is associated with a reduction of 50%-90% in tuna catch rates [*Myers and Worm*, 2003; *Polacheck*, 2006] and thus, can act as an additional stress factor which may tip the tuna catch rates to a point of no return. This will be disastrous for the emerging countries and islands of the South-West Indian Ocean and thus, this region should be meticulously monitored and investigated to prevent any collapse of the productive ecosystem.

Bibliography

Arakawa, A., and V. R. Lamb (1977), Computational design of the basic dynamical processes of the UCLA general circulation model, *Methods in computational physics*, *17*, 173—-265.

Arbic, B., J. Richman, J. Shriver, P. Timko, J. Metzger, and A. Wallcraft (2012), Global Modeling of Internal Tides Within an Eddying Ocean General Circulation Model, *Oceanography*, *25*(2), 20–29, doi:10.5670/oceanog.2012.38.

Aumont, O., and L. Bopp (2006), Globalizing results from ocean in situ iron fertilization studies, *Global Biogeochemical Cycles*, *20*(2), doi:10.1029/2005GB002591.

Aumont, O., E. Maier-Reimer, S. Blain, and P. Monfray (2003), An ecosystem model of the global ocean including Fe, Si, P colimitations, *Global Biogeochemical Cycles*, *17*(2), doi:10.1029/2001GB001745.

Barceló-Llull, B., P. Sangrà, E. Pallàs-Sanz, E. D. Barton, S. N. Estrada-Allis, A. Martínez-Marrero, B. Aguiar-González, D. Grisolía, C. Gordo, Á. Rodríguez-Santana, Á. Marrero-Díaz, and J. Arístegui (2017), Anatomy of a subtropical intrathermocline eddy, *Deep Sea Research Part I: Oceanographic Research Papers*, *124*(April), 126–139, doi:10.1016/j.dsr.2017.03.012.

Barnes, S. L. (1973), Mesoscale objective map analysis using weighted time-series observations, *NOAA. Tech. Memo.*, *60*.

Bashmachnikov, I., F. Neves, T. Calheiros, and X. Carton (2015), Properties and pathways of Mediterranean water eddies in the Atlantic, *Progress in Oceanography*, *137*, 149–172, doi:10.1016/j.pocean.2015.06.001.

Batteen, M. L., and M. J. Rutherford (1990), Modeling Studies of Eddies in the Leeuwin Current: The Role of Thermal Forcing, doi:10.1175/1520-0485(1990)020<1484:MSOEIT>2.0.CO;2.

Beal, L. M., and H. L. Bryden (1997), Observations of an Agulhas Undercurrent, *Deep Sea Research Part I: Oceanographic Research Papers*, *44*(9-10), 1715–1724, doi:10.1016/S0967-0637(97)00033-2.

Beal, L. M., W. P. M. De Ruijter, A. Biastoch, and R. Zahn (2011), On the role of the Agulhas system in ocean circulation and climate, *Nature*, *472*(7344), 429–436, doi:10.1038/nature09983.

Beckmann, A., and D. B. Haidvogel (1993), Numerical Simulation of Flow around a Tall Isolated Seamount. Part I: Problem Formulation and Model Accuracy, doi:10.1175/1520-0485(1993)023<1736:NSOFAA>2.0.CO;2.

Behera, S. K., and T. Yamagata (2001), Subtropical SST dipole events in the southern Indian Ocean, *Geophysical Research Letters*, *28*(2), 327–330, doi:10.1029/2000GL011451.

Behrenfeld, M. J., R. T. O'Malley, D. A. Siegel, C. R. McClain, J. L. Sarmiento, G. C. Feldman, A. J. Milligan, P. G. Falkowski, R. M. Letelier, and E. S. Boss (2006), Climate-driven trends in contemporary ocean productivity, *Nature*, *444*(7120), 752–755, doi:10.1038/nature05317.

Biastoch, A., and W. Krauss (1999), The Role of Mesoscale Eddies in the Source Regions of the Agulhas Current, *Journal of Physical Oceanography*, *29*(9), 2303–2317, doi:10.1175/1520-0485(1999)029<2303:TROMEI>2.0.CO;2.

Biastoch, A., C. J. Reason, J. R. Lutjeharms, and O. Boebel (1999), The importance of flow in the Mozambique Channel to seasonality in the greater Agulhas Current system, *Geophysical Research Letters*, *26*(21), 3321–3324, doi:10.1029/1999GL002349.

Biastoch, A., C. W. Böning, and J. R. E. Lutjeharms (2008), Agulhas leakage dynamics affects decadal variability in Atlantic overturning circulation, *Nature*, *456*(7221), 489–492, doi:10.1038/nature07426.

Birol, F., and R. Morrow (2003), Separation of quasi-semiannual Rossby waves from the eastern boundary of the Indian Ocean, *Journal of Marine Research*, *61*(6), 707–723, doi:10.1357/002224003322981110.

Blanke, B., and S. Raynaud (1997), Kinematics of the Pacific Equatorial Undercurrent: An Eulerian and Lagrangian Approach from GCM Results, *Journal of Physical Oceanography*, *27*(6), 1038–1053, doi:10.1175/1520-0485(1997)027<1038:KOTPEU>2.0.CO;2.

Böhme, L., and U. Send (2005), Objective analyses of hydrographic data for referencing profiling float salinities in highly variable environments, *Deep Sea Research Part II*, *52*(3-4), 651–664, doi:10.1016/j.dsr2.2004.12.014.

Bopp, L., O. Aumont, P. Cadule, S. Alvain, and M. Gehlen (2005), Response of diatoms distribution to global warming and potential implications: A global model study, *Geophysical Research Letters*, *32*(19), doi:10.1029/2005GL023653.

Bower, A. S., L. Armi, and I. Ambar (1997), Lagrangian Observations of Meddy Formation during A Mediterranean Undercurrent Seeding Experiment*, *Journal of Physical Oceanography*, *27*(12), 2545–2575, doi:10.1175/1520-0485(1997)027<2545:LOOMFD>2.0.CO;2.

Bower, A. S., R. M. Hendry, D. E. Amrhein, and J. M. Lilly (2013), Direct observations of formation and propagation of subpolar eddies into the Subtropical North Atlantic, *Deep Sea Research Part II*, *85*, 15–41, doi:10.1016/j.dsr2.2012.07.029.

Boyce, D. G., M. R. Lewis, and B. Worm (2010), Global phytoplankton decline over the past century, *Nature*, *466*(7306), 591–596, doi:10.1038/nature09268.

Boyer, T. P., J. I. Antonov, O. K. Baranova, C. Coleman, H. E. Garcia, A. Grodsky, D. R. Johnson, R. a. Locarnini, A. V. Mishonov, T. D. O'Brien, C. R. Paver, J. R. Reagan, D. Seidov, I. V. Smolyar, M. M. Zweng, T. D. O. Brien, C. R. Paver, J. R. Reagan, D. Seidov, I. V. Smolyar, M. M. Zweng, and K. D. Sullivan (2013), WORLD OCEAN DATABASE 2013, NOAA Atlas NESDIS 72, *Sydney Levitus, Ed.; Alexey Mishonoc, Technical Ed.*, *NOAA Atlas*, 209 pp, doi:10.7289/V5NZ85MT.

Capone, D. G., J. P. Zehr, H. W. Paerl, B. Bergman, J. Edward, and E. J. Carpenter (1997), Trichodesmium, a globally significant marine cyanobacterium, *Science*, *276*(5316), 1221–1229.

Carton, X., N. Daniault, J. Alves, L. Cherubin, and I. Ambar (2010), Meddy dynamics and interaction with neighboring eddies southwest of Portugal: Observations and modeling, *Journal of Geophysical Research*, *115*(C6), C06,017, doi:10.1029/2009JC005646.

Castelao, R. M. (2014), Mesoscale eddies in the South Atlantic Bight and the Gulf Stream Recirculation region: Vertical structure, *Journal of Geophysical Research: Oceans*, *119*(3), 2048–2065, doi:10.1002/2014JC009796.

Chacko, N. (2017), Chlorophyll bloom in response to tropical cyclone Hudhud in the Bay of Bengal: Bio-Argo subsurface observations, *Deep-Sea Research Part I: Oceanographic Research Papers*, *124*, 66–72, doi:10.1016/j.dsr.2017.04.010.

Chaigneau, A., M. Le Texier, G. Eldin, C. Grados, and O. Pizarro (2011), Vertical structure of mesoscale eddies in the eastern South Pacific Ocean: A composite analysis from altimetry and Argo profiling floats, *Journal of Geophysical Research*, *116*(C11), C11,025, doi:10.1029/2011JC007134.

Chakravorty, S., C. Gnanaseelan, J. S. Chowdary, and J.-J. Luo (2014), Relative role of El Niño and IOD forcing on the southern tropical Indian Ocean Rossby waves, doi:10.1002/2013JC009713.Received.

Chapman, P., S. F. Di Marco, R. E. Davis, and A. C. Coward (2003), Flow at intermediate depths around Madagascar based on ALACE float trajectories, *Deep-Sea Research Part II: Topical Studies in Oceanography*, *50*(12-13), 1957–1986, doi:10.1016/S0967-0645(03)00040-7.

Chassot, E., S. Bonhommeau, N. K. Dulvy, F. Mélin, R. Watson, D. Gascuel, and O. Le Pape (2010), Global marine primary production constrains fisheries catches, *Ecology Letters*, *13*(4), 495–505, doi:10.1111/j.1461-0248.2010.01443.x.

Chelton, D. B., M. G. Schlax, R. M. Samelson, and R. A. de Szoeke (2007), Global observations of large oceanic eddies, *Geophysical Research Letters*, *34*(15), L15,606, doi:10.1029/2007GL030812.

Chelton, D. B., P. Gaube, M. G. Schlax, J. J. Early, and R. M. Samelson (2011a), The Influence of Nonlinear Mesoscale Eddies on Near-Surface Oceanic Chlorophyll, *Science*, *334*(6054), 328–332, doi:10.1126/science.1208897.

Chelton, D. B., M. G. Schlax, and R. M. Samelson (2011b), Global observations of nonlinear mesoscale eddies, *Progress in Oceanography*, *91*(2), 167–216, doi:10.1016/j.pocean.2011.01.002.

Chu, P. C., Q. Wang, and R. H. Bourke (1999), A Geometric Model for the Beaufort/Chukchi Sea Thermohaline Structure, *Journal of Atmospheric and Oceanic Technology*, *16*(6), 613–632, doi:10.1175/1520-0426(1999)016<0613:AGMFTB>2.0.CO;2.

Clarke, A. J., and X. Liu (1994), Interannual Sea Level in the Northern and Eastern Indian Ocean, doi:10.1175/1520-0485(1994)024<1224:ISLITN>2.0.CO;2.

Cleveland, W. S., and S. J. Devlin (1988), Locally Weighted Regression: An Approach to Regression Analysis by Local Fitting, *Journal of the American Statistical Association*, *83*(403), 596–610.

Collins, C., C. J. Reason, and J. C. Hermes (2012), Scatterometer and reanalysis wind products over the western tropical Indian Ocean, *Journal of Geophysical Research: Oceans*, *117*(3), C03,045, doi:10.1029/2011JC007531.

Collins, C., J. C. Hermes, and C. J. Reason (2014), Mesoscale activity in the Comoros Basin from satellite altimetry and a high-resolution ocean circulation model, *Journal of Geophysical Research: Oceans*, *119*(8), 1–16, doi:10.1002/2014JC010008.

Collins, C. A., T. Margolina, T. A. Rago, and L. Ivanov (2013), Looping RAFOS floats in the California Current System, *Deep Sea Research Part II*, *85*, 42–61, doi:10.1016/j.dsr2.2012.07.027.

Currie, J. C., M. Lengaigne, J. Vialard, D. M. Kaplan, O. Aumont, S. W. Naqvi, and O. Maury (2013), Indian ocean dipole and El Niño/Southern Oscillation impacts on regional chlorophyll anomalies in the Indian Ocean, *Biogeosciences*, *10*(10), 6677–6698, doi:10.5194/bg-10-6677-2013.

Dale, A. W., L. Nickelsen, F. Scholz, C. Hensen, A. Oschlies, and K. Wallmann (2015), A revised global estimate of dissolved iron fluxes from marine sediments, *Global Biogeochemical Cycles*, *29*(5), 691–707, doi:10.1002/2014GB005017.

Davis, R. E. (2005), Intermediate-Depth Circulation of the Indian and South Pacific Oceans Measured by Autonomous Floats, *Journal of Physical Oceanography*, *35*(5), 683–707, doi:10.1175/JPO2702.1.

de Baar, H. J. W., J. T. M. de Jong, D. C. E. Bakker, B. M. Löscher, C. Veth, U. Bathmann, and V. Smetacek (1995), Importance of iron for plankton blooms and carbon dioxide drawdown in the Southern Ocean, *Nature*, *373*(6513), 412–415, doi:10.1038/373412a0.

de Boyer Montégut, C. (2004), Mixed layer depth over the global ocean: An examination of profile data and a profile-based climatology, *Journal of Geophysical Research*, *109*(C12), C12,003, doi:10.1029/2004JC002378.

De Ruijter, W. P., H. M. Van Aken, E. J. Beier, J. R. Lutjeharms, R. P. Matano, and M. W. Schouten (2004), Eddies and dipoles around South Madagascar: Formation, pathways and large-scale impact, *Deep-Sea Research Part I: Oceanographic Research Papers*, *51*(3), 383–400, doi:10.1016/j.dsr.2003.10.011.

De Ruijter, W. P. M., H. Ridderinkhof, and M. W. Schouten (2005), Variability of the southern Indian Ocean, *Phil. Trans. R. Soc. A*, *363*(1826), 63–76, doi:10.1098/rsta. Published.

Debreu, L., and E. Blayo (2008), Two-way embedding algorithms: a review, *Ocean Dynamics*, *58*(5-6), 415–428, doi:10.1007/s10236-008-0150-9.

Debreu, L., C. Vouland, and E. Blayo (2008), AGRIF: Adaptive grid refinement in Fortran, *Computers & Geosciences*, *34*(1), 8–13, doi:10.1016/j.cageo.2007.01.009.

Debreu, L., P. Marchesiello, P. Penven, and G. Cambon (2012), Two-way nesting in split-explicit ocean models: Algorithms, implementation and validation, *Ocean Modelling*, *49-50*, 1–21, doi:10.1016/j.ocemod.2012.03.003.

Dee, D. P., S. M. Uppala, A. J. Simmons, P. Berrisford, P. Poli, S. Kobayashi, U. Andrae, M. A. Balmaseda, G. Balsamo, P. Bauer, P. Bechtold, A. C. M. Beljaars, L. van de Berg, J. Bidlot, N. Bormann, C. Delsol, R. Dragani, M. Fuentes, A. J. Geer, L. Haimberger, S. B. Healy, H. Hersbach, E. V. Hólm, L. Isaksen, P. Kållberg, M. Köhler, M. Matricardi, A. P. McNally, B. M. Monge-Sanz, J.-J. Morcrette, B.-K. Park, C. Peubey, P. de Rosnay, C. Tavolato, J.-N. Thépaut, and F. Vitart (2011), The ERA-Interim reanalysis: configuration and performance of the data assimilation system, *Quarterly Journal of the Royal Meteorological Society*, *137*(656), 553–597, doi:10.1002/qj.828.

Dilmahamod, A. F., J. C. Hermes, and C. J. Reason (2016), Chlorophyll-a variability in the Seychelles-Chagos Thermocline Ridge: Analysis of a coupled biophysical model, *Journal of Marine Systems*, *154*, 220–232, doi:10.1016/j.jmarsys.2015.10.011.

DiMarco, S. F., P. Chapman, and J. Nowlin (2000), Satellite observations of upwelling on the continental shelf south of Madagascar, *Geophysical Research Letters*, *27*(24), 3965–3968, doi:10.1029/2000GL012012.

DiMarco, S. F., P. Chapman, W. D. Nowlin, P. Hacker, K. Donohue, M. Luther, G. C. Johnson, and J. Toole (2002), Volume transport and property distributions of the Mozambique Channel, *Deep-Sea Research Part II: Topical Studies in Oceanography*, *49*(7-8), 1481–1511, doi:10.1016/S0967-0645(01)00159-X.

Domingues, C. M., M. E. Maltrud, S. E. Wijffels, J. A. Church, and M. Tomczak (2007), Simulated Lagrangian pathways between the Leeuwin Current System and the upper-ocean circulation of the southeast Indian Ocean, *Deep-Sea Research Part II: Topical Studies in Oceanography*, *54*(8-10), 797–817, doi:10.1016/j.dsr2.2006.10.003.

Dong, C., J. C. McWilliams, Y. Liu, and D. Chen (2014), Global heat and salt transports by eddy movement, *Nature Communications*, *5*, 3294, doi:10.1038/ncomms4294.

Donohue, K. A., and J. M. Toole (2003), A near-synoptic survey of the Southwest Indian Ocean, *Deep-Sea Research Part II: Topical Studies in Oceanography*, *50*(12-13), 1893–1931, doi:10.1016/S0967-0645(03)00039-0.

Ducet, N., P. Y. Le Traon, and G. Reverdin (2000), Global high-resolution mapping of ocean circulation from TOPEX/Poseidon and ERS-1 and -2, *Journal of Geophysical Research: Oceans*, *105*(C8), 19,477–19,498, doi:10.1029/2000JC900063.

Dufois, F., N. J. Hardman-Mountford, J. Greenwood, A. J. Richardson, M. Feng, S. Herbette, and R. Matear (2014), Impact of eddies on surface chlorophyll in the South Indian Ocean, *Journal of Geophysical Research: Oceans*, *119*(11), 8061–8077, doi:10.1002/2014JC010164.

Dufois, F., N. J. Hardman-Mountford, J. Greenwood, A. J. Richardson, M. Feng, and R. J. Matear (2016), Anticyclonic eddies are more productive than cyclonic eddies in subtropical gyres because of winter mixing, *Science Advances*, *2*(5), e1600,282–e1600,282, doi:10.1126/sciadv.1600282.

Dufois, F., N. J. Hardman-Mountford, M. Fernandes, B. Wojtasiewicz, D. Shenoy, D. Slawinski, M. Gauns, J. Greenwood, and R. Toresen (2017), Observational insights into chlorophyll distributions of subtropical South Indian Ocean eddies, *Geophysical Research Letters*, *44*(7), 3255–3264, doi:10.1002/2016GL072371.

Dugdale, R., D. Menzel, and J. . Ryther (1961), Nitrogen fixation in the Sargasso Sea, *Deep-Sea Research*, *7*(December), 297–300, doi:10.1016/0146-6313(61)90051-X.

Duncombe Rae, C. M., S. L. Garzoli, and A. L. Gordon (1996), The eddy field of the southeast Atlantic Ocean: A statistical census from the Benguela Sources and Transports Project., *Journal of Geophysical Research*, *101*(C5), 11,949–11,964, doi:10.1029/95JC03360.

Dunn, J., and K. Ridgway (2002), Mapping ocean properties in regions of complex topography, *Deep Sea Research Part I*, *49*(3), 591–604, doi:10.1016/S0967-0637(01)00069-3.

Durgadoo, J. V., B. R. Loveday, C. J. C. Reason, P. Penven, and A. Biastoch (2013), Agulhas Leakage Predominantly Responds to the Southern Hemisphere Westerlies, *Journal of Physical Oceanography*, *43*(10), 2113–2131, doi:10.1175/JPO-D-13-047.1.

Eden, C. (2007), Eddy length scales in the North Atlantic Ocean, *Journal of Geophysical Research*, *112*(C6), C06,004, doi:10.1029/2006JC003901.

Edwards, M., and A. J. Richardson (2004), Impact of climate change on marine pelagic phenology and trophic mismatch, *Nature*, *430*(7002), 881–884, doi:10.1038/nature02808.

Esaias, W. E., M. R. Abbott, I. Barton, O. B. Brown, J. W. Campbell, K. L. Carder, D. K. Clark, R. H. Evans, F. E. Hoge, H. R. Gordon, W. M. Balch, R. Letelier, and P. J. Minnett (1998), An overview of MODIS capabilities for ocean science observations, *IEEE Transactions on Geoscience and Remote Sensing*, *36*(4), 1250–1265, doi:10.1109/36.701076.

Fairall, C. W., E. F. Bradley, D. P. Rogers, J. B. Edson, and G. S. Young (1996), Bulk parameterization of air-sea fluxes for Tropical Ocean-Global Atmosphere Coupled-Ocean Atmosphere Response Experiment, *Journal of Geophysical Research: Oceans*, *101*(C2), 3747–3764, doi:10.1029/95JC03205.

Fang, F., and R. Morrow (2003), Evolution, movement and decay of warm-core Leeuwin Current eddies, *Deep-Sea Research Part II: Topical Studies in Oceanography*, *50*(12-13), 2245–2261, doi:10.1016/S0967-0645(03)00055-9.

Ffield, A., J. Toole, and D. Wilson (1997), Seasonal circulation in the south Indian Ocean, *Geophysical Research Letters*, *24*(22), 2773–2776, doi:10.1029/97GL01253.

Filyushkin, B. N., M. A. Sokolovskiy, N. G. Kozhelupova, and I. M. Vagina (2011), Evolution of intrathermocline eddies moving over a submarine hill, *Doklady Earth Sciences*, *441*(2), 1757–1760, doi:10.1134/S1028334X11120269.

Flierl, G. R. (1981), No Particle motions in large-amplitude wave fields, *Geophyiscal & Astrophysics Fluid Dynamics*, *18 (1-2)*, 39–74.

Frajka-Williams, E., P. B. Rhines, and C. C. Eriksen (2009), Physical controls and mesoscale variability in the Labrador Sea spring phytoplankton bloom observed by Seaglider, *Deep Sea Research Part I: Oceanographic Research Papers*, *56*(12), 2144–2161, doi:10.1016/j.dsr.2009.07.008.

Garfield, N., C. A. Collins, R. G. Paquette, and E. Carter (1999), Lagrangian Exploration of the California Undercurrent, 1992–95, *Journal of Physical Oceanography*, *29*(4), 560–583.

Gaube, P., D. B. Chelton, P. G. Strutton, and M. J. Behrenfeld (2013), Satellite observations of chlorophyll, phytoplankton biomass, and Ekman pumping in nonlinear mesoscale eddies, *Journal of Geophysical Research: Oceans*, *118*(12), 6349–6370, doi:10.1002/2013JC009027.

Gaube, P., D. J. McGillicuddy, D. B. Chelton, M. J. Behrenfeld, and P. G. Strutton (2014), Regional variations in the influence of mesoscale eddies on near-surface chlorophyll, *Journal of Geophysical Research: Oceans*, *119*(12), 8195–8220, doi:10.1002/2014JC010111.

Gaube, P., D. B. Chelton, R. M. Samelson, M. G. Schlax, and L. W. O'Neill (2015), Satellite Observations of Mesoscale Eddy-Induced Ekman Pumping, *Journal of Physical Oceanography*, *45*(1), 104–132, doi:10.1175/JPO-D-14-0032.1.

Geider, R. J., H. L. Maclntyre, and T. M. Kana (1998), A dynamic regulatory model of phytoplanktonic acclimation to light, nutrients, and temperature, *Limnology and Oceanography*, *43*(4), 679–694, doi:10.4319/lo.1998.43.4.0679.

Gill, A. E., and P. P. Niiler (1973), The theory of the seasonal variability in the ocean, *Deep-Sea Research and Oceanographic Abstracts*, *20*(2), 141–177, doi:10.1016/0011-7471(73)90049-1.

Gnanaseelan, C., and B. H. Vaid (2010), Interannual variability in the Biannual Rossby waves in the tropical Indian Ocean and its relation to Indian Ocean Dipole and El Nino forcing, *Ocean Dynamics*, *60*(1), 27–40, doi:10.1007/s10236-009-0236-z.

Godfrey, J. S., and K. R. Ridgway (1985), The Large-Scale Environment of the Poleward-Flowing Leeuwin Current, Western Australia: Longshore Steric Height Gradients, Wind Stresses and Geostrophic Flow, doi:10.1175/1520-0485(1985)015<0481:TLSEOT>2.0.CO;2.

Gordon, A. L. (1986), Interocean exchange of thermocline water, *Journal of Geophysical Research*, *91*(C4), 5037, doi:10.1029/JC091iC04p05037.

Gordon, A. L., and R. A. Fine (1996), Pathways of water between the Pacific and Indian oceans in the Indonesian seas, doi:10.1038/379146a0.

Gordon, A. L., and J. L. McClean (1999), Thermohaline Stratification of the Indonesian Seas: Model and Observations*, *Journal of Physical Oceanography*, *29*, 198–216, doi:10.1175/1520-0485(1999)029<0198:TSOTIS>2.0.CO;2.

Gordon, A. L., C. F. Giulivi, C. M. Lee, H. H. Furey, A. Bower, and L. Talley (2002), Japan/East Sea Intrathermocline Eddies, *Journal of Physical Oceanography*, *32*(6), 1960–1974, doi:10.1175/1520-0485(2002)032<1960:JESIE>2.0.CO;2.

Gordon, A. L., E. Shroyer, and V. S. N. Murty (2017), An Intrathermocline Eddy and a tropical cyclone in the Bay of Bengal, *Scientific Reports*, *7*(October 2016), 46,218, doi:10.1038/srep46218.

Gregg, W. W., and M. E. Conkright (2001), Global seasonal climatologies of ocean chlorophyll: Blending in situ and satellite data for the Coastal Zone Color Scanner era, *Journal of Geophysical Research: Oceans*, *106*(C2), 2499–2515, doi:10.1029/1999JC000028.

Gründlingh, M. L. (1987), Anatomy of a cyclonic eddy of the mozambique ridge current, *Deep Sea Research Part A, Oceanographic Research Papers*, *34*(2), 237–251, doi:10.1016/0198-0149(87)90084-7.

Gründlingh, M. L. (1993), On the winter flow in the southern Mozambique channel, *Deep-Sea Research Part I*, *40*(2), 409–418, doi:10.1016/0967-0637(93)90011-Q.

Gründlingh, M. L. (1995), Tracking eddies in the southeast Atlantic and southwest Indian oceans with TOPEX/POSEIDON, *Journal of Geophysical Research*, *100*, 24,977–24,986.

Grundlingh 1985 (1985), Occurence of Red Sea Water in the Southwestern Indian Ocean, 1981, *Journal of Physical Oceanography*, *15*, 207–212.

Halliwell, G. R., G. Peng, and D. B. Olson (1994), Stability of the Sargasso Sea Subtropical Frontal Zone, doi:Doi10.1175/1520-0485(1994)024<1166:Sotsss>2.0.Co;2.

Halo, I., P. Penven, B. Backeberg, I. Ansorge, F. Shillington, and R. Roman (2014a), Mesoscale eddy variability in the southern extension of the East Madagascar Current: Seasonal cycle, energy conversion terms, and eddy mean properties, *Journal of Geophysical Research: Oceans*, *119*(10), 7324–7356, doi:10.1002/2014JC009820.

Halo, I., B. Backeberg, P. Penven, I. Ansorge, C. Reason, and J. Ullgren (2014b), Eddy properties in the Mozambique Channel: A comparison between observations and two numerical ocean circulation models, *Deep Sea Research Part II: Topical Studies in Oceanography*, *100*, 38–53, doi:10.1016/j.dsr2.2013.10.015.

Hanawa, K., and L. D.Talley (2001), Chapter 5.4 Mode waters, in *International Geophysics*, vol. 77, pp. 373–386, Elsevier, doi:10.1016/S0074-6142(01)80129-7.

Hansen, C., E. Kvaleberg, and A. Samuelsen (2010), Anticyclonic eddies in the Norwegian Sea; their generation, evolution and impact on primary production, *Deep-Sea Research Part I: Oceanographic Research Papers*, *57*(9), 1079–1091, doi:10.1016/j.dsr.2010.05.013.

Hastenrath, S., and L. Greischar (1991), The monsoonal current regimes of the tropical Indian Ocean: Observed surface flow fields and their geostrophic and wind-driven components, *Journal of Geophysical Research*, *96*(C7), 12,619, doi:10.1029/91JC00997.

Hebert, D., N. Oakey, and B. Ruddick (1990), Evolution of a Mediterranean Salt Lens: Scalar Properties, *Journal of Physical Oceanography*, *20*(9), 1468–1483.

Hedstrom, K. (1997), User's Manual for an S-Coordinate Primitive Equation Ocean Circulation Model SCRUM Version 3.0, *Institute of Marine and Coastal Sciences Rutgers University*.

Hedström, K. S. (2009), Technical Manual for a Coupled Sea-Ice / Ocean Circulation Model (Version 3) Technical Manual for a Coupled Sea-Ice / Ocean Circulation Model (Version 3).

Hermes, J. C., and C. J. C. Reason (2008), Annual cycle of the South Indian Ocean (Seychelles-Chagos) thermocline ridge in a regional ocean model, *Journal of Geophysical Research: Oceans*, *113*(4), C04,035, doi:10.1029/2007JC004363.

Hjort, J. (1926), Fluctuations in the year classes of important food fishes, *J. Cons. int. Explor. Mer*, *1*, 5–38.

Hogan, P. J., and H. E. Hurlburt (2006), Why do intrathermocline eddies form in the Japan/East Sea? A modeling perspective, *NAVAL RESEARCH LAB STENNIS SPACE CENTER MS OCEANOGRAPHY DIV*, *31*(0704).

Huhn, F., A. von Kameke, V. Pérez-Muñuzuri, M. J. Olascoaga, and F. J. Beron-Vera (2012), The impact of advective transport by the South Indian Ocean Countercurrent on the Madagascar plankton bloom, *Geophysical Research Letters*, *39*(6), doi:10.1029/2012GL051246.

Iskandar, I., H. Sasaki, Y. Sasai, Y. Masumoto, and K. Mizuno (2010), A numerical investigation of eddy-induced chlorophyll bloom in the southeastern tropical Indian Ocean during Indian Ocean Dipole 2006, *Ocean Dynamics*, *60*(3), 731–742, doi:10.1007/s10236-010-0290-6.

Jackett, D. R., and T. J. Mcdougall (1995), Minimal Adjustment of Hydrographic Profiles to Achieve Static Stability, doi:10.1175/1520-0426(1995)012<0381:MAOHPT>2.0.CO;2.

Jayne, S. R., and J. Marotzke (2002), The Oceanic Eddy Heat Transport*, *Journal of Physical Oceanography*, *32*(12), 3328–3345.

Jeandel, C., B. Peucker-Ehrenbrink, M. Jones, C. Pearce, E. Oelkers, Y. Godderis, F. Lacan, O. Aumont, and T. Arsouze (2011), Ocean margins: The missing term in oceanic element budgets?, *EOS (Transactions, American Geophysical Union)*, *92*(26), 217–224, doi:10.5194/bgd-.

Jerónimo, G., and J. Gómez-Valdés (2007), A subsurface warm-eddy off northern Baja California in July 2004, *Geophysical Research Letters*, *34*(6), 1–5, doi:10.1029/2006GL028851.

Jia, F., L. Wu, and B. Qiu (2011a), Seasonal Modulation of Eddy Kinetic Energy and Its Formation Mechanism in the Southeast Indian Ocean, *Journal of Physical Oceanography*, *41*(4), 657–665, doi:10.1175/2010JPO4436.1.

Jia, F., L. Wu, J. Lan, and B. Qiu (2011b), Interannual modulation of eddy kinetic energy in the southeast Indian Ocean by Southern Annular Mode, *Journal of Geophysical Research*, *116*(C2), C02,029, doi:10.1029/2010JC006699.

Johnson, G. C., and K. E. McTaggart (2010), Equatorial Pacific 13 C Water Eddies in the Eastern Subtropical South Pacific Ocean*, *Journal of Physical Oceanography*, *40*(1), 226–236, doi:10.1175/2009JPO4287.1.

Johnson, K. S., F. P. Chavez, and G. E. Friederich (1999), Continental-shelf sediment as a primary source of iron for coastal phytoplankton, *Nature*, *398*(6729), 697–700, doi:10.1038/19511.

José, Y. S., O. Aumont, E. Machu, P. Penven, C. L. Moloney, and O. Maury (2014), Influence of mesoscale eddies on biological production in the Mozambique Channel: Several contrasted examples from a coupled ocean-biogeochemistry model, *Deep-Sea Research Part II: Topical Studies in Oceanography*, *100*, 79–93, doi:10.1016/j.dsr2.2013.10.018.

José, Y. S., P. Penven, O. Aumont, E. Machu, C. L. Moloney, F. Shillington, and O. Maury (2016), Suppressing and enhancing effects of mesoscale dynamics on biological production in the Mozambique Channel, *Journal of Marine Systems*, *158*, 129–139, doi:10.1016/j.jmarsys.2016.02.003.

Kahru, M., and B. G. Mitchell (2010), Blending of ocean colour algorithms applied to the Southern Ocean, *Remote Sensing Letters*, *1*(2), 119–124, doi:10.1080/01431160903547940.

Kalnay, E., M. Kanamitsu, R. Kistler, W. Collins, D. Deaven, L. Gandin, M. Iredell, S. Saha, G. White, J. Woollen, Y. Zhu, M. Chelliah, W. Ebisuzaki, W. Higgins, J. Janowiak, K. C. Mo, C. Ropelewski, J. Wang, A. Leetmaa, R. Reynolds, R. Jenne, and D. Joseph (1996), The NCEP/NCAR 40-year reanalysis project, *Bulletin of the American Meteorological Society*, *77*(3), 437–471, doi:10.1175/1520-0477(1996)077<0437:TNYRP>2.0.CO;2.

Keerthi, M. G., M. Lengaigne, J. Vialard, C. de Boyer Montégut, and P. M. Muraleedharan (2012), Interannual variability of the Tropical Indian Ocean mixed layer depth, *Climate Dynamics*, *40*(3-4), 743–759, doi:10.1007/s00382-012-1295-2.

Kim, D., E. J. Yang, K. H. Kim, C.-W. Shin, J. Park, S. Yoo, and J.-H. Hyun (2012), Impact of an anticyclonic eddy on the summer nutrient and chlorophyll a distributions in the Ulleung Basin, East Sea (Japan Sea), *ICES Journal of Marine Science*, *69*(1), 23–29, doi:10.1093/icesjms/fsr178.

Koné, V., O. Aumont, M. Lévy, and L. Resplandy (2009), Physical and biogeochemical controls of the phytoplankton seasonal cycle in the Indian Ocean: A modeling study, *Geophysical Monograph Series*, *185*, 147–166, doi:10.1029/2008GM000700.

Kostianoy, A., and I. Belkin (1989), A Survey of Observations on Intrathermocline Eddies in the World Ocean, in *Elsevier oceanography series*, vol. 50, pp. 821–841, Elsevier, doi:10.1016/S0422-9894(08)70223-X.

Kumar, P., J. Vialard, M. Lengaigne, V. S. Murty, G. R. Foltz, M. J. McPhaden, S. Pous, and C. de Boyer Montégut (2014), Processes of interannual mixed layer temperature variability in the thermocline ridge of the Indian Ocean, *Climate Dynamics*, *43*(9-10), 2377–2397, doi:10.1007/s00382-014-2059-y.

Kundu, P. K., and J. P. McCreary (1986), On the Dynamics of the Throughflow from the Pacific into the Indian Ocean, doi:10.1175/1520-0485(1986)016<2191:OTDOTT>2.0.CO;2.

Lambert, E., D. Le Bars, and W. P. De Ruijter (2016), The connection of the Indonesian Throughflow, South Indian Ocean Countercurrent and the Leeuwin Current, *Ocean Science*, *12*(3), 771–780, doi:10.5194/os-12-771-2016.

Large, W. G., J. C. McWilliams, and S. C. Doney (1994), Oceanic vertical mixing: A review and a model with a nonlocal boundary layer parameterization, *Reviews of Geophysics*, *32*(4), 363, doi:10.1029/94RG01872.

Ledwell, J. R., D. J. McGillicuddy, and L. A. Anderson (2008), Nutrient flux into an intense deep chlorophyll layer in a mode-water eddy, *Deep Sea Research Part II: Topical Studies in Oceanography*, *55*(10-13), 1139–1160, doi:10.1016/j.dsr2.2008.02.005.

Lehahn, Y., F. D'Ovidio, M. Lévy, Y. Amitai, and E. Heifetz (2011), Long range transport of a quasi isolated chlorophyll patch by an Agulhas ring, *Geophysical Research Letters*, *38*(16), 1–6, doi:10.1029/2011GL048588.

Lemarié, F., J. Kurian, A. F. Shchepetkin, M. Jeroen Molemaker, F. Colas, and J. C. McWilliams (2012), Are there inescapable issues prohibiting the use of terrain-following coordinates in climate models?, *Ocean Modelling*, *42*, 57–79, doi:10.1016/j.ocemod.2011.11.007.

Lett, C., P. Verley, C. Mullon, C. Parada, T. Brochier, P. Penven, and B. Blanke (2008), A Lagrangian tool for modelling ichthyoplankton dynamics, *Environmental Modelling and Software*, *23*(9), 1210–1214, doi:10.1016/j.envsoft.2008.02.005.

Lévy, M. (2003), Mesoscale variability of phytoplankton and of new production: Impact of the large-scale nutrient distribution, *Journal of Geophysical Research*, *108*(C11), 3358, doi:10.1029/2002JC001577.

Lévy, M., D. Shankar, J. M. André, S. S. Shenoi, F. Durand, and C. de Boyer Montégut (2007), Basin-wide seasonal evolution of the Indian Ocean's phytoplankton blooms, *Journal of Geophysical Research: Oceans*, *112*(12), C12,014, doi:10.1029/2007JC004090.

Lévy, M., R. Ferrari, P. J. Franks, A. P. Martin, and P. Rivière (2012), Bringing physics to life at the submesoscale, *Geophysical Research Letters*, *39*(14), doi:10.1029/2012GL052756.

L'Hégaret, P., X. Carton, I. Ambar, C. Ménesguen, B. L. Hua, L. Chérubin, A. Aguiar, B. Le Cann, N. Daniault, and N. Serra (2014), Evidence of Mediterranean Water dipole collision in the Gulf of Cadiz, *Journal of Geophysical Research: Oceans*, *119*(8), 5337–5359, doi:10.1002/2014JC009972.

Li, C., Z. Zhang, W. Zhao, and J. Tian (2017a), A statistical study on the subthermocline submesoscale eddies in the northwestern Pacific Ocean based on Argo data, *Journal of Geophysical Research: Oceans*, *122*(5), 3586–3598, doi:10.1002/2016JC012561.

Li, H., F. Xu, W. Zhou, D. Wang, J. S. Wright, Z. Liu, and Y. Lin (2017b), Development of a global gridded Argo data set with Barnes successive corrections, *Journal of Geophysical Research: Oceans*, *122*(2), 866–889, doi:10.1002/2016JC012285.

Li, H., Z. Liu, J. Xu, X. Wu, C. Sun, S. Lu, and M. Cao (2017c), Manual of Global Ocean Argo gridded data set (BOA-Argo) (Version 2017), doi:10.1002/2016JC012285.6.

Lin, I., W. T. Liu, C.-C. Wu, G. T. F. Wong, C. Hu, Z. Chen, W.-D. Liang, Y. Yang, and K.-K. Liu (2003), New evidence for enhanced ocean primary production triggered by tropical cyclone, *Geophysical Research Letters*, *30*(13), 10–13, doi:10.1029/2003GL017141.

Longhurst, A. (2001), A major seasonal phytoplankton bloom in the Madagascar Basin, *Deep-Sea Research Part I: Oceanographic Research Papers*, *48*(11), 2413–2422, doi:10.1016/S0967-0637(01)00024-3.

Longhurst, A. (2010), *Ecological geography of the sea*, Elsevier.

Loveday, B. R., J. V. Durgadoo, C. J. C. Reason, A. Biastoch, and P. Penven (2014), Decoupling of the Agulhas Leakage from the Agulhas Current, *Journal of Physical Oceanography*, *44*(7), 1776–1797, doi:10.1175/JPO-D-13-093.1.

Lutjeharms, J. R., and E. Machu (2000), An upwelling cell inshore of the East Madagascar Current, *Deep-Sea Research Part I: Oceanographic Research Papers*, *47*(12), 2405–2411, doi:10.1016/S0967-0637(00)00026-1.

Lutjeharms, J. R. E. (1988), Remote sensing corroboration of retroflection of the East Madagascar Current, *Deep Sea Research Part A, Oceanographic Research Papers*, *35*(12), 2045–2050, doi:10.1016/0198-0149(88)90124-0.

Lutjeharms, J. R. E., and R. C. Van Ballegooyen (1988), The Retroflection of the Agulhas Current, doi:10.1175/1520-0485(1988)018<1570:TROTAC>2.0.CO;2.

Lutjeharms, J. R. E., N. D. Bang, and C. P. Duncan (1981), Characteristics of the currents east and south of Madagascar, *Deep Sea Research Part A, Oceanographic Research Papers*, *28*(9), 879–899, doi:10.1016/0198-0149(81)90008-X.

Macdonald, A. M. (1998), The global ocean circulation: A hydrographic estimate and regional analysis, *Progress in Oceanography*, *41*(3), 281–382, doi:10.1016/S0079-6611(98)00020-2.

Machu, E., and V. Garçon (2001), Phytoplankton seasonal distribution from SeaWiFS data in the Agulhas Current system, *Journal of Marine Research*, *59*, 795–812, doi:10.1357/002224001762674944.

Machu, E., J. R. E. Lutjeharms, A. M. Webb, and H. M. Van Aken (2002), First hydrographic evidence of the southeast Madagascar upwelling cell, *Geophysical Research Letters*, *29*(21), 1–5, doi:10.1029/2002GL015381.

Mackas, D. L., S. Batten, and M. Trudel (2007), Effects on zooplankton of a warmer ocean: Recent evidence from the Northeast Pacific, *Progress in Oceanography*, *75*(2), 223–252, doi:10.1016/j.pocean.2007.08.010.

Marchesiello, P., J. C. McWilliams, and A. Shchepetkin (2001), Open boundary conditions for long-term integration of regional oceanic models, *Ocean Modelling*, *3*(1-2), 1–20, doi:10.1016/S1463-5003(00)00013-5.

Marchesiello, P., L. Debreu, and X. Couvelard (2009), Spurious diapycnal mixing in terrain-following coordinate models: The problem and a solution, *Ocean Modelling*, *26*(3-4), 156–169, doi:10.1016/j.ocemod.2008.09.004.

McCreary Jr., J. P., R. Shetye, Satish, and P. K. Kundu (1986), Thermohaline forcing of eastern boundary currents : off the west coast of Australia, *Journal of Marine Research*, *44*, 71–92, doi:10.1357/002224086788460184.

McDowell, S. E., and H. T. Rossby (1978), Mediterranean Water: An Intense Mesoscale Eddy off the Bahamas., *Science (New York, N.Y.)*, *202*, 1085–1087, doi:10.1126/science.202.4372.1085.

McGillicuddy, D., and A. Robinson (1997), Eddy-induced nutrient supply and new production in the Sargasso Sea, *Deep Sea Research Part I: Oceanographic Research Papers*, *44*(8), 1427–1450, doi:10.1016/S0967-0637(97)00024-1.

McGillicuddy, D. J. (2015), Formation of Intrathermocline Lenses by Eddy Wind Interaction, *Journal of Physical Oceanography*, *45*(2), 606–612, doi:10.1175/JPO-D-14-0221.1.

McGillicuddy, D. J., L. A. Anderson, N. R. Bates, T. Bibby, K. O. Buesseler, C. A. Carlson, C. S. Davis, C. Ewart, P. G. Falkowski, S. A. Goldthwait, D. A. Hansell, W. J. Jenkins, R. Johnson, V. K. Kosnyrev, J. R. Ledwell, Q. P. Li, D. A. Siegel, and D. K. Steinberg (2007), Eddy/Wind Interactions Stimulate Extraordinary Mid-Ocean Plankton Blooms, *Science*, *316*(5827), 1021–1026, doi:10.1126/science.1136256.

Mcwilliams, J. C. (1985), Submesoscale Coherent Vortices in the Ocean, *Reviews of Geophysics*, *23*(2), 165–182.

Menezes, V. V., H. E. Phillips, A. Schiller, N. L. Bindoff, C. M. Domingues, and M. L. Vianna (2014), South Indian countercurrent and associated fronts, *Journal of Geophysical Research: Oceans*, *119*(10), 6763–6791, doi:10.1002/2014JC010076.

Menezes, V. V., H. E. Phillips, M. L. Vianna, and N. L. Bindoff (2016), Interannual variability of the South Indian Countercurrent, *Journal of Geophysical Research: Oceans*, *121*(5), 3465–3487, doi:10.1002/2015JC011417.

Meyers, G. (1996), Variation of Indonesian throughflow and the El Niño-Southern Oscillation, *Journal of Geophysical Research: Oceans*, *101*(C5), 12,255–12,263, doi: 10.1029/95JC03729.

Monod, J. (1942), *Recherches sur la croissance des cultures bacteriennes*, Hermann.

Morales, C. E., S. Hormazabal, M. Correa-Ramirez, O. Pizarro, N. Silva, C. Fernandez, V. Anabalón, and M. L. Torreblanca (2012), Mesoscale variability and nutrient-phytoplankton distributions off central-southern Chile during the upwelling season: The influence of mesoscale eddies, *Progress in Oceanography*, *104*, 1–16, doi:10.1016/j.pocean.2012.04.015.

Morrow, R., and F. Birol (1998), Variability in the southeast Indian Ocean from altimetry: Forcing mechanisms for the Leeuwin Current, *Journal of Geophysical Research: Oceans*, *103*(C9), 18,529–18,544, doi:10.1029/98JC00783.

Morrow, R., F. Birol, D. Griffin, J. Sudre, D. Giffin, and J. Sudre (2004), Divergent pathways of cylonic and anti-cyclonic ocean eddies, *Geophysical Research Letters*, *31*(24), 1–5, doi:10.1029/2004GL020974.

Myers, R. A., and B. Worm (2003), Rapid worldwide depletion of predatory fish communities, *Nature*, *423*(6937), 280–283, doi:10.1038/nature01610.

Naik, R. K., J. V. George, M. A. Soares, A. Devi, N. Anilkumar, R. Roy, P. V. Bhaskar, N. Murukesh, and C. T. Achuthankutty (2015), Phytoplankton community structure at the juncture of the Agulhas Return Front and Subtropical Front in the Indian Ocean sector of Southern Ocean: Bottom-up and top-down control, *Deep-Sea Research Part II: Topical Studies in Oceanography*, *118*, 233–239, doi: 10.1016/j.dsr2.2015.01.002.

Nauw, J. J., H. M. van Aken, J. R. E. Lutjeharms, and W. P. M. de Ruijter (2006), Intrathermocline eddies in the Southern Indian Ocean, *Journal of Geophysical Research*, *111*(C3), C03,006, doi:10.1029/2005JC002917.

Nauw, J. J., H. M. van Aken, A. Webb, J. R. Lutjeharms, and W. P. de Ruijter (2008), Observations of the southern East Madagascar Current and undercurrent and countercurrent system, *Journal of Geophysical Research: Oceans*, *113*(8), C08,006, doi:10.1029/2007JC004639.

New, A. L., S. G. Alderson, D. A. Smeed, and K. L. Stansfield (2007), On the circulation of water masses across the Mascarene Plateau in the South Indian Ocean, *Deep-Sea Research Part I: Oceanographic Research Papers*, *54*(1), 42–74, doi:10.1016/j.dsr.2006.08.016.

Niu, L., P. H. van Gelder, C. Zhang, Y. Guan, and J. K. Vrijling (2016), Physical control of phytoplankton bloom development in the coastal waters of Jiangsu (China), *Ecological Modelling*, *321*, 75–83, doi:10.1016/j.ecolmodel.2015.10.008.

O'Connor, B. M., R. A. Fine, and D. B. Olson (2005), A global comparison of subtropical underwater formation rates, *Deep Sea Research Part I*, *52*(9), 1569–1590, doi:10.1016/j.dsr.2005.01.011.

Oka, E., K. Toyama, and T. Suga (2009), Subduction of North Pacific central mode water associated with subsurface mesoscale eddy, *Geophysical Research Letters*, *36*(8), L08,607, doi:10.1029/2009GL037540.

Oschlies, A. (2002), Can eddies make ocean deserts bloom?, *Global Biogeochemical Cycles*, *16*(4), 53–1–53–11, doi:10.1029/2001GB001830.

Ou, H.-W., and A. Gordon (2002), Subduction along a Midocean Front and the Generation of Intrathermocline Eddies: A Theoretical Study*, *Journal of Physical Oceanography*, *32*(6), 1975–1986, doi:10.1175/1520-0485(2002)032<1975:SAAMFA>2.0.CO;2.

Owens, W. B., and A. P. Wong (2009), An improved calibration method for the drift of the conductivity sensor on autonomous CTD profiling floats by θ–S climatology, *Deep Sea Research Part I*, *56*(3), 450–457, doi:10.1016/j.dsr.2008.09.008.

Palastanga, V., P. J. van Leeuwen, and W. P. de Ruijter (2006), A link between low-frequency mesoscale eddy variability around Madagascar and the large-scale Indian Ocean variability, *Journal of Geophysical Research: Oceans*, *111*(9), C09,029, doi:10.1029/2005JC003081.

Palastanga, V., P. J. van Leeuwen, M. W. Schouten, and W. P. M. de Ruijter (2007), Flow structure and variability in the subtropical Indian Ocean: Instability of the South Indian Ocean Countercurrent, *Journal of Geophysical Research: Oceans*, *112*(1), C01,001, doi:10.1029/2005JC003395.

Pelland, N. A., C. C. Eriksen, and C. M. Lee (2013), Subthermocline Eddies over the Washington Continental Slope as Observed by Seagliders, 2003–2009, *Journal of Physical Oceanography*, *43*(10), 2025–2053, doi:10.1175/JPO-D-12-086.1.

Penven, P., J. R. Lutjeharms, and P. Florenchie (2006a), Madagascar: A pacemaker for the Agulhas Current system?, *Geophysical Research Letters*, *33*(17), L17,609, doi:10.1029/2006GL026854.

Penven, P., L. Debreu, P. Marchesiello, and J. C. McWilliams (2006b), Evaluation and application of the ROMS 1-way embedding procedure to the central california upwelling system, *Ocean Modelling*, *12*(1-2), 157–187, doi:10.1016/j.ocemod.2005.05.002.

Penven, P., P. Marchesiello, L. Debreu, and J. Lefèvre (2008), Software tools for pre- and post-processing of oceanic regional simulations, *Environmental Modelling and Software*, *23*(5), 660–662, doi:10.1016/j.envsoft.2007.07.004.

Penven, P., I. Halo, S. Pous, and L. Marié (2014), Cyclogeostrophic balance in the Mozambique Channel, *Journal of Geophysical Research: Oceans*, *119*(2), 1054–1067, doi:10.1002/2013JC009528.

Platt, T., D. S. Broomhead, S. Sathyendranath, A. M. Edwards, and E. J. Murphy (2003), Phytoplankton biomass and residual nitrate in the pelagic ecosystem, *Proceedings of the Royal Society A: Mathematical, Physical and Engineering Sciences*, *459*(2033), 1063–1073, doi:10.1098/rspa.2002.1079.

Polacheck, T. (2006), Tuna longline catch rates in the Indian Ocean: Did industrial fishing result in a 90% rapid decline in the abundance of large predatory species?, *Marine Policy*, *30*(5), 470–482, doi:10.1016/j.marpol.2005.06.016.

Ponsoni, L., B. Aguiar-González, L. R. Maas, H. M. van Aken, and H. Ridderinkhof (2015), Long-term observations of the East Madagascar Undercurrent, *Deep-Sea Research Part I: Oceanographic Research Papers*, *100*, 64–78, doi:10.1016/j.dsr.2015.02.004.

Ponsoni, L., B. Aguiar-González, H. Ridderinkhof, and L. R. M. Maas (2016), The East Madagascar Current: Volume Transport and Variability Based on Long-Term Observations*, *Journal of Physical Oceanography*, *46*(4), 1045–1065, doi:10.1175/JPO-D-15-0154.1.

Poulton, A. J., M. C. Stinchcombe, and G. D. Quartly (2009), High numbers of Trichodesmium and diazotrophic diatoms in the southwest Indian Ocean, *Geophysical Research Letters*, *36*(15), doi:10.1029/2009GL039719.

Provenzale, A. (1999), Transport by coherent barotropic vortices, *Annual review of fluid mechanics*, *31*(1), 55–93.

Qiu, B., and S. Chen (2005), Eddy-Induced Heat Transport in the Subtropical North Pacific from Argo, TMI, and Altimetry Measurements, *Journal of Physical Oceanography*, *35*(4), 458–473, doi:10.1175/JPO2696.1.

Quadfasel, D., A. Frische, and G. Cresswell (1996), The circulation in the source area of the South Equatorial Current in the eastern Indian Ocean, *Journal of Geophysical Research*, *101*(C5), 12,483, doi:10.1029/96JC00437.

Quartly, G., J. Buck, M. Srokosz, and A. Coward (2006), Eddies around Madagascar — The retroflection re-considered, *Journal of Marine Systems*, *63*(3-4), 115–129, doi:10.1016/j.jmarsys.2006.06.001.

Quartly, G. D., and M. A. Srokosz (2002), SST Observations of the Agulhas and East Madagascar Retroflections by the TRMM Microwave Imager, *Journal of Physical Oceanography*, *32*(5), 1585–1592, doi:10.1175/1520-0485(2002)032<1585:SOOTAA>2.0.CO;2.

Quartly, G. D., and M. A. Srokosz (2004), Eddies in the southern Mozambique Channel, *Deep-Sea Research Part II: Topical Studies in Oceanography*, *51*(1-3), 69–83, doi:10.1016/j.dsr2.2003.03.001.

Raj, R. P., B. N. Peter, and D. Pushpadas (2010), Oceanic and atmospheric influences on the variability of phytoplankton bloom in the Southwestern Indian Ocean, *Journal of Marine Systems*, *82*(4), 217–229, doi:10.1016/j.jmarsys.2010.05.009.

Ramanantsoa, J. D., M. Krug, P. Penven, M. Rouault, and J. Gula (2018a), Coastal upwelling south of Madagascar: Temporal and spatial variability, *Journal of Marine Systems*, *178*(October 2017), 29–37, doi:10.1016/j.jmarsys.2017.10.005.

Ramanantsoa, J. D., P. Penven, M. Krug, J. Gula, and M. Rouault (2018b), Uncovering a New Current: The Southwest MAdagascar Coastal Current, *Geophysical Research Letters*, *45*(4), 1930–1938, doi:10.1002/2017GL075900.

Rao, L. V. G., and P. S. Ram (2005), Upper ocean physical processes in the Tropical Indian Ocean, *Tech. Rep. April*, National Institute of Oceanography Regional Centre.

Rao, R. R., R. L. Molinari, and J. F. Festa (1989), Evolution of the climatological near-surface thermal structure of the tropical Indian Ocean: 1. Description of mean monthly mixed layer depth, and sea surface temperature, surface current, and surface meteorological fields, *Journal of Geophysical Research*, *94*(C8), 10,801, doi:10.1029/JC094iC08p10801.

Rao, S. A., and S. K. Behera (2005), Subsurface influence on SST in the tropical Indian Ocean: Structure and interannual variability, *Dynamics of Atmospheres and Oceans*, *39*(1-2 SPEC. ISS.), 103–135, doi:10.1016/j.dynatmoce.2004.10.014.

Rast, M., J. L. Bézy, and S. Bruzzi (1999), The ESA Medium Resolution Imaging Spectrometer MERIS a review of the instrument and its mission, *International Journal of Remote Sensing*, *20*(9), 1681–1702, doi:10.1080/014311699212416.

Reason, C. J. (2001), Subtropical Indian Ocean SST dipole events and southern African rainfall, *Geophysical Research Letters*, *28*(11), 2225–2227, doi:10.1029/2000GL012735.

Reason, C. J., R. J. Allan, J. A. Lindesay, and T. J. Ansell (2000), Enso and climatic signals across the Indian Ocean basin in the global context: Part I, Interannual composite patterns, *International Journal of Climatology*, *20*(11), 1285–1327, doi:10.1002/1097-0088(200009)20:11<1285::AID-JOC536>3.0.CO;2-R.

Reid, J. L. (2003), On the total geostrophic circulation of the Indian Ocean: flow patterns, tracers, and transports, *Progress in Oceanography*, *56*(1), 137–186, doi:10.1016/S0079-6611(02)00141-6.

Renault, L., M. J. Molemaker, J. C. McWilliams, A. F. Shchepetkin, F. Lemarié, D. Chelton, S. Illig, and A. Hall (2016), Modulation of Wind Work by Oceanic Current Interaction with the Atmosphere, *Journal of Physical Oceanography*, *46*(6), 1685–1704, doi:10.1175/JPO-D-15-0232.1.

Resplandy, L., J. Vialard, M. Lévy, O. Aumont, and Y. Dandonneau (2009), Seasonal and intraseasonal biogeochemical variability in the thermocline ridge of the southern tropical Indian Ocean, *Journal of Geophysical Research: Oceans*, *114*(7), C07,024, doi:10.1029/2008JC005246.

Richardson, K. (1997), *Harmful or Exceptional Phytoplankton Blooms in the Marine Ecosystem*, vol. Volume 31, 301–385 pp., Elsevier, doi:http://dx.doi.org/10.1016/S0065-2881(08)60225-4.

Richardson, P. L. (1983), Eddy kinetic energy in the North Atlantic from surface drifters, *Journal of Geophysical Research*, *88*(C7), 4355, doi:10.1029/JC088iC07p04355.

Ridderinkhof, W., D. Le Bars, A. S. Von Der Heydt, and W. P. M. De Ruijter (2013), Dipoles of the South East Madagascar Current, *Geophysical Research Letters*, *40*(3), 558–562, doi:10.1002/grl.50157.

Ridgway, K. R., J. R. Dunn, and J. L. Wilkin (2002), Ocean Interpolation by Four-Dimensional Weighted Least Squares–Application to the Waters around Australasia, *Journal of Atmospheric and Oceanic Technology*, *19*(9), 1357–1375.

Riser, S. C., H. J. Freeland, D. Roemmich, S. Wijffels, A. Troisi, M. Belbéoch, D. Gilbert, J. Xu, S. Pouliquen, A. Thresher, P. Y. Le Traon, G. Maze, B. Klein, M. Ravichandran, F. Grant, P. M. Poulain, T. Suga, B. Lim, A. Sterl, P. Sutton, K. A. Mork, P. J. Vélez-Belchí, I. Ansorge, B. King, J. Turton, M. Baringer, and S. R. Jayne (2016), Fifteen years of ocean observations with the global Argo array, *Nature Climate Change*, *6*(2), 145–153, doi:10.1038/nclimate2872.

Robinson, A. (1983), Overview and summary of eddy science, in *Eddies in marine science*, pp. 3–15, Springer.

Robinson, A. R. (2012), *Eddies in marine science*, Springer Science \& Business Media.

Roemmich, D., and J. Gilson (2001), Eddy Transport of Heat and Thermocline Waters in the North Pacific: A Key to Interannual/Decadal Climate Variability?, *Journal of Physical Oceanography*, *31*(3), 675–687, doi:10.1175/1520-0485(2001)031<0675:ETOHAT>2.0.CO;2.

Rouault, M. J., and P. Penven (2011), New perspectives on Natal Pulses from satellite observations, *Journal of Geophysical Research*, *116*(C7), C07,013, doi:10.1029/2010JC006866.

Rouault, M. J., A. Mouche, F. Collard, J. A. Johannessen, and B. Chapron (2010), Mapping the Agulhas Current from space: An assessment of ASAR surface current velocities, *Journal of Geophysical Research*, *115*(C10), C10,026, doi:10.1029/2009JC006050.

Roullet, G., X. Capet, and G. Maze (2014), Global interior eddy available potential energy diagnosed from Argo floats, *Geophysical Research Letters*, *41*(5), 1651–1656, doi:10.1002/2013GL059004.

Roxy, M. K., K. Ritika, P. Terray, and S. Masson (2014), The Curious Case of Indian Ocean Warming* ,+, *Journal of Climate*, *27*(22), 8501–8509, doi:10.1175/JCLI-D-14-00471.1.

Ryther, J. H. (1969), Photosynthesis and Fish Production in the Sea, *Science*, *166*(3901), 72–76, doi:10.1126/science.166.3901.72.

Saji, N. H., B. N. Goswami, P. N. Vinayachandran, and T. Yamagata (1999), A dipole mode in the tropical Indian ocean, *Nature*, *401*(6751), 360–363, doi:10.1038/43855.

Sallée, J. B., K. Speer, R. Morrow, and R. Lumpkin (2008), An estimate of Lagrangian eddy statistics and diffusion in the mixed layer of the Southern Ocean, *Journal of Marine Research*, *66*(4), 441–463, doi:10.1357/002224008787157458.

Sangrà, P., A. Pascual, Á. Rodríguez-Santana, F. Machín, E. Mason, J. C. McWilliams, J. L. Pelegrí, C. Dong, A. Rubio, J. Arístegui, Á. Marrero-Díaz, A. Hernández-Guerra, A. Martínez-Marrero, and M. Auladell (2009), The Canary Eddy Corridor: A major pathway for long-lived eddies in the subtropical North Atlantic, *Deep Sea Research Part I*, *56*(12), 2100–2114, doi:10.1016/j.dsr.2009.08.008.

Sapiano, M. R. P., C. W. Brown, S. Schollaert Uz, and M. Vargas (2012), Establishing a global climatology of marine phytoplankton phenological characteristics, *Journal of Geophysical Research: Oceans*, *117*(C8), doi:10.1029/2012JC007958.

Sarmiento, J. (2013), *Ocean biogeochemical dynamics.*, Princeton University Press.

Schlax, M. G., and D. B. Chelton (2016), The "Growing Method" of Eddy Identification and Tracking in Two and Three Dimensions, *College of Earth, Ocean and Atmospheric Sciences, Oregon State University*.

Schott, F. (1983), Monsoon response of the Somali Current and associated upwelling, *Progress in Oceanography*, *12*(3), 357–381, doi:10.1016/0079-6611(83)90014-9.

Schott, F., M. Fieux, J. Kindle, J. Swallow, and R. Zantopp (1988), The boundary currents east and north of Madagascar: 2. Direct measurements and model comparisons, *Journal of Geophysical Research*, *93*(C5), 4963, doi:10.1029/JC093iC05p04963.

Schott, F. A., and J. P. McCreary (2001), The monsoon circulation of the Indian Ocean, *Progress in Oceanography*, *51*(1), 1–123, doi:10.1016/S0079-6611(01)00083-0.

Schott, F. A., S.-P. Xie, and J. P. McCreary Jr (2009), Indian Ocean Circulation and Climate Variability, *Reviews of Geophysics*, *47*(2007), 1–46, doi:10.1029/2007RG000245.1.INTRODUCTION.

Schouten, M. W., W. P. de Ruijter, and P. J. van Leeuwen (2002), Upstream control of Agulhas Ring shedding, *Journal of Geophysical Research*, *107*(23), 1–11, doi:10.1029/2001JC000804.

Shapiro, G., and S. Meschanov (1991), Distribution and spreading of Red Sea Water and salt lens formation in the northwest Indian Ocean, *Deep Sea Research Part A*, *38*(1), 21–34, doi:10.1016/0198-0149(91)90052-H.

Sharma, G. S. (1976), Water characteristics and current structure at 65°E during the southwest monsoon, doi:10.1007/BF02107985.

Sharma, G. S., A. D. Gouveia, and S. Satyendranath (1978), Incursion of the Pacific Ocean Water into the Indian Ocean, *Journal of Earth System Science*, *87*(3), 29–45.

Shchepetkin, A. F. (2003), A method for computing horizontal pressure-gradient force in an oceanic model with a nonaligned vertical coordinate, *Journal of Geophysical Research*, *108*(C3), 3090, doi:10.1029/2001JC001047.

Shchepetkin, A. F., and J. C. McWilliams (2005), The regional oceanic modeling system (ROMS): A split-explicit, free-surface, topography-following-coordinate oceanic model, *Ocean Modelling*, *9*(4), 347–404, doi:10.1016/j.ocemod.2004.08.002.

Shchepetkin, A. F., and J. C. McWilliams (2009), Computational Kernel Algorithms for Fine-Scale, Multiprocess, Longtime Oceanic Simulations, in *Handbook of Numerical Analysis*, vol. 14, pp. 121–183, Elsevier B.V., doi:10.1016/S1570-8659(08)01202-0.

Shi, W., and M. Wang (2007), Observations of a Hurricane Katrina-induced phytoplankton bloom in the Gulf of Mexico, *Geophysical Research Letters*, *34*(11), 1–5, doi:10.1029/2007GL029724.

Siedler, G., M. Rouault, and J. R. Lutjeharms (2006), Structure and origin of the subtropical South Indian Ocean Countercurrent, *Geophysical Research Letters*, *33*(24), L24,609, doi:10.1029/2006GL027399.

Siedler, G., M. Rouault, A. Biastoch, B. Backeberg, C. J. C. Reason, and J. R. E. Lutjeharms (2009), Modes of the southern extension of the East Madagascar Current, *Journal of Geophysical Research*, *114*(C1), C01,005, doi:10.1029/2008JC004921.

Siegel, D. A., P. Peterson, D. J. McGillicuddy, S. Maritorena, and N. B. Nelson (2011), Bio-optical footprints created by mesoscale eddies in the Sargasso Sea, *Geophysical Research Letters*, *38*(13), 1–6, doi:10.1029/2011GL047660.

Simpson, J. J., and R. J. Lynn (1990), A mesoscale eddy dipole in the offshore California Current, *Journal of Geophysical Research*, *95*(C8), 13,009, doi:10.1029/JC095iC08p13009.

Smith, R. L., A. Huyer, J. S. Godfrey, and J. a. Church (1991), The Leeuwin Current off Western Australia, 1986–1987, doi:10.1175/1520-0485(1991)021<0323:TLCOWA>2.0.CO;2.

Song, Y., and D. Haidvogel (1994), A Semi-implicit Ocean Circulation Model Using a Generalized Topography-Following Coordinate System, *Journal of Computational Physics*, *115*(1), 228–244, doi:10.1006/jcph.1994.1189.

Souza, J. M. A. C., C. de Boyer Montégut, C. Cabanes, and P. Klein (2011), Estimation of the Agulhas ring impacts on meridional heat fluxes and transport using ARGO floats and satellite data, *Geophysical Research Letters*, *38*(21), doi:10.1029/2011GL049359.

Spall, M. a. (1995), Frontogenesis, subduction, and cross-front exchange at upper ocean fronts, *Journal of Geophysical Research*, *100*(C2), 2543, doi:10.1029/94JC02860.

Sprintall, J., A. L. Gordon, R. Murtugudde, and R. D. Susanto (2000), A semiannual Indian Ocean forced Kelvin wave observed in the Indonesian seas in May 1997, *Journal of Geophysical Research*, *105*(C7), 17,217–17,230, doi:10.1029/2000jc900065.

Srokosz, M. A., and G. D. Quartly (2013), The Madagascar Bloom: A serendipitous study, *Journal of Geophysical Research: Oceans*, *118*(1), 14–25, doi:10.1029/2012JC008339.

Srokosz, M. A., G. D. Quartly, and J. J. H. Buck (2004), A possible plankton wave in the Indian Ocean, *Geophysical Research Letters*, *31*(13), doi:10.1029/2004GL019738.

Srokosz, M. A., J. Robinson, H. McGrain, E. E. Popova, and A. Yool (2015), Could the Madagascar bloom be fertilized by Madagascan iron?, *Journal of Geophysical Research: Oceans*, *120*(8), 5790–5803, doi:10.1002/2015JC011075.

Stammer, D. (1997), Global Characteristics of Ocean Variability Estimated from Regional TOPEX/POSEIDON Altimeter Measurements, *Journal of Physical Oceanography*, *27*(8), 1743–1769, doi:10.1175/1520-0485(1997)027<1743:GCOOVE>2.0.CO;2.

Stammer, D. (1998), On Eddy Characteristics, Eddy Transports, and Mean Flow Properties, *Journal of Physical Oceanography*, *28*(4), 727–739, doi:10.1175/1520-0485(1998)028<0727:OECETA>2.0.CO;2.

Stramma, L., and J. R. E. Lutjeharms (1997), The flow field of the subtropical gyre of the South Indian Ocean, *Journal of Geophysical Research*, *102*(15), 5513–5530, doi:10.1029/96JC03455.

Subrahmanyam, B., K. H. Rao, N. Srinivasa Rao, V. S. N. Murty, and R. J. Sharp (2002), Influence of a tropical cyclone on Chlorophyll-a Concentration in the Arabian Sea, *Geophysical Research Letters*, *29*(22), 22–1–22–4, doi:10.1029/2002GL015892.

Swallow, J., M. Fieux, and F. Schott (1988), The Boundary Currents East and North of Madagascar 1. Geostrophic Currents and Transports, *Journal of Geophysical Research*, *93*(7), 4951–4962, doi:10.1029/JC093iC05p04951.

Tagliabue, A., L. Bopp, and O. Aumont (2009), Evaluating the importance of atmospheric and sedimentary iron sources to Southern Ocean biogeochemistry, *Geophysical Research Letters*, *36*(13), L13,601, doi:10.1029/2009GL038914.

Takahashi, T., S. C. Sutherland, R. Wanninkhof, C. Sweeney, R. A. Feely, D. W. Chipman, B. Hales, G. Friederich, F. Chavez, C. Sabine, A. Watson, D. C. Bakker, U. Schuster, N. Metzl, H. Yoshikawa-Inoue, M. Ishii, T. Midorikawa, Y. Nojiri, A. Körtzinger, T. Steinhoff, M. Hoppema, J. Olafsson, T. S. Arnarson, B. Tilbrook, T. Johannessen, A. Olsen, R. Bellerby, C. Wong, B. Delille, N. Bates, and H. J. de Baar (2009), Climatological mean and decadal change in surface ocean pCO2, and net sea–air CO2 flux over the global oceans, *Deep Sea Research Part II: Topical Studies in Oceanography*, *56*(8-10), 554–577, doi:10.1016/j.dsr2.2008.12.009.

Talley, L. D., and J. Sprintall (2005), Deep expression of the Indonesian Throughflow: Indonesian Intermediate Water in the South Equatorial Current, *Journal of Geophysical Research C: Oceans*, *110*(10), 1–30, doi:10.1029/2004JC002826.

Tegen, I., and I. Fung (1995), Contribution to the atmospheric mineral aerosol load from land surface modification., *Journal of Geophysical Research*, *100*, 18,707–18,726.

Tett, P. (1987), The ecophysiology of exceptional blooms, *Rapport et Proces–verbaux des Reunions. Conseil international pour l'Exploration de la Mer*, *187*, 47—-60.

Thomalla, S. J., N. Fauchereau, S. Swart, and P. M. Monteiro (2011), Regional scale characteristics of the seasonal cycle of chlorophyll in the Southern Ocean, *Biogeosciences*, *8*(10), 2849–2866, doi:10.5194/bg-8-2849-2011.

Thomas, L. N. (2008), Formation of intrathermocline eddies at ocean fronts by wind-driven destruction of potential vorticity, *Dynamics of Atmospheres and Oceans*, *45*(3-4), 252–273, doi:10.1016/j.dynatmoce.2008.02.002.

Thompson, R. (1987), Continental-shelf-scale model of the Leeuwin Current, *Journal of Marine Research*, *45*(1984), 813–827.

Thompson, R. O. R. Y. (1984), Observations of the Leeuwin Current off Western Australia, doi:10.1175/1520-0485(1984)014<0623:OOTLCO>2.0.CO;2.

Thomsen, S., T. Kanzow, G. Krahmann, R. J. Greatbatch, M. Dengler, and G. Lavik (2016), The formation of a subsurface anticyclonic eddy in the Peru-Chile Undercurrent and its impact on the near-coastal salinity, oxygen, and nutrient distributions, *Journal of Geophysical Research: Oceans*, *121*(1), 476–501, doi:10.1002/2015JC010878.

Thorpe, S. A. (2007), *An introduction to ocean turbulence*, 1–291 pp., Cambridge University Press., doi:10.1017/CBO9780511801198.

Tomczak, M., and J. S. Godfrey (1994), Regional Oceanography: An Introduction, *Elsevier Science LTD*, *660*, 10,591—-5153.

Trenary, L., and W. Han (2012), Intraseasonal-to-interannual variability of South Indian Ocean sea level and thermocline: Remote versus local forcing, *Journal of Physical Oceanography*, *42*(4), 602–627, doi:http://dx.doi.org/10.1175/JPO-D-11-084.1.

Tsubouchi, T., T. Suga, and K. Hanawa (2010), Indian Ocean Subtropical Mode Water: its water characteristics and spatial distribution, *Ocean Science*, *6*(1), 41–50, doi:10.5194/os-6-41-2010.

Uz, B. M. (2007), What causes the sporadic phytoplankton bloom southeast of Madagascar?, *Journal of Geophysical Research: Oceans*, *112*(9), C09,010, doi:10.1029/2006JC003685.

Valiela, I. (2013), *Marine ecological processes.*, Springer Science & Business Media.

Vinayachandran, P. N., J. Kurian, and C. P. Neema (2007), Indian Ocean response to anomalous conditions in 2006, *Geophysical Research Letters*, *34*(15), 1–6, doi:10.1029/2007GL030194.

Voldsund, A., B. Aguiar-gonzález, T. Gammelsrød, J.-O. Krakstad, and J. Ullgren (2017), Observations of the East Madagascar Current system :, *Journal of Marine Research*, *75*(4), 531–555.

Volkov, D. L., T. Lee, and L. L. Fu (2008), Eddy-induced meridional heat transport in the ocean, *Geophysical Research Letters*, *35*(20), 1–5, doi:10.1029/2008GL035490.

Watson, A. J., C. Robinson, J. E. Robinson, P. J. le B. Williams, and M. J. R. Fasham (1991), Spatial variability in the sink for atmospheric carbon dioxide in the North Atlantic, *Nature*, *350*(6313), 50–53, doi:10.1038/350050a0.

Weaver, A. J., and J. H. Middleton (1989), On the Dynamics of the Leeuwin Current, doi:10.1175/1520-0485(1989)019<0626:OTDOTL>2.0.CO;2.

Wijffels, S., and G. Meyers (2004), An Intersection of Oceanic Waveguides: Variability in the Indonesian Throughflow Region, *Journal of Physical Oceanography*, *34*(5), 1232–1253, doi:10.1175/1520-0485(2004)034<1232:AIOOWV>2.0.CO;2.

Williams, S., M. Petersen, P.-t. Bremer, M. Hecht, V. Pascucci, J. Ahrens, M. Hlawitschka, and B. Hamann (2011), Adaptive Extraction and Quantification of Geophysical Vortices, *IEEE transactions on visualization and computer graphics*, *17*(12), 2088–2095.

Wilson, C. (2003), Late summer chlorophyll blooms in the oligotrophic North Pacific Subtropical Gyre, *Geophysical Research Letters*, *30*(18), 1942, doi:10.1029/2003GL017770.

Wilson, C., and X. Qiu (2008), Global distribution of summer chlorophyll blooms in the oligotrophic gyres, *Progress in Oceanography*, *78*(2), 107–134, doi:10.1016/j.pocean.2008.05.002.

Wong, A. P. S. (2005), Subantarctic Mode Water and Antarctic Intermediate Water in the South Indian Ocean based on profiling float data 2000–2004, *Journal of Marine Research*, *63*(4), 789–812, doi:10.1357/0022240054663196.

Wong, A. P. S., G. C. Johnson, and W. B. Owens (2003), Delayed-Mode Calibration of Autonomous CTD Profiling Float Salinity Data by θ–S Climatology*, *Journal of Atmospheric and Oceanic Technology*, *20*(2), 308–318.

Wyrtki, K. (1962), The oxygen minima in relation to ocean circulation, *Deep Sea Research and Oceanographic Abstracts*, *9*, 11–23, doi:10.1016/0011-7471(62)90243-7.

Wyrtki, K. (1971), *Oceanographic atlas of the international Indian Ocean expedition*, National Science Foundation.

Xie, P., and P. A. Arkin (1997), Global Precipitation: A 17-Year Monthly Analysis Based on Gauge Observations, Satellite Estimates, and Numerical Model Outputs, *Bulletin of the American Meteorological Society*, *78*(11), 2539–2558, doi:10.1175/1520-0477(1997)078<2539:GPAYMA>2.0.CO;2.

Yamada, K., J. Ishizaka, S. Yoo, H.-c. Kim, and S. Chiba (2004), Seasonal and interannual variability of sea surface chlorophyll a concentration in the Japan/East Sea (JES), *Progress in Oceanography*, *61*(December), 193–211, doi:10.1016/j.pocean.2004.06.001.

Yamagata, T., S. K. Behera, J.-J. Luo, S. Masson, M. R. Jury, and S. A. Rao (2004), Coupled ocean-atmosphere variability in the tropical Indian Ocean, *Geophysical Monograph Series*, *147*, 189–211, doi:10.1029/147GM12.

Yang, G., F. Wang, Y. Li, and P. Lin (2013), Mesoscale eddies in the northwestern subtropical Pacific Ocean: Statistical characteristics and three-dimensional structures, *Journal of Geophysical Research: Oceans*, *118*(4), 1906–1925, doi:10.1002/jgrc.20164.

Yang, G., W. Yu, Y. Yuan, X. Zhao, F. Wang, G. Chen, L. Liu, and Y. Duan (2015), Characteristics, vertical structures, and heat/salt transports of mesoscale eddies in the southeastern tropical Indian Ocean, *Journal of Geophysical Research: Oceans*, *120*(10), 6733–6750, doi:10.1002/2015JC011130.

Yoder, J. A., and M. A. Kennelly (2003), Seasonal and ENSO variability in global ocean phytoplankton chlorophyll derived from 4 years of SeaWiFS measurements, *Global Biogeochemical Cycles*, *17*(4), doi:10.1029/2002GB001942.

Yoder, J. A., C. R. McClain, G. C. Feldman, and W. E. Esaias (1993), Annual cycles of phytoplankton chlorophyll concentrations in the global ocean: A satellite view, *Global Biogeochemical Cycles*, *7*(1), 181–193, doi:10.1029/93GB02358.

Yu, J.-Y., and K. M. Lau (2005), Contrasting Indian Ocean SST variability with and without ENSO influence: A coupled atmosphere-ocean GCM study, *Meteorology and Atmospheric Physics*, *90*(3-4), 179–191, doi:10.1007/s00703-004-0094-7.

Yu, W., B. Xiang, L. Liu, and N. Liu (2005), Understanding the origins of interannual thermocline variations in the tropical Indian Ocean, *Geophysical Research Letters*, *32*(24), 1–4, doi:10.1029/2005GL024327.

Zhang, Z., W. Wang, and B. Qiu (2014), Oceanic mass transport by mesoscale eddies, *Science*, *345*(6194), 322–324, doi:10.1126/science.1252418.

Zhang, Z., P. Li, L. Xu, C. Li, W. Zhao, J. Tian, and T. Qu (2015), Subthermocline eddies observed by rapid-sampling Argo floats in the subtropical northwestern Pacific Ocean in Spring 2014, *Geophysical Research Letters*, *42*(15), 6438–6445, doi:10.1002/2015GL064601.

Zhang, Z., R. Lowe, G. Ivey, J. Xu, and J. Falter (2016), The combined effect of transient wind-driven upwelling and eddies on vertical nutrient fluxes and phytoplankton dynamics along Ningaloo Reef, Western Australia, *Journal of Geophysical Research: Oceans*, *121*(7), 4994–5016, doi:10.1002/2016JC011791.

Zheng, S., Y. Du, J. Li, and X. Cheng (2015), Eddy characteristics in the South Indian Ocean as inferred from surface drifters, *Ocean Science*, *11*(3), 361–371, doi:10.5194/os-11-361-2015.

List of Acronyms A

-

AC	-	Agulhas Current
ACC	-	Antarctic Circumpolar Current
ADT	-	Absolute Dynamic Topography
ASHSW	-	Arabian Sea High Salinity Water
BUS	-	Benguela Upwelling System
CROCO	-	Coastal and Regional Ocean Community Model
CUI	-	Coastal Upwelling Index
DCM	-	Deep Chlorophyll Maximum
DOM	-	Dissolved Organic Matter
EACC	-	East African Coastal Current
EEZ	-	Exclusive Economic Zone
EGC	-	Easter Gyral Current
EKE	-	Eddy Kinetic Energy
EMC	-	East Madagascar Current
ENSO	-	El Niño Southern Oscillation
FTLE	-	Finite-time Lyapunov Exponents
FTZD	-	Finite Time Zonal Drift
GEBCO	-	General Bathymetric Chart of the Oceans
GLORYS	-	Global Ocean Reanalysis
IEW	-	Indian Equatorial Water
IOD	-	Indian Ocean Dipole
IOSMW	-	Indian Ocean Subtropical Mode Water
ITCZ	-	Intertropical Convergence Zone

ITF	-	Indonesian Throughflow
LC	-	Leeuwin Current
LCS	-	Lagrangian Coherent Structures
MLD	-	Mixed Layer Depth
MZC	-	Mozambique Channel
NEMC	-	North-East Madagascar Current
NPZD	-	Nutrients Phytoplankton Zooplankton Detritus
PISCES	-	Pelagic Interactions Scheme for Carbon and Ecosystem Studies
POC	-	Pelagic Interactions Scheme for Carbon and Ecosystem Studies
POM	-	Particulate Organic Carbon
ROMS	-	Regional Ocean Modelling System
SEC	-	South Equatorial Current
SEMC	-	South-East Madagascar Current
SICC	-	South Indian Ocean Countercurrent
SICW	-	South Indian Central Water
SIDDIES	-	South Indian Ocean Eddies
SIO	-	South Indian Ocean Dipole
SLA	-	Sea Level Anomaly
SMACC	-	South-west Madagascar Coastal Current
SSH	-	Sea Surface Height
STE	-	Subthermocline Eddy
STUW	-	Subtropical Underwater
subSIDDIES	-	Surface South Indian Ocean Eddies
surfSIDDIES	-	Subsurface South Indian Ocean Eddies
SWIO	-	South-West Indian Ocean
TSW	-	Tropical Surface Water
WSC	-	Wind Stress Curl